

# Applied Research Laboratory

AD-A222 569

## Technical Report

AN EXPERIMENTAL SYSTEM FOR  
MEASURING THE WAVENUMBER-FREQUENCY  
RESPONSE OF TIMOSHENKO BEAMS

by

K. Grosh  
W. J. Hughes  
C. B. Burroughs

DTIC  
ELECTE  
JUN 04 1990  
S E D

PENNSSTATE



**DISTRIBUTION STATEMENT A**

Approved for public release;  
Distribution Unlimited

90 06 01 105

4

The Pennsylvania State University  
**APPLIED RESEARCH LABORATORY**  
P.O. Box 30  
State College, PA 16804

**AN EXPERIMENTAL SYSTEM FOR  
MEASURING THE WAVENUMBER- FREQUENCY  
RESPONSE OF TIMOSHENKO BEAMS**

by

K. Grosh  
W. J. Hughes  
C. B. Burroughs

Technical Report No. TR 90-007  
June 1990

Supported by:  
Space and Naval Warfare Systems Command

L.R. Hettche, Director  
Applied Research Laboratory

Approved for public release; distribution unlimited

**REPORT DOCUMENTATION PAGE**Form Approved  
OMB No. 0704-0188

Public reporting burden for this collection of information is estimated to average 1 hour per response, including the time for reviewing instructions, searching existing data sources, gathering and maintaining the data needed, and completing and reviewing the collection of information. Send comments regarding this burden estimate or any other aspect of this collection of information, including suggestions for reducing this burden, to Washington Headquarters Service, Directorate for Information Operations and Reports, 1215 Jefferson Davis Highway, Suite 1204, Arlington, VA 22202-4302, and to the Office of Management and Budget, Paperwork Reduction Project (0704-0188), Washington, DC 20503.

**1. AGENCY USE ONLY (Leave blank)****2. REPORT DATE**

April 1990

**3. REPORT TYPE AND DATES COVERED****4. TITLE AND SUBTITLE**

An Experimental System for Measuring the Wavenumber-Frequency Response of Timoshenko Beams

**5. FUNDING NUMBERS**

N-00039-88-C-0051

**6. AUTHOR(S)**

K. Grosh, W. J. Hughes, C. B. Burroughs

**7. PERFORMING ORGANIZATION NAME(S) AND ADDRESS(ES)**

Applied Research Laboratory  
Penn State University  
P. O. Box 30  
State College, PA 16801

**8. PERFORMING ORGANIZATION  
REPORT NUMBER**

TR-90-007

**9. SPONSORING/MONITORING AGENCY NAME(S) AND ADDRESS(ES)**

Space and Naval Warfare Systems Command  
Department of the Navy  
Washington, DC 20373-5100

**10. SPONSORING/MONITORING  
AGENCY REPORT NUMBER****11. SUPPLEMENTARY NOTES****12a. DISTRIBUTION/AVAILABILITY STATEMENT**

Distribution "A", approved for public release,  
distribution unlimited

**12b. DISTRIBUTION CODE****13. ABSTRACT (Maximum 200 words)**

The wavenumber-frequency response of Timoshenko beams to multiple point drives is studied in this thesis. An experimental system to excite a free-free Timoshenko beam and measure the resulting velocity is developed. Piezoelectric shakers/force gage units are designed and built to excite the beam and measure the applied forces. Experiments varying the number of shakers used and the wavenumber to which the drive voltage sent to the shakers is steered are performed. The wavenumber-frequency dependence of the force and velocity are measured and compared to theoretical predictions. These comparisons show excellent agreement between the measured and theoretical results. A theoretical investigation into the effect of the velocity measurement array is performed. Also, the finite beam admittance is examined. The piezoelectric shakers are modeled using equivalent circuits, which successfully predict the force output and the force gage sensitivity.

The experiments show that the wavenumber content of the discrete shakers could be steered to the wavenumbers chosen over a wide frequency range (the frequency range of measurement was 2-12 kHz). The finite beam admittance is shown to approach the infinite beam admittance in regions where the wavenumber content of the forcing function are high.

**14. SUBJECT TERMS**

wavenumber-frequency response, Timoshenko beam  
shaker

**15. NUMBER OF PAGES****16. PRICE CODE****17. SECURITY CLASSIFICATION  
OF REPORT**

Unclassified

**18. SECURITY CLASSIFICATION  
OF THIS PAGE**

Unclassified

**19. SECURITY CLASSIFICATION  
OF ABSTRACT**

Unclassified

**20. LIMITATION OF ABSTRACT**

UL

## ABSTRACT

The wavenumber-frequency response of Timoshenko beams to multiple point drives is studied in this thesis. An experimental system to excite a free-free Timoshenko beam and measure the resulting velocity is developed. Piezoelectric shakers/force gage units are designed and built to excite the beam and measure the applied forces. Experiments varying the number of shakers used and the wavenumber to which the drive voltage sent to the shakers is steered are performed. The wavenumber-frequency dependence of the force and velocity are measured and compared to theoretical predictions. These comparisons show excellent agreement between the measured and theoretical results. A theoretical investigation into the effect of the velocity measurement array is performed. Also, the finite beam admittance is examined. The piezoelectric shakers are modeled using equivalent circuits, which successfully predict the force output and the force gage sensitivity.

The experiments show that the wavenumber content of the discrete shakers could be steered to the wavenumbers chosen over a wide frequency range (the frequency range of measurement was 2-12 kHz). The finite beam admittance is shown to approach the infinite beam admittance in regions where the wavenumber content of the forcing function are high.



Accession For	
NTIS GRA&I	<input checked="" type="checkbox"/>
DTIC TAB	<input checked="" type="checkbox"/>
Unannounced	<input type="checkbox"/>
Justification	<input type="checkbox"/>
By _____	
Distribution/	
Availability Codes	
Dist _____	
A-1	

## TABLE OF CONTENTS

	<u>Page</u>
LIST OF FIGURES .....	vii
LIST OF TABLES .....	xiv
ACKNOWLEDGMENTS .....	xv
<u>Chapter</u>	
1. INTRODUCTION .....	1
1.1. Literature Review .....	3
1.2. Experimental Approach .....	4
1.2.1. Experimental Method .....	4
1.2.2. System Requirements .....	5
1.3. Outline of Thesis .....	7
2. DESCRIPTION OF EXPERIMENTS .....	9
2.1. Introduction .....	9
2.2. Experimental Description .....	9
2.2.1. Beam Geometry .....	9
2.2.2. Experimental Test Matrix .....	10
2.2.3. Measurement Instrumentation and Procedure .....	11
2.3. Shaker/Force Gage Units .....	15
2.3.1. Shaker/Force Gage Design .....	16
2.3.2. Construction .....	20
2.3.3. Force Gage Calibration .....	21

## TABLE OF CONTENTS (continued)

<u>Chapter</u>	<u>Page</u>
2.4. Signal Processing Aspects .....	23
2.4.1. Discrete Fourier Transform of the Velocity .....	26
2.4.2. Wavenumber-Frequency Sensitivity of Arrays .....	27
2.4.3. Windowing Considerations .....	33
2.4.4. Spacing of the Accelerometers for the Experiments .....	35
2.4.5. Wavenumber Content of an Array of Point Forces ...	35
2.4.6. Steering the Wavenumber Content of an Array of Point Forces .....	36
3. BEAM THEORY .....	42
3.1. Introduction .....	42
3.2. Spatial-Frequency Response of a Finite Beam .....	42
3.3. Forced Spatial-Frequency Response of a Finite Beam .....	47
3.4. Wavenumber Response of a Finite Beam .....	48
3.5. Wavenumber Response of an Infinite Beam .....	52
3.6. Relationship between Force and Velocity in Wavenumber Space for a Finite Beam .....	56
4. EQUIVALENT CIRCUIT MODELLING OF THE SHAKER/FORCE GAGE UNIT .....	63
4.1. Introduction .....	63
4.2. Equivalent Circuit Analysis for Transducers .....	63
4.3. Equivalent Circuit Model for Shaker Force Output .....	68
4.4. Equivalent Circuit Model for Force Gage Section .....	73

## TABLE OF CONTENTS (continued)

<u>Chapter</u>	<u>Page</u>
5. EXPERIMENTAL AND THEORETICAL RESULTS .....	80
5.1. Introduction .....	80
5.2. Theoretical versus Measured Spatial-Frequency Response ..	80
5.3. Effects of the Spatial Measurement Array.....	96
5.4. Wavenumber-Frequency Dependence of the Force and Velocity .....	109
5.4.1. Nine Shaker Experiments .....	111
5.4.2. Seventeen Shaker Experiments .....	127
5.5. Relationship between Force and Velocity in Wavenumber-Space .....	149
6. CONCLUSIONS AND RECOMMENDATIONS .....	159
6.1. Conclusions .....	159
6.2. Recommendations .....	160
APPENDIX A: PVF-2 FORCE GAGE DESIGN .....	161
APPENDIX B: MASS LOADING OF THE FORCE GAGE .....	164
APPENDIX C: CITED COMPUTER CODE.....	167
APPENDIX D: EXPERIMENTAL EXCEPTIONS .....	193
BIBLIOGRAPHY .....	195

## LIST OF FIGURES

<u>Figure</u>		<u>Page</u>
1.1	Discrete forcing function weighted to a wavenumber (after Hutto [9]).....	6
2.1	Photograph of nine shakers glued to the beam.....	12
2.2	Flow chart of the measurement system.....	13
2.3	Final shaker/force gage design. ....	17
2.4	Calibration system.....	22
2.5	Maximum and minimum force sensitivity (amplitude and phase) for five shakers.....	24
2.6	Geometry of single sensor in a velocity field. ....	28
2.7	Multiple sensors in a velocity field.....	31
2.8	Shifted and unshifted force spectra for nine shakers, (a) $k_d = 0. \text{ cm}^{-1}$ , (b) $k_d=0.332 \text{ cm}^{-1}$ .....	38
2.9	Shifted and unshifted force spectra for seventeen shakers, (a) $k_d = 0. \text{ cm}^{-1}$ , (b) $k_d=0.332 \text{ cm}^{-1}$ .....	39
2.10	Effect of Kaiser-Bessel window on unshifted spectra, (a) for nine shakers, (b) for seventeen shakers.....	41
3.1	Location of the poles and contours for the residue evaluation.	55
3.2	The dispersion relation for the beam used in the experiment. The freebending wavenumbers for the infinite beam are shown as well as the resonant wavenumbers (and frequencies) for the finite beam. ....	57
4.1	Equivalent circuit for (a) piezoelectric 33 coupled sections, (b) Non-piezoactive sections [23]. ....	65
4.2	Local coordinate system for the ceramic.....	67
4.3	Low frequency equivalent circuit for (a) piezoelectric sections, (b) non-piezoactive sections. ....	69
4.4	Equivalent circuit model for the force output of the transducer.	71

## LIST OF FIGURES (continued)

<u>Figure</u>		<u>Page</u>
4.5	Equivalent circuit model for the forced output of the transducer with electrical elements transformed into the mechanical domain.....	73
4.6	Transmitting voltage response for unloaded shaker, theory versus experiment.....	74
4.7	Equivalent circuit for force gage sensitivity. ....	76
5.1	Comparison of the theoretical and experimental driving-point admittance, magnitude (dB re 1 cm/dyne-s) and phase for Experiment 7 at the location $\xi = 0.5$ . ....	82
5.2	Comparison of the theoretical and experimental transfer admittance, magnitude (dB re 1 cm/dyne-s) and phase for Experiment 7 at the location $\xi = 0.368$ . ....	84
5.3	Comparison of the theoretical and experimental transfer admittance, magnitude (dB re 1 cm/dyne-s) and phase for Experiment 7 at the location $\xi = 0.632$ . ....	85
5.4	Comparison of the theoretical and experimental transfer admittance, magnitude (dB re 1 cm/dyne-s) and phase for Experiment 7 at the location $\xi = 0.078$ . ....	86
5.5	Comparison of the theoretical and experimental transfer admittance, magnitude (dB re 1 cm/dyne-s) and phase for Experiment 1 at the location $\xi = 0.368$ . ....	88
5.6	Comparison of the theoretical and experimental transfer admittance, magnitude (dB re 1 cm/dyne-s) and phase for Experiment 2 at the location $\xi = 0.368$ . ....	89
5.7	Comparison of the theoretical and experimental transfer admittance, magnitude (dB re 1 cm/dyne-s) and phase for Experiment 3 at the location $\xi = 0.368$ . ....	90
5.8	Comparison of the theoretical and experimental transfer admittance, magnitude (dB re 1 cm/dyne-s) and phase for Experiment 4 at the location $\xi = 0.368$ . ....	91
5.9	Comparison of the theoretical and experimental transfer admittance, magnitude (dB re 1 cm/dyne-s) and phase for Experiment 5 at the location $\xi = 0.368$ . ....	92

## LIST OF FIGURES (continued)

<u>Figure</u>		<u>Page</u>
5.10	Comparison of the theoretical and experimental transfer admittance, magnitude (dB re 1 cm/dyne-s) and phase for Experiment 6 at the location $\xi = 0.368$ .....	93
5.11	Comparison of the theoretical and experimental transfer admittance, magnitude (dB re 1 cm/dyne-s) and phase for Experiment 8 at the location $\xi = 0.368$ .....	94
5.12	Comparison of the theoretical and experimental transfer admittance, magnitude (dB re 1 cm/dyne-s) and phase for Experiment 9 at the location $\xi = 0.368$ .....	95
5.13	The Fourier transform of the array function for 37 accelerometers with a spacing of 1 cm.....	97
5.14	The Fourier transform of the array function for nineteen accelerometers with a spacing of 2 cm.....	98
5.15	The Fourier transform of the array function for nine accelerometers with a spacing of 4 cm.....	99
5.16	Comparison of the magnitude of the continuous and discrete Fourier transforms of the velocity for Experiment 9 at a frequency of 8 kHz. The array for the FFT consisted of 37 elements ( $\Delta x = 1.02$ cm).....	101
5.17	Comparison of the magnitude of the continuous and discrete Fourier transforms of the velocity for Experiment 9 at a frequency of 8 kHz. The array for the FFT consisted of 19 elements ( $\Delta x = 2$ cm).....	103
5.18	Comparison of the magnitude of the continuous and discrete Fourier transforms of the velocity for Experiment 9 at a frequency of 8 kHz. The array for the FFT consisted of nine elements ( $\Delta x = 4$ cm).....	104
5.19	Comparison of the magnitude of the continuous and discrete Fourier transforms of the velocity for Experiment 9 at a frequency of 8 kHz. The array for the FFT consisted of 21 elements ( $\Delta x = 1.8$ cm).....	105
5.20	Wavenumber content of the force relative to the center shaker for Experiment 9 at a frequency of 8 kHz.....	107

## LIST OF FIGURES (continued)

<u>Figure</u>		<u>Page</u>
5.21	Comparison of the magnitude of the continuous and discrete Fourier transforms of the velocity for Experiment 9 at a frequency of 8 kHz. The array for the FFT consisted of 37 elements ( $\Delta x = 1.0$ cm).....	108
5.22	Comparison of the magnitude of the continuous and discrete Fourier transforms of the velocity for Experiment 9 at a frequency of 8 kHz. The array for the FFT consisted of seventeen elements ( $\Delta x = 2.0$ cm), placed at the shaker locations.....	110
5.23	Wavenumber-frequency surface-contour plot of the measured force spectrum for Experiment 1. Force relative to $F_c(\omega)$ . ....	112
5.24	Wavenumber-frequency surface-contour plot of the predicted velocity spectrum (spectrum via the continuous transform) for Experiment 1. Velocity relative to $F_c(\omega)$ . ....	115
5.25	Wavenumber-frequency surface-contour plot of the predicted velocity spectrum (spectrum via the FFT) for Experiment 1. Velocity relative to $F_c(\omega)$ . ....	116
5.26	Wavenumber-frequency surface-contour plot of the measured velocity spectrum for Experiment 1. Velocity relative to $F_c(\omega)$ . ....	117
5.27	Comparison of the magnitude of the predicted versus the measured spectrum for Experiment 1 at a frequency of 11.5 kHz..	119
5.28	Wavenumber-frequency surface-contour plot of the measured force spectrum for Experiment 2. Force relative to $F_c(\omega)$ . ....	120
5.29	Wavenumber-frequency surface-contour plot of the predicted velocity spectrum (spectrum via the continuous transform) for Experiment 2. Velocity relative to $F_c(\omega)$ . ....	121
5.30	Wavenumber-frequency surface-contour plot of the measured velocity spectrum for Experiment 2. Velocity relative to $F_c(\omega)$ . ....	122
5.31	Wavenumber-frequency surface-contour plot of the measured force spectrum for Experiment 3. Force relative to $F_c(\omega)$ . ....	124
5.32	Wavenumber-frequency surface-contour plot of the predicted velocity spectrum (spectrum via the continuous transform) for Experiment 3. Velocity relative to $F_c(\omega)$ . ....	125

## LIST OF FIGURES (continued)

<u>Figure</u>		<u>Page</u>
5.33	Wavenumber-frequency surface-contour plot of the measured velocity spectrum for Experiment 3. Velocity relative to $F_c(\omega)$ .	126
5.34	Wavenumber-frequency surface-contour plot of the measured force spectrum for Experiment 4. Force relative to $F_c(\omega)$ . ....	127
5.35	Wavenumber-frequency surface-contour plot of the predicted velocity spectrum (spectrum via the continuous transform) for Experiment 4. Velocity relative to $F_c(\omega)$ . ....	129
5.36	Wavenumber-frequency surface-contour plot of the measured velocity spectrum for Experiment 4. Velocity relative to $F_c(\omega)$ .	130
5.37	Wavenumber-frequency surface-contour plot of the measured force spectrum for Experiment 5. Force relative to $F_c(\omega)$ . ....	132
5.38	Wavenumber-frequency surface-contour plot of the predicted velocity spectrum (spectrum via the continuous transform) for Experiment 5. Velocity relative to $F_c(\omega)$ . ....	133
5.39	Wavenumber-frequency surface-contour plot of the measured velocity spectrum for Experiment 5. Velocity relative to $F_c(\omega)$ .	134
5.40	Wavenumber-frequency surface-contour plot of the measured force spectrum for Experiment 6. Force relative to $F_c(\omega)$ . ....	135
5.41	Wavenumber-frequency surface-contour plot of the predicted velocity spectrum (spectrum via the continuous transform) for Experiment 6. Velocity relative to $F_c(\omega)$ . ....	136
5.42	Wavenumber-frequency surface-contour plot of the measured velocity spectrum for Experiment 6. Velocity relative to $F_c(\omega)$ .	137
5.43	Wavenumber-frequency surface-contour plot of the measured force spectrum for Experiment 7. Force relative to $F_c(\omega)$ . ....	138
5.44	Wavenumber-frequency surface-contour plot of the predicted velocity spectrum (spectrum via the continuous transform) for Experiment 7. Velocity relative to $F_c(\omega)$ . ....	139
5.45	Wavenumber-frequency surface-contour plot of the measured velocity spectrum for Experiment 7. Velocity relative to $F_c(\omega)$ .	140

## LIST OF FIGURES (continued)

<u>Figure</u>		<u>Page</u>
5.46	Wavenumber-frequency surface-contour plot of the measured force spectrum for Experiment 8. Force relative to $F_c(\omega)$ . ....	141
5.47	Wavenumber-frequency surface-contour plot of the predicted velocity spectrum (spectrum via the continuous transform) for Experiment 8. Velocity relative to $F_c(\omega)$ . ....	142
5.48	Wavenumber-frequency surface-contour plot of the measured velocity spectrum for Experiment 8. Velocity relative to $F_c(\omega)$ . ....	143
5.49	Wavenumber-frequency surface-contour plot of the measured force spectrum for Experiment 9. Force relative to $F_c(\omega)$ . ....	145
5.50	Wavenumber-frequency surface-contour plot of the predicted velocity spectrum (spectrum via the continuous transform) for Experiment 9. Velocity relative to $F_c(\omega)$ . ....	146
5.51	Wavenumber-frequency surface-contour plot of the measured velocity spectrum for Experiment 9. Velocity relative to $F_c(\omega)$ . ....	147
5.52	Comparison of the magnitude of the predicted spectrum versus the measured spectrum for Experiment 9 at a frequency of 11.9 kHz. ....	148
5.53	Plots of the analytic and experimental finite beam admittance along with the admittance of the infinite beam at $k_x = 0$ . $\text{cm}^{-1}$ for (a) Experiment 1 and (b) Experiment 5. ....	151
5.54	Plots of the analytic and experimental finite beam admittance along with the admittance of the infinite beam at $k_x = 0.147 \text{ cm}^{-1}$ for (a) Experiment 2 and (b) Experiment 6. ....	152
5.55	Plots of the analytic and experimental finite beam admittance along with the admittance of the infinite beam at $k_x = 0.344 \text{ cm}^{-1}$ for (a) Experiment 3 and (b) Experiment 7. ....	153
5.56	Plots of the analytic and experimental finite beam admittance along with the admittance of the infinite beam at $k_x = 0.74 \text{ cm}^{-1}$ for (a) Experiment 4 and (b) Experiment 8. ....	155
5.57	Plot of the analytic and experimental finite beam admittance along with the admittance of the infinite beam at $k_x = 1.57 \text{ cm}^{-1}$ for Experiment 9. ....	156

## LIST OF FIGURES (continued)

<u>Figure</u>		<u>Page</u>
5.58	Plot of the analytic and experimental finite beam admittance along with the admittance of the infinite beam at $k_x = 0.69 \text{ cm}^{-1}$ for Experiment 2.....	157
A.1	Schematic of the PVF-2 force gage design. ....	162
B.1	Measured versus corrected driving point admittance for Experiment 3 at the center of the beam. ....	166

## LIST OF TABLES

<u>Table</u>		<u>Page</u>
2.1	Steel material parameters used in this thesis.....	10
2.2	Experimental test matrix. ....	11
2.3	Dimensions and materials used in the transducer. ....	16
2.4	Sensitivities of the force gages.....	25
3.1	Resonant frequencies and wavenumbers.....	58
4.1	Nominal material properties.....	72
4.2	Material properties for PZT-4.....	72
A.1	Materials used in PVF-2 transducer.....	163

## ACKNOWLEDGMENTS

The author wishes to thank his thesis advisors, Dr. W. Jack Hughes and Dr. Courtney B. Burroughs. Their guidance, support and friendship were invaluable in the completion of this thesis. This work was supported by the Exploratory and Foundational research program at the Applied Research Lab under Dr. Richard Stern.

The author would also like to thank a few of the people who assisted the author in this research. The author is appreciative of the efforts of Fredrick M. Hutto, whose initial work on this topic and computer code form a basis for this research. The author is indebted to Dale J. Sackrider for technical support and cooperation in showing him the procedures for data acquisition and transducer construction. Also, James E. Phillips is acknowledged for his invaluable assistance in the construction of the shakers and his aid in computer programming. The active participation of Dr. Roger L. Kerlin in this research is appreciated by the author. The author also thanks Dr. William Thompson, Jr., for valuable assistance in the modelling of shaker/force gage units. The author wishes to thank Dr. Richard P. McNitt for being a member of the thesis committee.

Finally, the author wishes to express his deepest appreciation for the support and love of his family during his education; to his parents, Ann and John, for their enthusiastic support, guidance and financial assistance throughout his educational endeavors; and to his wife, Linda, for her understanding attitude and her constant positive encouragement. Without their aid, this thesis may never have been completed.

## Chapter 1

### INTRODUCTION

The interaction of the pressure fluctuations beneath a turbulent boundary layer (TBL) and a structure cause that structure to vibrate. These vibrations may cause unwanted effects such as radiated noise in jet aircraft, spacecraft, naval vehicles and air conditioning systems; or self noise in transducer systems. The TBL pressure fluctuations can usually be described as random stationary processes in space and time. It is generally useful to characterize the spatial and temporal variations in terms of their Fourier transforms, wavenumber and frequency. The vibrations of a structure excited by these pressure fields also are random stationary processes. It is the wavenumber-frequency dependence of these structural vibrations that is of interest in this study.

The wavenumber-frequency response of the forced transverse vibrations of a one-dimensional structure, represented by a beam, is under consideration for this study. The excitation consists of discrete shakers with measured force levels instead of random pressure fluctuations. The velocity is sampled along the length of the beam. Both the force and velocity spatial distributions are transformed into wavenumber-frequency space via the Fourier transform. As the frequency response of structures is generally well understood and easy to measure, the emphasis of this study is placed on understanding the wavenumber response.

The general objective of this study is to characterize the wavenumber filtering characteristics of a finite beam over a large region of wavenumber-frequency space. The study is both theoretical and experimental. Results from theoretical models on the beam response, characteristics of the shakers used to excite the beam and algorithms used in taking Fourier transforms over spatially finite domains are used to assist in the design of the experiments and analysis of the

measurement results.

Just as an impulsive load in time has a white or flat frequency spectrum, so does a spatially impulsive load (i.e. a point source). Initially it seems, a good method would be to excite the beam with a single shaker and measure the wavenumber velocity response with an array of accelerometers. As the input force wavenumber spectrum would be flat, all velocity wavenumbers would be excited. However, there are several difficulties with this idea. One is the fact that the spatial location of the shaker is important to the velocity, not just the relative distance between the excitation point and the measurement sensor. Hence, even at a single frequency, the output wavenumber velocity spectrum will depend on the location of the drive force. Two, the beam is a fairly selective wavenumber filter. At any frequency there is a preferred wavenumber, the freebending wavenumber, at which the velocity response of the beam will peak. This is the wavenumber that corresponds to the wavelength of a freely propagating wave on an infinite beam at that frequency. Measurement of the beam response at this wavenumber is easy because the signal is very high. With only one point force exciting the structure, the freebending wavenumber would dominate the response making measurement at other wavenumbers difficult. In an attempt to excite the beam to measurable levels at wavenumbers other than the freebending wavenumber, a forcing function weighted to a particular wavenumber other than the freebending wavenumber could be used. This requires multiple point drives to be used. In this way, the energy of force excitation as well as the velocity response would be concentrated in a region of wavenumber-frequency space centered around the drive wavenumber. The velocity response would be measured by the accelerometer array, which provides a further concentration of the measurement in the desired wavenumber frequency region.

The philosophy of driving the beam at a particular wavenumber is similar to steady state frequency analysis. The difference is that in the temporal domain a signal of indefinite length can be used while spatially the signal length is limited to the length of the structure. Indeed, the meaning of Fourier transforms over the finite length of the structure is different than that for the infinite domain.

What is proposed is the development of a system to measure the wavenumber-frequency characteristics of a beam by using multiple point drives and measuring the velocity response with an array of accelerometers. Hence, it is necessary to understand the theoretical aspects and hardware realization of the measurement system. Predictions of the response of the beam are derived so that experimental results on both point admittances and wavenumber spectra may be validated. The signal processing necessary to measure the wavenumber spectra of the force and the velocity is developed. The signal processing aspects of imposing the desired spatial force distribution on the beam is also derived. The transducers for exciting the beam and measuring the exciting forces are developed as well as an equivalent circuit model to predict the response of the force transducer. Finally, the equipment and procedure used for data acquisition are developed.

### 1.1. Literature Review

The early work on the wavenumber response of structures seems to be motivated by the need to understand the vibrations induced by jet and rocket TBL pressure fluctuations [1,2]. Some of the later work is more motivated toward the measurement of flow induced TBL due to vehicles moving through a fluid [3,4]. Essentially, each of these papers studies the relation between the applied pressure field and the resulting vibration or radiated pressure due to the induced vibration.

Starting with Uberoi and Kovasznay [5], the wavenumber sensitivity of

sensors with finite extent has been studied. Maidanik and Jorgensen [6] developed the wavenumber sensitivity of arrays of flush mounted pressure transducers. Blake and Chase [7] examine arrays of pressure sensors with more complicated wavenumber pressure sensitivity. In this thesis, the sensitivity of arrays of accelerometers is predicted using the analysis of Blake and Chase [7] as well as of Gaskill [8].

Hutto [9] investigated the use of multiple point drives weighted to a wavenumber to excite a beam. His theoretical study into this method forms some of the basis of this research. Roberts and Sabot [10] employ a similar technique utilizing multiple point drives. However, they attempt to simulate the TBL pressure fluctuations on a plate. Hutto's work on the response of Timoshenko beams to point drives is extended in this thesis. The multiple shaker system is constructed and experiments are compared to theoretical predictions based on Timoshenko beam theory. A system for the measurement of the wavenumber-frequency pressure response of structures is discussed by Strawderman [11].

## 1.2. Experimental Approach

The basic experimental approach employed in the remainder of this thesis for measuring the wavenumber-frequency response of a beam is outlined in this section. Also discussed are the analytic and experimental requirements imposed by the proposed system which forms much of the basis for this thesis.

### 1.2.1. Experimental Method

The experimental method consists of driving the structure at a particular wavenumber and measuring the velocity response as a function of frequency. To achieve the force distribution, multiple drivers are placed along the length of the beam. The voltage input to the shakers is weighted to a particular

wavelength by setting the voltage inputs to the shakers to  $\cos(k_d x_m)$ , where  $k_d$  is the drive wavenumber and  $x_m$  is the location of a shaker. The resulting velocity distribution is measured by an accelerometer placed at discrete points along the beam using a common reference. The Fourier transforms of the force and velocity are performed to obtain the wavenumber response of both quantities. It is the relationship between these wavenumber dependencies that characterizes the spatial filtering action of the beam or the admittance of the finite beam in wavenumber-frequency space.

A typical force amplitude distribution weighted to a particular wavenumber is shown in Figure 1.1. By using multiple drives in a standing wave pattern, the peak of the forced wavenumber content is steered to the drive wavenumber,  $k_d$ , without the need for continuous control of the phase of each of the drive voltages, as would be required by a traveling wave pattern. The measurement of the velocity distribution by the array of accelerometers also allows a filtering of the wavenumber dependence. The use of the discrete Fourier transform applied to the velocity data, steers the measurement wavenumber to the different bins of the discrete transform (Chapter 2). The hardware and analytic implications of this method are described next.

### 1.2.2. System Requirements

Clearly, one of the most important requirements is the need for multiple shakers (force exciters). Because the force is to be measured at each excitation point, each shaker must have an integral force gage. Measurement of the force is required for two main reasons. First, the force measurement allows for the determination of whether or not the force wavenumber spectrum tracks with the applied drive voltage wavenumber spectrum. A feedback-control system could be used to control the force at each of the shakers, but this is a much more

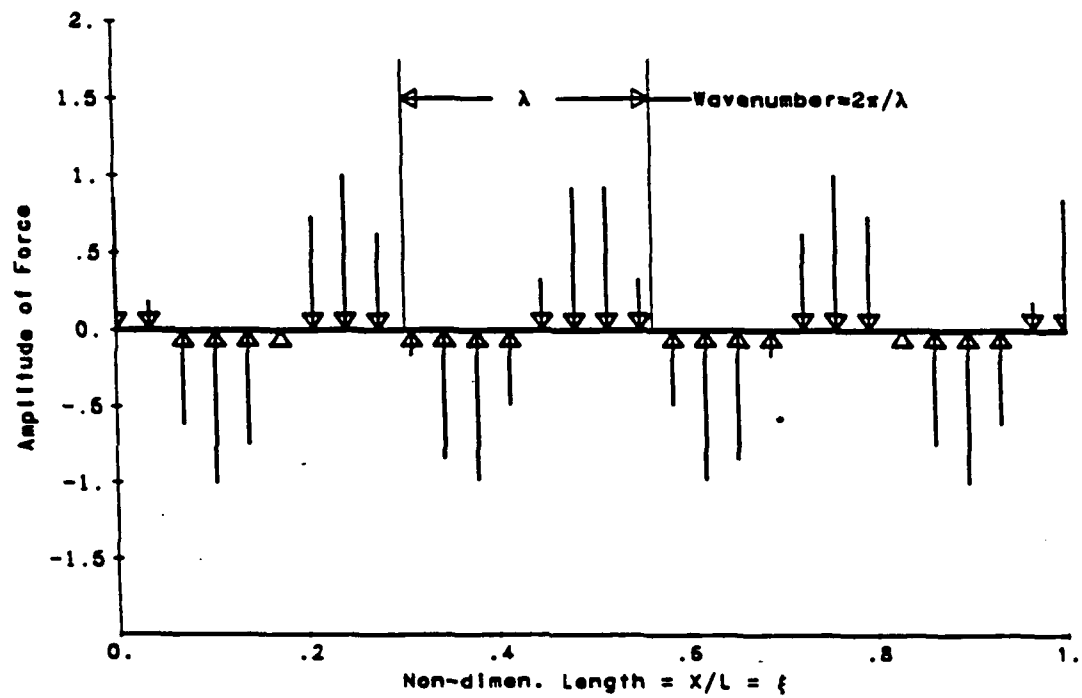


Figure 1.1 Discrete forcing function weighted to a wavenumber (after Hutto [9]).

complicated implementation. Second, the forces at each of the shakers are the input to the analytic models which predict the velocity along the beam. To prescribe the desired drive voltage distribution, a multiple channel amplitude weighting system is essential. This amplitude weighting system must have the ability to drive each of the shakers at an arbitrary amplitude (real, positive or negative amplitude). The requirement of one channel per shaker is cut in half by using a symmetric weighting pattern as in Figure 1.1. The weighting distribution used is symmetric about the center and equal to  $\cos k_d(x - L/2)$ , where  $L$  is the length of the beam. The velocity of the beam at an array of locations must be measured.

Both the force and velocity measurements must be transformed into wave-number space via Fourier transforms. Because the velocity may only be measured at discrete points, the continuous Fourier transform is simulated by the discrete Fourier transform. Because of the finite length of the beam, the velocity and force only exist over a finite length.

Validation of the measurements is required. The force gages must be calibrated and resonant effects in the force gages identified. This requires analytic modeling of the shaker/force gage units used in the measurements. Also, results from the measured response of the beam must be validated. Analytic modeling of the beam response is employed to validate the measurement results.

### 1.3. Outline of Thesis

In Chapter 2, the means by which the wavenumber-frequency spectra of the force and velocity are measured is described. The entire experimental measurement system is described. The basis for the signal processing assumptions is presented. A description of the shaker/force gage unit is given. In Chapter 3, the analytic model for Timoshenko beams is derived and discussed.

First the spatial-frequency response of free-free beams to multiple point drives is derived following Hutto [9]. The wavenumber-frequency response of free-free finite beams and infinite beams is developed. Finally, the relationship between the wavenumber content of the forcing function and the velocity response is examined. In Chapter 4 the combination force gage/shaker units are modeled using equivalent circuit analysis. The results of the experiments are compared to the various theoretical results in Chapter 5. Lastly, the conclusions and recommendations for future research are drawn in Chapter 6.

## Chapter 2

### DESCRIPTION OF MEASUREMENTS

#### 2.1. Introduction

In this chapter, the implementation of the experimental method proposed in Chapter 1 is described. First, a general outline of the experiments is given; including descriptions of the experiments, measurement system and procedure. The design, construction and calibration of the shaker/force gage units follow the experimental description. Next, the signal processing used both to process the force and velocity data as well as calculate the amplitudes of the voltages sent to the shakers is presented. The analysis in this final section spells out the various assumptions made in the signal processing aspects of handling the data.

#### 2.2. Experimental Description

In this section, the overall description of the experiments is presented. First, the beam geometry and material properties are listed. The forcing functions that define the nine experiments performed are described next. The system and procedure by which the force and velocity data are obtained are detailed. Also, the means of force excitation is given. Finally, general aspects of performing the experiments are enumerated.

##### 2.2.1. Beam Geometry

The steel beam used in the experiments is 37.9 cm long by 1.27 cm wide by 1.92 cm high (or thick). The material properties of the beam are listed in Table 2.1. The length of the beam was determined by two constraints. The number of channels available for driving the shakers is ten; using a symmetric weighting function with respect to the center of the beam the number of shakers

that could be driven is nineteen (with the center shaker having no symmetric pair). The closest center to center shaker spacing that is feasible is 2 cm; hence a 38 cm beam would be fully covered by nineteen shakers.

Table 2.1 Steel material parameters used in this thesis.

Material Parameter	Symbol	Value (units)
Elastic Modulus	$E$	$210 \times 10^{10}$ (dyne/cm <sup>2</sup> )
Shear Modulus	$G$	$77 \times 10^{10}$ (dyne/cm <sup>2</sup> )
Density	$\rho$	7.8 (grams/cm <sup>3</sup> )
Damping Loss Factor	$\eta$	.05 <sup>#1</sup>

<sup>#1</sup> This is the damping loss factor of shaker-beam system, not just of the steel beam.

The beam is supported on two highly porous foam wedges, typically used in air anechoic rooms. Hutto [9] showed that this method of support closely approximates a free boundary condition. One of the drawbacks to the use of the wedges is that approximately 1 cm is required to support the beam at either end. Hence, for the 2 cm shaker separation distance, only seventeen and not nineteen shakers could be used. This is because there is not enough room to place the last two shakers on the beam and still properly support the beam.

The beam was scored at 1 cm intervals to aide in the location of the shakers and the accelerometer. The first mark is at 0.95 cm and the last mark is at 36.95 cm. These spacings are symmetric with respect to the middle of the beam. It is at each scored location that the acceleration is measured.

### 2.2.2. Experimental Test Matrix

The experimental test matrix is shown on Table 2.2. The values under the heading "wavelengths across the beam" are equal to the drive wavelength (see Figure 1.1) divided by the length of the beam. The drive wavenumber is  $k_d =$

$2\pi/\lambda$ . The nine shakers were located 4 cm apart emanating from the center of the beam; with four shakers to the left of center shaker and four to the right of the center. The seventeen shakers were spaced 2 cm apart, also symmetrically from the center. The procedure by which the voltage amplitudes are determined is detailed later in this chapter in the section on signal processing.

Table 2.2 Experimental test matrix.

Experiment No.	Wavelengths Across the Beam	Drive Wavenumber ( $\text{cm}^{-1}$ )	Number of Shakers
1	0	0.000	9
2	1	0.166	9
3	2	0.332	9
4	4.5	0.746	9
5	0	0.000	17
6	1	0.166	17
7	2	0.332	17
8	4.5	0.746	17
9	9	1.492	17

### 2.2.3. Measurement Instrumentation and Procedures

The overall plan for the measurement scheme is outlined in Chapter 1. Each experiment is characterized by the number of shakers used to excite the beam and the voltage distribution applied to the shakers. For each of the experiments, the spatial distribution of both the force and velocity must be measured in order to describe the wavenumber-frequency filtering characteristics of the beam. A description of the instrumentation and procedure by which the force and velocity are measured, as well as the means of exciting the beam, are found in this section.

The shakers are glued to the beam using epoxy (Epoxy-Patch 309 gray made by the Hysol division of Dexter). Before attaching the shakers with this fast

setting, high tensile strength epoxy, all surfaces must be cleaned. First, any rust is removed from the beam by using steel wool. Then, both the attachment point on the beam and the shaker headmass are cleaned using a three part process. First, a cotton swab is immersed in toluene and rubbed on the surface to be cleaned until no further residue can be seen. This procedure is repeated with alcohol and then acetone. After the surfaces are cleaned, each surface is coated with epoxy and held together either by hand or by a vise until set. In Figure 2.1, a photograph of seventeen shakers glued to the beam is shown.

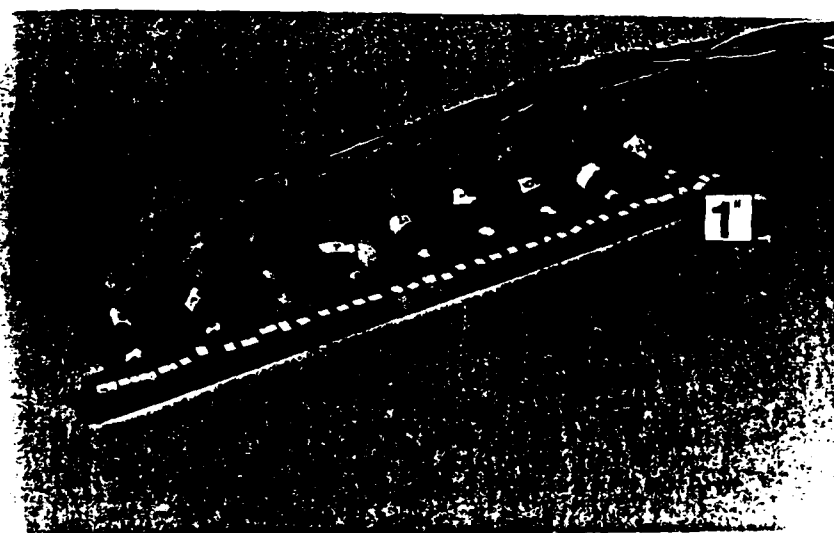


Figure 2.1 Photograph of nine shakers glued to the beam.

A flowchart of the measurement system is shown in Figure 2.2. An IBM PC-AT controls the experiments by driving an HP 4102A impedance analyzer through a GP-IB (General Purpose-Interface Bus). The impedance analyzer sends an oscillator signal at a specified voltage and frequency through a low pass filter set at 12 kHz to an HP 465A voltage amplifier. The measurements are all

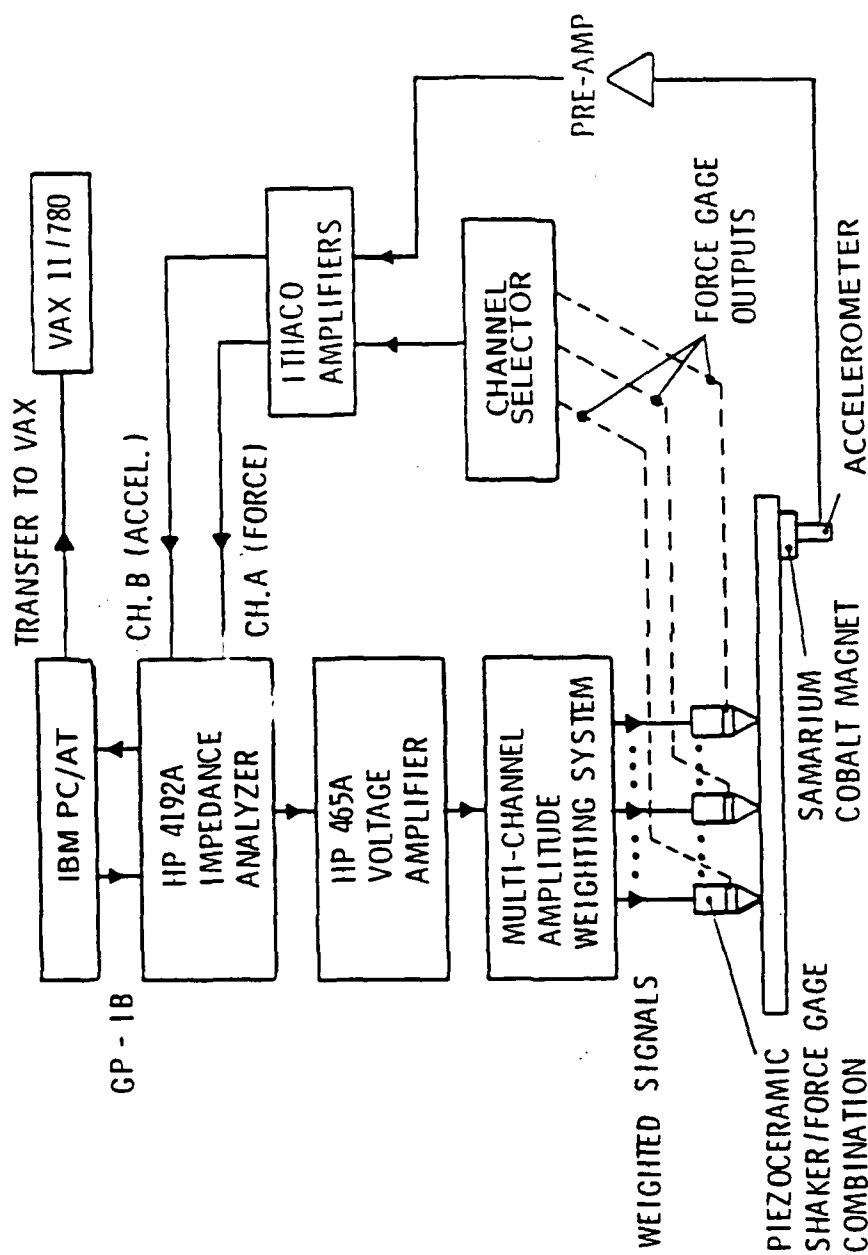


Figure 2.2 Flow chart of the measurement system.

taken using a step frequency method. Note that this figure is shown specifically performing a measurement of transfer admittance. For the measurement of the force ratios, the accelerometer signal is removed and a force signals is sent to the impedance analyzer.

The amplified and filtered signal is feed into the multi-channel amplitude weighting system (MAWS). The system has the ability to use the single input from the voltage amplifier to transmit up to ten separate voltage signals. These signals will have arbitrary gains and either a zero or 180 degree phase difference from the oscillator signal. MAWS allows the amplitude of the drive signal of the array of shakers to be tuned to a particular wavenumber by dialing in the voltage signals for each of the shakers to precalculated values using the procedure described in Section 2.4. Because MAWS has only zero or 180 degree phase control, only a real spatial voltage distribution may be imposed unto the drive signals. As previously stated, there are only ten channels; a symmetric force distribution is used so that up to twenty shakers may be driven by this ten channel system.

The center shaker is used as the reference shaker. The signal from each of the other force gages is sent to a channel selector, which is simply a switch that can select any of the output signals from the force gages. The force output voltages from the reference and measurement force gages are amplified by Ithaco 450 amplifiers. The amplitude and phase of the ratio of the two force gage signals are measured by the impedance analyzer. Of course, this measurement is taken while all of the other shakers are being driven. The results are stored by the PC as a function of frequency. This procedure is repeated until the ratios of all of the shakers to the center shaker are measured. The stored data are later transferred to the mainframe computer.

The velocity distribution is measured in a manner similar to the measurement of force ratios. An accelerometer glued to a samarium-cobalt magnet serves as the velocity probe. The same epoxy used to glue the shakers to the beam is used to attach the magnet to the accelerometer. The magnet performs very well in the frequency range of interest [9]. The beam is made of magnetic steel so the velocity is sampled simply by moving the accelerometer down the length of the beam. It was found that the response of the accelerometer/magnet combination is enhanced by using Kistler force gage grease between the beam surface and the magnet. At each scored location along the beam the ratio of the voltage from the accelerometer to the center force gage is measured using the impedance analyzer. As part of the data acquisition program this ratio is converted into admittance (velocity divided by force) and the admittance as a function of frequency and location is stored on the PC.

### 2.3. Shaker/Force Gage Units

The requirements for the hardware of the measurement system were laid out in Chapter 1. These requirements are placed into two categories; transducer and data acquisition requirements. The data acquisition system was just described. In the sections on transducer development, the design and construction of the final shaker is described along with interim design steps. A brief description of construction techniques is followed by the method for the calibration of the force gages. In Chapter 4, an equivalent circuit model describing the overall response of the shaker, and the response of the force gage section is developed. This model serves as a check on the measurements made on these transducers.

The design and construction of the combination force gage and driver (or shaker) is a major part of this study. Because shakers of a diameter of less than 1.27 cm required in this study are not commercially available, it is necessary to

fabricate them. The original design concept of the drive section included the use of PZT-4 (Lead Zirconate Titanate) piezoceramic disks as the active element. The use of two of these disks and a passive tailmass were added to the shaker design during the iterative steps of the design process. Also in the original design, the piezo-film PVDF (also known as PVF-2) was used in the force gage section. This design was abandoned after many iterations due to mechanical difficulties and PZT-4 was used in the final force gage design. The force gage design using the PVDF film is shown in Appendix A.

### 2.3.1. Shaker/Force Gage Design

A schematic of the final design is shown in Figure 2.3. The three sections of the shaker are labeled on the figure. The sections are the drive section, the decoupler section and the force gage section. The dimensions of the various components and materials used are given in Table 2.3.

Table 2.3 Dimensions and materials used in the transducer.

Description of Section	Material	Dimensions (cm)
Drive	PZT-4	.635 long x 1.27 Diam.
Tailmass	Brass	.635 long x 1.27 Diam.
Decoupler	Aluminium	1.905 long x 1.27 Diam.
Force gage	PZT-4	.3175 thick x 1.27 O.D. and .762 I.D. <sup>#1</sup>
Headmass	Aluminium	1.59 long x 1.27 Diam. <sup>#2</sup>

<sup>#1</sup> I.D. and O.D. stand for inner and outer diameter respectively.

<sup>#2</sup> The headmass section narrows to an area of .3175 cm x 1.27 cm at the top portion.

The drive section consists of two PZT-4 disks, three corrugated nickel electrodes, and a brass tailmass. The PZT-4 elements are polarized toward the

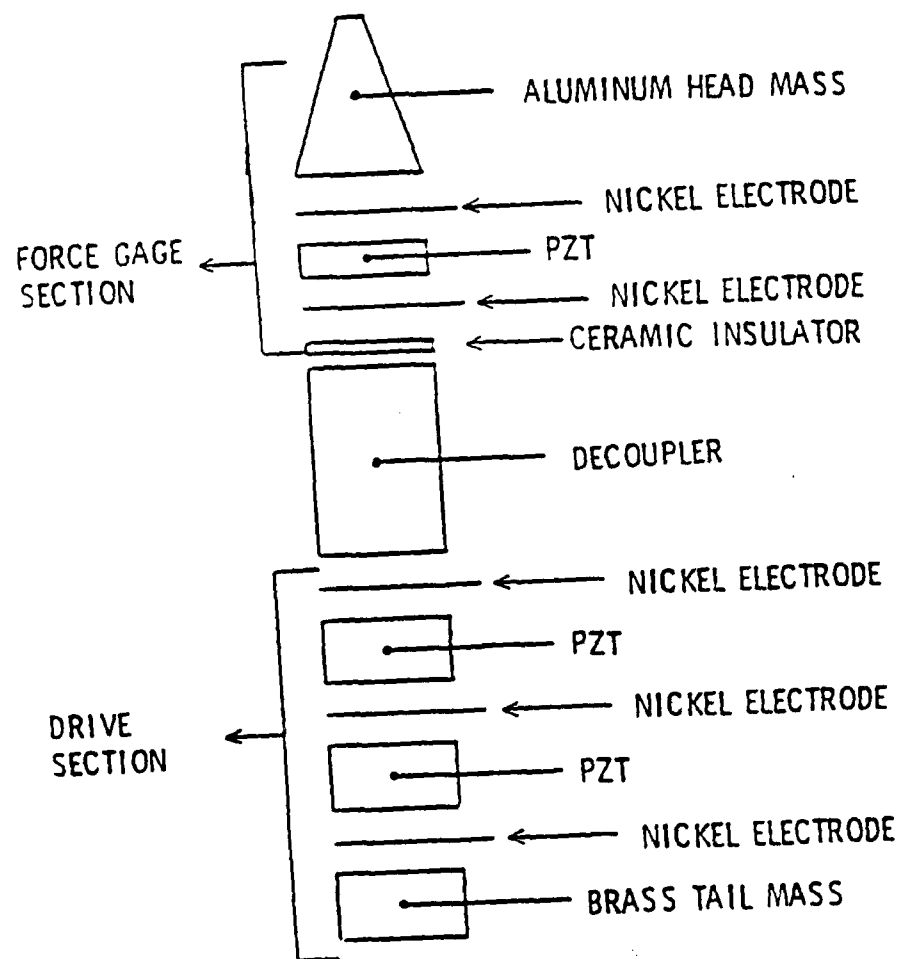


Figure 2.3 Final shaker/force gage design.

center electrode and are electrically in parallel. The negative terminals (ground) are the two outward facing electrodes; this configuration aides in shielding the force gage signal from the drive signal. The contamination of the force gage signal from the drive voltage is called cross-talk. Proper grounding techniques are discussed later in this section. The PZT-4 disks are 33 coupled, which means that the direction of the applied electric field is the same as the resulting motion (or force). Since both disks are polarized toward the center electrode and are electrically in parallel, an applied electric field causes the disks to beat against each other. In other words, both disks contract toward the center electrode and expand away in unison. At low frequencies, the action of the two piezoceramic disks is the same as a single PZT-4 disk with twice the length of the original disk [12]. The motivation for this design and the use of the brass tailmass, is to increase the overall compliance and mass of the transducer drive section so as to lower the resonant frequency of the system. Thus, the low frequency force output of the shaker is increased.

The negative terminals are connected using an insulated wire to eliminate the possibility of shorting out the positive terminal since the positive terminal is between the two negative terminals. The wire is soldered to the electrodes and then to the black lead of a twisted wire with a shield. The positive lead of the twisted pair (the red wire) is soldered to the center electrode of the shaker. Both wires are then glued to the side of the shaker with epoxy to strain relieve the connection. A General Radio or Pomona type, two prong connector is used at the other end of the twisted pair wire with the outer shield connected to the ground terminal at this connector.

The decoupler section consists of an aluminum cylinder. There are two main reasons for the decoupler. The first reason is an extension of the mechanical

design of the drive section, that is to lower overall stiffness of the shaker. So as not to block the output of the drive section at higher frequencies, a material lighter than brass is used. By increasing the compliance of the shaker, the use of the aluminum decoupler increases the low frequency axial force output of the shaker. Second, the use of the decoupler also reduces the effect of electronic cross-talk. Since the drive section acts as an antenna, it is beneficial to place the force cell as far from the drive section as possible to reduce the effects of the electronic cross-talk. The aluminum decoupler must be connected to ground in order to act as a shield for the force gage.

The force gage section is designed to measure the applied force to the test structure and to transmit a line force across the width of the beam. The force gage section consists of an annular cylinder 33 coupled PZT-4 piece, two electrodes, an alsmaig ceramic insulating disk (ceramic insulator in Figure 2.3), and an aluminum headmass. The positive electrode of the force gage is insulated from the decoupler by the alsmaig disk. The ground side of the force gage is connected to the aluminum headmass. The electrodes are soldered to low noise coaxial cable. The center conductor of this cable is the positive or high side and the outer conductor is the shield. At the end of the coaxial wire a Micro-Tech connector is used to help reduce unwanted cross-talk. The cable is stress relieved in a similar manner to the drive section; by gluing the wire to the side of the force gage. The aluminum headmass allows for light stiff connection of the shaker to the test structure. At the attachment point the cross-section of the headmass is narrowed to simulate a line force. The headmass design enables the shaker to easily and safely be attached and removed from the test structure. The effect of the headmass on the response of the force gage is examined in Chapter 4.

The proper grounding technique is a critical element of the shaker design as

well as for the entire measurement system. The shakers must be designed so that the force gage signal is insulated from the drive signal. The ground plane of the drive section and the force gage section must be the same so that no ground loop exists. All metal elements of the shaker are grounded to prevent charge from accumulating on these components and becoming an emitter of electro-magnetic noise. The ground planes of all of the equipment must be the same. This can be accomplished by running all of the amplifiers, oscilloscopes and any other equipment connected to the shaker off of the same power line.

### 2.3.2. Construction

The transducer is constructed by gluing the surfaces of the components together using epoxy. The surfaces must be meticulously cleaned before the glue is applied. After the construction is complete, the strength of the glue joints is greater than the ceramic in bending. These procedures were arrived upon by experimentation with different methods as well as through discussions with the personnel at the Applied Research Lab (ARL) at Penn State [13].

The first step is to clean the assembled components. Metallic surfaces that are to be glued (electrodes, tailmass and decoupler) are first etched in a mild acid bath to remove oxide coatings. The metallic surfaces, the electroded surfaces of the PZT and the alumaig insulating disk are next abraded with a fiberglass brush for further cleaning. Then all of the surfaces to be glued undergo the three part solvent cleaning process of toluene, alcohol, and acetone; this process is performed under an exhaust hood.

After cleaning, the components are glued together using Shell EA-6 epoxy. First, the glue is applied in a thin coat to both surfaces that are to be joined. The entire transducer is assembled sequentially from the tailmass up. Upon completion of the gluing, the transducer is placed in an alignment jig which also

supplies axial compression to insure a good bond. The transducer, now in the jig, is placed in an oven at 80 degrees Celsius for six to eight hours. The jig and transducer are removed from the oven. The residual charge across the electrode terminals from the heating and cooling of the piezoceramic is shorted out. All of this work is performed in the transducer clean room at ARL.

Next, the electrodes are bent slightly toward the body of the shaker to prevent the electrodes from protruding. Wires are then soldered to the terminals of the PZT-4 elements and then stress relieved. Finally, the outer part of the transducer is covered by shrink wrap so that the electrodes are not exposed and are protected during handling.

#### 2.3.4. Force Gage Calibration

The method of calibration is simply a comparison calibration which employs Newton's law. The shaker is loaded with a known mass. The acceleration of the mass is measured with an accelerometer. From the ratio of the force gage voltage to the accelerometer voltage, the sensitivity of the force gage is determined. A diagram of the calibration set-up is shown in Figure 2.4

A personal computer controls the calibration by sending instructions to an HP 4192A impedance analyzer using a GP-IB. The impedance analyzer has the ability to send an oscillator signal at a prescribed voltage and frequency as well as measuring the ratio of two signals and their relative phase. A data acquisition computer program was written to run the calibration and store the data. The program steps the oscillator through the frequency range of interest (2-12 kHz), while the oscillator signal from the HP 4192A is sent to an HP 465A voltage amplifier. The amplified drive signal excites the shaker which, in turn, excites the known calibration mass. The signal from the force gage and the attached accelerometer are amplified and then sent to the impedance analyzer. The

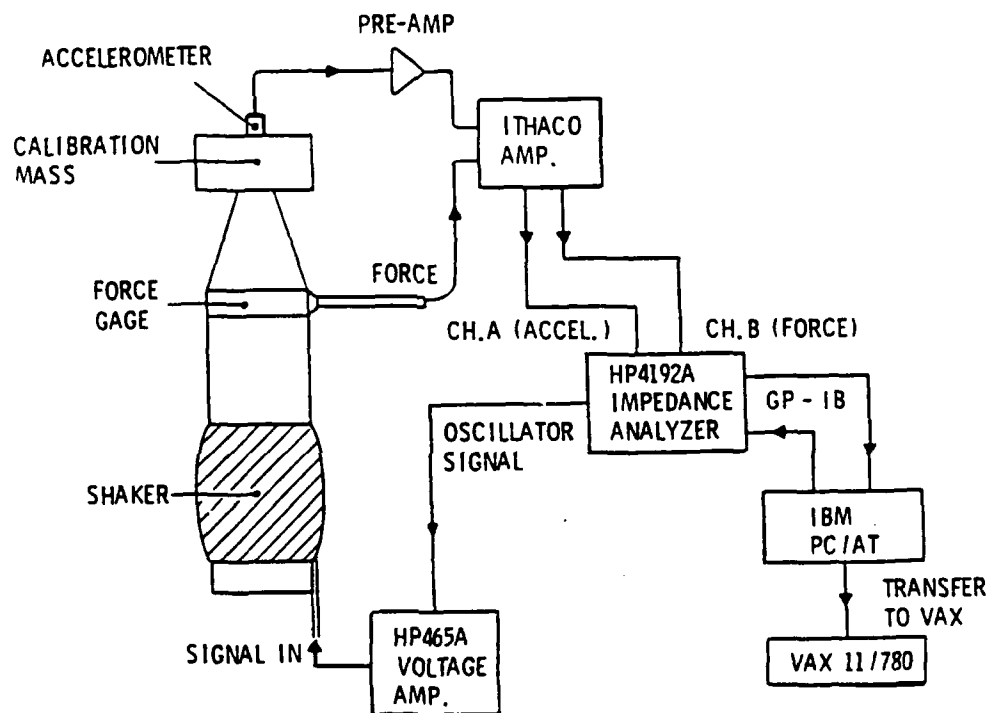


Figure 2.4 Calibration system.

amplitude and phase of this ratio are used to calculate the unknown sensitivity of the force gage. The sensitivity data are sent to the VAX 11/780 mainframe for plotting.

The sensitivity is calculated from the following formula,

$$S(\omega) = \frac{R(\omega)S_a}{M_c + M_{hm} + M_a} \quad , \quad (2.1)$$

where,  $S(\omega)$  is the frequency dependent force sensitivity,  $S_a$  is the sensitivity of the accelerometer,  $M_{hm}$  is the mass of the head mass,  $M_c$  is the calibration mass,  $M_a$  is the mass of the accelerometer, and  $R(\omega)$  is the ratio of the voltage from the force gage to the accelerometer voltage. This formula comes from the application of Newton's Law.

The maximum and minimum sensitivity for five different shakers is shown in Figure 2.5 over the frequency range of 2-12 kHz. Since the value of the force gage sensitivity is very flat over the frequency range of interest, a single sensitivity is assigned. This sensitivity is the average of the frequency dependent sensitivity over the frequency range. The averaged values of the sensitivity and phase for all of the force gages is tabulated in Table 2.4. Each of the shakers has a number associated to it; these are the numbers used to identify the shakers and their sensitivities. A discussion of the variations of the force gage sensitivity is found in Chapter 4.

#### 2.4. Signal Processing Aspects

In this section, the signal processing aspects of measuring the wavenumber response of the beam are examined. First, the discrete Fourier transform is introduced. Next, the wavenumber sensitivity of accelerometer arrays is developed. This development begins with a general treatment of the problem, so that the simplifications made when using the discrete Fourier transform can be

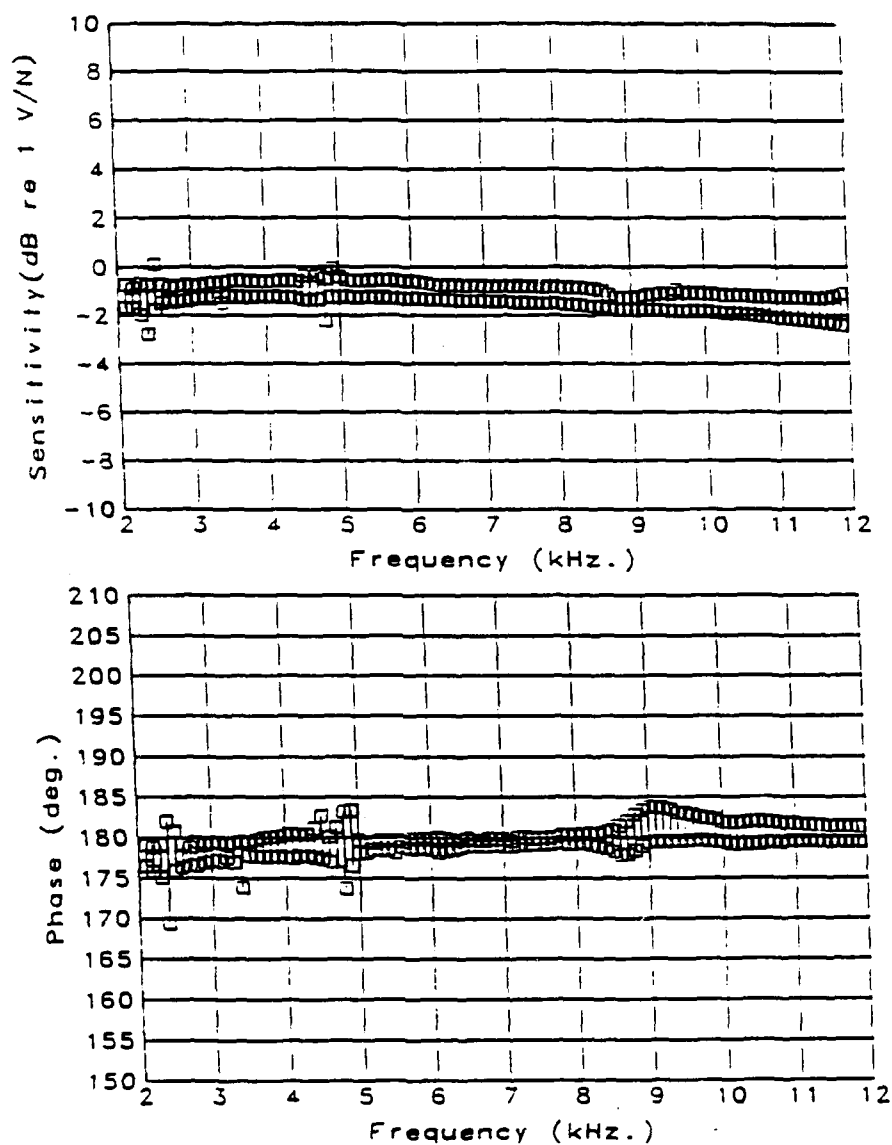


Figure 2.5 Maximum and minimum force sensitivity (amplitude and phase) for five shakers.

Table 2.4      Sensitivities of the force gages.

Shaker number	Sensitivity (V/N)	Phase (deg.)
1	.94	179.
2	.88	179.
3	.95	180.
4	.88	180.
5	.93	180.
6	.92	181.
7	.99	181.
8	.94	181.
9	.98	181.
10	.98	181.
11	.97	180.
12	.97	181.
13	.97	181.
14	.97	180.
15	.99	180.
16	1.0	180.
17	.98	180.
18	1.0	180.
19	1.0	180.
20	.98	180.
21	.94	180.
22	.98	180.

identified and justified. Also, the measurement of the wavenumber content of the forcing function is developed and a method of steering the forced wavenumber content is developed.

#### 2.4.1. Discrete Fourier Transform of the Velocity

The Fourier transform of  $f$  is defined to be

$$F(k_x) = \int_{-\infty}^{\infty} f(x) e^{-jk_x x} dx, \quad (2.2)$$

and the inverse transform is

$$f(x) = \frac{1}{2\pi} \int_{-\infty}^{\infty} F(k_x) e^{jk_x x} dk_x, \quad (2.3)$$

where the wavenumber is  $k_x$  and the spatial variable is  $x$ .

The discrete Fourier transform (DFT) is a means of estimating the wavenumber spectrum from measured and predicted spatial data. The DFT may be applied to results of spatial-frequency model or to experimental data. The DFT of the displacement  $y(x)$  is

$$\tilde{Y}_d(k) = \Delta x \sum_{\ell=0}^{N-1} y(\ell \Delta x) e^{(-j\ell \Delta x k)}. \quad (2.4)$$

The factor  $k$  is the wavenumber counting index,  $\ell$  is the sample number and  $N$  is the total number of points. The factor  $\Delta x$  is the spacing between sample locations. The multiplying  $\Delta x$  is the proper normalization for the DFT [14]. The transform of a complex sequence of  $N$  points results in  $N$  separate spectral lines, the first  $N/2$  spectral lines represent the positive wavenumber spectrum and the mirror image of the second represent the negative spectrum. The counting index  $k$  corresponds to the wavenumber  $k_x$  in the following manner,

$$k_x = \begin{cases} \frac{2\pi k}{N\Delta x}, & \text{for } k = 0, 1 \dots N/2 - 2, N/2 - 1 \\ \frac{2\pi(k-N)}{N\Delta x}, & \text{for } k = N/2, N/2 + 1 \dots, N \end{cases}. \quad (2.5)$$

In the discretization, both the spectrum and the original sequence are considered periodic. Zero padding of the data interpolates between points in wavenumber space with a  $\sin(x)/x$  function [15]. Zero padding better defines the spectrum by this interpolation, but does not increase the resolution capabilities of the given transform. The points are interpolated between the existing points, but the maximum wavenumber ( $\pi/\Delta x$ ) remains the same.

All of the processing of experimental velocity data utilizes the DFT. In the next section, the assumptions that are implicit in the use of the discrete transform are discussed. The discrete transform is used as an approximation to the exact transform; the exact transform is performed analytically on the predicted beam velocity in Chapter 3 and used as a means of assessing the impact of the spatial sampling required in the measurements.

For the processing of discrete transforms a Fast Fourier Transform (FFT) algorithm is used by zero padding [14,15] to a power of two. This speeds the calculation of the transform, which is important even though the transforms considered in this thesis are not large.

#### 2.4.2. Wavenumber Frequency Sensitivity of Accelerometer Arrays

What is sought here is the sensitivity of an array of sensors (in this case an array of accelerometers) in wavenumber-frequency space. The objective of performing this analysis is to understand the wavenumber filtering effect of the array and to determine the spacing of the sensors needed to measure the wavenumber spectra. Specific results in this section are presented for point or ideal sensors, but the analysis may be applied to a more general class of sensors [7].

The starting point of the analysis is to derive the wavenumber sensitivity for a single sensor. It is postulated that there exists a large class of sensors whose

voltage output due to some excitation can be cast in the form of a convolution integral [5,6]. In other words, there exists an impulse response function for the transducer. Additionally, the impulse response function is taken to be separable in space and in time; in other words the space-time impulse response function may be written as

$$g(x, t) = h(x)f(t) \quad (2.6)$$

In Figure 2.6 the geometry of the single sensor is shown symbolically measuring some physical phenomenon. The specific sensor under consideration here is an accelerometer so that the terms accelerometer and sensor are used synonymously in this section. The measurement center of the accelerometer is at  $x_0$  units from the origin with some finite width as shown in Figure 2.6. There is some voltage output from the sensor which is proportional to the velocity (this is buried in  $f(t)$  as velocity is the quantity of interest).

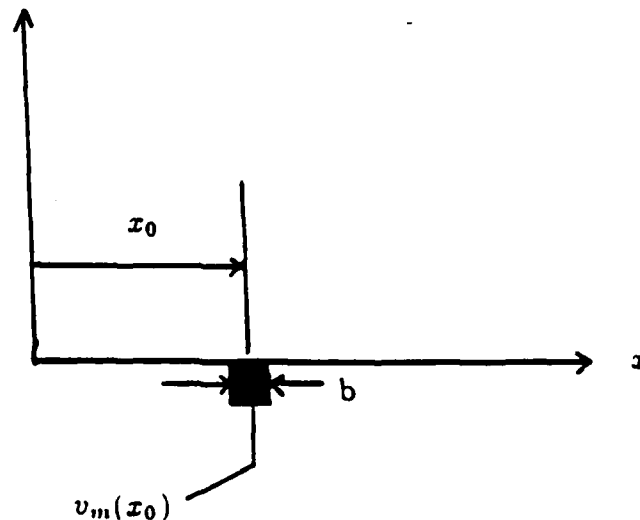


Figure 2.6 Geometry of single sensor in a velocity field.

The form of the convolution integral applied to obtain the measured velocity by a sensor located at  $x_0$  is

$$v_m = \int_{-\infty}^{\infty} \int_{-\infty}^{\infty} v(\alpha, \tau) h(x_0 - \alpha) f(t - \tau) d\tau d\alpha. \quad (2.7)$$

Since the steady state response is of interest, the remaining analysis proceeds in frequency domain. Taking the Fourier transform with respect to time results in

$$v_m = F(\omega) \int_{-\infty}^{\infty} v(\alpha, \omega) h(x_0 - \alpha) d\alpha, \quad (2.8)$$

where the convolution theorem has been applied to the frequency dependence [15]. For brevity, the frequency dependence is dropped from the equations. Using the asterisk notation for the convolution operation on  $x$ , Equation (2.8) becomes

$$v_m = [v(x) * h(x)] \delta(x - x_0), \quad (2.9)$$

where the use of the Dirac delta function in Equation (2.9) is detailed in Bracewell and Gaskill [8,15]. This use of the delta function locates the sensor at  $x_0$ . In order to examine the wavenumber filtering effect of a single sensor, the spatial Fourier transform is applied to the right hand side of Equation (2.9). This results in

$$V_m = [V(k_x) H(k_x)] * e^{-jk_x x_0}, \quad (2.10)$$

here the asterisk notation indicates convolution on  $k_x$ . If  $x_0$  is zero, then the output measured from the sensor is

$$V_m = \int_{-\infty}^{\infty} V(k_x) H(k_x) dk_x. \quad (2.11)$$

If the sensor is a point sensor then  $H(k_x) = 1$  because  $h(x) = \delta(x)$  and the output of the sensor is just the integral over all wavenumbers. For  $h(x)$  not equal to a  $\delta(x)$ , then  $H(k_x)$  represents the filtering action of the sensor.

For all real sensors  $h(x)$  is not a delta function, but at low wavenumbers the response approximates a delta function; i.e., the sensor is equally sensitive to all wavenumbers below a certain wavenumber. An analysis of a spatial impulse response function that is not a delta function is found in Blake and Chase [7]. Their analysis finds that, for a sensor with uniform sensitivity to velocity over the contact surface, if the wavelengths meet the following criterion,

$$\lambda > 4.2R \quad (2.12)$$

where  $R$  is the radius of the sensor, the sensitivity will not be attenuated by spatial averaging by more than 3 dB. This assumes that the magnet attached to the structure has a uniform velocity sensitivity. This may not be true for our situation but is probably a close approximation. Because of spatial averaging, the sensor is a sort of low pass wavenumber filter. However, at wavenumbers past the cutoff wavenumber (defined in Equation (2.12)) there are regions of increased sensitivity (i.e., sidelobes in the filter function).

By examining the wavenumber response of a single sensor, the wavenumber filtering action is obtained. There is no ability to select (other than the low pass filtering action) which particular wavenumber is to be examined. Using an array of accelerometers allows for a certain degree of wavenumber selectivity to be achieved.

The velocity sampled by  $N$  identical transducers is just a variation of Equation (2.9) with the addition of  $N$  sensors. A schematic for this situation is shown in Figure 2.7. Mathematically, this array can be represented as,

$$\begin{aligned} v_m(x) &= \left[ \int_{-\infty}^{\infty} v(\alpha) h(x - \alpha) d\alpha \right] \sum_{n=0}^{N-1} g_n \delta(x - n\Delta x) \\ &= [v(x) * h(x)] A(x), \end{aligned} \quad (2.13)$$

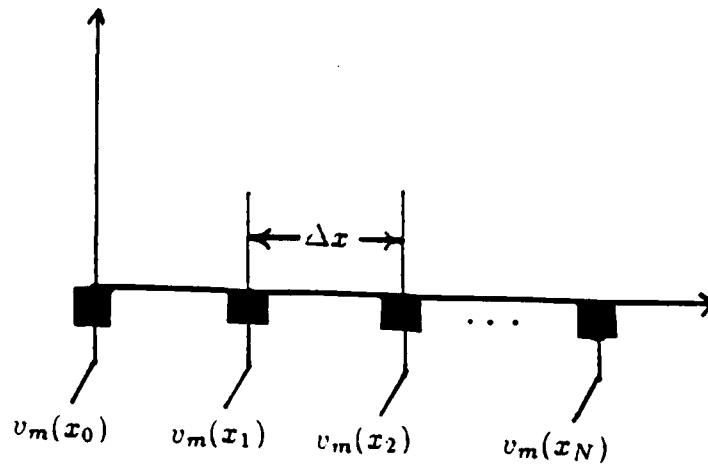


Figure 2.7 Multiple sensors in a velocity field.

where

$$A(x) = \sum_{n=0}^{N-1} g_n \delta(x - n\Delta x). \quad (2.14)$$

$A(x)$  is the array function and the  $g_n$ 's are arbitrary weights applied to the outputs of the sensors which are spaced  $\Delta x$  units apart. Taking the spatial Fourier transform of Equation (2.13) and making use of the convolution theorem again results in

$$V_m(k_x) = [V(k_x)H(k_x)] * \tilde{A}(k_x). \quad (2.15)$$

For an array of ideal sensors the velocity spectrum is

$$V_m(k_x) = V(k_x) * \tilde{A}(k_x). \quad (2.16)$$

The term  $\tilde{A}(k_x)$  is the Fourier transform of the array function or

$$\tilde{A}(k_x) = \sum_{n=0}^{N-1} g_n e^{-jk_x n \Delta x}. \quad (2.15)$$

The term  $\tilde{A}(k_x)$  represents the filtering action in wavenumber space of the array of sensors. The DFT of the velocity,

$$V_m(k_x) = \Delta x \sum_{n=0}^{N-1} g_n v_m(n\Delta x) e^{-jk_x n\Delta x} \quad , \quad (2.18)$$

is equivalent to Equation (2.16). The DFT is the most efficient way to calculate the wavenumber response. Additionally, in almost all cases, this is the only way to calculate the wavenumber response for, in order to evaluate Equation (2.15), the true spectrum  $V(k_x)$  must be known a priori. However, the DFT representation tells nothing about the filtering action of the array as do Equations (2.15) and (2.16).  $H(k_x)$  represents the wavenumber sensitivity of a single accelerometer and  $\tilde{A}(k_x)$  of the array.  $H(k_x)$  is a multiplicative term that rides over the entire spectrum. By assuming the sensor to be ideal, the wavelengths must be larger than the sensor (i.e. the criterion of Equation (2.12) must be met).

For real sensors the wavenumber sensitivity cuts off after a certain wavenumber, because, when the wavelengths in the structure are small relative to the size of the sensor, there is an averaging effect which tends to attenuate the voltage output of the sensor. Equation (2.15) represents the wavenumber sensitivity of an array of real sensors. If a single sensor is unable to measure the velocity at a particular wavenumber, then the array of sensors is likewise unable measure the velocity at that wavenumber. Using an array of sensors, a wavenumber band-pass filter is created by the summation of the outputs of the sensors, but only below the cut-off wavenumber of an individual sensor. The use of an array enables a selectivity within the range of the measurable wavenumbers not available with just one sensor. The convolution integral of Equation (2.16) is an integration of a shifted version of the array function times the true velocity spectrum which results in the measured spectrum at  $k_x$ .

### 2.4.3. Windowing Considerations

The effect of windowing the output of the sensors measuring the velocity on a finite structure must be viewed from a different standpoint than for an infinite structure. Using window functions is an attempt to smooth the artificial discontinuity caused by truncation of the data sequence. For the finite beam the truncation is not artificial, the velocity distribution on the beam truly exists only over a finite length, outside this domain the velocity is zero.

It is useful to define the rectangle function as

$$\text{rect}\left(\frac{x - x_0}{b}\right) = \begin{cases} 0, & \text{for } |(x - x_0)/b| > 1/2; \\ 1/2, & \text{for } |(x - x_0)/b| = 1/2 \\ 1, & \text{for } |(x - x_0)/b| < 1/2. \end{cases} \quad (2.19)$$

The amplitude of the Fourier transform of the rectangle is the sinc function defined as,

$$\text{sinc}(\zeta) = \frac{\sin(\zeta)}{\zeta}. \quad (2.20)$$

There is an additional multiplicative phase factor if the rect function is not centered at  $x = 0$ . If a pure sinusoidal wave exists only over the length of the structure it can be represented as

$$u(x) = \sin(k_{x0}x) \text{rect}\left(\frac{x}{L}\right), \quad (2.21)$$

where the Fourier transform of  $u(x)$  is  $U(k_x)$ ,

$$U(k_x) = \frac{1}{2j} \{ \delta(k_x - k_{x0}) - \delta(k_x + k_{x0}) \} * \{ \text{sinc}(k_x L/2) \}. \quad (2.22)$$

Let  $U(k_x)$  be the true velocity distribution on some finite structure, then the measured wavenumber spectrum can be obtained from Equation (2.16). Here it is postulated that for a finite structure with an array of closely spaced point sensors the proper weighting is a uniform one (i.e. all of the  $g_n$ 's equal to one).

Hence,  $\tilde{A}(k_x)$  is the sinc function and Equation (2.16) becomes,

$$\begin{aligned} U_m(k_x) &= U(k_x) * \text{sinc}(k_x L/2), \\ &= \frac{1}{2j} \{ \delta(k_x - k_{x0}) - \delta(k_x + k_{x0}) \} * \{ \text{sinc}(k_x L/2) \} * \{ \text{sinc}(k_x L/2) \}. \end{aligned} \quad (2.23)$$

The convolution of two sinc functions of the same length results in one sinc function or,

$$\text{sinc}(k_x L/2) * \text{sinc}(k_x L/2) = \text{sinc}(k_x L/2). \quad (2.24)$$

It follows that,

$$U_m(k_x) = U(k_x). \quad (2.25)$$

In this case, the true spectrum is measured. Of course in reality  $\tilde{A}(k_x)$  only approximates a sinc function. But in the case where the sampling is very fine, the array function closely approximates the ideal case. Thus, it is argued (heuristically) that the proper weighting is uniform.

Of course Equation (2.25) is an expected result. However, if the spatial window function (the  $g_n$ 's) is other than a uniform window, even if the sampling interval is infinitesimally small, Equation (2.25) would not hold. If the velocity field is sampled across the entire length of the beam, then the only errors inherent in the DFT are due to aliasing [14]. If some spatial weighting is used, obviously, the estimate will vary from the continuous transform due to both aliasing and the window.

In the measurement of the Fourier transform of the velocity on a finite structure using the DFT, aliasing cannot be avoided as the spectrum is not band limited. The effects of aliasing can be reduced by choosing a spacing that moves the aliasing lobes of the array function to a region of wavenumber space where the spectrum has very low values. In Section 5.3, the effect of varying the spacing of the accelerometers is examined. The goal in the array design is to

use as fine a spacing as possible and to obtain an array function whose Fourier transform is close to the proper sinc function.

#### 2.4.4. Spacing of Accelerometers for the Experiment

The dispersion relation for the beam, which is derived in Chapter 3 and pictured in Figure 3.2, shows that the highest freebending wavenumber expected is about  $0.6 \text{ cm}^{-1}$ . The spectrum for the finite beam falls off as a sinc function centered at the freebending wavenumber. In other words the spectrum should fall off around 30 dB after three octaves or at  $k_x = 2.4 \text{ cm}^{-1}$ . Hence, a spacing of 1 cm, which yields a Nyquist rate of  $\pi \text{ cm}^{-1}$  and would reduce aliasing, is used.

The other item with which to contend is the criterion of Equation (2.12). The accelerometer used has a radius of 0.5 cm. The criterion for this size transducer is that the minimum wavelength should be greater than 2.1 cm. The measured wavenumber spectra would exhibit a slight attenuation compared to an exact analytic treatment, except of course for the aliasing that would tend to accentuate the higher wavenumbers. It is left to the results section to examine which, if either, effect evidences itself.

#### 2.4.5. Wavenumber Content of an Array of Point Forces

Each of the shakers in the array is considered delta functions in space. Thus, the array of  $M$  shakers where  $q_m$  is the complex force amplitude and  $x_m$  is the shaker location can be represented as,

$$\begin{aligned} q(x) &= \sum_{m=1}^M q_m \delta(x - x_m), \\ &= \sum_{m=1}^M q_m \delta(x - m\Delta x), \end{aligned} \tag{2.26}$$

where  $x_m = m\Delta x$ . The force is zero everywhere except at a shaker. Thus, the external forcing function is completely described. The Fourier transform may be

performed exactly and is

$$Q(k_x) = \sum_{m=1}^M q_m e^{-jk_x m \Delta x}. \quad (2.27)$$

This is the wavenumber spectrum of the array of point forces.

#### 2.4.6. Steering the Wavenumber Content of an Array of Point Forces

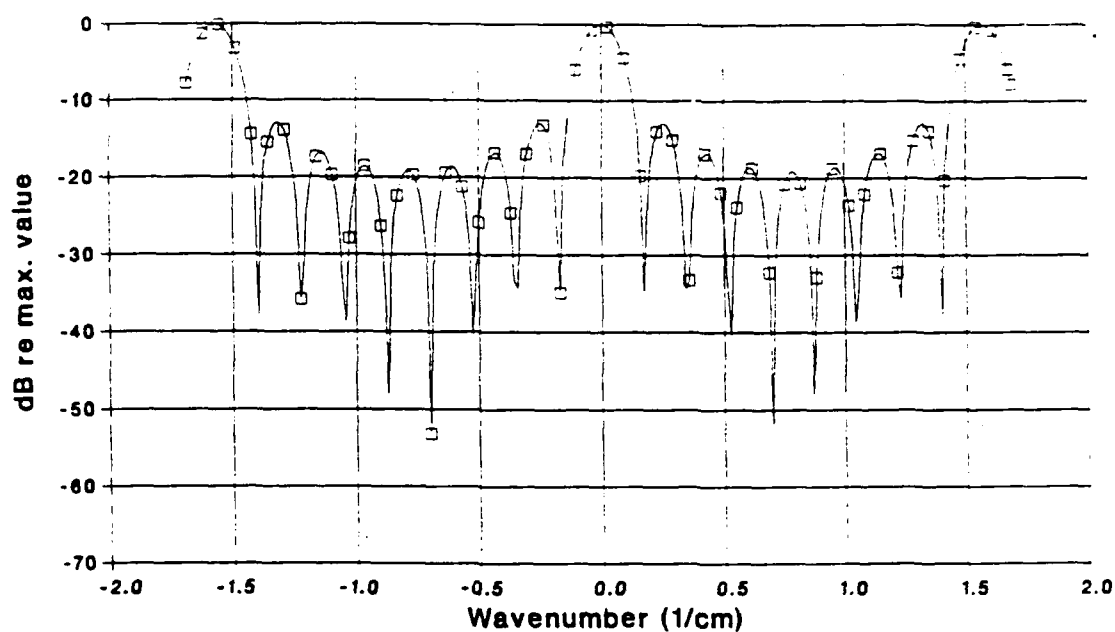
In order to obtain better measurements of the velocity at a particular wavenumber, it is helpful to concentrate the energy of the forcing function at that wavenumber. The objective is to steer the peak of the forced wavenumber spectrum to the desired or drive wavenumber,  $k_d$ . The peak of the forced wavenumber spectrum may be steered to  $k_d$  by amplitude shading of the forced amplitudes.

As mentioned previously, this is done by setting the  $q_m$ 's to  $\cos(k_d(x_m - L/2))$ , which modulates the spatial signal so that there are peaks in the wavenumber spectrum at  $k_x = \pm k_d$ . This holds if the Nyquist criterium is met, i.e.  $k_d < \pi/\Delta x$ . There must be at least two shakers for each wavelength. Additionally, there are peaks in the spectrum at  $k_x = \pm(2\pi/\Delta x - k_d)$ . The location of these peaks can be predicted by examining the convolution of the Fourier transform of the cosine function and the array of point forces. The finite spatial aperture of the forcing function will broaden the peaks of the force spectrum and cause the appearance of sidelobes. The peaks at  $k_x = \pm k_d$  are called main-lobes while the secondary peaks are called grating lobes; collectively, the main-lobes and the grating lobes are referred to as major-lobes. The sidelobes are smaller in amplitude than the major-lobes and fall between the major-lobes. Lastly, the force spectrum of an array of point forces is periodic, with period equal to  $2\pi/\Delta x$ . This characteristic is important as the pattern seen in the region  $0 < k_x < 2\pi/\Delta x$  is repeated periodically in the positive and negative  $k_x$  directions.

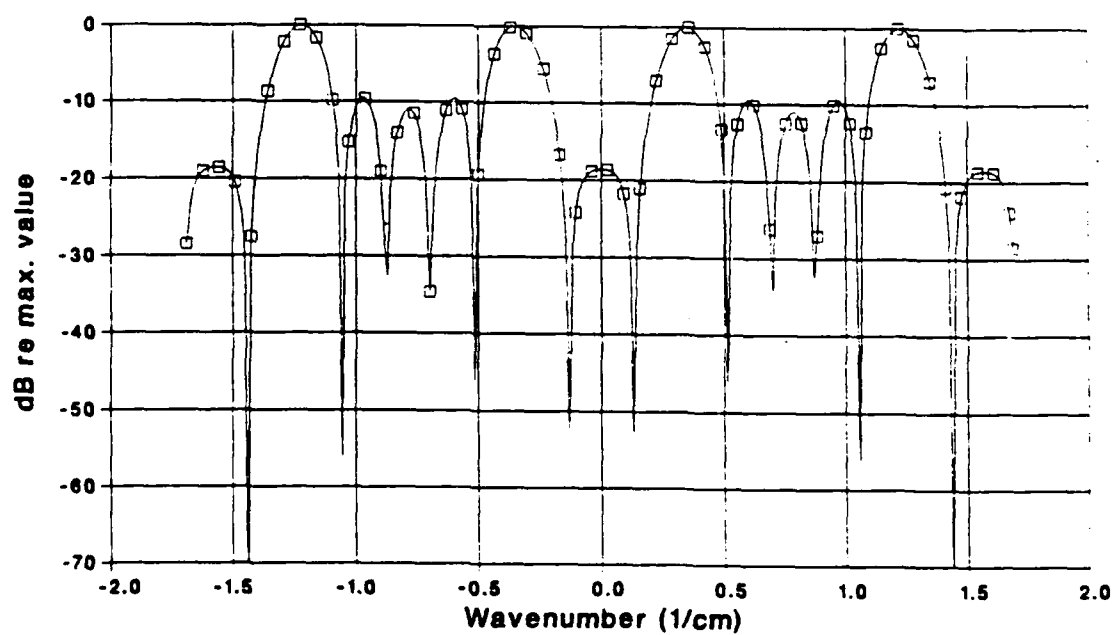
While it is easy to theoretically specify the force amplitudes, it is a completely different matter to experimentally enforce these amplitudes. The voltages applied to the shakers are controllable, so that the drive wavenumber can be steered to the desired wavenumber by steering the drive voltages. This assumes that the force applied to the beam tracks with the voltage in wavenumber space and a complicated feedback-control system between the voltage applied and the force output can be avoided. For the remainder of this section, the  $q_m$ 's (the force output at the shaker) is assumed to be controllable.

Some results of the wavenumber spectra of the forces seen at the shakers (i.e., the applied voltages) are now presented for the spacing and number of shakers used in the experiments. For the nine shaker experiments ( $\Delta x = 4$  cm), the wavenumber spectrum for the unsteered force distribution ( $k_d = 0$  cm<sup>-1</sup>) and a steered force distribution with  $k_d = 0.332$  cm<sup>-1</sup> (two wavelengths over the length of the beam) are shown in Figure 2.8a and 2.8b, respectively. The peaks at  $\pm k_d$  and at  $k_x = 2\pi/\Delta x - k_d$  can be seen. It is important to note that, due to the periodic nature of the spectrum, by prescribing a drive wavenumber between 0 and  $\pi/\Delta x$  a peak force wavenumber response may be steered to any wavenumber. There are always an infinite number of peaks. This fact is both an advantage and a drawback. Without the grating lobes, the only way to excite the very high wavenumbers is to decrease the spacing, which requires smaller shakers. However, the grating lobes can complicate the interpretation of the spectrum, by exciting the velocity in an unwanted region.

Results of the force wavenumber spectra for seventeen shakers are shown in Figure 2.9. For seventeen shakers  $\Delta x$  is equal to 2 cm. Note that the grating lobes do not appear in these plots because the grating lobes are outside the chosen wavenumber range. By examining these plots it is interesting to note that the

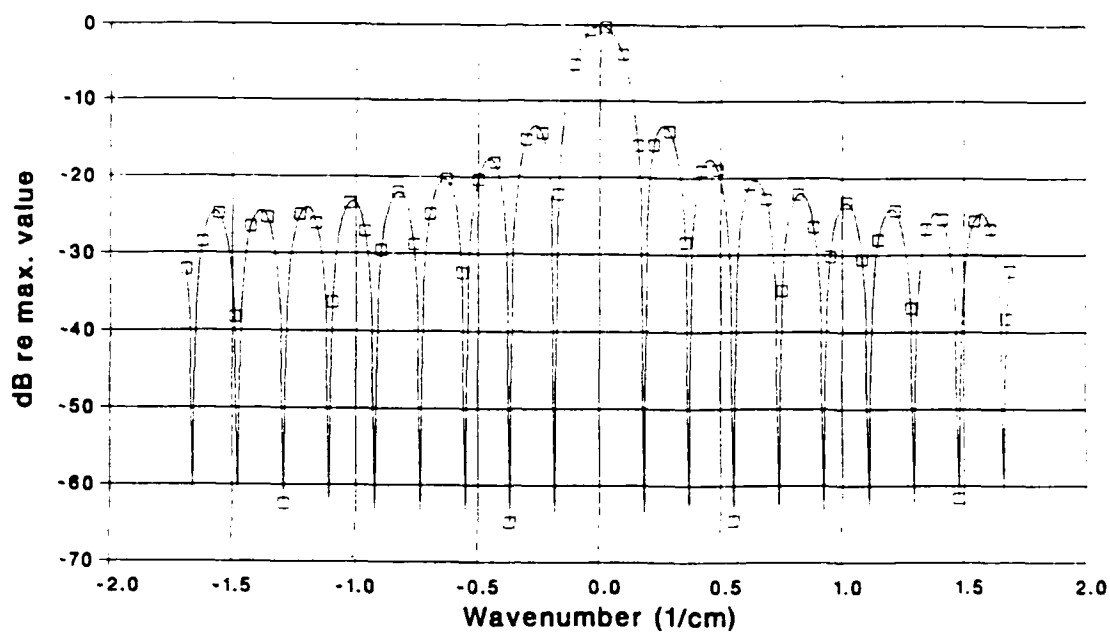


(a)

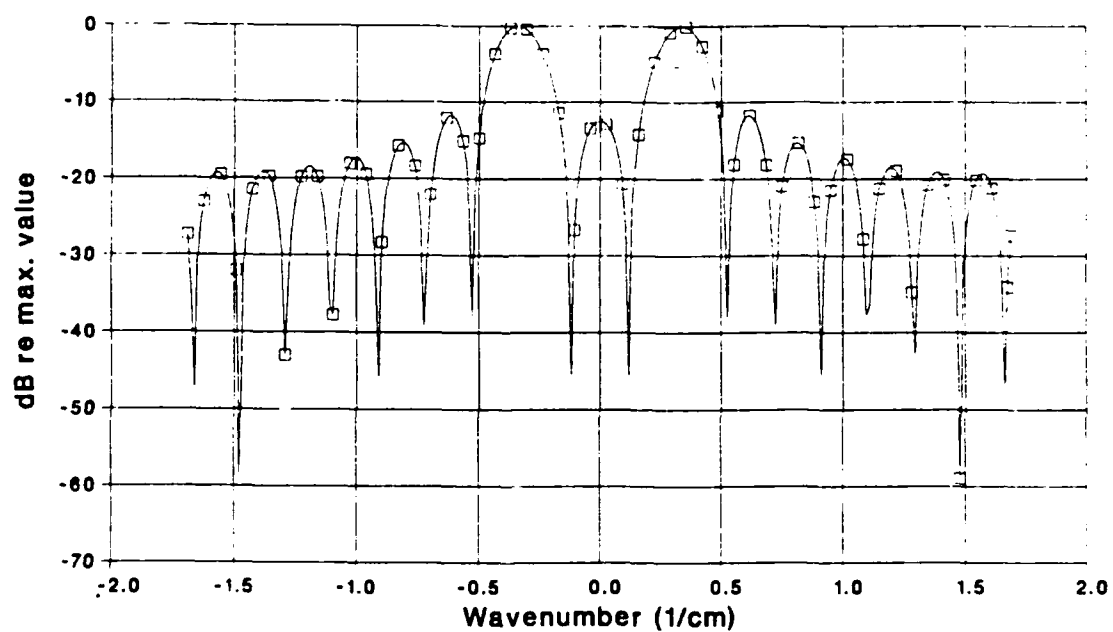


(b)

Figure 2.8 Shifted and unshifted force spectra for nine shakers.  
 (a)  $k_d = 0. \text{ cm}^{-1}$ , (b)  $k_d = .332 \text{ cm}^{-1}$ .



(a)



(b)

Figure 2.9 Shifted and unshifted force spectra for seventeen shakers, (a)  $k_d = 0 \text{ cm}^{-1}$ , (b)  $k_d = .332 \text{ cm}^{-1}$ .

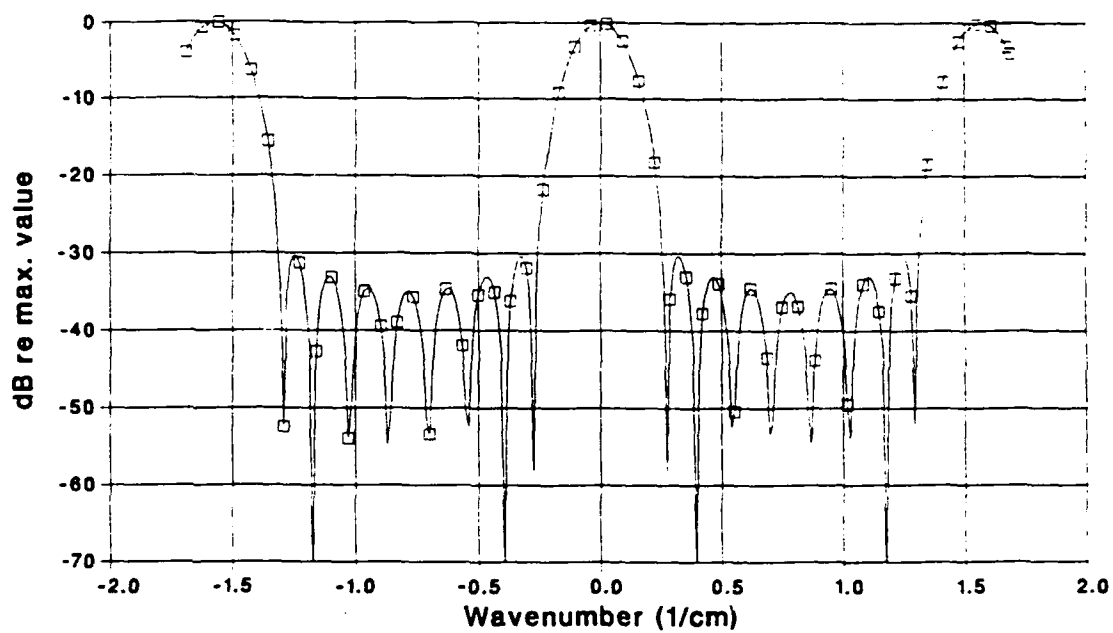
width of the major-lobes is a function of  $M\Delta x$ , or the length of the spatial signal and any spatial windowing which may be added to the shaker weighting during steering (this is described next). Hence, if the spatial windowing is the same for the nine shakers as for seventeen, the major lobes have the same width.

While the steering of the voltage input moves the peak of the wavenumber content to a desired wavenumber, the high sidelobes caused by rectangular windowing may produce undesirable effects. These sidelobes may cause higher velocity response than the main-lobes if the sidelobes occur in a region of high admittance. By applying a windowing function, the sidelobes are reduced at the cost of a broader main-lobe. The values of the voltages for the windowed and shifted distribution become,

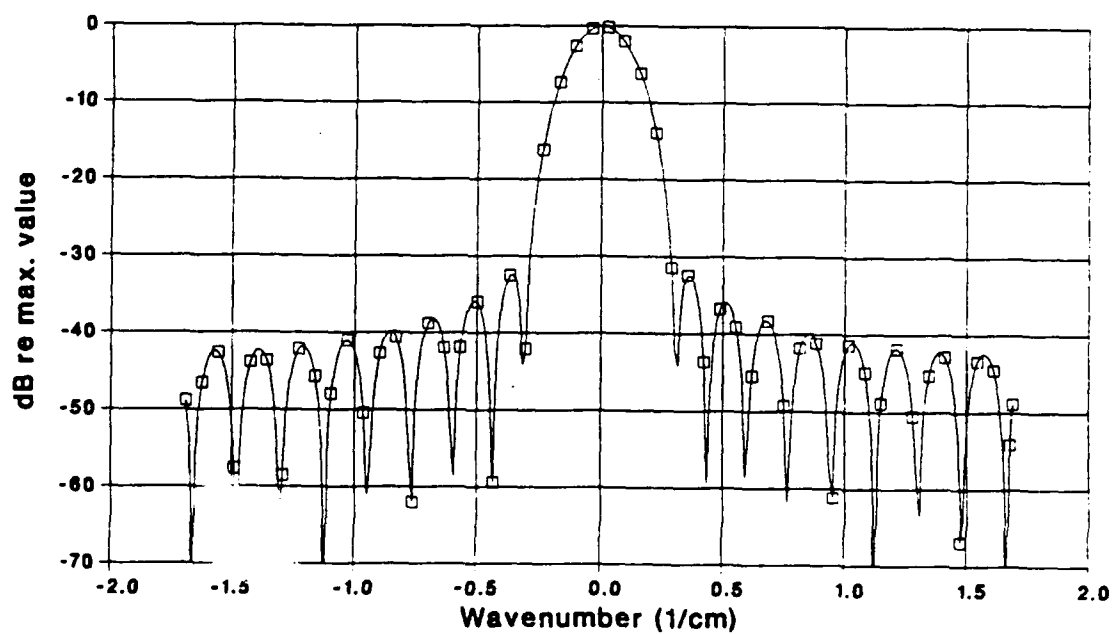
$$q_m = W(x_m) \cos(k_d(x_m - L/2)) \quad , \quad (2.28)$$

where  $W(x)$  is the selected window function. Different windows may be applied to the shaker forces in order to alter the sidelobe structure which is done at the sacrifice of increasing the width of the main-lobe. A Kaiser-Bessel window with it's variable parameter alpha set to 1.5 is used in the results presented in Figure 2.10. This window type is described in reference [16]. By windowing, the energy of the forcing function is less likely to leak into the nearby wavenumbers. The periodic main-lobes are not affected except for broadening. In Figure 2.10,  $k_d = 0 \text{ cm}^{-1}$  and a Kaiser-Bessel window is used with nine and seventeen shakers.

The FORTRAN program FORCE\_FILTER, is used to obtain the wavenumber spectrum and the correct amplitude shading for all of these cases. This code is found in Appendix C.



(a)



(b)

Figure 2.10 Effect of Kaiser-Bessel window on unshifted spectra, (a) for nine shakers, (b) for seventeen shakers.

## Chapter 3

### BEAM THEORY

#### 3.1. Introduction

In the experiments, a beam is excited by multiple shakers. The number of shakers is varied and the response is measured at accelerometer locations spaced along the beam. The accelerometer data are used to obtain the wavenumber response via the discrete Fourier transform. In order to validate and understand the experimental results, the theoretical response of the beam to multiple forces is developed in both the spatial and wavenumber domains according to Timoshenko beam theory.

The normal mode solution for the velocity of a Timoshenko beam is briefly developed in this chapter and the results given by Hutto [9] are restated. These results allow the validation of the measured velocity at a point due to an arbitrary forcing function; this is called the forced spatial-frequency response of the beam. The theoretical wavenumber response, defined as the Fourier transform of the velocity, may be obtained by taking the discrete Fourier transform of the predicted results or by performing the Fourier transform analytically. The wavenumber-frequency response of an infinite Timoshenko beam is derived to obtain the freebending wavenumbers and as a transition step in understanding the relationship between force and velocity in wavenumber space. Finally, the theory of the finite Fourier transform is applied to obtain predictions of the wavenumber-frequency admittance of the finite free-free Timoshenko beam.

#### 3.2. Spatial-Frequency Response of a Finite Beam

The coupled differential equations with internal damping for a Timoshenko type beam with the total transverse deflection,  $y$ , and the slope due to bending,

$\psi$ , are [9,17]

$$\kappa G^* A \left( \frac{\partial^2 y(x,t)}{\partial x^2} - \frac{\partial \psi(x,t)}{\partial x} \right) - \frac{\rho A \partial^2 y(x,t)}{\partial t^2} = q(x,t) \quad , \quad (3.1)$$

$$E^* I \frac{\partial^2 \psi(x,t)}{\partial x^2} + \kappa G^* A \left( \frac{\partial y(x,t)}{\partial x} - \psi(x,t) \right) - \rho I \frac{\partial^2 \psi(x,t)}{\partial t^2} = 0 \quad , \quad (3.2)$$

where  $q$  is the forcing function, the complex elastic modulus is  $E^* = E(1 + j\eta)$ , the complex shear modulus is  $G^* = G(1 + j\eta)$ ,  $I$  is the second moment of inertia of the cross sectional area,  $\rho$  is the density,  $A$  is the cross sectional area, and  $\kappa$  the numerical shape factor [18]. The loss factor,  $\eta$ , is taken to be equal for rotation and translation. Only the time harmonic case is considered. with time dependence  $e^{j\omega t}$ ,  $\omega$  being radian frequency and  $j = \sqrt{-1}$ . Making the following substitutions in Equations (3.1) and (3.2)

$$y(x,t) = Y(x)e^{j\omega t} \quad , \quad (3.3)$$

$$\psi(x,t) = \Psi(x)e^{j\omega t} \quad , \quad (3.4)$$

$$q(x,t) = Q(x)e^{j\omega t} \quad , \quad (3.5)$$

and omitting the time dependence yields,

$$\kappa G^* A Y''(x) - \kappa G^* A \Psi'(x) + \rho A \omega^2 Y(x) = Q(x) \quad , \quad (3.6)$$

$$E^* I \Psi''(x) + \kappa G^* A (Y'(x) - \Psi(x)) + \rho I \omega^2 \Psi(x) = 0. \quad (3.7)$$

Where the primes indicate differentiation with respect to  $x$  the spatial variable. These are the dimensional time harmonic differential equations which are used later in this chapter. In the development of the finite beam response, it is useful to non-dimensionalize the above equations. The non-dimensional variable  $\xi$  is used where,

$$\xi = x/L. \quad (3.8)$$

Making the substitution into Equations (3.6) and (3.7), the non-dimensional time harmonic differential equations are,

$$\frac{\kappa G^* A}{L^2} Y''(\xi) - \frac{\kappa G^* A}{L} \Psi'(\xi) + \rho A \omega^2 Y(\xi) = Q(\xi) \quad , \quad (3.8)$$

$$\frac{E^* I}{L^2} \Psi''(\xi) + \kappa G^* A \left( \frac{1}{L} Y'(\xi) - \Psi(\xi) \right) + \rho I \omega^2 \Psi(\xi) = 0. \quad (3.9)$$

The primes here indicate differentiation with respect to the  $\xi$ . To obtain the normal mode equations, first the homogeneous problem is solved. In references [9,17], the homogeneous forms of Equations (3.8) and (3.9) are decoupled in  $Y$  and  $\Psi$  resulting in,

$$Y'''' + b^2(r^2 + s^2)Y'' - b^2(1 - b^2 r^2 s^2)Y = 0, \quad (3.10)$$

$$\Psi'''' + b^2(r^2 + s^2)\Psi'' - b^2(1 - b^2 r^2 s^2)\Psi = 0, \quad (3.11)$$

where

$$b^2 = \frac{\rho A}{EI} \omega^2 L^4 \quad , \quad (3.12)$$

$$r^2 = \frac{I}{AL^2} \quad , \quad (3.13)$$

$$s^2 = \frac{EI}{\kappa AGL^2} \quad . \quad (3.14)$$

The general solutions for  $Y$  and  $\Psi$  are,

$$Y(\xi) = C_1 \cosh(b\alpha\xi) + C_2 \sinh(b\alpha\xi) + C_3 \cos(b\beta\xi) + C_4 \sin(b\beta\xi) \quad , \quad (3.15)$$

$$\Psi(\xi) = C'_1 \sinh(b\alpha\xi) + C'_2 \cosh(b\alpha\xi) + C'_3 \sin(b\beta\xi) + C'_4 \cos(b\beta\xi) \quad , \quad (3.16)$$

where

$$\frac{\alpha}{\beta} = \frac{1}{\sqrt{2}} \{ \mp(r^2 + s^2) + [(r^2 - s^2)^2 + \frac{4}{b^2}]^{\frac{1}{2}} \}^{\frac{1}{2}} \quad . \quad (3.17)$$

The general relationship between  $C_i$  and  $C'_i$  is given in [9]. Only the relationship between  $C_1$  and  $C'_1$  is needed to describe the bending slope; that relation is given

later. The boundary conditions for the free-free beam applied at the ends of the beam  $\xi = 0$  and  $\xi = 1$  are that the bending moment is zero or,

$$\Psi' = 0 \quad , \quad (3.18)$$

and the total shear force is zero or,

$$\frac{1}{L}Y' - \Psi = 0 \quad . \quad (3.19)$$

Applying the boundary conditions to Equations (3.15) and (3.16) results in a four by four matrix to solve for three of the unknown  $C$ 's. By setting the determinant to zero the characteristic equation is found; it is

$$2 - 2 \cosh(b\alpha) \cos(b\beta) + \frac{b}{(1 - b^2 r^2 s^2)^{1/2}} \times \\ [b^2 r^2 (r^2 - s^2)^2 + (3r^2 - s^2)] \sinh(b\alpha) \sin(b\beta) = 0 \quad . \quad (3.20)$$

This transcendental equation is solved for the natural frequencies of the beam. In the computer code that solves for the natural frequencies it is important to apply a high argument approximation to the hyperbolic functions (that is  $\sinh(x) = \cosh(x)$  as  $x$  becomes large). Otherwise, errors occur.

The mode shapes are now known to within a multiplicative constant. Let the subscript  $i$  denote a mode number corresponding to a natural frequency  $\omega_i$ . Define the following constants,

$$\zeta_i = \frac{\alpha_i^2 + r^2}{\alpha_i^2 + s^2} = \frac{\beta_i^2 - s^2}{\beta_i^2 - r^2} = \frac{\alpha_i^2 + r^2}{\beta_i^2 - r^2} = \frac{\beta_i^2 - s^2}{\alpha_i^2 + s^2} \quad , \quad (3.21)$$

$$\lambda_i = \frac{\alpha_i}{\beta_i} \quad , \quad (3.22)$$

and

$$\delta_i = \frac{\cosh(b_i \alpha_i) - \cos(b_i \beta_i)}{\lambda_i \sinh(b_i \alpha_i) - \zeta_i \sin(b_i \beta_i)} \quad . \quad (3.23)$$

Using the notation introduced above, the mode shapes are

$$Y_i(\xi) = C_1 [\cosh(b_i \alpha_i \xi) + \frac{1}{\zeta_i} \cos(b_i \beta_i \xi) - \lambda_i \delta_i \sinh(b_i \alpha_i \xi) - \delta_i \sin(b_i \beta_i \xi)] \quad , \quad (3.24)$$

$$\Psi_i(\xi) = C'_1 [\sinh(b_i \alpha_i \xi) - \lambda_i \sin(b_i \beta_i \xi) - \lambda_i \delta_i \cosh(b_i \alpha_i \xi) - \delta_i \lambda_i \zeta_i \cos(b_i \beta_i \xi)] \quad (3.25)$$

where the approximations to the hyperbolic functions of large argument are used for the mode shapes also. When  $b_i \alpha_i \gg 1$ ,  $\delta_i \rightarrow \frac{1}{\lambda_i}$  and when  $b_i \alpha_i \xi \gg 1$   $\cosh(b_i \alpha_i \xi) - \sinh(b_i \alpha_i \xi) \rightarrow 0$ , which results in the reduction of Equations (3.24) and (3.25) to

$$Y_i(\xi) = C_1 \left[ \frac{1}{\zeta_i} \cos(b_i \beta_i \xi) - \frac{1}{\lambda_i} \sin(b_i \beta_i \xi) \right] \quad (3.26)$$

$$\Psi_i(\xi) = -C_1 \frac{b_i \alpha_i^2 + s^2}{L \alpha_i} [\lambda_i \sin(b_i \beta_i \xi) + \delta_i \lambda_i \zeta_i \cos(b_i \beta_i \xi)] \quad (3.27)$$

Where  $C'_1$  has been substituted for in terms of  $C_1$ . The resonant wavenumbers of the Timoshenko beam are  $b_i \beta_i$ . Later, it will be seen that these are the free-bending wavenumbers of the solution to the infinite beam that also fit the free-free boundary conditions to produce resonance in the beam.

Since the boundary conditions for the free-free beam allow for rigid body motion, there exists non-trivial solutions for the zero natural frequency. The two rigid body modes are

$$Y_{01} = C_{01} \quad (3.28)$$

$$Y_{02} = C_{02}(\xi - 1/2) \quad (3.29)$$

The orthogonality conditions for the free-free Timoshenko beam are given in [19]. They are

$$\int_0^1 [\rho A Y_i(\xi) Y_j(\xi) + \rho I \Psi_i(\xi) \Psi_j(\xi)] d\xi = 0 \quad i \neq j \quad (3.30)$$

$$= \rho A M_i \quad i = j$$

where  $M_i$  is the normalization constant for the  $i$ th mode.

### 3.3. Forced Spatial-Frequency Response of a Finite Beam

In the normal mode solution to the forced or non-homogeneous Timoshenko beam equations,  $Y$  and  $\Psi$  are expressed in terms of the eigenmodes of the homogeneous solution,

$$Y(\xi) = \sum_{i=0}^{\infty} a_i Y_i(\xi) \quad , \quad (3.31)$$

$$\Psi(\xi) = \sum_{i=0}^{\infty} a_i \Psi_i(\xi) \quad . \quad (3.32)$$

The constants  $a_i$  are the modal expansion coefficients to be determined. The constant  $C_1$  is absorbed into the  $a_i$ 's. By substituting Equations (3.31) and (3.32) into the non-homogeneous differential Equations (3.6) and (3.7), and using the orthogonality integral expressions the unknown  $a_i$ 's are found. The details are found in reference [9]. The general form of the solution for  $a_i$  due to an arbitrary forcing function is,

$$a_i = \frac{\int_0^1 Q(\xi) Y_i(\xi) d\xi}{\rho A M_i [\omega_i^2 (1 + j\eta) - \omega^2]} \quad . \quad (3.33)$$

The integration represents a measure of the orthogonality between the forcing function and the  $i$ th normal mode. If the force distribution is the same as a mode shape, then that mode may have a very high modal constant. Of course, the steady state frequency  $\omega$  plays an important role; mode shapes whose natural frequencies are far removed from the applied frequency have little effect on the beam velocity.

The experimental measurements are taken using shakers that closely approximate point sources. In the  $x$  direction the extent of the shakers is small, and the width of the shaker nearly spans the width of the beam. So the shakers are line sources in three dimensions, but, since the beam is approximated as a one dimensional continuum, a forcing function consisting of an array of such shakers

can be modeled as an array of point sources, so that  $Q(\xi)$  is

$$Q(\xi) = \sum_{m=1}^M q_m \delta(\xi - \xi_m) \quad , \quad (3.34)$$

where  $q_m$  is the complex amplitude of the force located at  $\xi = \xi_m$ . Using the above in Equation (3.33) results in,

$$a_i = D_i \sum_{m=1}^M \frac{q_m}{L} [\cosh(b_i \alpha_i \xi_m) + \frac{1}{\zeta_i} \cos(b_i \beta_i \xi_m) - \lambda_i \delta_i \sinh(b_i \alpha_i \xi_m) - \delta_i \sin(b_i \beta_i \xi_m)] \quad , \quad (3.35)$$

or,

$$a_i = D_i \sum_{m=1}^M \frac{q_m}{L} Y_i(\xi_m) \quad (3.36)$$

where,

$$D_i = \frac{1}{\rho A M_i (\omega_i^2 (1 + j\eta) - \omega^2)} \quad , \quad (3.37)$$

and  $Y_i(\xi_m)$  is value of the mode shape evaluated at  $\xi = \xi_m$ . It should be noted that experimentally, the values  $q_m$  are functions of drive frequency. The modal constants for the translational and rotational rigid body modes are respectively,

$$a_{01} = D_{01} \sum_{m=1}^M \frac{q_m}{L} \quad , \quad (3.38)$$

$$a_{02} = D_{02} \sum_{m=1}^M \frac{q_m}{L} (\xi_m - .5) \quad . \quad (3.39)$$

This is the analytic model developed to validate experiments for the velocity at a point due to an array of point sources exciting a beam at a given frequency.

### 3.4. Wavenumber Response of a Forced Finite Beam

In this section the spatial Fourier transform of the velocity response of a Timoshenko beam excited by multiple point drives is derived. The spatial Fourier transform is,

$$F(k_x) = \int_{-\infty}^{\infty} f(x) e^{-jk_x x} dx \quad , \quad (3.40)$$

and the inverse transform is .

$$f(x) = \frac{1}{2\pi} \int_{-\infty}^{\infty} F(k_x) e^{jk_x x} dk_x \quad (3.41)$$

The wavenumber is  $k_x$  and  $x$  is the spatial variable. In order to obtain the wavenumber-frequency response of the beam, Equation (3.40) is applied to Equation (3.31). The velocity distribution of Equation (3.31) exists from  $0 \leq \xi \leq 1$  and is taken to be zero elsewhere. Thus, the limits of integration in Equation (3.32) are now zero and one. Applying the Fourier transform to Equation (3.31) yields

$$\begin{aligned} \tilde{Y}(k_\xi) &= \int_0^1 Y(\xi) e^{-jk_\xi \xi} d\xi \\ &= \sum_{i=0}^{\infty} a_i \int_0^1 Y_i(\xi) e^{-jk_\xi \xi} d\xi \\ &= \sum_{i=0}^{\infty} a_i \tilde{Y}_i(k_\xi). \end{aligned} \quad (3.42)$$

$\tilde{Y}_i(k_\xi)$  is the spatial Fourier transform of each mode shape, obtained by applying the Fourier transform to Equation (3.24). For the non-rigid body modes  $\tilde{Y}_i(k_\xi)$  is

$$\begin{aligned} \tilde{Y}_i(k_\xi) &= \frac{1}{k_\xi^2 + (b_i \alpha_i)^2} \left\{ e^{-jk_\xi} [jk_\xi \cosh(b_i \alpha_i) + b_i \alpha_i \sinh(b_i \alpha_i)] \right. \\ &\quad \left. - \lambda_i \delta_i (jk_\xi \sinh(b_i \alpha_i) + b_i \alpha_i \cosh(b_i \alpha_i)) - (jk_\xi - \delta_i \lambda_i b_i \alpha_i) \right\} \\ &\quad + \frac{1}{k_\xi^2 - (b_i \beta_i)^2} \left\{ e^{-jk_\xi} [1/\zeta_i (jk_\xi \cos(b_i \beta_i) - b_i \beta_i \sin(b_i \beta_i)) \right. \\ &\quad \left. - \delta_i (jk_\xi \sin(b_i \beta_i) + b_i \beta_i \cos(b_i \beta_i))] + (jk_\xi/\zeta_i - \delta_i b_i \beta_i) \right\} \quad , \quad (3.43) \end{aligned}$$

or,

$$\tilde{Y}_i(k_\xi) = \Gamma_{i1}(k_\xi) + \Gamma_{i2}(k_\xi) \quad , \quad (3.44)$$

where  $\Gamma_{i1}(k_\xi)$  represents the first six terms of Equation (3.43) and  $\Gamma_{i2}(k_\xi)$  represents the second six terms. There are two special cases to consider. One, when  $k_\xi = b_i\beta_i$  the factor  $\Gamma_{i2}(k_\xi)$  becomes,

$$\Gamma_{i2}(k_\xi) = e^{-jk_\xi} \left[ \frac{1}{\zeta_i} \left( \frac{1}{2j} + \frac{e^{-2jk_\xi}}{4k_\xi} \right) - \delta_i \left( \frac{1}{2j} - \frac{e^{-2jk_\xi}}{4k_\xi} \right) \right] - \left[ \frac{1}{4k_\xi\zeta_i} + \frac{\delta_i}{4k_\xi} \right] \quad (3.45)$$

Two, when  $b_i\alpha_i$  becomes large with respect to the numerical precision of the computer,  $\Gamma_{i1}(k_\xi)$  reduces to

$$\Gamma_{i1}(k_\xi) = \frac{-j}{k_\xi + j(b_i\alpha_i)} \quad (3.46)$$

For the rigid body modes, the transforms of the translational and rotational modes are

$$\tilde{Y}_{01}(k_\xi) = \frac{j}{k_\xi} (e^{-jk_\xi} - 1) \quad (3.47)$$

$$\tilde{Y}_{02}(k_\xi) = \frac{1}{k_\xi^2} (e^{-jk_\xi} - 1) + \frac{j}{k_\xi} (e^{-jk_\xi} + 1) \quad (3.48)$$

The transform of each mode shape consists of one component due to the trigonometric functions and another due to the hyperbolic functions. The contribution due to the hyperbolic functions is basically a linear decay in wavenumber. The sine and cosine parts produce a  $\sin(x)/x$  function which has a peak at  $k_\xi = b_i\beta_i$ . The  $b_i\beta_i$  terms are called the resonant wavenumbers of the beam. Equation (3.43) is the transform of a single mode and is a relatively complicated form; complicated in that even if a single mode was excited on the structure the Fourier spectrum would not consist of delta functions at the resonant wavenumber. The dependence of the velocity on the forcing function is held in the  $a_i$ 's

The transform is in terms of the non-dimensional wavenumber  $k_\xi$ . It is desirable to express the transform in terms of the dimensional wavenumber,  $k_x$ . The problem of finding the mapping relation between the transform of the

displacement in terms of the dimensional and non-dimensional wavenumber is cast in terms of the functions  $f$  and  $\hat{f}$ . The proof presented here is general for functions where the relation between  $f$  and  $\hat{f}$  is simply,  $f(\xi) = \hat{f}(L\xi)$  and  $\xi$  is defined to be equal to  $x/L$ . These are the conditions that relate the spatial dependence of the dimensional and non-dimensional forms of the displacement. The relationship between the Fourier transforms of  $f$  and  $\hat{f}$  is desired. The following definitions are made

$$F(k_\xi) = \int_{-\infty}^{\infty} f(\xi) e^{-jk_\xi \xi} d\xi \quad ,$$

$$\hat{F}(k_x) = \int_{-\infty}^{\infty} \hat{f}(x) e^{-jk_x x} dx \quad .$$

In order to find how the values of  $\hat{F}$  may be obtained from  $F$ , first the change of variables  $x = L\xi$  is made in the second definition resulting in

$$\hat{F}(k_x) = L \int_{-\infty}^{\infty} \hat{f}(L\xi) e^{-jk_x L\xi} d\xi \quad .$$

Using the relationship between  $\hat{f}$  and  $f$  to obtain,

$$\hat{F}(k_x) = L \int_{-\infty}^{\infty} f(\xi) e^{-jk_x L\xi} d\xi \quad ,$$

and finally using the first definition yields the desired result

$$\hat{F}(k_x) = LF(k_x L) \quad . \quad (3.49)$$

Similarly one may obtain,

$$F(k_\xi) = \frac{1}{L} \hat{F}(k_\xi / L) \quad . \quad (3.50)$$

This is the relation by which the values of  $\hat{F}$  may be obtained from  $F$ . For the quotient of two functions of the transformed variable the multiplicative  $L$

term would cancel. The method of proof is suggested by the derivation of the similarity theorem in [15] and also by [20].

The exact Fourier transform of the spatial response of the forced Timoshenko beam serves as a basis for comparison for experimental and theoretical estimates of the Fourier spectrum.

### 3.5. Wavenumber Response of an Infinite Beam

In this section, predictions of the wavenumber response of an infinite beam are derived using Timoshenko beam theory. Using this result, the dispersion relation for an infinite beam is obtained. The derivation basically follows the development of Magrab [21].

Equations (3.6) and (3.7), the dimensional differential equations, re-written here,

$$\kappa G^* A Y''(x) - \kappa G^* A \Psi'(x) + \rho A \omega^2 Y(x) = Q(x) \quad ,$$

$$E^* I \Psi''(x) + \kappa G^* A (Y'(x) - \Psi(x)) + \rho I \omega^2 \Psi(x) = 0 \quad ,$$

are the starting point of the analysis. The Fourier transform as defined in Equation (3.40) is used to transform the above into wavenumber domain. Let  $\mathcal{F}$  represent the Fourier transform operator, the following identity from Bracewell [15],  $\mathcal{F}\{f'(x)\} = jk_x \mathcal{F}\{f(x)\}$  is used in obtaining,

$$\tilde{Y}(k_x)[k_x^2 \kappa G^* A + \rho A \omega^2] + \tilde{\Psi}(k_x)[-jk_x \kappa G^* A] = \tilde{Q}(k_x) \quad (3.51)$$

$$\tilde{Y}(k_x)[-jk_x \kappa G^* A] + \tilde{\Psi}(k_x)[-k_x E^* I + \rho I \omega^2 - \kappa G^* A] = 0 \quad , \quad (3.52)$$

after applying the Fourier transform to Equations (3.7) and (3.8). Define the following terms;

$$\begin{aligned} \Omega &= \rho A \omega^2 \quad , \\ \Theta &= \rho I \omega^2 \quad , \end{aligned} \quad (3.53)$$

$$\nu = \kappa G^* A$$

Also, let the freebending wavenumber for the Bernoulli Euler beam as defined in Junger and Feit [22] be  $k_{BE}^4 = \Omega/E^*I$ . Use the expressions in Equation (3.53) to simplify Equations (3.51) and (3.52) to

$$\tilde{Y}(k_x)[-k_x^2\nu + \Omega] + \tilde{\Psi}(k_x)[-jk_x\nu] = \tilde{Q}(k_x) \quad (3.54)$$

$$\tilde{Y}(k_x)[jk_x\nu] + \tilde{\Psi}(k_x)[-k_x E^*I + \Theta - \nu] = 0 \quad (3.55)$$

Equations (3.54) and (3.55) represent two coupled algebraic equations in  $\tilde{Y}(k_x)$  and  $\tilde{\Psi}(k_x)$ . By using Cramer's rule both unknowns may be found. Applying Cramer's rule to solve for  $\tilde{Y}(k_x)$  results in

$$\tilde{Y}(k_x) = \frac{\tilde{Q}(k_x)[\Theta - k_x^2 E^*I - \nu]}{k_x^4 E^*I\nu - k_x^2[\Theta\nu + \Omega E^*I] + \Omega[\Theta - \nu]}$$

Dividing top and bottom by  $E^*I\nu$  results in,

$$\tilde{Y}(k_x) = \frac{\tilde{Q}(k_x)[\frac{1}{E^*I}(\Theta/\nu - 1) - k_x^2/\nu]}{k_x^4 - k_x^2[\Theta/E^*I + \Omega/\nu] + k_{BE}^4[\Theta/\nu - 1]} \quad (3.56)$$

The wavenumber-frequency admittance is defined as the quotient of the Fourier transforms of the velocity and the force, for the infinite beam

$$H_\infty(k_x) = j\omega \frac{\frac{1}{E^*I}(\Theta/\nu - 1) - k_x^2/\nu}{k_x^4 - k_x^2[\Theta/E^*I + \Omega/\nu] + k_{BE}^4[\Theta/\nu - 1]} \quad (3.57)$$

where the multiplicative  $j\omega$  comes from the conversion of displacement to velocity. Thus, the wavenumber-frequency response of an infinite beam to an arbitrary forcing function has been derived according to the assumptions of Timoshenko beam theory. For a Bernoulli-Euler type beam  $\Theta \rightarrow 0$  and  $\nu \rightarrow \infty$  ( $\nu$  as defined in (3.53) not Poisson's ratio) [22], and Equation (3.57) becomes

$$\tilde{Y}(k_x) = \frac{-\tilde{Q}(k_x)/E^*I}{k_x^4 - k_{BE}^4} \quad (3.58)$$

From this it can be seen that  $k_{BE}$  is the wavenumber at which the admittance for the Bernoulli-Euler beam has its peak.

The zeros of the denominator of Equation (3.58) are

$$\begin{aligned}\gamma_{1,2,3,4} &= \pm \left\{ \frac{1}{2} \left[ \frac{\Theta}{EI} + \frac{\Omega}{\nu} \pm \sqrt{\left( \frac{\Theta}{EI} + \frac{\Omega}{\nu} \right)^2 - 4k_{BE}^4 \left( \frac{\Theta}{\nu} - 1 \right)} \right] \right\}^{\frac{1}{2}} \\ &= \pm \left\{ \frac{1}{2} \left[ \frac{\Theta}{EI} + \frac{\Omega}{\nu} \pm \sqrt{\left( \frac{\Theta}{EI} - \frac{\Omega}{\nu} \right)^2 + 4k_{BE}^4} \right] \right\}^{\frac{1}{2}},\end{aligned}\quad (3.59)$$

noting  $k_{BE}^4 \Theta / \nu = \Omega \Theta / E^* I \nu$ . The  $\gamma$ 's are the poles of the solution.

In order to interpret the meaning of the poles of the admittance, the inverse Fourier transform of the solution must be examined. Subject to,

$$\frac{\Theta}{EI} + \frac{\Omega}{\nu} < \sqrt{\left( \frac{\Theta}{EI} - \frac{\Omega}{\nu} \right)^2 + 4k_{BE}^4}, \quad (3.60)$$

and the damping taking the form  $E^* = E(1 + j\eta)$ , the poles of the Equation (3.59) are located approximately as shown in Figure 3.1. If the damping is zero, then the roots of the denominator are either purely real or imaginary. The inverse Fourier transform solution for the displacement is,

$$Y(x) = \frac{1}{2\pi j\omega} \int_{-\infty}^{\infty} \bar{Q}(k_x) H_{\infty}(k_x) e^{jk_x x} dk_x.$$

Since the forcing function under consideration is a series of delta functions, it suffices to examine the solution for a single point force located at  $x = x_0$ , in which case the preceding equation simplifies to,

$$Y(x) = \frac{1}{2\pi j\omega} \int_{-\infty}^{\infty} H_{\infty}(k_x) e^{jk_x(x-x_0)} dk_x. \quad (3.61)$$

This integral may be evaluated using the theory of residues. To use residue theory, the integrand must decay at infinity and consist of only outgoing waves. Hence there are two cases. One, for  $x - x_0 < 0$ , where the integrand is evaluated using the two residues in the upper half plane (UHP in Figure 3.1). Two, for

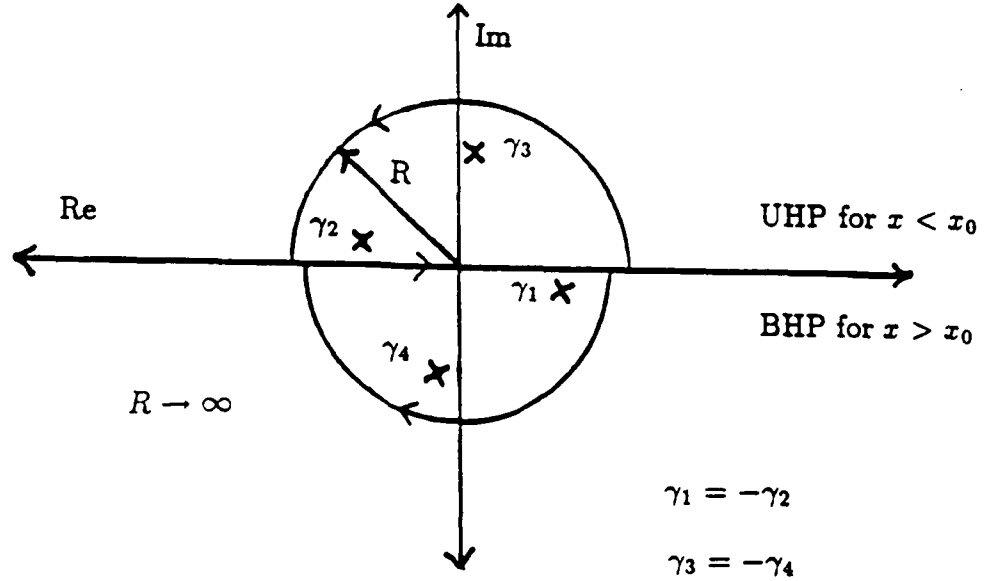


Figure 3.1 Location of the poles and contours for the residue evaluation.

$x - x_0 > 0$  the integrand is evaluated using the two residues in the bottom half plane (BHP in Figure 3.1).

It can be seen in Equation (3.61) that the poles near the real axis represent the propagating part of the velocity field and the poles near the imaginary axis the evanescent field. The freebending wavenumber at a particular frequency is defined as

$$k_f = \gamma_1 \quad (3.62)$$

It can be easily shown that the freebending wavenumber should be the same as the resonant wavenumbers at the resonant frequencies. Upon examining the definitions of Equations (3.12)-(3.14) and Equation (3.53), the following relations

are found

$$b^2 r^2 = L^2 \Theta / E^* I.$$

$$b^2 s^2 = L^2 \Omega / \nu,$$

$$b^2 = L^4 k_{BE}^4.$$

Using these in Equation (3.59) the free-bending wavenumbers results in,

$$\begin{aligned} \gamma_{1,2,3,4} &= \pm \frac{b}{\sqrt{2}L} \left[ r^2 + s^2 \pm \sqrt{(r^2 - s^2)^2 + 4/b^2} \right]^{1/2} \\ &= \pm b\beta/L, \pm j b\alpha/L \end{aligned} \quad (3.63)$$

The resonant frequencies are just those frequencies for which the freebending wavenumber satisfies the boundary conditions. It is very useful to examine the overall dispersion relation in order to better tell what wavenumbers to expect at the frequencies of interest. In Figure 3.2, the resonant wavenumbers are plotted using solid dots and the freebending wavenumber for an infinite Timoshenko beam using a solid line. The freebending wavenumber for a Bernoulli-Euler beam is also plotted in the same figure. In Table 3.1, the resonant frequencies and the resonant wavenumbers for the beam are listed. The dispersion diagram is helpful in two ways. First, it provides a guide in spacing the accelerometers to measure the velocity field. Also, this plot may be used to see what wavenumbers might be excited in a beam. In Section 2.4.4, the highest freebending wavenumber that is expected for the velocity is read from this figure. The calculations were made using the parameters for the beam used in the experiments (see Chapter 2 for material constants).

### 3.6. Relation between Force and Velocity in Wavenumber Space for a Finite Beam

As seen in Equation (3.57), the admittance of an infinite beam is a that function of only the physical and geometric properties of the beam and

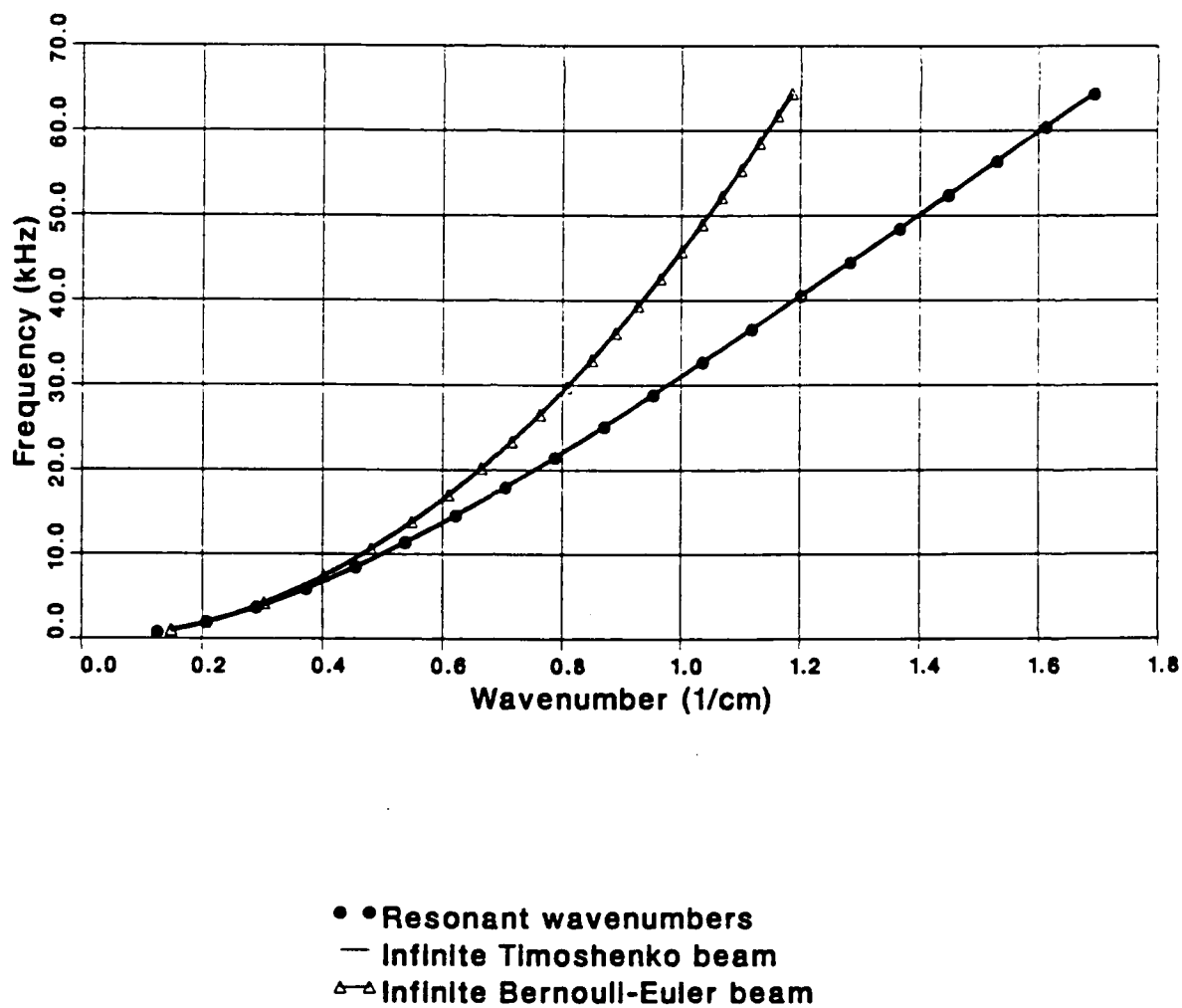


Figure 3.2 The dispersion relation for the beam used in the experiment. The freebending wavenumbers for the infinite beam are shown as well as the resonant wavenumbers (and frequencies) for the finite beam.

Table 3.1 Resonant frequencies and wavenumbers.

Mode No.	Resonant Frequency (Hz)	Resonant Wavenumber ( $\text{cm}^{-1}$ )
1	703.	0.124
2	1904.	0.207
3	3644.	0.290
4	5847.	0.373
5	8439.	0.456
6	11350.	0.539
7	14519.	0.622
8	17893.	0.705
9	21427.	0.787
10	25087.	0.871
11	28845.	0.953
12	32673.	1.036
13	36557.	1.118
14	40483.	1.201
15	44436.	1.284
16	48403.	1.366
17	52384.	1.448
18	56365.	1.530
19	60342.	1.612
20	64302.	1.693

independent of the forcing function. However, Equations (3.33) and (3.42) imply that the admittance function for a finite beam, formed by dividing the velocity wavenumber spectrum by the force wavenumber spectrum, is a function that depends on the form of the forcing function as well as the properties of the beam. Because we are forced to deal with finite beams, quantification of the dependence of the admittance, computed as the ratio of the velocity and force wavenumber spectra, on the physical properties of the beam as well as the properties of the forcing function is required.

For linear, shift invariant systems, the impulse response function completely determines the system. Both the finite and the infinite beam are linear systems, but only the infinite beam is a shift invariant system. Physically, shift invariance means that only the distance between the shaker and the accelerometer are needed to define the response, not their absolute locations. For the finite beam the location of force and the sensor are needed.

In an attempt to quantify the meaning of the quantity  $\tilde{Y}(k_x)/\tilde{Q}(k_x)$  for a finite beam, the finite Fourier transform is applied to the governing differential equations of the Timoshenko type beam. As defined in Bracewell, the finite Fourier transform is

$$F(k_x, a, b) = \int_a^b f(x) e^{-jk_x x} dx \quad (3.64)$$

The inverse finite Fourier transform takes the form of a series,

$$f(x) = \frac{1}{2\pi L} \sum_{n=-\infty}^{\infty} F(2n\pi/L, a, b) e^{j2\pi n x/L} \quad (3.65)$$

The finite Fourier transform of  $f'(x)$  the spatial derivative of  $f(x)$  is

$$\int_a^b f'(x) e^{-jk_x x} dx = jk_x F(k_x, a, b) + f(b) e^{-jk_x b} - f(a) e^{-jk_x a} \quad (3.66)$$

Higher order derivatives may also be obtained from the above formula. This relation is different than relations for the infinite transform. The interval

under consideration is the non-dimensional length of the beam  $0 < \xi < 1$ , for convenience and brevity the following notation is introduced,

$$F_f(k_x) \stackrel{\text{def}}{=} F(k_x, 0, 1) \quad . \quad (3.67)$$

The transform variable for the non-dimensional equations is  $k_\xi$  and the transforms of the displacement, bending slope and force are defined in Equation (3.67)

or,

$$\tilde{Y}_f(k_\xi) = \int_0^1 Y(\xi) e^{-jk_\xi \xi} d\xi \quad , \quad (3.68)$$

$$\tilde{\Psi}_f(k_\xi) = \int_0^1 \Psi(\xi) e^{-jk_\xi \xi} d\xi \quad , \quad (3.69)$$

$$\tilde{Q}_f(k_\xi) = \int_0^1 Q(\xi) e^{-jk_\xi \xi} d\xi \quad . \quad (3.70)$$

Applying the definition of the finite Fourier transform to the non-dimensional equations of motion for the Timoshenko beam (Equations (3.8) and (3.9)) yields

$$\begin{aligned} \frac{\nu}{L^2} \left\{ [Y'(\xi) + jk_\xi Y(\xi)] e^{-jk_\xi \xi} \Big|_{\xi=0}^{\xi=1} - k_\xi^2 \tilde{Y}_f(k_\xi) \right\} \\ - \frac{\nu}{L} [\Psi(\xi) e^{-jk_\xi \xi} \Big|_{\xi=0}^{\xi=1} + jk_\xi \tilde{\Psi}_f(k_\xi)] + \Omega \tilde{Y}_f(k_\xi) = \tilde{Q}_f(k_\xi) \quad . \end{aligned} \quad (3.71)$$

By using the first boundary condition, given Equation (3.10)

$$\frac{1}{L} Y'(\xi) - \Psi(\xi) = 0 \quad \text{for} \quad \xi = 0 \quad \text{and} \quad \xi = 1$$

Equation (3.71) simplifies to

$$\tilde{Y}_f(k_\xi) \left[ \frac{-\nu k_\xi^2}{L^2} + \Omega \right] + \tilde{\Psi}_f(k_\xi) [-jk_\xi/L] = \tilde{Q}_f(k_\xi) - \frac{j\nu k_\xi}{L^2} Y(\xi) e^{-jk_\xi \xi} \Big|_{\xi=0}^{\xi=1} \quad . \quad (3.72)$$

Taking the finite Fourier transform of the second differential and using the second boundary condition ( $\Psi'(0) = \Psi'(1) = 0$ ) results in,

$$\tilde{Y}_f(k_\xi) \left[ \frac{j\nu k_\xi}{L} \right] + \tilde{\Psi}_f(k_\xi) \left[ \frac{E^* I}{L^2} k_\xi^2 + \Theta - \nu \right] = \left[ \frac{-\nu}{L} Y(\xi) - \frac{E^* I}{L^2} \Psi(\xi) \right] e^{-jk_\xi \xi} \Big|_{\xi=0}^{\xi=1} \quad . \quad (3.73)$$

The terms that contain the values of the displacement and bending slope at the endpoint are contained in the following terms.

$$B_1(k_\xi) = \frac{-j\nu k_\xi}{L^2} Y(\xi) e^{-jk_\xi \xi} \Big|_{\xi=0}^{\xi=1} \quad (3.74)$$

$$B_2(k_\xi) = \left[ \frac{-\nu}{L} Y(\xi) - \frac{E^* I}{L^2} \Psi(\xi) \right] e^{-jk_\xi \xi} \Big|_{\xi=0}^{\xi=1} \quad (3.75)$$

Using the definitions in Equations (3.74) and (3.75) to rewrite the transformed differential equations in a form ready for solution of the unknowns yields

$$\tilde{Y}_f(k_\xi) \left[ \frac{-\nu k_\xi^2}{L^2} + \Omega \right] + \tilde{\Psi}_f(k_\xi) \left[ \frac{-jk_\xi}{L} \right] = \tilde{Q}_f(k_\xi) + B_1(k_\xi) \quad , \quad (3.76)$$

$$\tilde{Y}_f(k_\xi) \left[ \frac{j\nu k_\xi}{L} \right] + \tilde{\Psi}_f(k_\xi) \left[ \frac{E^* I}{L^2} k_\xi^2 + \Theta - \nu \right] = B_2(k_\xi) \quad . \quad (3.77)$$

These equations are solved using Cramer's rule for  $\tilde{Y}_f(k_\xi)$ , which results in ,

$$\tilde{Y}_f(k_\xi) = \frac{[\tilde{Q}_f(k_\xi) + B_1(k_\xi)] \left[ -\frac{E^* I}{L^2} k_\xi^2 + \Theta - \nu \right] + B_2(k_\xi) j k_\xi \frac{\nu}{L}}{k_\xi^4 \frac{E^* I}{L^4} - \frac{k_\xi^2}{L^2} [\nu \Theta - E^* I \Omega] + \Omega [\Theta - \nu]} \quad . \quad (3.78)$$

Using the fact that  $H_\infty(k_x) = H_\infty(k_\xi/L)$  the above equation can be written as

$$\tilde{Y}_f(k_\xi) = \frac{1}{j\omega} H_\infty(k_\xi/L) \left[ \tilde{Q}_f(k_\xi) + B_1(k_\xi) + \frac{B_2(k_\xi)}{\frac{E^* I}{L\nu} j k_\xi + \frac{L}{j k_\xi \nu} (\Theta - \nu)} \right] \quad . \quad (3.79)$$

The admittance for the finite beam is

$$\begin{aligned} H_f(k_\xi) &= \frac{j\omega \tilde{Y}_f(k_\xi)}{\tilde{Q}_f(k_\xi)} \\ &= H_\infty(k_\xi/L) \left\{ 1 + \frac{1}{\tilde{Q}_f(k_\xi)} \left[ B_1(k_\xi) + \frac{B_2(k_\xi)}{\frac{E^* I}{L\nu} j k_\xi + \frac{L}{j k_\xi \nu} (\Theta - \nu)} \right] \right\} . \quad (3.80) \end{aligned}$$

The wavenumber response of the finite beam consists of a part that is the same as for an infinite beam and another part that depends on the boundary values of the displacement and bending slope. Since the constants  $B_1(k_\xi)$  and  $B_2(k_\xi)$  depend on the values of the spatial variables, to solve for the wavenumber response the spatial response must be obtained as well. Although it is not done here, the constants would be evaluated by inverting the Equation (3.78) and considering

$Y(0)$ ,  $Y(1)$ ,  $\Psi(0)$  and  $\Psi(1)$  as unknown constants. Upon inversion these constants could be evaluated and then substituted into the wavenumber response.

There are several implications from Equation (3.80). First, the wavenumber admittance of the free-free Timoshenko beam is dependent on the location and amplitude of the forces applied to the beam. This means that a wavenumber admittance that is a function of only the physical and geometric properties of the beam is not obtained simply by forming the quotient of the wavenumber velocity spectrum and force spectrum. The infinite beam part of the admittance is invariant with respect to change in the forcing function. At wavenumbers where the amplitude of the forcing function is high, the admittance measured with the finite beam approximates the infinite beam wavenumber admittance. The velocity response of the beam at a particular wavenumber is a function of how near this wavenumber is to the freebending wavenumber and how well this wavenumber matches the boundary conditions. When both of these conditions are met resonance occurs. Since the impedance of the beam is low at resonance, it is expected that the amplitude of the force wavenumber spectra would be low if the forcing function matches the structural mode shape. With a matched forcing function, the finite beam admittance at resonance is a poor approximation to the infinite beam admittance. It is important to note that even at a resonant frequency the resulting velocity contribution from the resonant mode shape would be small if the value from the spatial integration that occurs in Equation (3.33) is small, i.e., if the force distribution does not match the mode shape.

## Chapter 4

EQUIVALENT CIRCUIT MODELING OF  
THE SHAKER FORCE/GAGE UNITS

## 4.1. Introduction

In this chapter, the response of the combination shaker/force gage units is modeled using equivalent circuits. The basic Mason equivalent circuits for piezoelectric and non-piezoelectric materials are shown. From these circuits the low frequency approximations are derived. First, the equivalent circuit for the overall force output of the transducer is developed. From this model, the levels and resonance frequencies of the force output due to an arbitrary termination impedance are found. Also, the relationship between the voltage output from the force gage section and the force applied to the structure is obtained through the use of equivalent circuits. The effect on the force gage output due to added cable capacitance, mass loading and contact stiffness is obtained. The method of calibration and its consequences are also be examined.

## 4.2. Equivalent Circuit Analysis for Transducers

The dynamic response of shakers can be represented by using Mason equivalent circuits. These circuits, in their exact form, represent a solution to the electrical and elastic differential equations that govern the transducer system. For piezo-active elements, a catalogue of lumped impedance, equivalent circuits for different boundary conditions and piezoelectric couplings have been developed [23]. The analysis of electro-mechanical circuits in general is found in Beranek[24]. The Mason equivalent circuits of the piezoelectric elements and the non-piezoactive elements may be cascaded together to form the model for the entire transducer system. In this study, the low frequency approximation to the

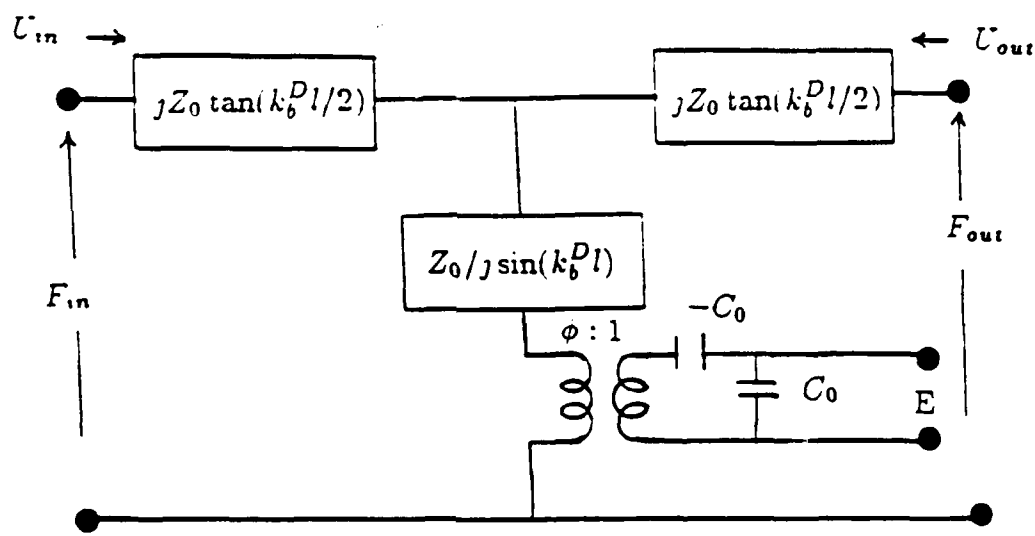
exact solution is used.

By constructing the complete circuit representation of the transducer, the resonance frequency, output force and force sensitivity of the system can be approximated as well as the effect of changing any of the transducer parameters. The equivalent circuit analysis yields solutions for the desired quantities, the overall force output and the force gage sensitivity, in terms of the material properties of the shaker, excitation frequency and load impedance.

The equivalent circuits are a representation of the solution of the differential equations governing the elements of the transducer. Certain boundary conditions have been applied to the non-active areas (in this case the radial faces). Basically, the boundary conditions are that the radial faces are stress free and the electric field lines do not fringe. The wave motion through the transducer is assumed to be a plane wave traveling in the axial direction. Because the length to diameter ratio is large, the response of the shaker is almost entirely in the axial direction. Berlincourt et al. [23] describe in detail the boundary conditions assumed for the equivalent circuits mentioned above. The non-piezoelectric elements of the transducer are modeled as longitudinally vibrating rods or bars.

The equivalent circuits utilized are of the mechanical impedance type. In the mechanical impedance representation, the flow quantity is velocity and the potential quantity is force. The boundary conditions for the force and velocity transmitting surfaces are left as arbitrary impedances. Each section of the transducer that has different material properties will be modeled using a similar equivalent circuit, but with different material properties. The rest of the model can be constructed by cascading the equivalent circuits one after the other.

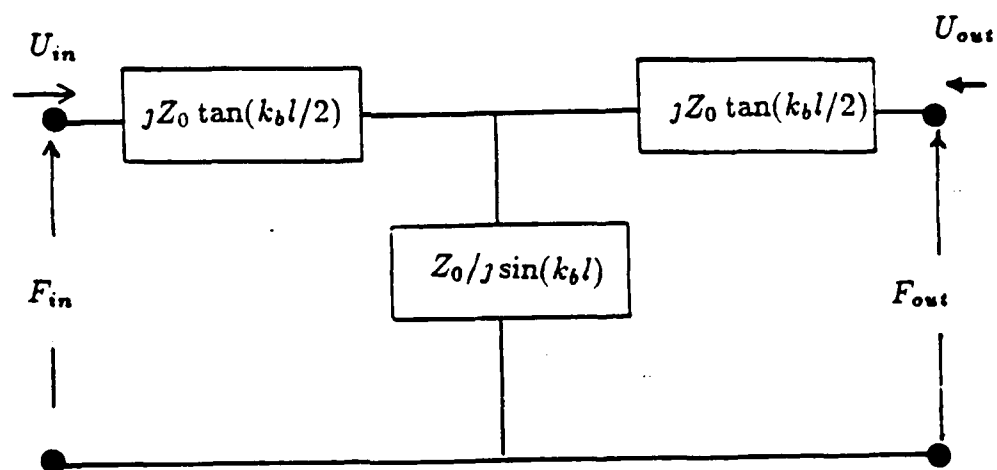
The equivalent circuit for the 33 coupled piezoceramic is shown in Figure 4.1a. The equivalent circuit for the non-piezoelectric elements is shown in Figure 4.1b.



$$Z_0 = \rho A v_b^D, \quad \phi = \frac{A d_{33}}{l s_{33}^E}, \quad k_b^D = \frac{\omega}{v_b^D}$$

$$C_0 = \frac{A \epsilon_{33}^T s_{33}^D}{s_{33}^E l}, \quad v_b^D = \sqrt{\frac{1}{\rho s_{33}^D}}$$

(a)



$$Z_0 = \rho A v_b, \quad k_b = \frac{\omega}{v_b}, \quad v_b = \sqrt{\frac{1}{\rho s_{33}}}$$

(b)

Figure 4.1 Equivalent circuit for (a) piezoelectric 33 coupled sections, (b) Non-piezoelectric sections [23].

[23]. In these figures,  $U$  is the velocity and  $F$  is the force. These are the solutions to the differential equations for the so called 'length expander' case. The values for the impedances in the equivalent circuits are calculated from the formulas given below the circuit diagrams in Figure 4.1. The nomenclature used to describe the constants defining the impedances and the impedances themselves is a combination of that used in [23,25]. Since piezoceramics are anisotropic materials the notation used in the definition of the constants use indicial notation. Additionally, since there are both electrical and elastic boundary conditions to be denoted, there must exist a flexibility in the nomenclature to describe these conditions.

The numerical subscripts (for example  $g_{33}$ ) have the following meaning. The first index indicates the axis to which the electroded surface is perpendicular, or the direction of the poling of the crystal. The second index indicates the direction the forces will be applied (either piezoelectrically induced or externally applied). The coordinate system for a crystal is shown in Figure 4.2 and is a local coordinate system for each element of the transducer. There are several different alphabetic subscripts and superscripts. The superscripts  $D$  and  $E$  are used in reference to elastic constants,  $E$  means that the constants were measured with a constant electric field, and  $D$  that the charge density was constant. The superscripts  $T$  and  $S$  are used in reference to the electric or piezoelectric constants,  $T$  means that the constants were measured with the free elastic boundary conditions, and  $S$  with the boundary conditions clamped. These boundary conditions are implicit in the solution of the governing equations and assumed not to change. For example, the radial surface of the 33 coupled transducer is assumed to be stress free, hence the electric properties are indicated with the  $T$  superscript. The subscript  $b$  used in conjunction with the wavenumber

$k_b^E$  and the wave velocity  $v_b^E$  indicates that the length expander or bar mode is the prominent mode. With the subscript and superscript notation described, the material constants are defined. The constants  $g_{33}$  and  $d_{33}$  are piezoelectric constants. The load bearing area and the electroded area (which are the same for the piezoelectric materials with the 33 coupling) is denoted as  $A$  and the axial length as  $l$ . The material density is  $\rho$ .  $C_0$  is the electrical capacitance and  $\phi$  or  $\psi$  will be used in this chapter to denote the transformation factor which converts from the electrical domain to the mechanical. The relative dielectric constant of the piezoceramic is  $\epsilon_{33}$  and the free space constant is  $\epsilon_0$ . The elastic compliance is  $s_{33}$  which is the inverse of the elastic modulus.

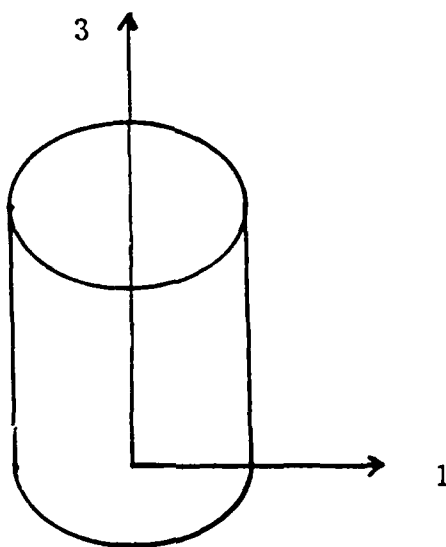


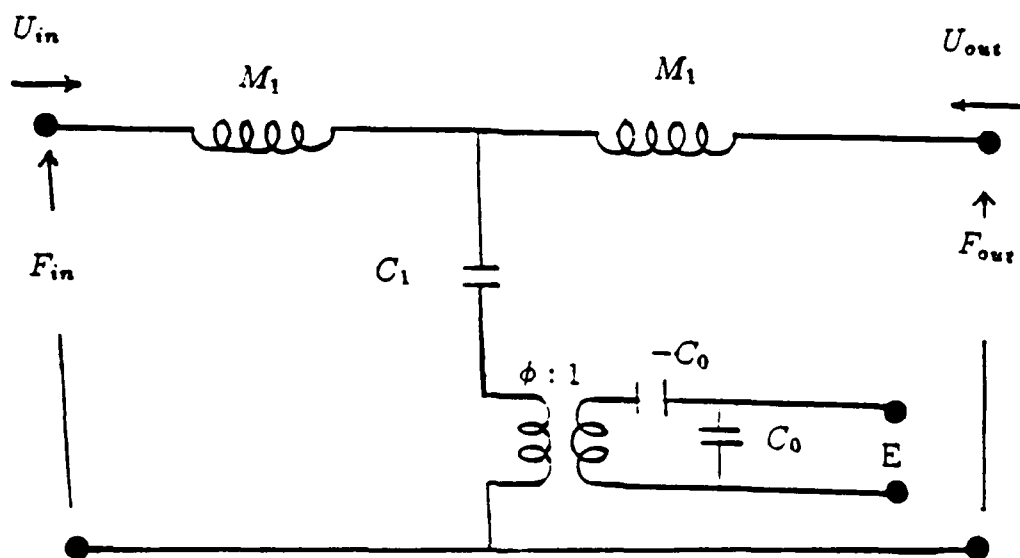
Figure 4.2 Local coordinate system for the ceramic.

The representations in Figures 4.1a and 4.1b are the solutions to the governing differential equations and have no frequency limitation except that

the boundary conditions will break down at high frequency. These representations become cumbersome to program and it is efficacious to use the small argument approximation for the sine and cosine functions. The validity of these assumptions breaks down when the error in the small argument approximation in any one of the elements becomes appreciable. For example, one would expect the small argument approximation to become invalid in the decoupler section first. The small argument model (which amounts to a low frequency approximation) is shown in Figure 4.3a for the piezoactive element and Figure 4.3b for the elastic element. This model reduces to lumping the static mass and stiffness of the elements of the transducer into the branches of the circuit. This approach allows some engineering approximations to be made. When the frequency is low, the stiffness and mass of some adjacent elements may be combined to simplify the resulting equivalent circuit without a significant loss of accuracy. The overall transducer model is obtained by cascading the equivalent circuits for each section one after the other. To be precise, every different material of the transducer should be modeled separately. This could result in a very large equivalent circuit with many branches. Thus, the initial iterations of the model are made by making simplifying assumptions about what are the important elements of the transducer. For example, with respect to the overall force output of the shaker, the force gage plays a small part. So in order to remove a loop of the total equivalent circuit, the mass and compliance of the force gage ceramic are lumped with the headmass and the decoupler sections.

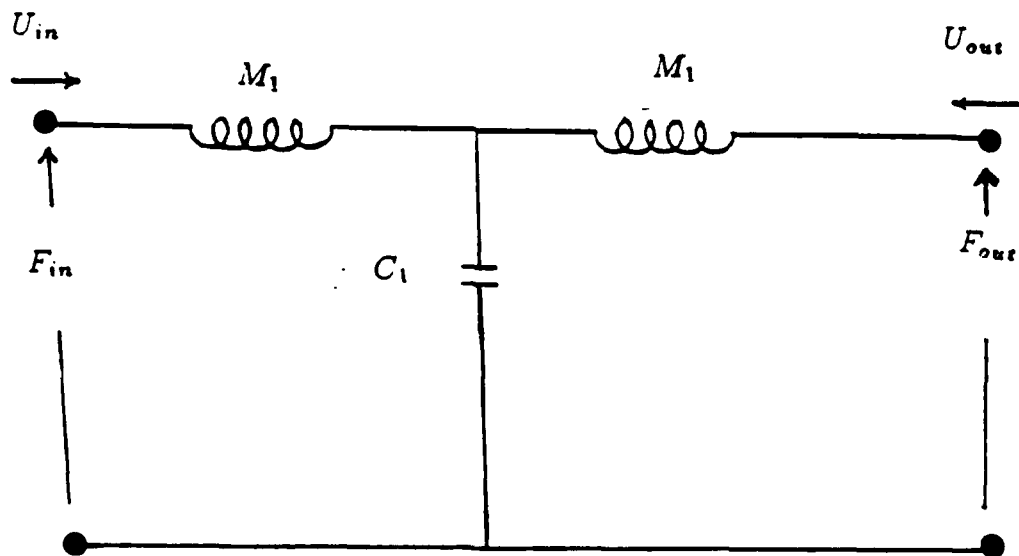
#### 4.3. Equivalent Circuit Model for the Shaker Force Output

The transducer described in Section 2.3 is modeled in this section. The modeling process is iterative. Complexity is added to the model until predicted results match measurements.



$$M_1 = 1/2 \text{ mass of ceramic}, \quad C_1 = \frac{l s_{33} E}{A}$$

(a)



$$M_1 = 1/2 \text{ mass of the element}, \quad C_1 = \frac{l s}{A}$$

(b)

Figure 4.3 Low frequency equivalent circuit for (a) piezoelectric sections, (b) non-piezoelectric sections.

Figure 4.4 shows the equivalent circuit for the entire shaker, force gage transducer system using the low frequency approximations of Figures 4.3a and 4.3b. Since the branches of each section of the circuit form a T, these circuits are called T circuits. The first T circuit represents the drive section and the tailmass section. The compliances of the two PZT disks and the brass tailmass are included in  $C_1$ . At low frequencies, these elements act as a combined stiffness [12]. The mass of the tailmass and one half the mass of a PZT disk are lumped into  $M_1$ . The mass of one and one half PZT disks are included in the calculation of  $M_2$ . The second T circuit includes the effect of the decoupler alone. The compliance  $C_2$  is the compliance of the decoupler. Half of the decoupler mass is lumped into each of  $M_2$  and  $M_3$ . The third T circuit includes the effect of the headmass and the PZT force cell in a manner similar to the first T circuit. The effect of the added mass due to the glue used to stress relieve the lead wire attachments is added to  $M_1$ ,  $M_2$  and  $M_3$  in proportion to their estimated amounts. The values of the elastic and piezoelectric constants needed for calculation of the impedances in the equivalent circuit are found in Table 4.1 and 4.2.

Explicitly, the values of the impedances in Figure 4.4 are calculated from;

$$M_1 = 1/2 \text{ mass of PZT driver} + \text{mass of brass tailmass},$$

$$M_2 = 3/2 \text{ mass of PZT driver} + 1/2 \text{ mass of decoupler},$$

$$M_3 = 1/2( \text{mass of decoupler} + \text{mass force gage} + \text{mass of headmass}),$$

$$M_4 = 1/2( \text{mass force gage} + \text{mass of headmass}),$$

$$C_0 = \text{electrical capacitance of PZT driver},$$

$$C_1 = \text{mechanical compliance of drive section},$$

$$C_2 = \text{compliance of decoupler},$$

$$C_3 = \text{compliance of headmass} + \text{force gage},$$

$$Z_t = \text{termination impedance},$$

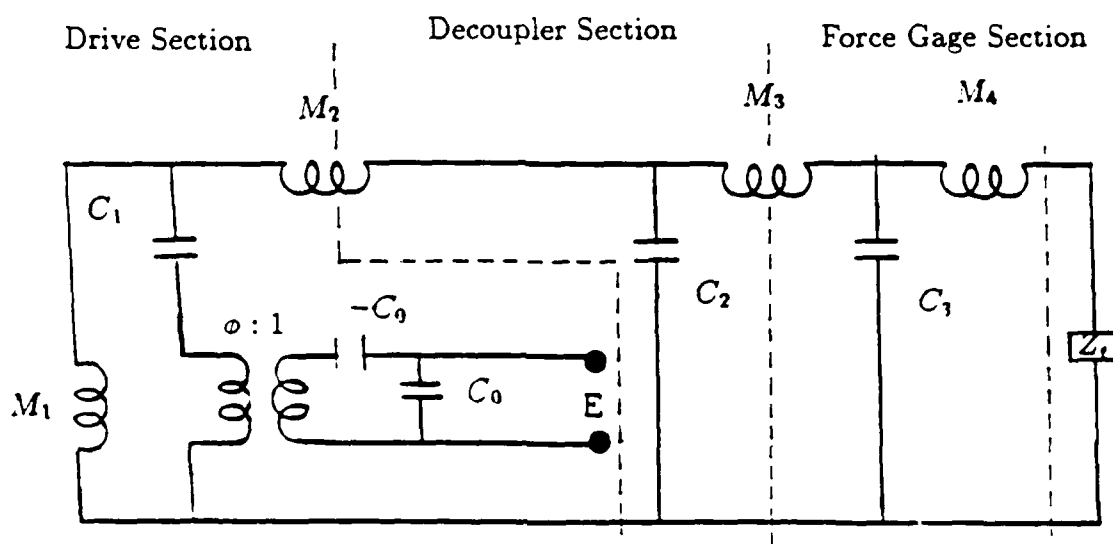


Figure 4.4 Equivalent circuit model for the force output of the transducer.

$\phi$  = transformation factor.

These values are calculated using the formulas given in Figure 4.2. After combining similar impedances and reflecting electrical elements through the transformers to convert them into the mechanical domain, the circuit takes the form of Figure 4.5. The compliance of this branch is  $C_1^*$  which now takes into account the effect of the electrical impedance.

The loop equations for this circuit, using the currents shown in Figure 4.5 (noting that current is velocity and voltage is force) are;

$$E\phi = I_1(j\omega M_1 + \frac{1}{j\omega C_1^*}) + I_2(\frac{-1}{j\omega C_1^*}), \quad (4.1a)$$

$$-E\phi = I_1(\frac{-1}{j\omega C_1^*}) + I_2(j\omega M_2 + \frac{1}{j\omega C_1^*} + \frac{1}{j\omega C_2}) + I_3(\frac{-1}{j\omega C_2}), \quad (4.1b)$$

$$0 = I_2(\frac{-1}{j\omega C_2}) + I_3(j\omega M_3 + \frac{1}{j\omega C_2} + \frac{1}{j\omega C_3}) + I_4(\frac{-1}{j\omega C_3}) \quad (4.1c)$$

Table 4.1 Nominal material properties.

Material	Elastic compliance (m <sup>2</sup> /N)	Density (kg/m <sup>3</sup> )
Aluminium	$1.41 \times 10^{-11}$	2700
Brass	$9.62 \times 10^{-12}$	8500
PZT-4	not applicable	7750

Table 4.2 Material properties for PZT-4.

Material Property	Value (units)
$g_{33}$	$26.1 \times 10^{-3}$ (Vm/N)
$d_{33}$	$289 \times 10^{-12}$ (m/N)
$s_{33}^D$	$7.9 \times 10^{-12}$ (m <sup>2</sup> /N)
$s_{33}^E$	$15.5 \times 10^{-12}$ (m <sup>2</sup> /N)
$\epsilon_{33}^T / \epsilon_0$	1300

$$0 = I_3 \left( \frac{-1}{j\omega C_3} \right) + I_4 \left( j\omega M_4 + \frac{1}{j\omega C_3} + Z_t \right). \quad (4.1d)$$

These equations can be cast in matrix form, and solved using Cramer's rule for any of the unknowns. The potential drop across the termination impedance represents the force applied to the structure. In the next section the relation of the force gage voltage output to the force is examined. In the current model the force applied to the structure is,

$$F_{out} = I_4 Z_t. \quad (4.2)$$

The results of applying the equivalent circuit model to the shaker are compared with theory in Figure 4.6. The results show good agreement especially in the low frequency range. The theoretical resonance frequency is 29.8 kHz.

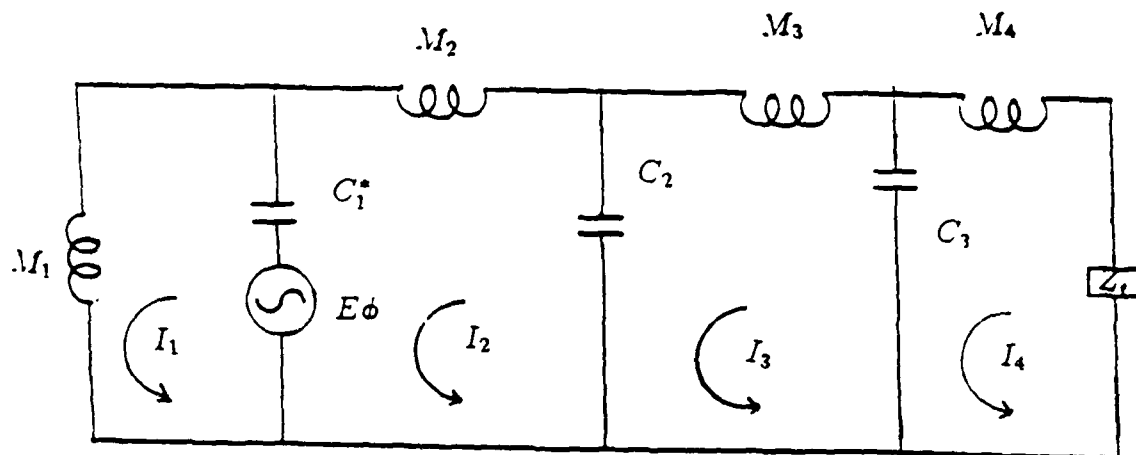


Figure 4.5 Equivalent circuit model for the forced output of the transducer with electrical elements transformed into the mechanical domain.

while the experimental value is 29.6 kHz. The fact that the analytic shaker model does not include any damping or loss mechanism accounts for some of the discrepancy of the amplitude between experiment and theory. Additionally, the error associated with the low frequency approximation is becoming appreciable at 30 kHz. At this frequency, the error associated with the low argument approximation is 8 percent.

#### 4.4. Equivalent Circuit Model for the Force Gage Section

In Section 4.3, the force gage section was modeled as having only high frequency resonances, hence the details of its voltage response were ignored. In this section, the equivalent circuit for the force gage section driven by an arbitrary force into an arbitrary impedance is examined. The purpose of this section is to determine the response of the force gage, and its relationship to the

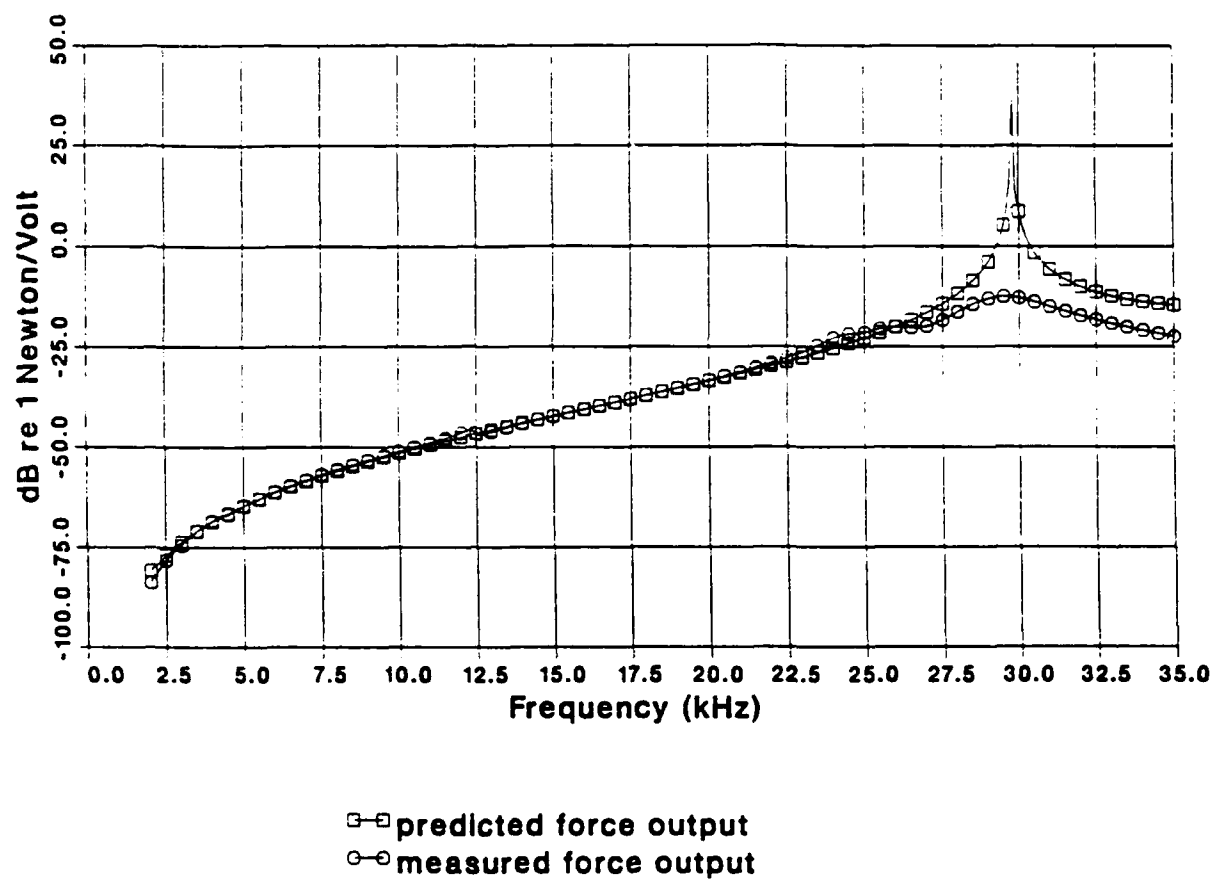


Figure 4.6 Transmitting voltage response for unloaded shaker, theory versus experiment.

force applied to the structure. Also, calibration procedures are examined and the normal assumptions regarding the sensitivity of force gages (that the sensitivity is constant with respect to frequency and load impedance) are analyzed.

The model for the force gage is shown in Figure 4.7. It has been constructed using the low frequency approximations in Figure 4.3a and 4.3b. The force source represents the rest of the transducer, which is modeled as some arbitrary input force. In the calculation of the sensitivity of the force gage, if the input force cancels out, then the sensitivity is independent of the drive section and decoupler section of the shaker. Note in Figure 4.7, that since the electrical terminals are open, the positive and negative capacitances cancel if the cable capacitance,  $C_{cable}$ , is zero or small. Even though the capacitances are in series, their net effect is zero because the positive and negative impedances of the two capacitors cancel when added. First the effect of the cable capacitance is ignored, then a correction factor is listed to take into account the effect of the finite cable capacitance. In Figure 4.7,  $M'_1$ ,  $M'_2$ ,  $C'_1$ ,  $C'_2$ ,  $C'_0$ ,  $Z_t$ , and  $\psi$  are:

$$M'_1 = 1/2 \text{ (mass of PZT force gage + aluminum headmass),}$$

$$M'_2 = 1/2 \text{ mass of aluminum headmass,}$$

$$C'_1 = \text{compliance of the force gage,}$$

$$C'_2 = \text{compliance of the aluminum headmass,}$$

$$C'_0 = \text{electrical capacitance of the force gage,}$$

$$Z_t = \text{termination impedance,}$$

$$\psi = \text{transformation factor.}$$

The sampled voltage is in the electric domain and we must take into account the transformation factor in calculating the output voltage. The current that flows through the capacitor across which the output voltage is measured is  $\psi$  times the velocity of that branch of the circuit. The output voltage of the force

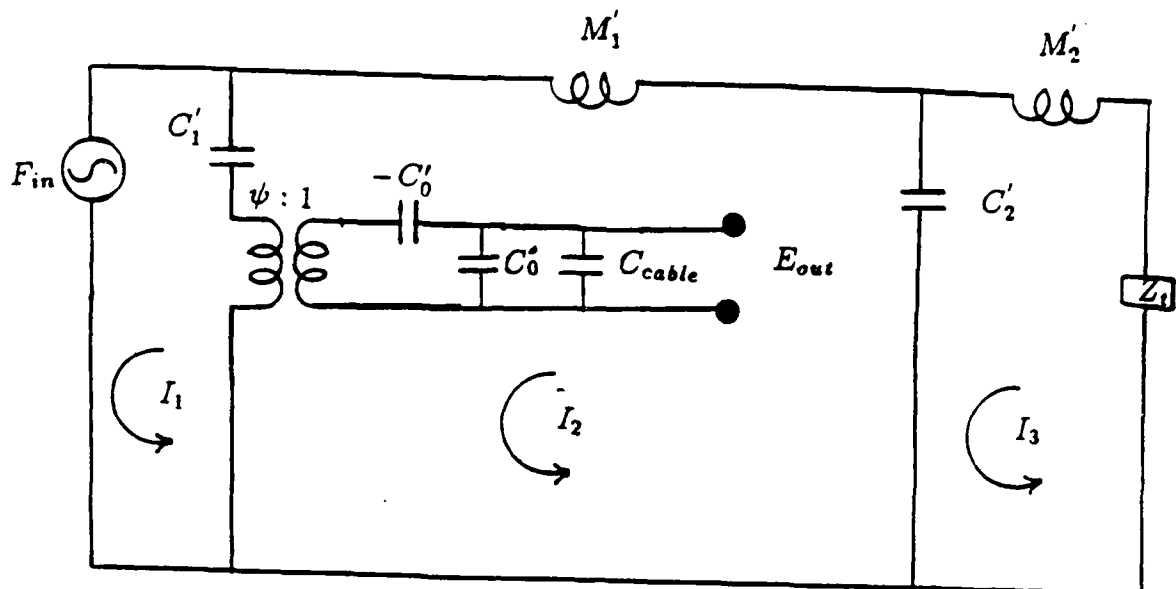


Figure 4.7 Equivalent circuit for force gage sensitivity.

gage is then

$$E_{out} = (I_2 - I_1) \frac{\psi}{j\omega C'_0}. \quad (4.3)$$

The output force is

$$F_{out} = I_3 Z_t. \quad (4.4)$$

This is the force imparted to the structure. The first item of interest is the ratio of the output voltage of the force gage to the force applied to the structure. In order to obtain this, the loop equations must again be solved. The equations for the loop currents (velocities) are

$$F_{in} = I_1 \left( \frac{1}{j\omega C'_1} \right) + I_2 \left( \frac{-1}{j\omega C'_1} \right), \quad (4.5a)$$

$$0 = I_1 \left( \frac{-1}{j\omega C'_1} \right) + I_2 \left( j\omega M'_1 + \frac{1}{j\omega C'_1} + \frac{1}{j\omega C'_2} \right) + I_3 \left( \frac{-1}{j\omega C'_2} \right), \quad (4.5b)$$

$$0 = I_2 \left( \frac{-1}{j\omega C'_2} \right) + I_3 \left( j\omega M'_2 + \frac{1}{j\omega C'_2} + Z_t \right). \quad (4.5c)$$

Upon solving the equations using Cramer's rule for the velocities, the ratio of the output voltage to the output force is

$$R_1 = E_{out}/F_{out}$$

which is just Equation (4.3) divided by Equation (4.4). A constant proportionality between the two is desired. The solution of the above results in the following:

$$R_1 = \frac{-\psi C'_1}{C'_0} \left( 1 + j\omega \frac{M'_1 + M'_2}{Z_t} - \omega^2 M'_1 C'_2 - j\omega^3 \frac{M'_1 M'_2 C'_2}{Z_t} \right) \quad , \quad (4.6)$$

The common factor  $\frac{\psi C'_1}{C'_0}$  simplifies to  $g_{33}t/A$  which is the low frequency sensitivity of the ceramic. This is the nominal sensitivity that we try to measure. However, away from  $\omega = 0$  the response of the output voltage to the actual force appears to become more complicated. Actually, most of the other terms are negligible in the frequency range examined in this study. If the force gage would be ideal, in other words massless and infinitely stiff,  $C'_2$ ,  $M'_1$ , and  $M'_2$  would be zero and the sensitivity would be independent of  $Z_t$  and frequency. The non-zero values complicate matters. The term multiplying  $j\omega$  is due to the mass loading by the mass between the force gage and structure. The actual force that reaches the structure is less by the velocity times  $j\omega(M'_1 + M'_2)$ . This factor may be subtracted out electronically during the measurement or via computer software afterward. At the lower frequencies, this term is the most significant source of errors in the measurement of the force. This error is usually neglected. It is a major source of error only when the impedance of the structure is low; i.e., at a resonance of the structure. The other terms in higher powers of  $\omega$  have an effect only at higher frequencies. If these effects need be examined, the equivalent circuit of Figure 4.1a and 4.1b must be used. When the admittance of the structure drops to a level comparable to the mass below the force gage, then the mass subtraction should be used if precise impedance levels are required (see Appendix B).

The object of a calibration of the force gage is to obtain the nominal sensitivity of the force gage section. A standard method is to mass load the shaker and mount an accelerometer on the termination mass. Knowing the mass, its acceleration and the output voltage from the sensor the sensitivity can be inferred. The mass that loads the force gage is  $M_t' + M_1' + M_2'$ . The sensitivity,  $S_f$  is approximately the voltage output of the force gage divided by the acceleration times the mass loading. Solving for this we obtain,

$$S_f = \frac{-\psi C_1'}{C_0'} (1 - \omega^2 M_1' C_2' \frac{M_t + M_2'}{M_1' + M_2' + M_t}) \quad (4.7)$$

this is the sensitivity measured using Equation 2.1. If,

$$M_1' \ll M_2' + M_t,$$

then Equation (4.7) becomes

$$S_f = \frac{-\psi C_1'}{C_0'} (1 - \omega^2 M_1' C_2') \quad (4.8)$$

The calibration described here and in Section 2.3.3 provides a good estimate of the low frequency force sensitivity. If the compliance  $C_2'$  includes only the compliance of the aluminum headmass, the term  $\omega^2 M_1' C_2'$  is much smaller than one even at 100 kilohertz. However, the glue layer attaching the shaker headmass to the structure to be tested increases this compliance. The sensitivity characteristically rolls off at higher frequencies due to this contact point or glue layer compliance.

Now the effect of cable capacitance for the 33 coupled force gage is examined. The cable capacitance can almost double the mechanical compliance of the force gage section in the shaker used in this study. This is not a problem in predicting the entire shaker's dynamic response because the compliance of the force gage will still be much less than the compliance of the decoupler and the drive sections.

Hence, the cable capacitance will not effect the dynamics of the system. However, the cable capacitance may all but cripple the sensitivity of the force gage if the cable capacitance is too high. The cable length is the length of the cable to the first amplifier or buffer. In cases where the cable length must be very long, a charge amplifier must be used. To account for the effect of the cable capacitance the following changes to the above equations are made. In the circuit diagram in Figure 4.7,  $C'_0$  is replaced by

$$C''_0 = C'_0 + C_{cable} \quad ,$$

and mechanical compliance  $C'_1$  is everywhere replaced by  $C^*$  which is found from

$$1/C^* = 1/C'_1 - \psi^2/C'_0 + \psi^2/C''_0.$$

After these two substitutions are made in the circuit, the loop Equations (4.5) are re-solved and the resulting low frequency sensitivity is

$$S_f = \frac{-\psi C'_1/C'_0}{1 + C_{cable}(\frac{1}{C'_0} - \psi^2 \frac{C'_1}{C''_0})} \quad . \quad (4.9)$$

Thus if  $C_{cable}$  is zero then the sensitivity is  $g_{33}t/A$ . If the cable capacitance is very high, the sensitivity is lowered.

The average measured sensitivity for the force gage is 0.95 V/N as tabulated in Table 2.3. The predicted value of  $g_{33}t/A$  is 1.02 V/N which matches the measured values closely. Average cable capacitance for the type and length of cable used in the construction of the force gage is 45 picofarads. Plugging this value into Equation (4.9) results in a sensitivity of 0.89 V/N, again close to the measured value. This close agreement indicates that there are no significant errors in the construction or the calibration of the transducer.

## Chapter 5

## EXPERIMENTAL AND THEORETICAL RESULTS

## 5.1. Introduction

The experimental results of the implementation of the wavenumber drive system with nine and seventeen shakers are presented in this chapter. First, the experimental transfer admittance at various spatial locations along the beam is compared with the theoretically predicted values. This comparison allows for a point by point validation of the measurements. Next, the effect of varying the number and spacing of the sensors used to measure the wavenumber spectrum is analyzed using predicted results. Subsequently, the wavenumber-frequency dependence of the measured forcing function is presented. The measured and predicted velocity responses to this forcing function are examined. Finally, the relationship between the wavenumber content of the forcing function and the velocity is explored.

## 5.2. Measured and Predicted Point Admittances

The measured admittance at various locations on the beam is compared to the predicted admittance as a function of frequency. As mentioned in Section 2.4.4, the velocity is measured at 37 locations on the beam, with the actual locations, in centimeters, given by

$$x_i = ((i - 1) + 0.95) \quad ,$$

and, in non-dimensional coordinates, by

$$\xi_i = ((i - 1) + 0.95)/37.9 \quad .$$

The admittances are all measured with respect to the center shaker, so all but the measurement of the velocity at the center location are considered transfer

admittances defined here as

$$\hat{v}_i(\omega) = v_i(\omega)/F_c(\omega) \quad , \quad (5.1)$$

where  $v_i$  is the velocity measured at location  $i$  and  $F_c$  is the force measured at the center shaker. Since the beam is being driven by nine or seventeen shakers, the admittance takes on a much different appearance than it would for a single drive point.

The FORTRAN program VALTIM (see Appendix C) employs the beam theory in Chapter 3 to predict the admittance of the beam at the different spatial locations using the measured forces read from a data file. VALTIM also reads the measured values of the admittance and then plots both the theoretical and experimental data at an observation point as a function of frequency.

The forcing condition is defined by the experiment number given in Table 2.2. As the agreement between experiment and theory is generally very good, Experiment 7 has been chosen as a representative measurement. Several locations for the comparison of the predicted and measured admittances for Experiment 7 are presented while only a single plot is shown for the other experiments. The seventeen shaker experiments are more complicated (i.e., more sources for error), so the representative data set was chosen from the last five experiments. Also, many of the features for the nine shaker experiments are the same as for the seventeen shaker experiments, so it is not necessary to specifically examine in detail all of the data sets from the nine and seventeen shaker experiments.

The admittance for the center location ( $\xi = 0.5$ ) is shown in Figure 5.1 from Experiment 7. The good agreement between theory and experiment is seen. The first peak around 3.1 kHz is due to the system resonance caused by the interaction between the beam and shakers. At this frequency the force and velocity at nearly every location on the beam has a peak in amplitude with respect to the force

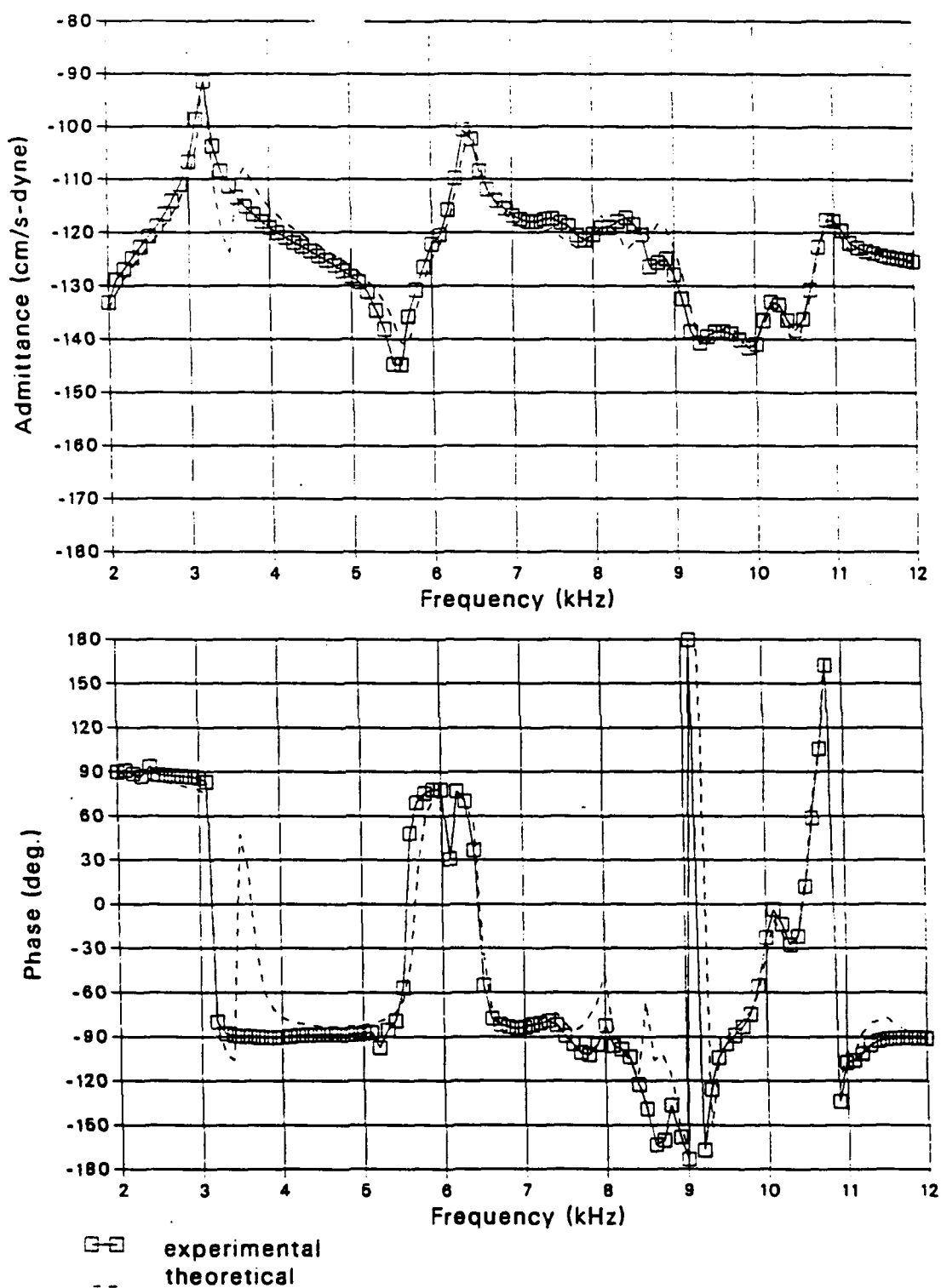


Figure 5.1. Comparison of the theoretical and experimental driving point admittance, magnitude (dB re 1 cm/dyne-s) and phase for Experiment 7 at the location  $\xi = .5$ .

seen at the center shaker. In other words, the driving-point impedance at the center of the beam is nearly zero, consequently the driving force is nearly zero. This resonance peak occurs around 3.1 kHz for all of the experiments, however the location of this peak is a function of the number of shakers and the weighting pattern of the drive voltages. The shifting of this peak from experiment to experiment may be due to mass loading of the force gage (for a brief discussion of mass loading see Appendix B), however, the reasons behind the shifting of this peak are not investigated in detail.

The predicted admittance shows a peak at the resonance frequencies of 3.6 kHz and 8.4 kHz, while these peaks are not seen in the experimental data. These are even or symmetric modes (with respect to the center of the beam) and therefore are excited more by the symmetric forcing function than the antisymmetric modes. The absence of these predicted resonance effects in the experimental data could be due to the use of a damping coefficient in the predictions (0.05 is used) that is lower than the actual damping coefficient. This damping is due to having shakers glued to the beam.

Figures 5.2 and 5.3 show the transfer admittance for Experiment 7 at a location 5 cm to the left and to the right of the center of the beam ( $\xi = 0.368$  and  $0.632$ ). If the forcing function were perfectly symmetric these admittances would be exactly the same. While they are quite similar there are differences, indicating that the forcing function was not perfectly symmetric. In Figure 5.4, the results for position number 3 at  $\xi = 0.078$  are presented. While the magnitude and phase of the predicted and measured drive point admittances match at frequencies below 6 kHz except at the resonance frequencies, in Figures 5.2-5.4 there are deviations between the predicted and measured results above 6 kHz.

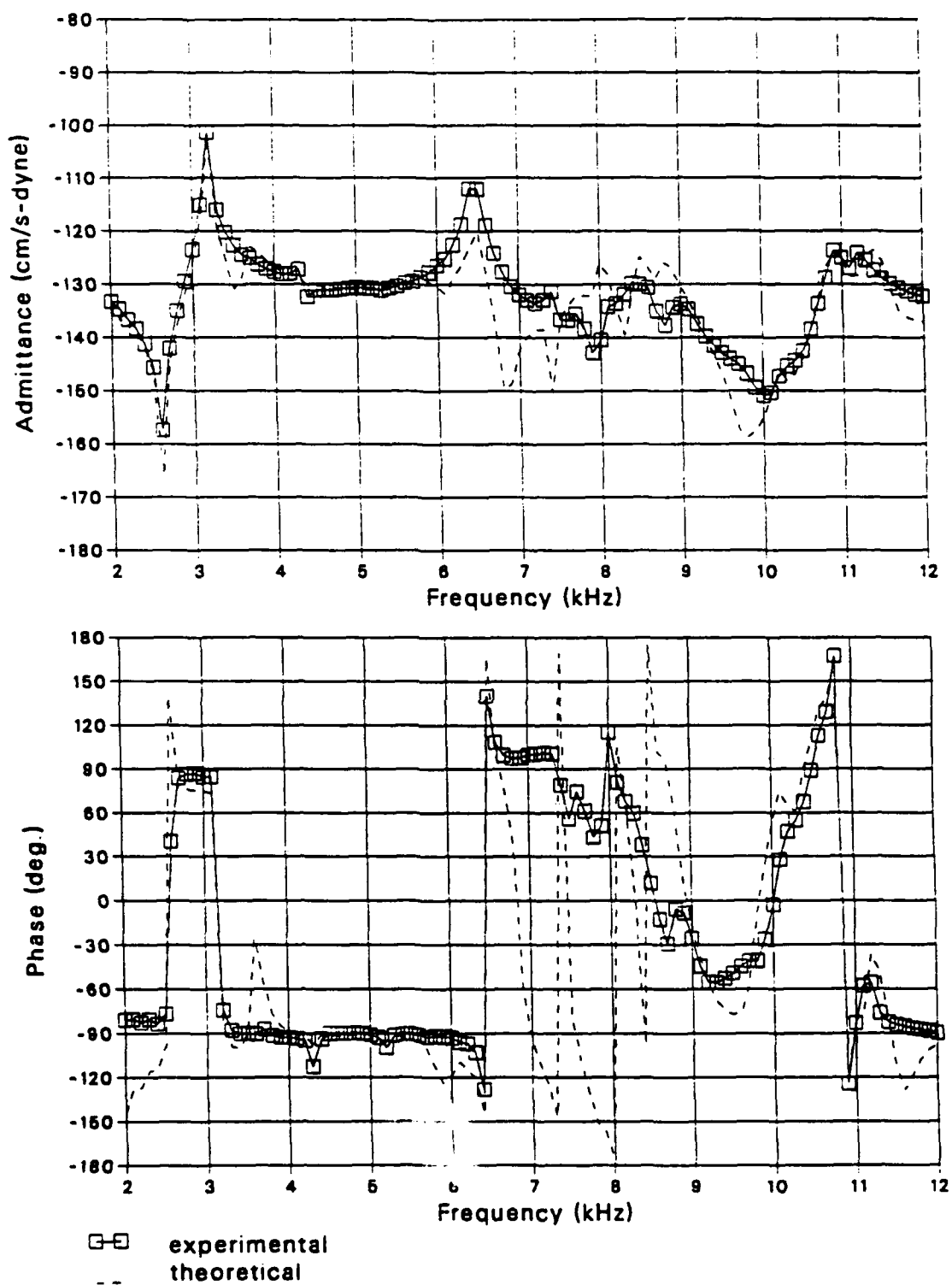


Figure 5.2. Comparison of the theoretical and experimental transfer admittance, magnitude (dB re 1 cm/dyne-s) and phase for Experiment 7 at the location  $\xi = .368$ .

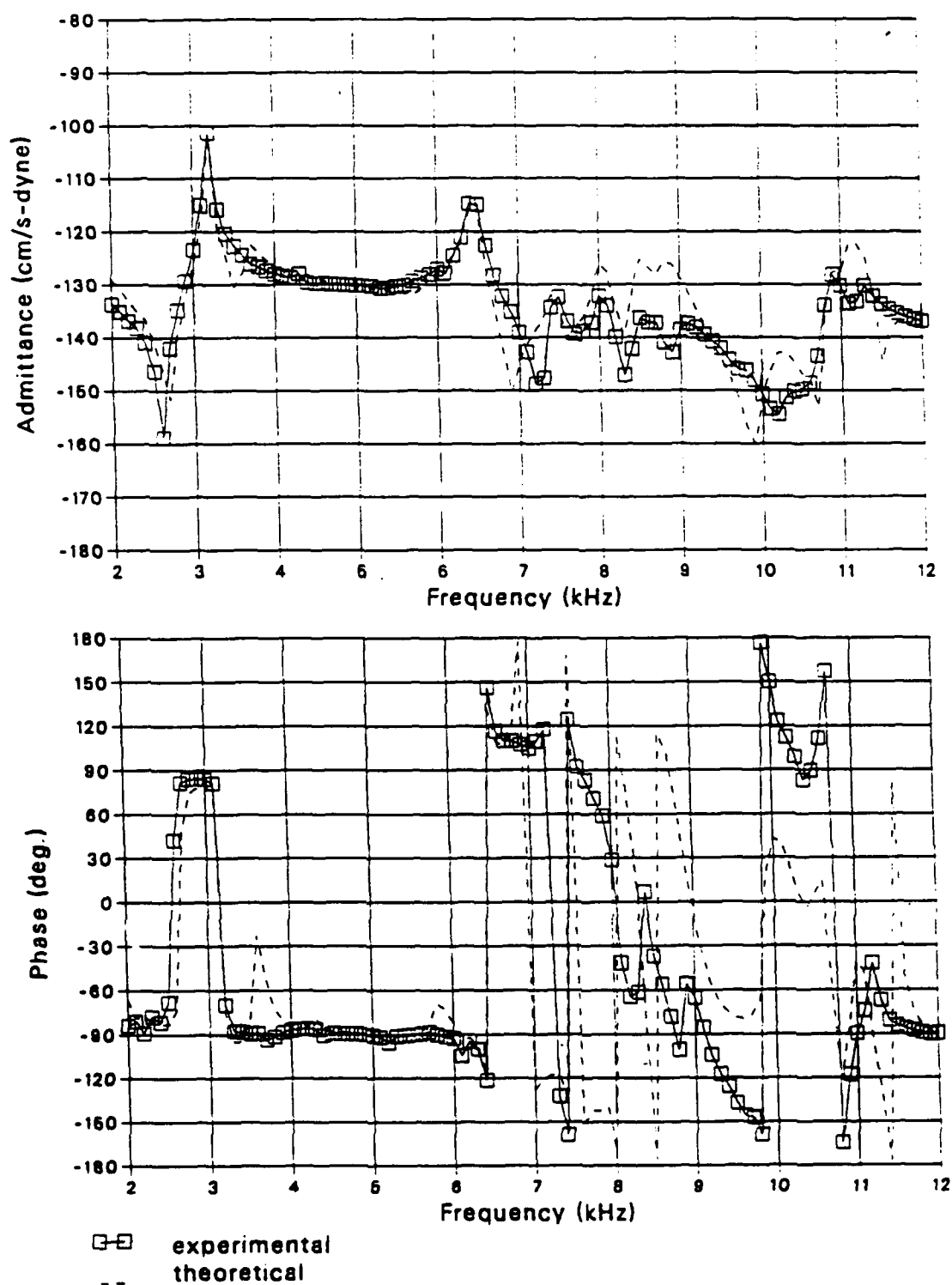


Figure 5.3. Comparison of the theoretical and experimental transfer admittance, magnitude (dB re 1 cm/dyne-s) and phase for Experiment 7 at the location  $\xi = .632$ .

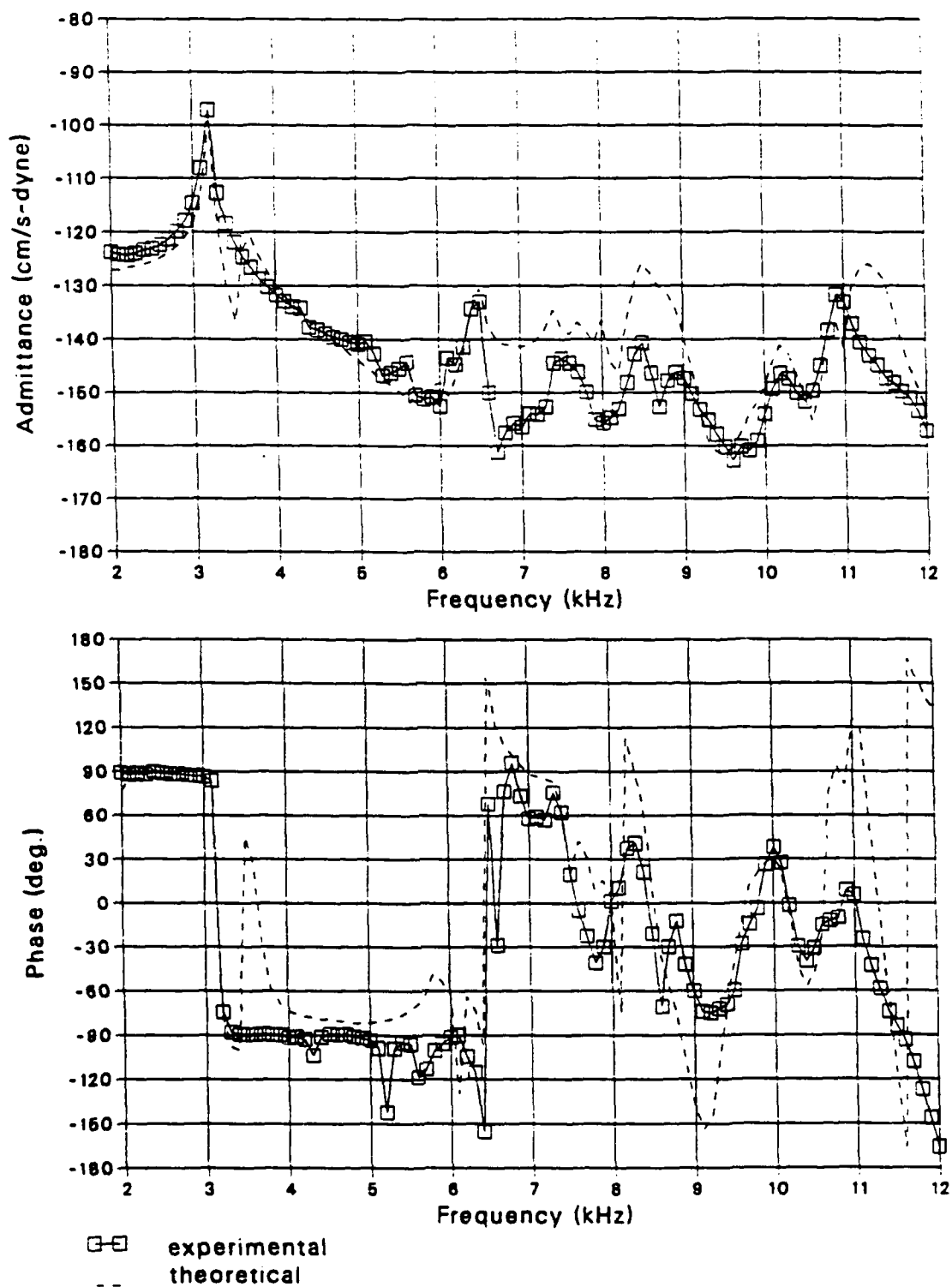


Figure 5.4. Comparison of the theoretical and experimental transfer admittance, magnitude (dB re 1 cm/dyne-s) and phase for Experiment 7 at the location  $\xi = .078$ .

The transfer admittances at location 14 ( $\xi = 0.368$ ) for Experiments 1-6 and 8-9 are shown in Figures 5.5-5.12. From these plots, the excellent agreement between theory and experiment can be seen. Again, the resonance peaks appear in the predicted results that are not found in the experimental results. These peaks are found around 3.6 kHz (e.g. Figure 5.7) or 8.4 kHz (e.g. Figure 5.10).

The suppression of the resonance peaks in the measurements is notable. The use of multiple shakers changes the usual interpretations of the admittance especially when the forcing function is weighted to a particular wavenumber. With only one or two shakers on the beam, the mode of the nearest resonance frequency almost always contributes the most to any measured response. The exception is when the measurement or excitation point is on a node of a mode. With multiple shakers, the orthogonality of the forcing function to a particular mode may result in that mode having at least as much influence on the velocity response as the mode whose resonance frequency is actually closer to the drive frequency. Also, the gluing of nine or seventeen shakers to a beam increases the damping of the beam due to the presence of the glue, which also suppresses the measured resonance responses. Thus, with the array of shakers the resonance may be suppressed by a mismatch between the spatial response of the resonance mode and the spatial distribution of the applied forces.

Finally, the drive wavenumber for Experiments 4, 8 and 9 corresponds to a freebending wavenumber whose frequency falls far outside the measurement frequency range (compare Tables 2.1 and 3.2). The overall admittance for these experiments is much lower than for the other experiments.

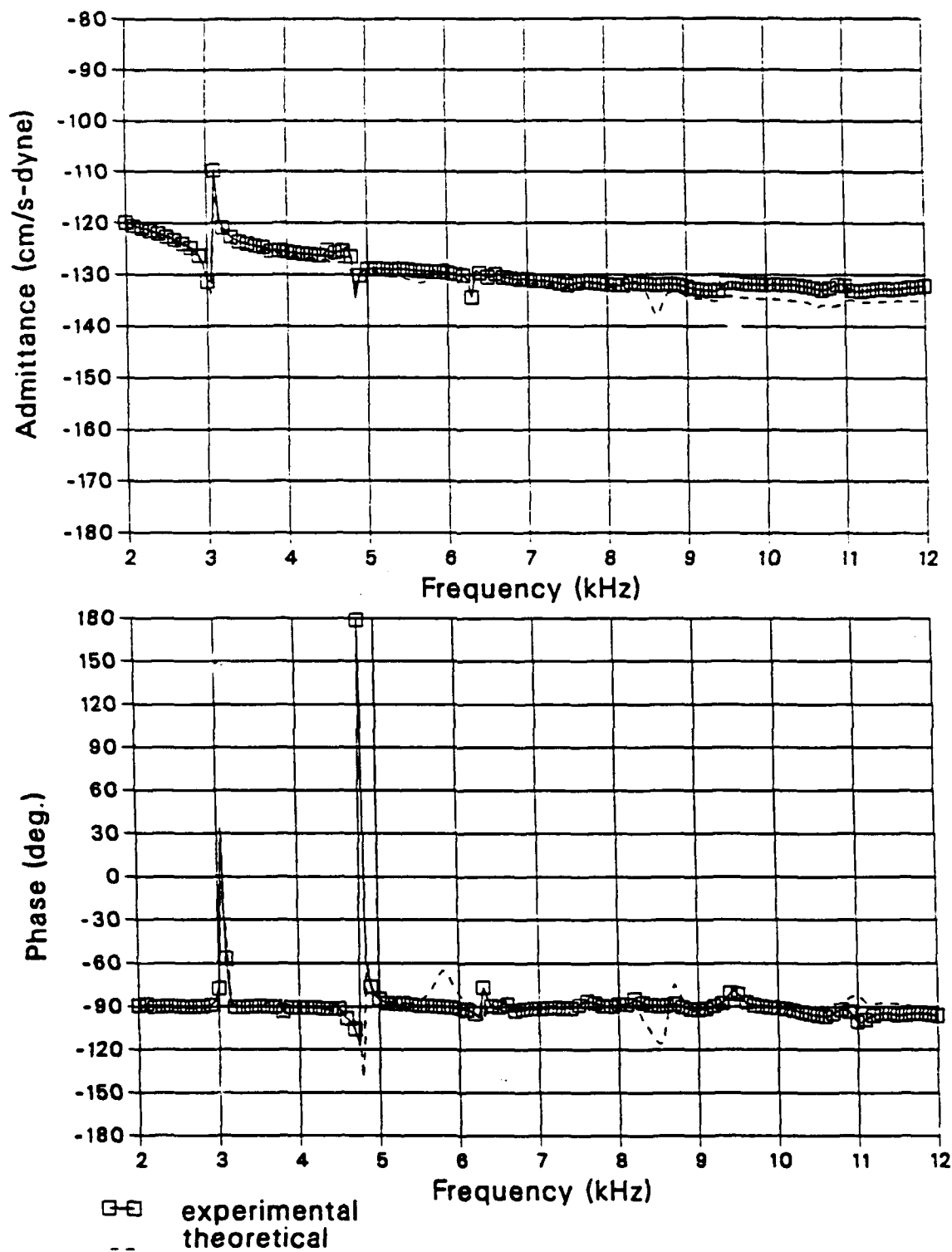


Figure 5.5 Comparison of the theoretical and experimental transfer admittance, magnitude (dB re 1 cm/dyne-s) and phase for Experiment 1 at the location  $\xi = 0.368$ .

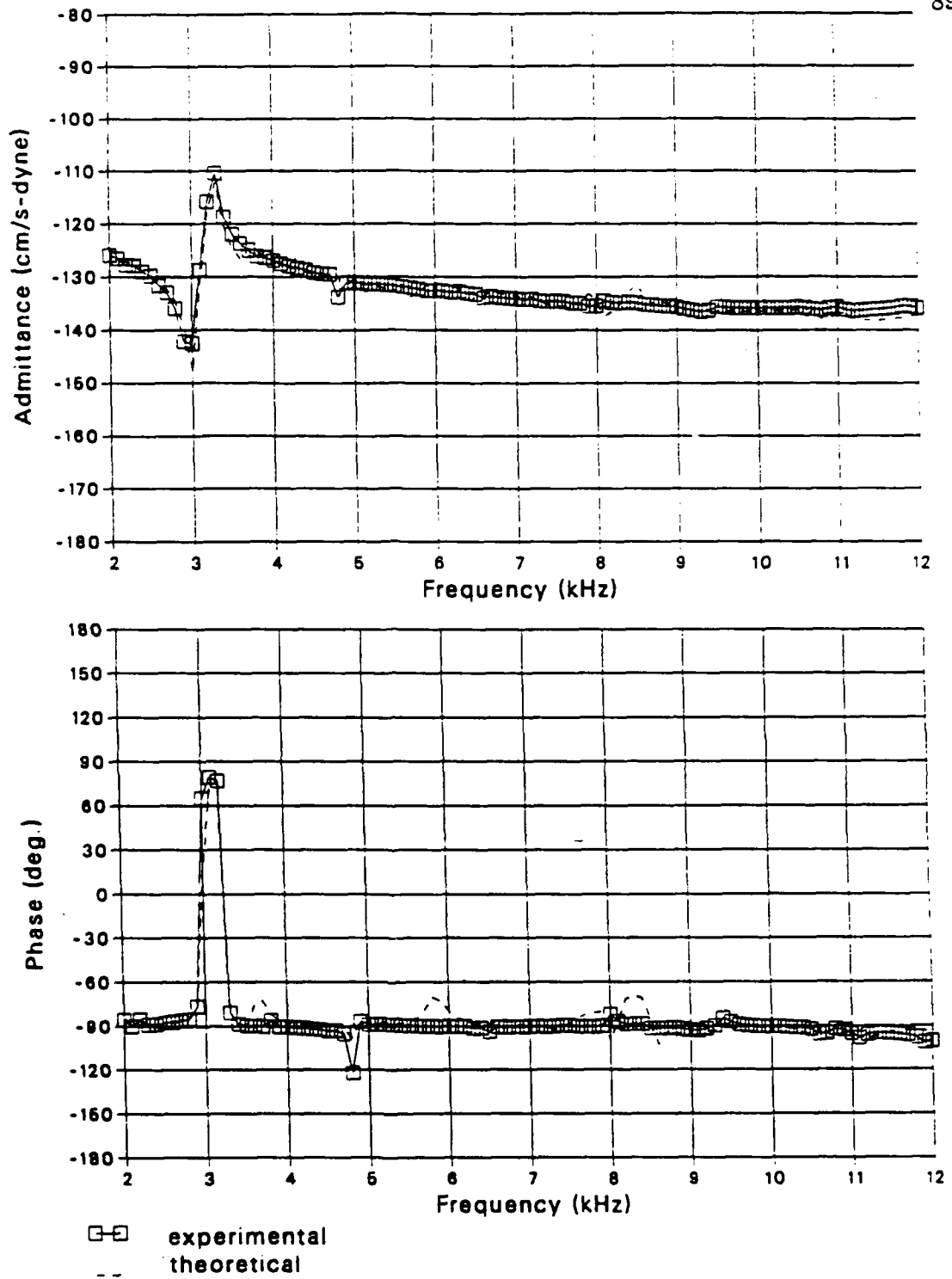


Figure 5.6 Comparison of the theoretical and experimental transfer admittance, magnitude (dB re 1 cm/dyne-s) and phase for Experiment 2 at the location  $\xi = 0.368$ .

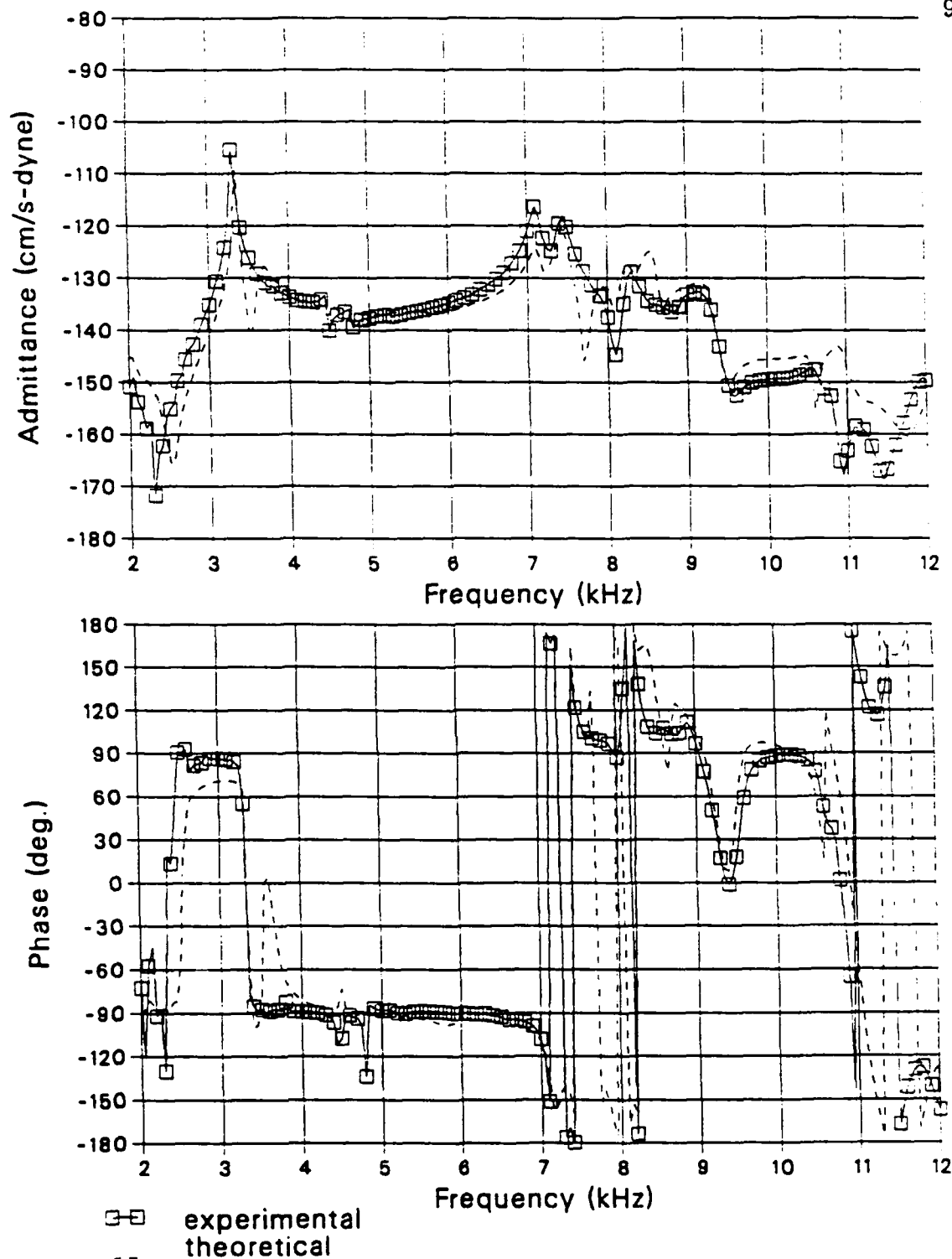


Figure 5.7 Comparison of the theoretical and experimental transfer admittance, magnitude (dB re 1 cm/dyne-s) and phase for Experiment 3 at the location  $\xi = 0.368$ .

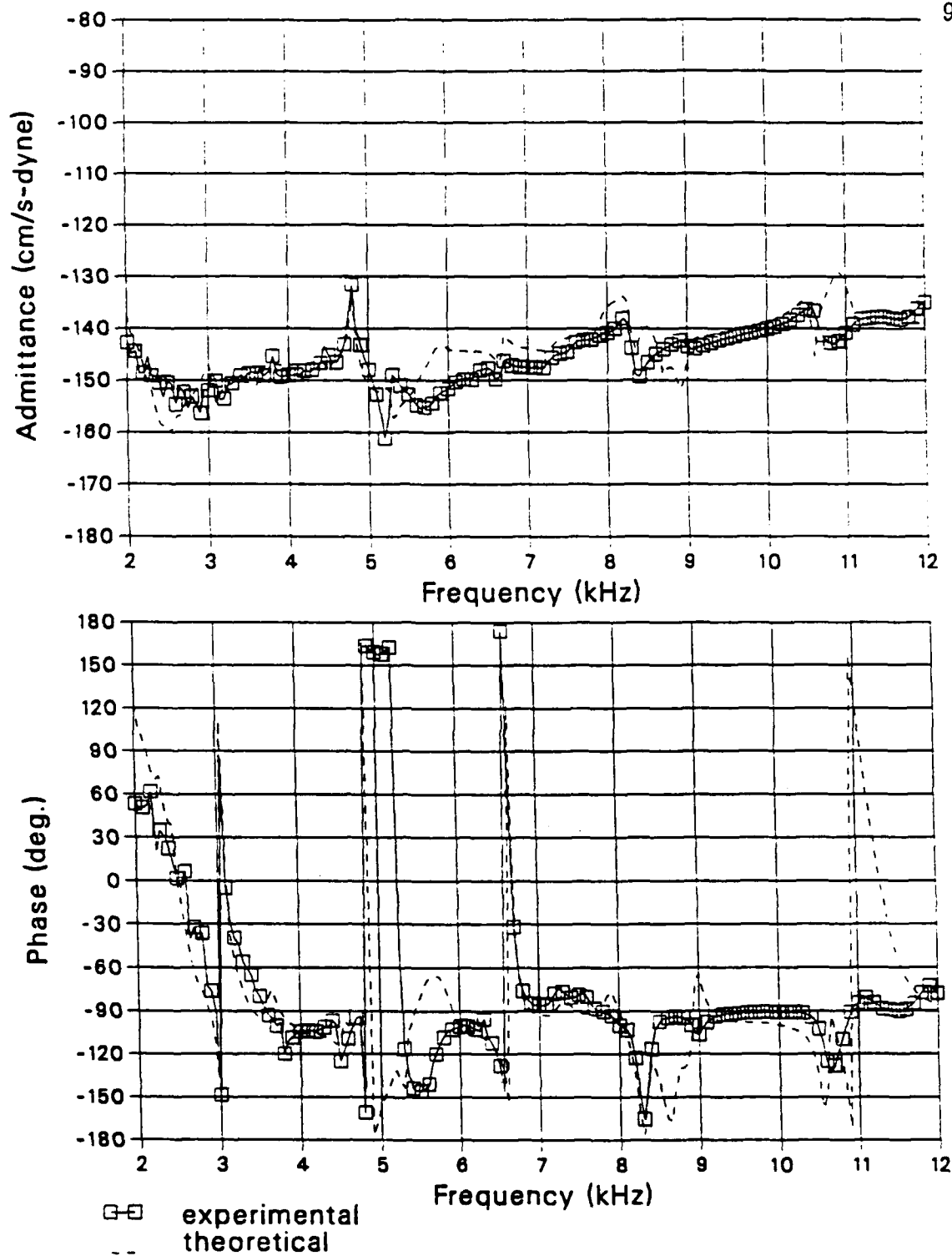


Figure 5.8 Comparison of the theoretical and experimental transfer admittance, magnitude (dB re 1 cm/dyne-s) and phase for Experiment 4 at the location  $\xi = 0.368$ .

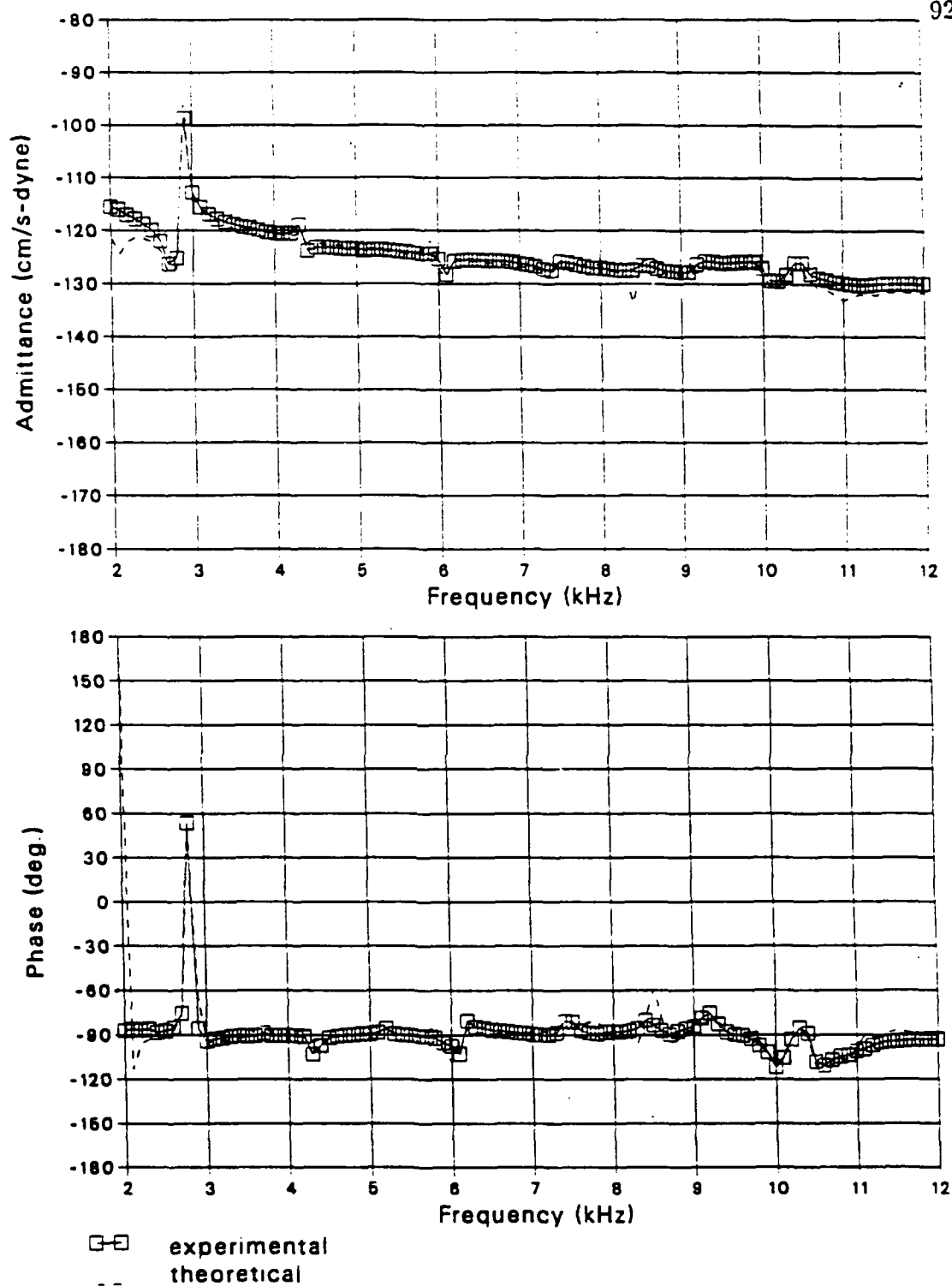


Figure 5.9 Comparison of the theoretical and experimental transfer admittance, magnitude (dB re 1 cm/dyne-s) and phase for Experiment 5 at the location  $\xi = 0.368$ .

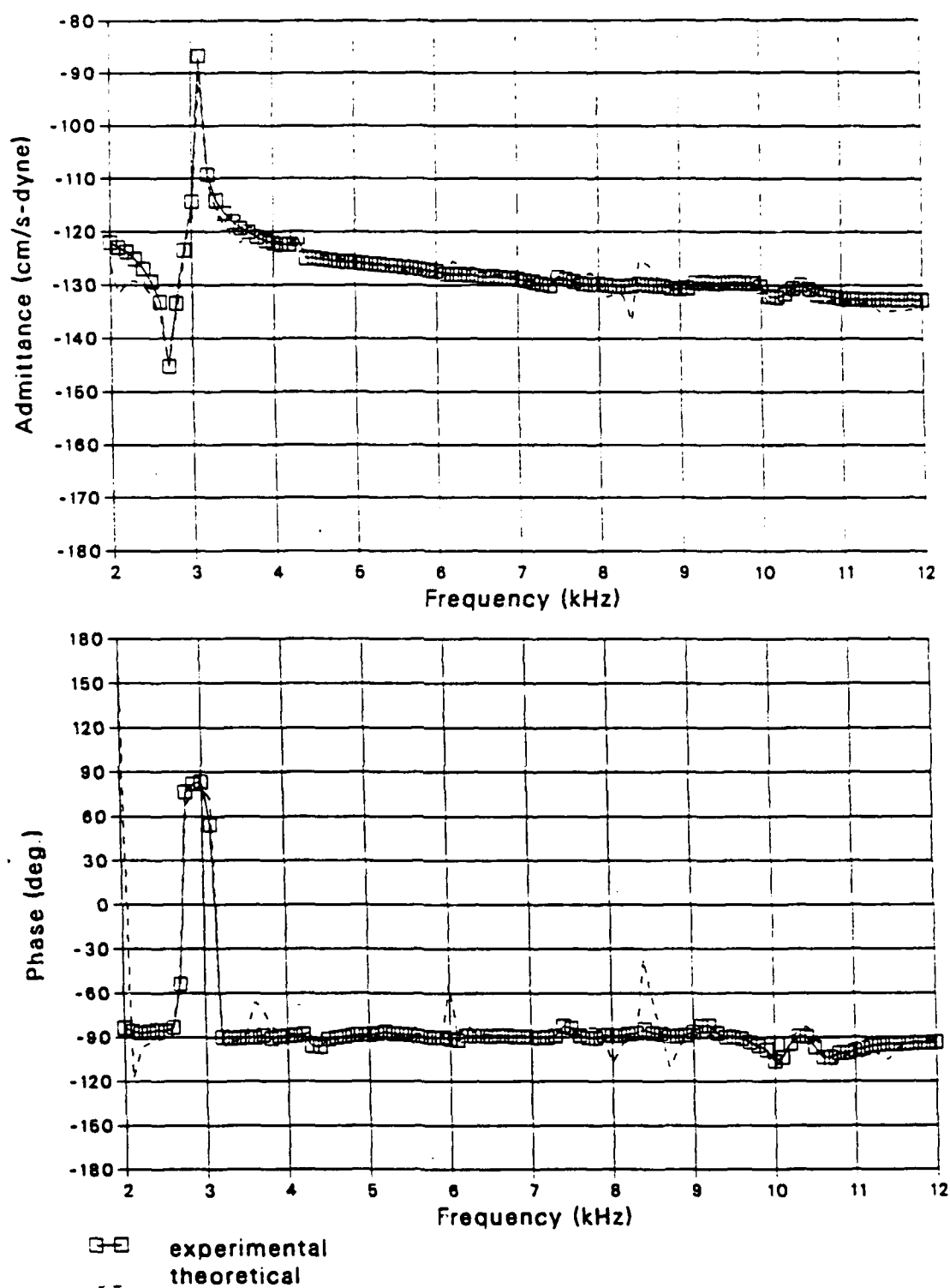


Figure 5.10

Comparison of the theoretical and experimental transfer admittance, magnitude (dB re 1 cm/dyne-s) and phase for Experiment 6 at the location  $\xi = 0.368$ .

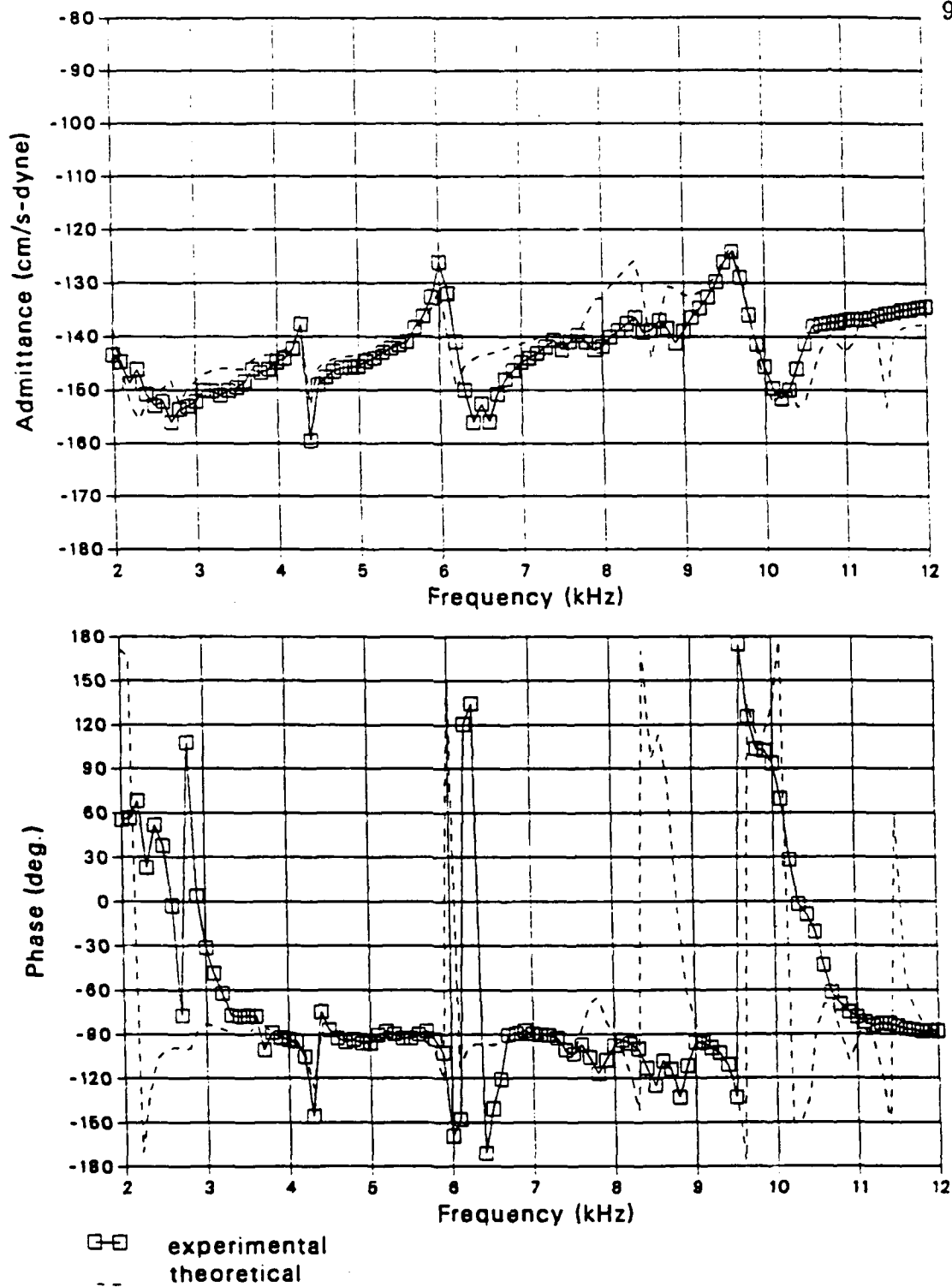


Figure 5.11 Comparison of the theoretical and experimental transfer admittance, magnitude (dB re 1 cm/dyne-s) and phase for Experiment 8 at the location  $\xi = 0.368$ .

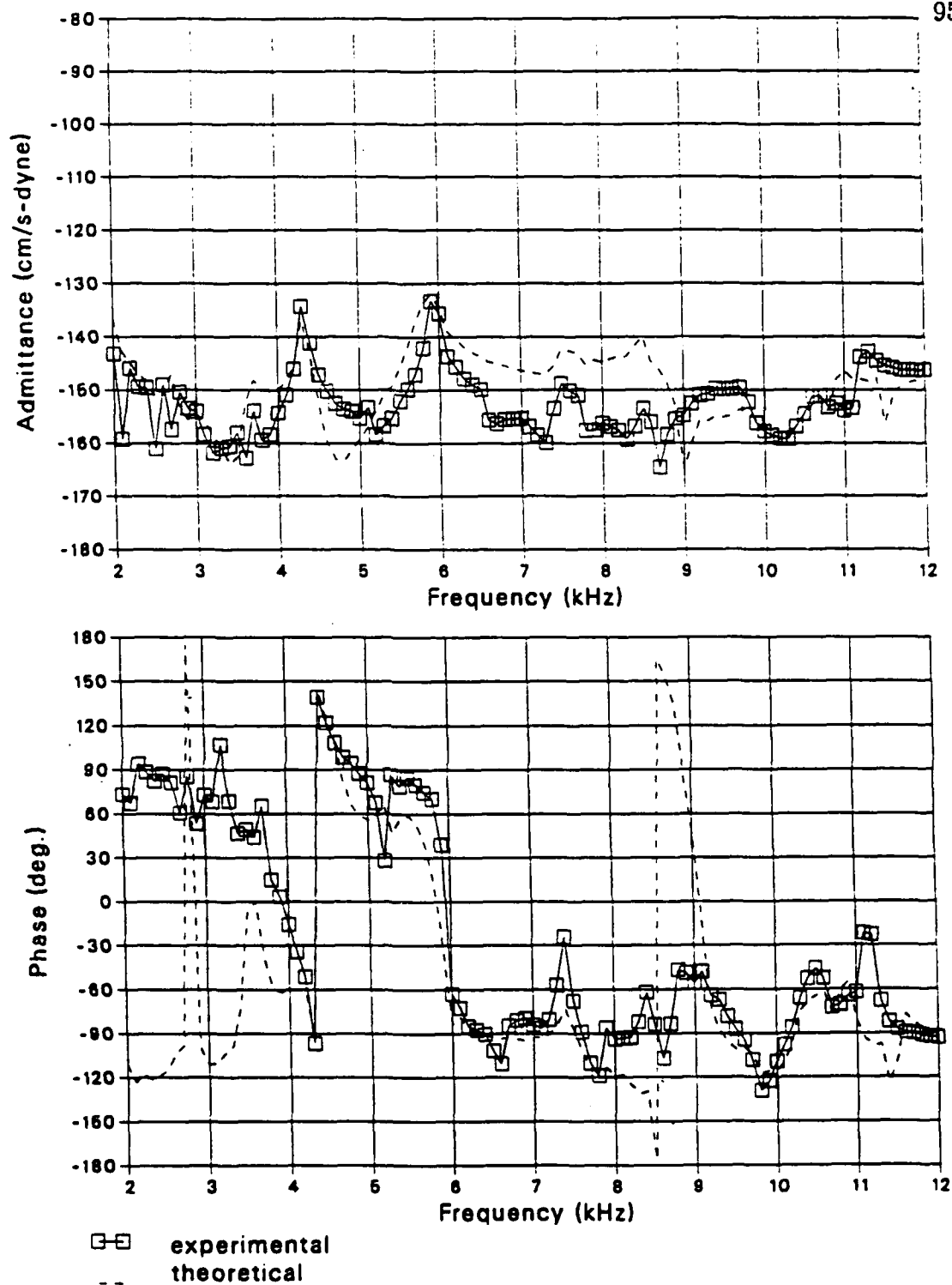


Figure 5.12

Comparison of the theoretical and experimental transfer admittance, magnitude (dB re 1 cm/dyne-s) and phase for Experiment 9 at the location  $\xi = 0.368$ .

### 5.3. Effects of the Spatial Measurement Array

In this section, the effect of varying the accelerometer spacing on the estimation of the normalized wavenumber velocity response is examined. The normalized wavenumber-frequency velocity spectrum,  $\hat{V}(k_x, \omega)$ , is

$$\hat{V}(k_x, \omega) = \frac{1}{F_c(\omega)} V(k_x, \omega) \quad , \quad (5.2)$$

where  $V(k_x, \omega)$  is the Fourier transform of the velocity. To assess the effect of spatial sampling, the DFT is performed on the theoretically predicted spatial velocity response and compared to the analytic or continuous transform as given in Section 3.4. The DFT is calculated using a 128 point FFT; the number of the actual data points varies but the data length is always zero-padded to a length of 128. Only the 64 bins corresponding to the positive spectrum are plotted. The FORTRAN program ARRAY\_EFFECT implements the calculation of both the analytic and the discrete transforms then plots the results.

Before examining the results of these calculations, the Fourier transforms of the array pattern or  $\tilde{A}(k_x)$ , as defined in Chapter 2, is plotted for spacings of 1 cm, 2 cm and 4 cm in Figures 5.13-5.15.  $\tilde{A}(k_x)$  also is called the array pattern. Only the positive part of array function spectrum is plotted, the negative part of the spectrum is symmetric. Re-writing Equation (2.12) in terms of the current variables,

$$\hat{V}_m(k_x) = \hat{V}(k_x) * \tilde{A}(k_x) \quad . \quad (5.3)$$

This is the measured wavenumber velocity spectrum (after dropping the frequency dependence). In this equation, the convolution integral for the measured response at a wavenumber  $k_x$  can be interpreted as the integration of a shifted version of  $\tilde{A}(k_x)$  times  $\hat{V}(k_x)$  over all wavenumbers. In Figures 5.13-5.15, the

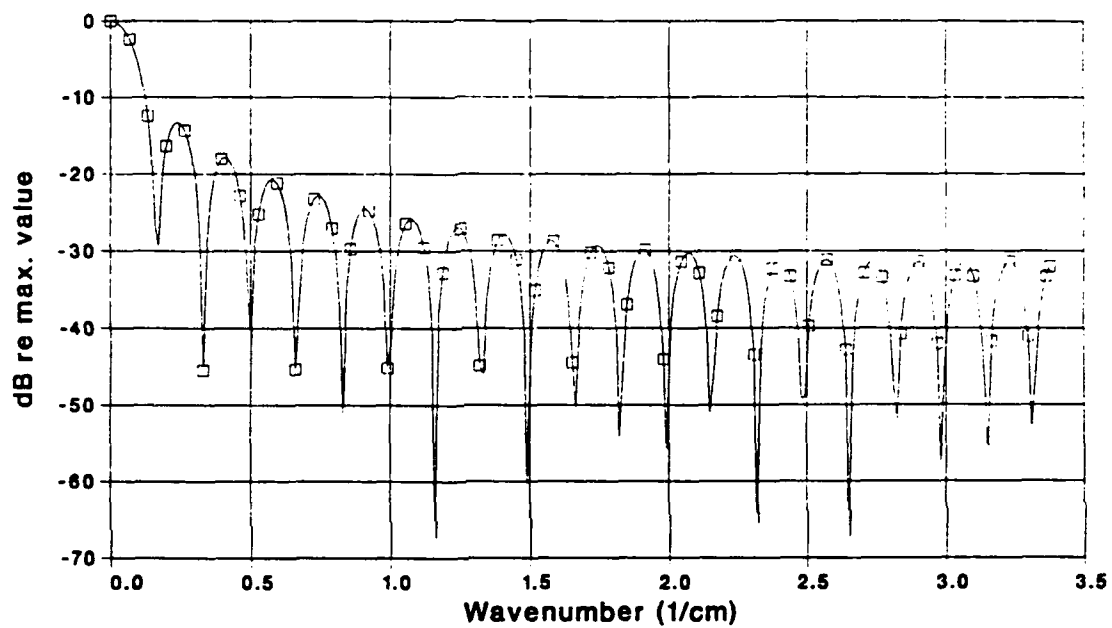


Figure 5.13 The Fourier transform of the array function for 37 accelerometers with a spacing of 1 cm.

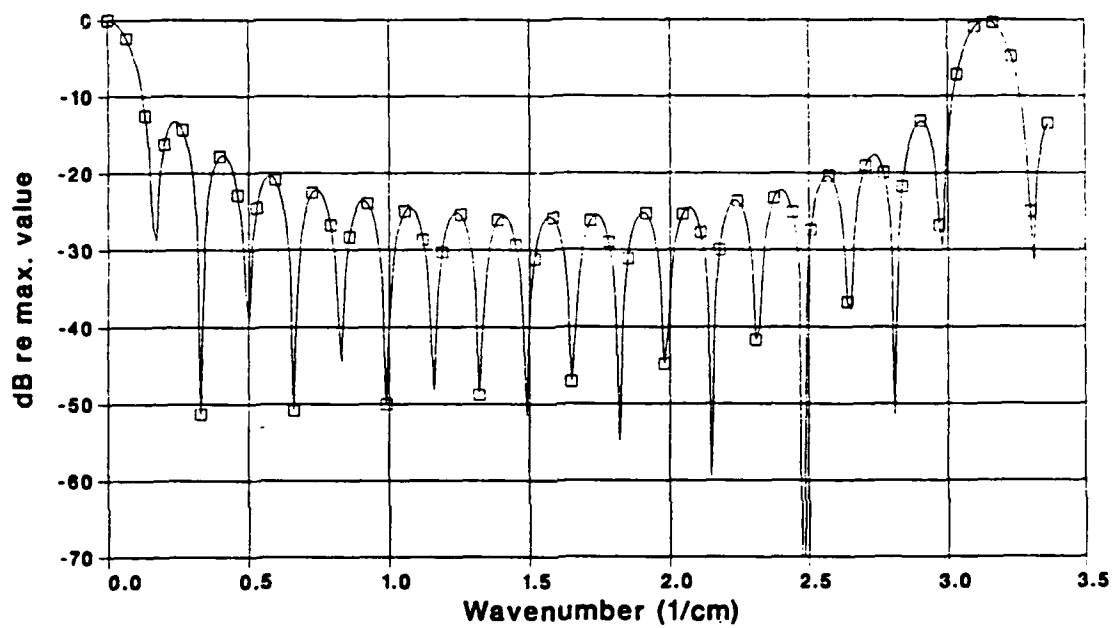


Figure 5.14 The Fourier transform of the array function for nineteen accelerometers with a spacing of 2 cm.

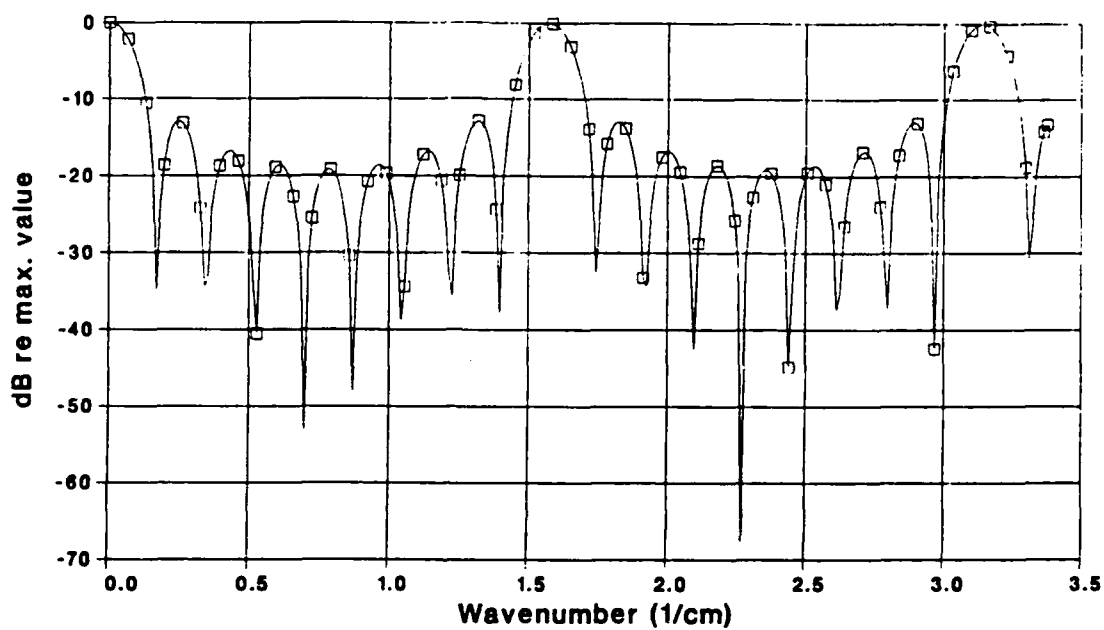


Figure 5.15 The Fourier transform of the array function for nine accelerometers with a spacing of 4 cm.

main-lobe of  $\tilde{A}(k_x)$  is located at  $k_x = 0 \text{ cm}^{-1}$ , the lobes appearing at

$$k_x = \pm 2\pi l / \Delta x \quad \text{for } l = 1, 2, \dots$$

are called aliasing lobes. As the measurement wavenumber increases, the array pattern, as shown in Figures 5.13-5.15, is shifted to the right and the convolution integration is performed to produce  $\hat{V}_m(k_x)$ . So, as the measured wavenumber nears  $\pi/\Delta x$  the first negative aliasing lobe nears  $-\pi/\Delta x$  from the left. Since  $\hat{V}(k_x)$  is almost symmetric, if we see peaks past  $\pi/\Delta x$  in the positive part of the spectrum there are peaks also in the negative part of the spectrum. It is these peaks in the negative part of the spectrum that alias into the positive part of the spectrum. The ideal array pattern is a  $\text{sinc}(k_x L/2)$  function as discussed in Chapter 2; the array pattern for the 1 cm spacing most closely resembles that sinc function.

For the comparison of different array spacings, the forcing function from Experiment 9 in Table 2.2 is used. Because the drive wavenumber for this experiment is the highest of the experiments conducted ( $k_d = 1.49 \text{ cm}^{-1}$ ), more energy should be seen in the higher wavenumbers of the velocity spectrum. With more energy input into the high wavenumber end of the spectrum than any of the other experiments, the velocity should be the most challenging to measure. The wavenumber dependence at 8.0 kHz is examined. In Figure 5.16, an array of 37 accelerometers equally spaced from the center of the beam and covering the entire length of the beam (in this case  $\Delta x = 1.02 \text{ cm}$ ) is used to estimate the wavenumber spectrum of the velocity. As shown in Figure 5.16, the agreement between the continuous and discrete transforms of the predicted velocity is excellent except at the higher wavenumbers. There, the aliasing effects tend to cause the levels calculated by the FFT to fall off less rapidly than the continuous transform.

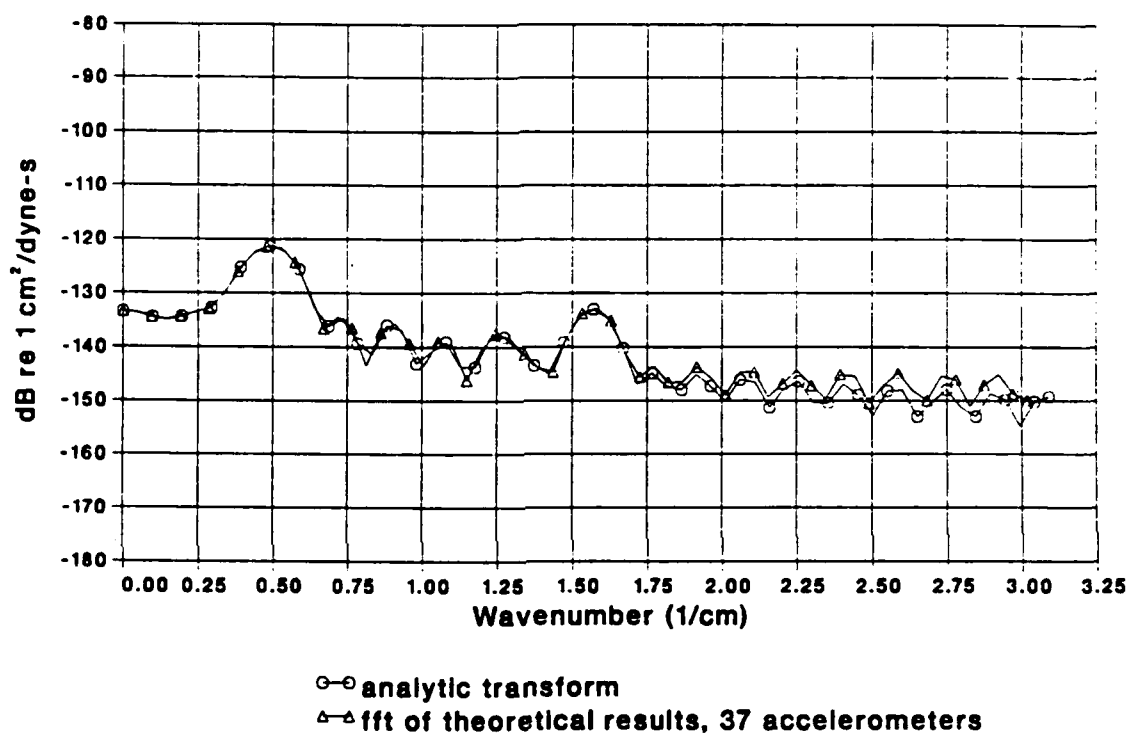


Figure 5.16 Comparison of the magnitude of the continuous and discrete Fourier transforms of the velocity for Experiment 9 at a frequency of 8 kHz. The array for the FFT consisted of 37 elements ( $\Delta x = 1.02$  cm).

Using a nineteen element array consisting of accelerometers located at 2 cm intervals equally spaced away from the center of the beam, also produces good agreement between the discrete and continuous transforms for Experiment 9 as presented in Figure 5.17. At the Nyquist wavenumber (defined here as  $\pi/\Delta x$ ) the local peak in the response causes the discrete transform to overestimate once again. The results for an array using nine accelerometers is shown in Figure 5.18. Considering that the Nyquist wavenumber for this array,  $0.75 \text{ cm}^{-1}$ , is one half the drive wavenumber, the results are remarkably good. It seems that the aliasing effects have somehow canceled out in the convolution integral. Generally, so long as the largest amplitude seen in the velocity spectrum is contained within the Nyquist rate of the array, the FFT approximates the general features of the spectrum very well.

Returning to the nineteen accelerometer array, the effects of a slight decrease in the inter-element spacing is now examined. By decreasing  $\Delta x$  the aliasing wavenumber is increased slightly. By doing so, the local peak in the true wavenumber spectrum now falls below the aliasing lobe of the array pattern if the  $\Delta x$  is chosen correctly. The result of using an array of 21 accelerometers is shown in Figure 5.19. While the discrete transform still overestimates the value of the spectrum slightly around  $\pi/2 \text{ cm}^{-1}$ , the shape of the true spectrum is faithfully followed. It is noteworthy that merely by using two more accelerometers the results may be noticeably improved.

The importance of knowing the highest wavenumber at which a peak is to be seen has been demonstrated. While examining the dispersion relation for the beam (see Figure 3.2) yields an idea of what the highest freebending wavenumber to expect for a particular frequency range, the content of the forced wavenumber content must be known as well. At 8.0 kHz the forced wavenumber

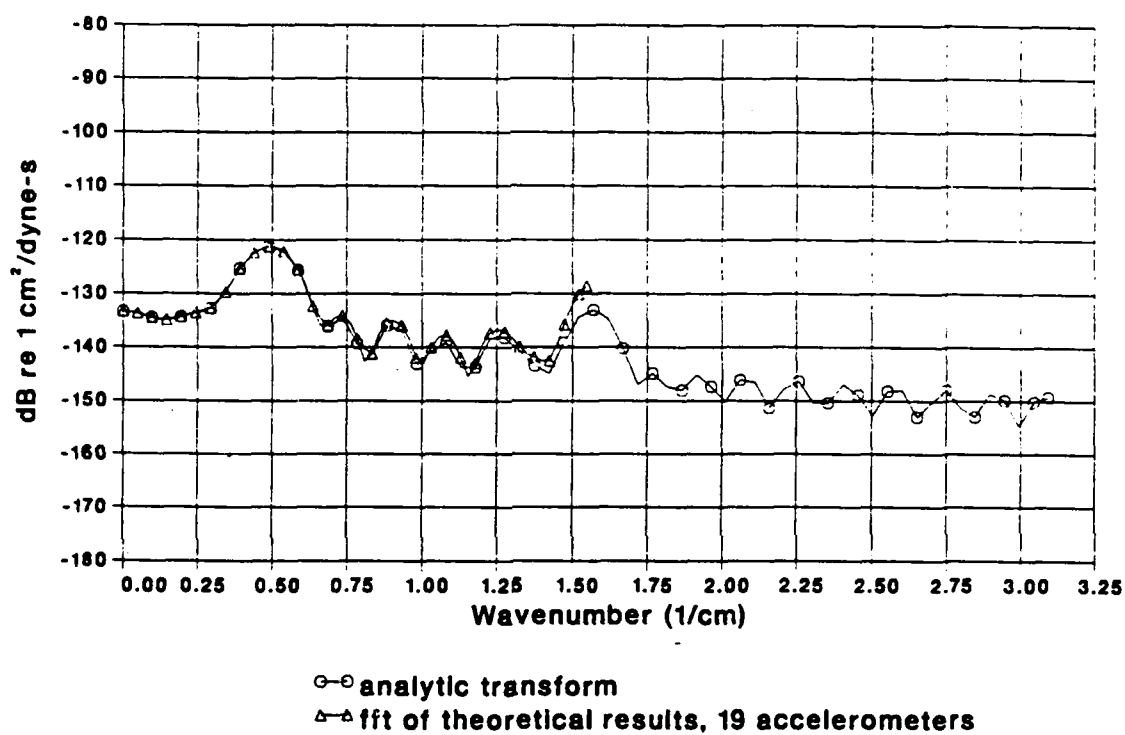


Figure 5.17

Comparison of the magnitude of the continuous and discrete Fourier transforms of the velocity for Experiment 9 at a frequency of 8 kHz. The array for the FFT consisted of 19 elements ( $\Delta x = 2$  cm).

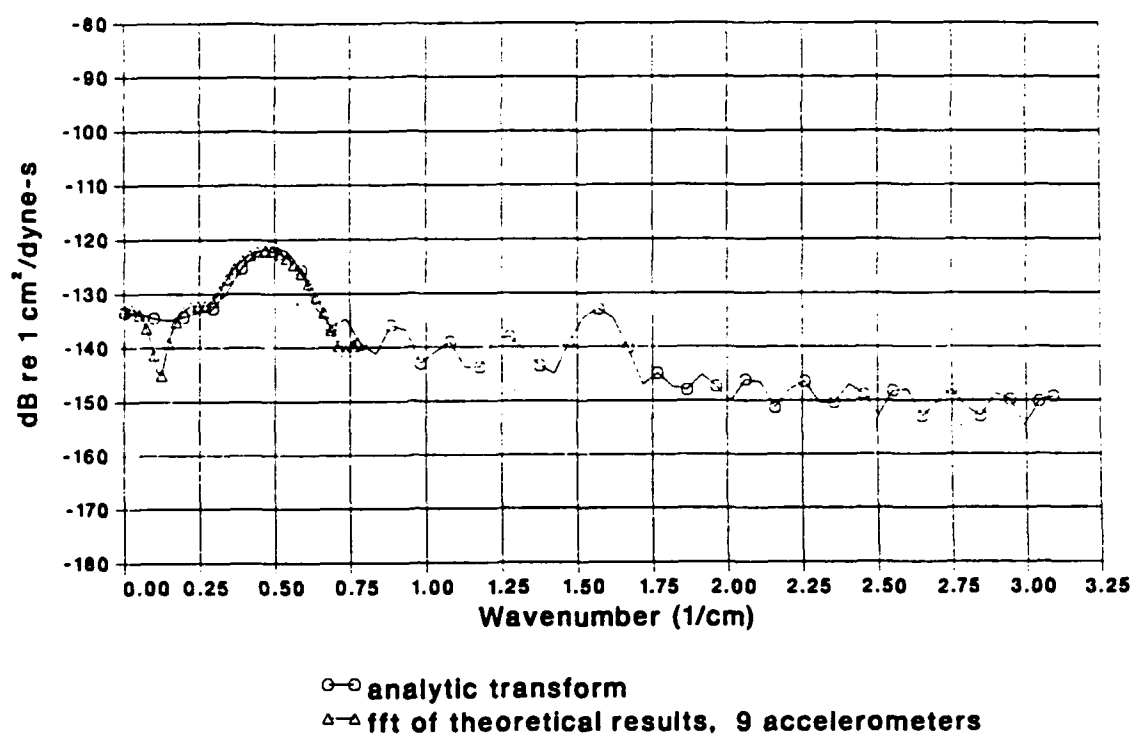


Figure 5.18

Comparison of the magnitude of the continuous and discrete Fourier transforms of the velocity for Experiment 9 at a frequency of 8 kHz. The array for the FFT consisted of nine elements ( $\Delta x = 4$  cm).

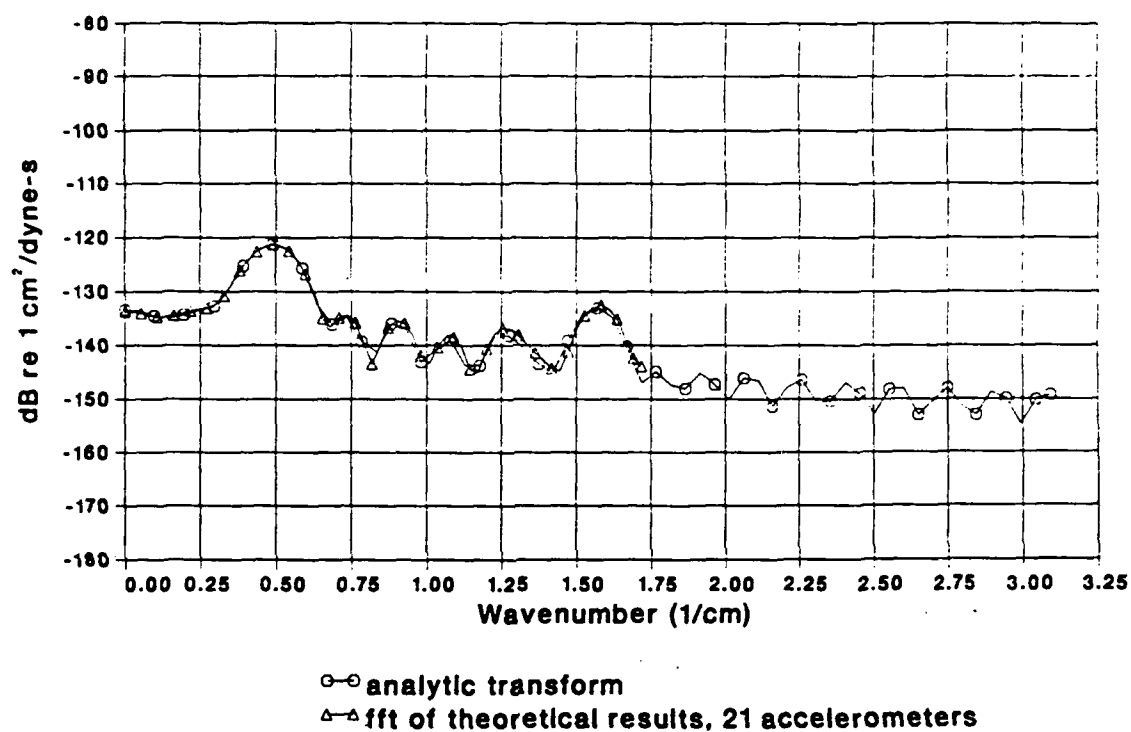


Figure 5.19 Comparison of the magnitude of the continuous and discrete Fourier transforms of the velocity for Experiment 9 at a frequency of 8 kHz. The array for the FFT consisted of 21 elements ( $\Delta x = 1.8$  cm).

content is shown in Figure 5.20. This shows that for this frequency the force wavenumber content has been successfully steered to the desired wavenumber. However, the main-lobe of the wavenumber pattern is fairly broad and extends past the Nyquist wavenumber for a spacing of 2 cm. By realizing the extent of the force wavenumber spectrum, the measurement array can be adjusted for proper measurement.

The final array effect to be examined is that of truncation error. The length of a discrete transform is  $L_t$ ,

$$L_t = N\Delta x \quad , \quad (5.4)$$

where  $N$  is the number of samples. As was mentioned previously, it is desirable to have the Fourier transform of the array function match the sinc function with the correct length,  $L_t$ . The location of the actual measurements is given in the very beginning of this chapter. The length of the FFT is  $N\Delta x = 37$  cm; the length should have been forced to be 38 cm either by using a different spacing or by using a different starting point (which would allow the use of another accelerometer). The effect of truncation error is noticeable as a shifting of the location of the sidelobe structure at wavenumbers approaching the Nyquist wavenumber. The spacing used in the experiment is input to `ARRAY_EFFECT` to calculate the beam response at 8.0 kHz for Experiment 9 and the wavenumber response is obtained via the FFT. The results are shown in Figure 5.21. The shifting of the sidelobe pattern is clearly visible. The array used to calculate the spectrum in Figure 5.16 used a data window whose length is nearly 38 cm, and the results are much better. The truncation error causes the width of the main-lobe of the array pattern to be wider than that of the proper sinc function. The sidelobes at the higher wavenumbers are misaligned.

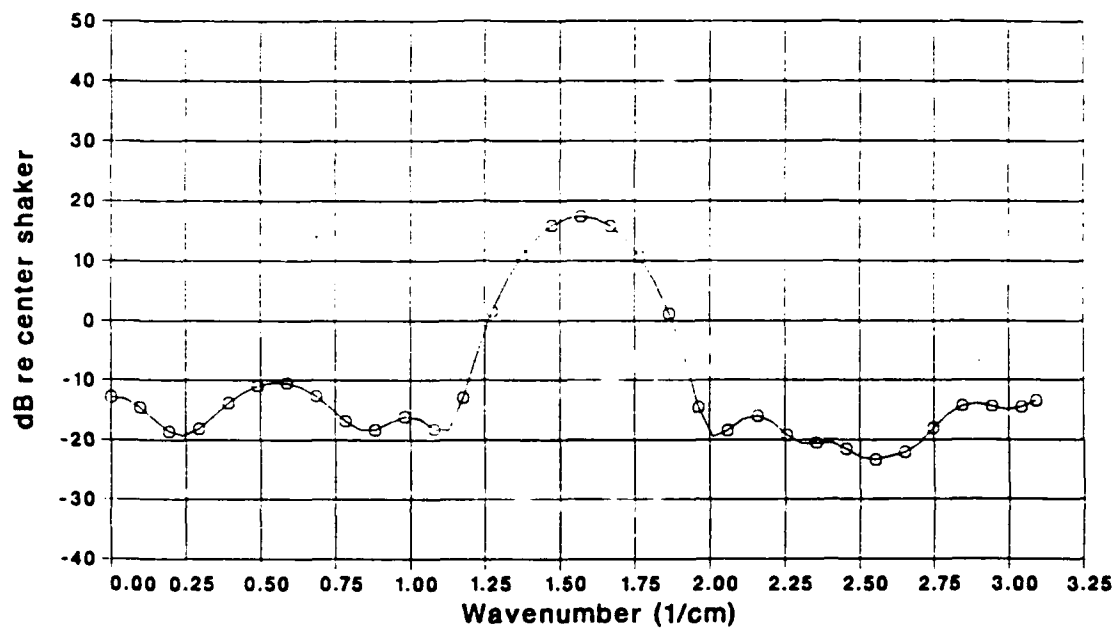


Figure 5.20 Wavenumber content of the force relative to the center shaker for Experiment 9 at a frequency of 8 kHz.

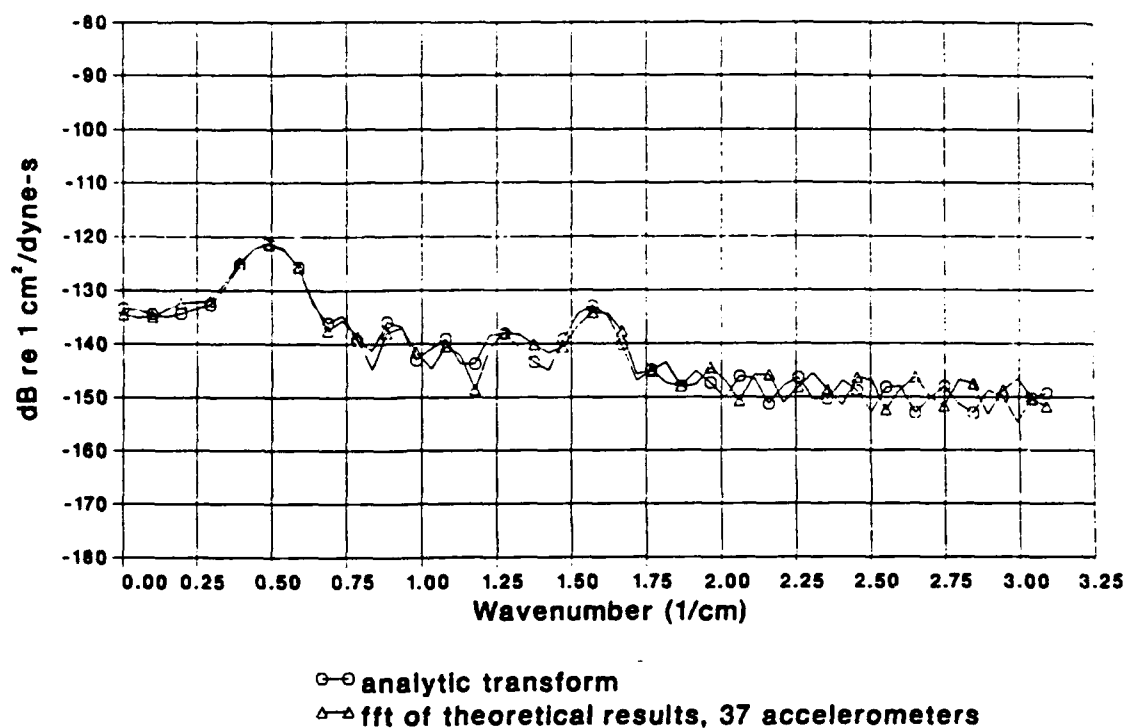


Figure 5.21 Comparison of the magnitude of the continuous and discrete Fourier transforms of the velocity for Experiment 9 at a frequency of 8 kHz. The array for the FFT consisted of 37 elements ( $\Delta x = 1.0$  cm).

Although the error of 1 cm causes only a small deviation, the truncation problem can be more severe. For example, for an accelerometer spacing of 2 cm it is tempting to place accelerometers only at seventeen shaker locations. This spacing yields a Nyquist wavenumber which is the same as the Nyquist wavenumber for the array that produced the plot in Figure 5.16; but  $L_t$ , the aperture length, for this case is only 34 cm. The results for this truncated array are shown in Figure 5.22. This result clearly points out the danger of truncation error.

In this section, the effects of the spacing and length of the measurement array on the estimated wavenumber spectrum have been investigated. The spacing must be close enough to enable the peaks at the higher wavenumbers to be measured.  $\tilde{A}(k_x)$  must be as close as possible to a  $\text{sinc}(k_x L/2)$ , hence the length of the transform must be almost that of the structure. The length should fall within  $0.5\Delta x$  of the length of the beam.

#### 5.4. Wavenumber-Frequency Dependence of the Force and Velocity

The main results of this thesis are presented in this section. The wavenumber-frequency dependence of the measured force as well as the measured and predicted velocity are presented in surface-contour plots. The surface portion of the plots allow for a qualitative examination of the main features of the spectrum. The contours of the surface are shown in a plane beneath the surface. From these contours, more detailed information about the values of the spectrum can be obtained. From these plots, two of the most important questions with respect to the success of the wavenumber-frequency measurement system are answered. The first is whether or not the force wavenumber content of the array of point forces can be steered to a desired wavenumber by amplitude shading of the drive voltages sent to the shakers. Second, contingent upon steering the force

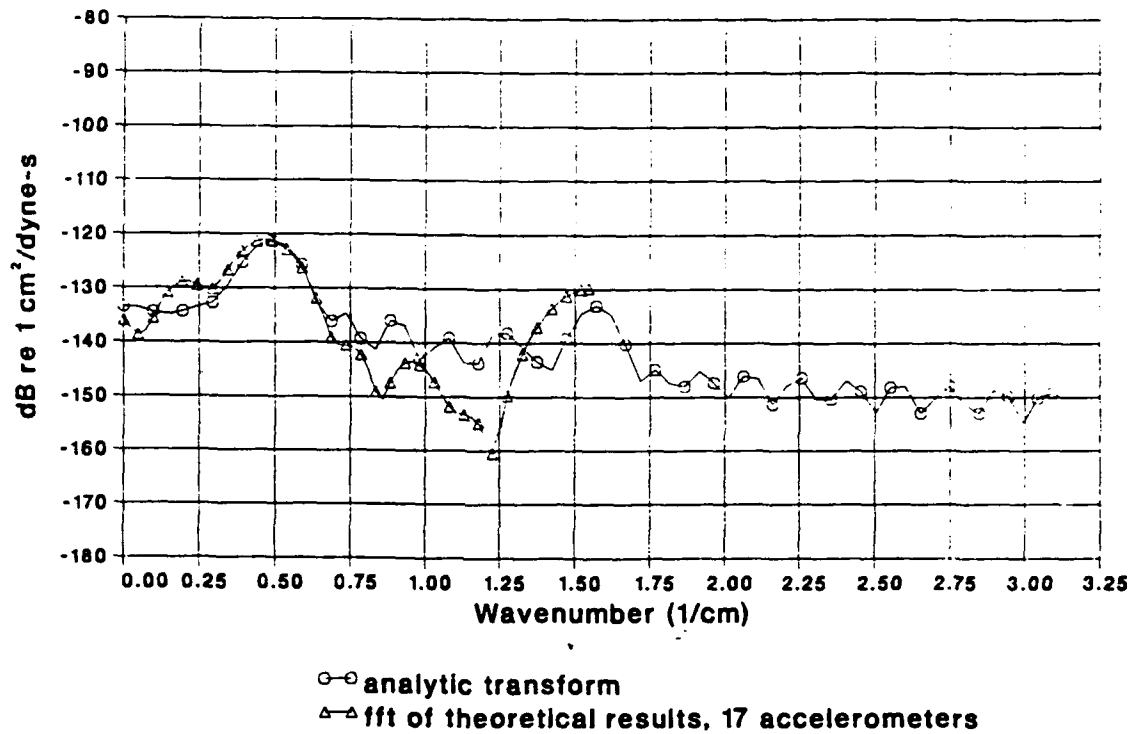


Figure 5.22

Comparison of the magnitude of the continuous and discrete Fourier transforms of the velocity for Experiment 9 at a frequency of 8 kHz. The array for the FFT consisted of seventeen elements ( $\Delta x = 2.0$  cm), placed at the shaker locations.

wavenumber content. what enhancement in the measurement of the velocity is obtained by exciting the beam in this fashion. In other words, are we able to measure the presence of the higher wavenumber velocity fields, which have so far been unmeasurable.

For each of the nine experiments (listed in Table 2.2), the spatial Fourier transform of the measured force relative to the force at the center shaker is plotted. The units of this function are centimeters. Additionally, the predicted normalized wavenumber velocity spectra (using the analytic Fourier transform as formulated in Section 3.4) are presented. As before, the velocity is normalized to the force at the center shaker, hence the Fourier transform has the units of admittance times centimeters. The experimental velocity data are processed in the following manner: the 37 normalized velocities are read into a computer program which zero pads the data to a length of 128 points and then performs an FFT. The general processing of the data is discussed in Chapter 2. Since all of the quantities present in this section are normalized to the center shaker's force, the designation "normalized" is dropped for brevity. Also, any peculiarities associated with any of the data sets (e.g., missing accelerometer locations) can be found in Appendix D.

#### 5.4.1. Nine Shaker Experiments

For the first experiment, the drive wavenumber is  $k_d = 0 \text{ cm}^{-1}$ . The wavenumber dependence of the force spectra is shown in Figure 5.23. The force wavenumber is characterized by four main features, the forced wavenumber ridge, the freebending wavenumber influence, system resonance and the periodicity of the spectrum.

The forced wavenumber ridge is the ridge apparent at the drive wavenumber in Figure 5.23. it is a high amplitude region for constant  $k_x$ . The forced

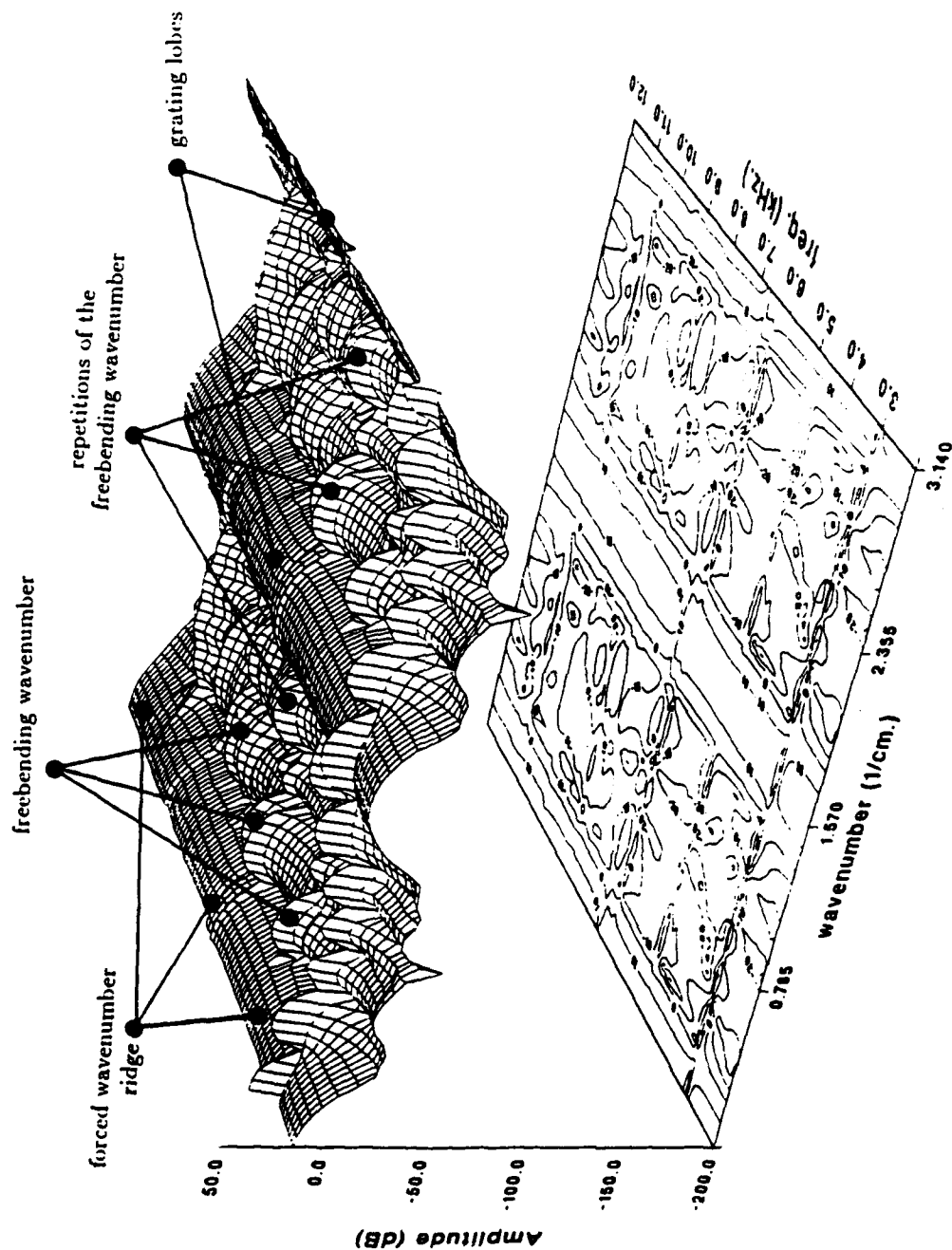


Figure 5.23 Wavenumber-frequency surface-contour plot of the measured force spectrum for Experiment 1. Force relative to  $F_c(\omega)$ .

wavenumber ridge is also called the main-lobe of the force wavenumber spectrum. A coherent ridge occurs when the amplitude shading of the input voltages has succeeded in imposing a similar distribution on the forces at the shakers. The grating lobes are due to the inherent periodicity of the spectrum of discrete point forces (the period is  $2\pi/\Delta x$ ). Hence, if the forced wavenumber ridge has been successfully enforced there also are grating lobes present at  $k_x = \pm 2\pi l/\Delta x \pm k_d, l = \pm 1, \pm 2, \dots$ . For the first experiment, the main-lobe and the grating lobes can be clearly seen at  $0, \pi/2$  and  $\pi \text{ cm}^{-1}$ .

The system resonance is described in Section 5.2. On the surface plots, the system resonance appears as a sharp ridge for constant frequency. This is a consequence of the low impedance seen by the center shaker and the low force output due to this small impedance. At resonance, all of the normalized forces and velocities appear high because they are measured with respect to the force at the center shaker. The system resonance is not labeled on Figure 5.23, but can be seen around 3.0 kHz.

The freebending wavenumber for the Timoshenko beam has approximately a square root dependency on frequency (see Figure 3.2) for frequencies below 12 kHz. For a Bernoulli-Euler beam, the relationship for the freebending wavenumber is exactly a square root dependency. Due to the high admittance of the beam at the freebending wavenumber, it is expected that there is a region around a parabolic line where the influence of the freebending wavenumber can be seen. The parabola has a positive  $k_x$  branch and a negative  $k_x$  branch. The influence of the positive branch on the spectrum can be seen in Figure 5.23. Regions where the effect of the higher admittance at the freebending wavenumber can be seen are denoted by the label 'freebending wavenumber' on the plots (in Figure 5.23). Even though the drive voltage is not steered to the freebending

wavenumbers, the force spectrum exhibits a ridge at these wavenumbers because the beam response is high enough to drive the shakers. For all of the plots, not every local ridge associated with this effect is pointed out explicitly. The periodicity of the spectrum means that there is a repetition of this parabola centered at  $k_x = \pm 2\pi l / \Delta x$ ,  $l = \pm 1, \pm 2, \dots$ ; these periodic repetitions can be seen at  $\pi/2 \text{ cm}^{-1}$  and  $\pi \text{ cm}^{-1}$  (labeled in Figure 5.23 as periodic repetitions of the freebending wavenumber).

The wavenumber-frequency velocity spectrum predicted using the measured forcing function from Experiment 1 is shown in Figures 5.24 and 5.25. The first plot is the analytic Fourier transform and the second is the FFT of the predicted velocity. As these plots are almost identical, only the analytic Fourier transform is shown for the rest of the experiments. The measured wavenumber-frequency velocity response is shown in Figure 5.26.

The wavenumber-frequency velocity surfaces are characterized by three main features, the forced wavenumber ridge, the freebending wavenumber and the system resonance. Note that there is no inherent periodicity in the transform of the continuous velocity field. The freebending wavenumber ridge is due to the high admittance in this region and the forced wavenumber ridge is due to the large amplitude of the force wavenumber spectrum in this region. In Figures 5.24-5.26, the forced wavenumber ridge and the freebending wavenumber peaks can be seen clearly as marked on the plots. The agreement between theory and experiment is quite good. The system resonance can be seen at 3.1 kHz on all of the plots. Both of the theoretically produced plots have a ridge at the first grating lobe of the force wavenumber spectrum, at  $k_x = \pi/2 \text{ cm}^{-1}$  (labeled as "forced wavenumber ridge" on the plot). In order to show this peak, a slice is made through the surface at a frequency of 11.5 kHz. This plot of the analytic and measured wavenumber

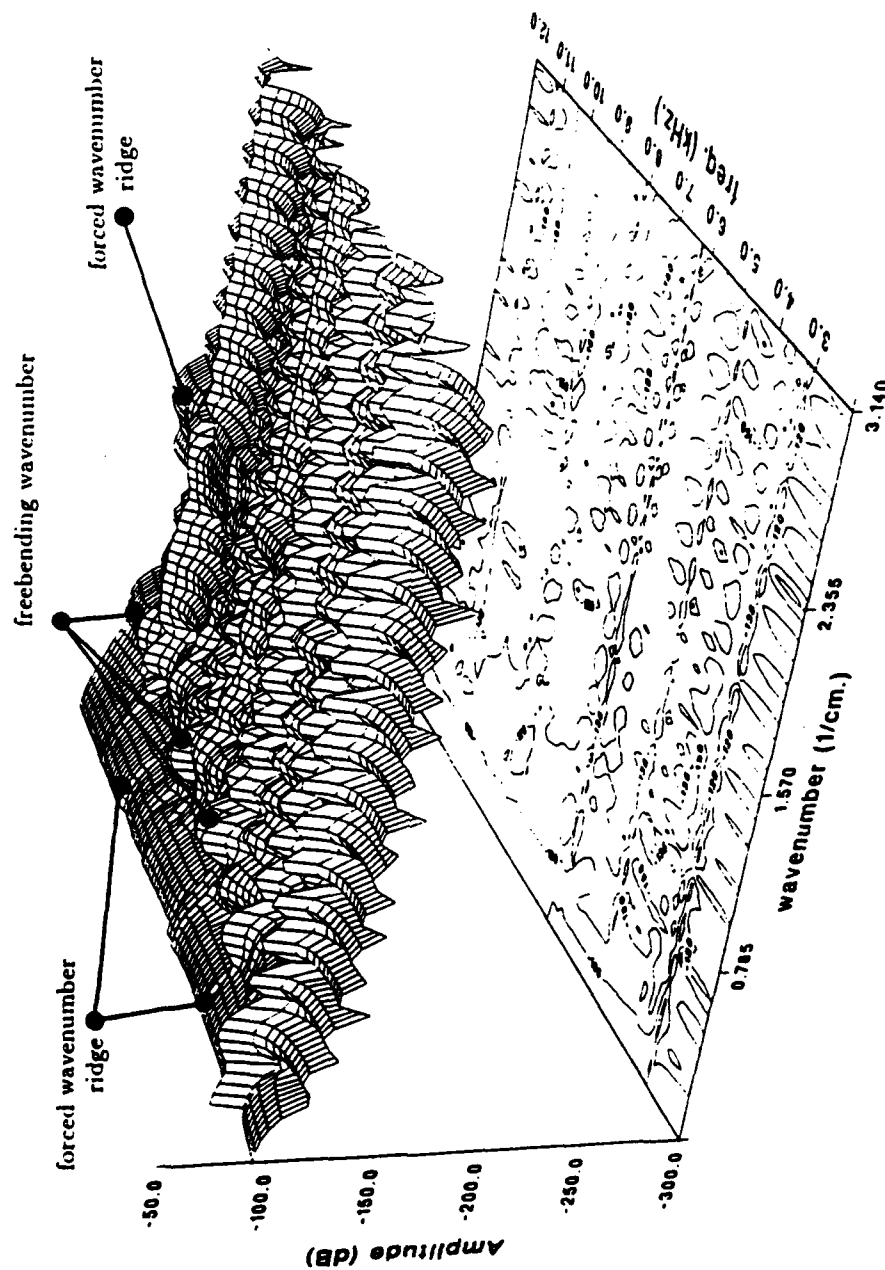


Figure 5.24 Wavenumber-frequency surface-contour plot of the predicted velocity spectrum (spectrum via the continuous transform) for Experiment 1. Velocity relative to  $F_c(\omega)$ .

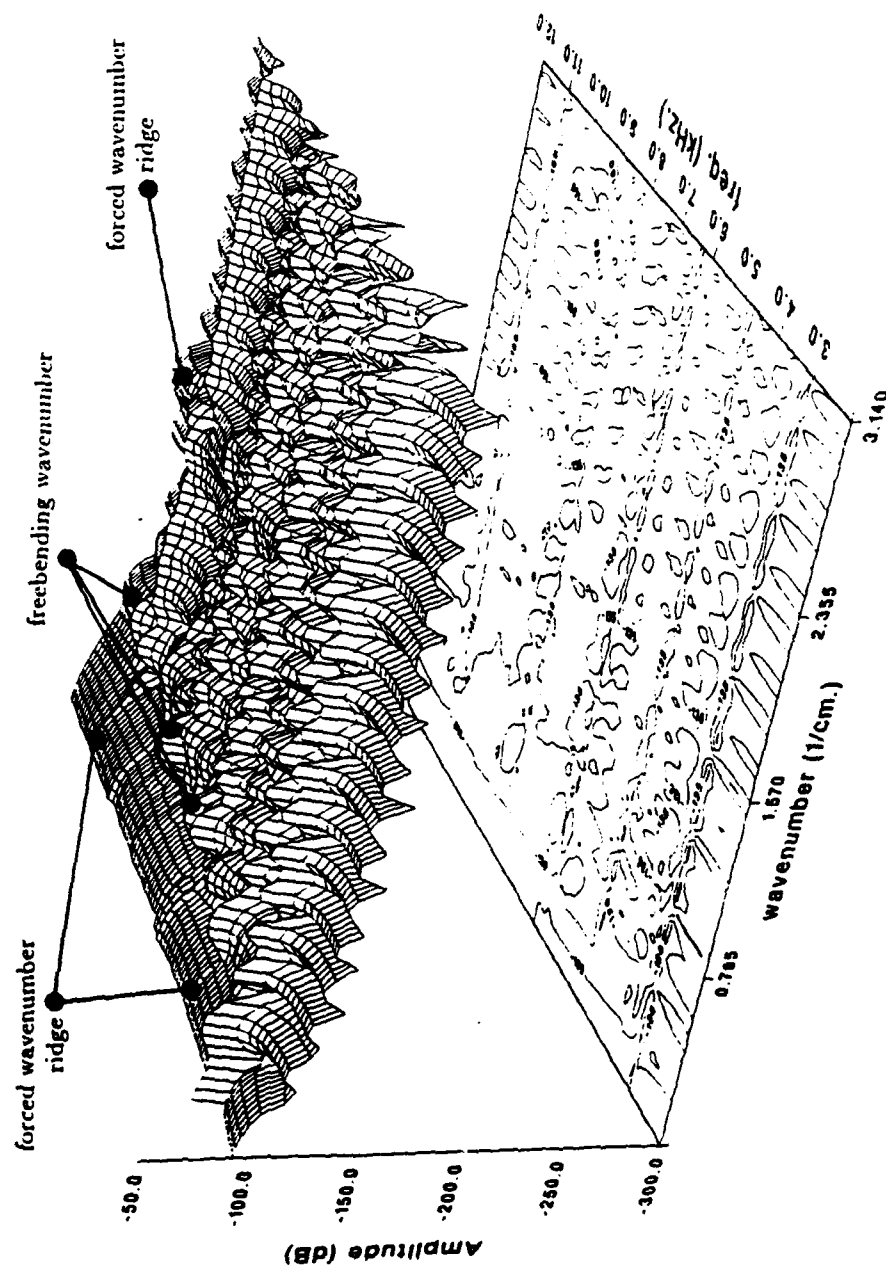


Figure 5.25 Wavenumber-frequency surface-contour plot of the predicted velocity spectrum (spectrum via the FFT) for Experiment 1. Velocity relative to  $F_c(\omega)$ .

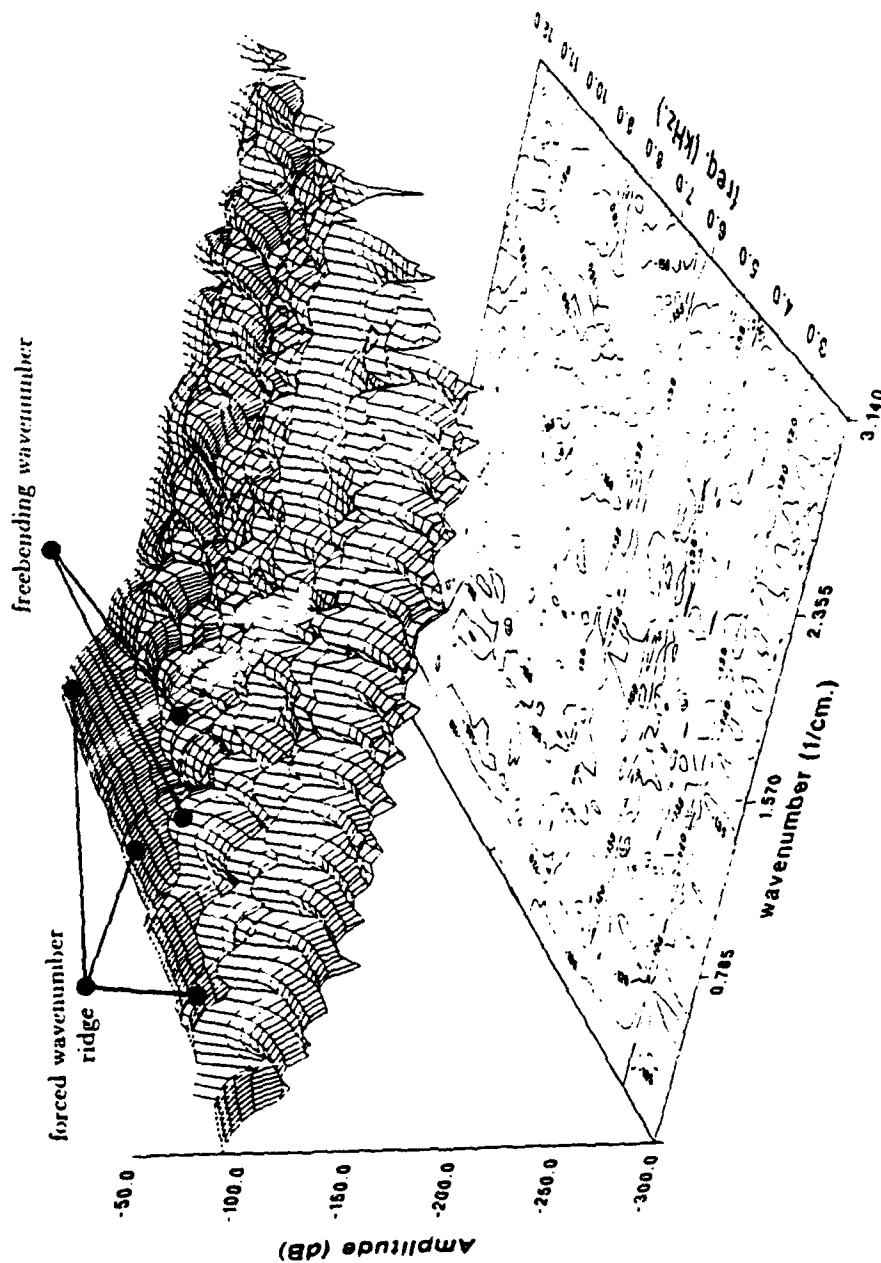


Figure 5.26 Wavenumber-frequency surface-contour plot of the measured velocity spectrum for Experiment 1. Velocity relative to  $F_c(\omega)$ .

velocity is shown on Figure 5.27. The peak can be seen in the predicted results. The measurements do not reflect this however, and it may be that the large amplitude of the spectrum at the lower wavenumbers somehow overwhelms the spectrum at the higher wavenumbers. A possible mechanism for the burying of the higher wavenumber components in the measured data is the following; the accelerometer is more sensitive at the lower wavenumbers, the peak at the zero wavenumber and the associated sidelobes are given more weight than the smaller peak at the higher wavenumbers. In this way, the stronger component at the lower wavenumbers buries the weaker components at the higher wavenumbers in the measurement; but the theory has no such sensor error and is able to measure the higher wavenumber peak.

In Experiment 2, the drive wavenumber is  $0.16 \text{ cm}^{-1}$ . Due to the width of the main-lobe in the force spectrum, the peaks at  $\pm k_d$  overlap as shown in Figure 5.28. The grating lobes and the main-lobe create force wavenumber passband regions. The freebending wavenumber influence is not as noticeable as in Experiment 1, because the forced wavenumber ridge is present where the freebending wavenumber effect would be seen. The system resonance is seen again at 3.1 kHz.

The measured and predicted wavenumber velocity responses are shown in Figures 5.29 and 5.30. Again, the forced wavenumber ridge is clearly present and theory and experiment agree nicely, especially below  $k_x = 1.5 \text{ cm}^{-1}$ . The grating lobe effect around  $k_x = \pi/2 \text{ cm}^{-1}$  can be seen in the predicted velocity spectrum but not in the measured spectrum. This ridge in the predicted velocity is present above 9.0 kHz. The system resonance occurs at 3.1 kHz. Only slight local peaks can be seen in the region where the freebending wavenumber influence is expected.

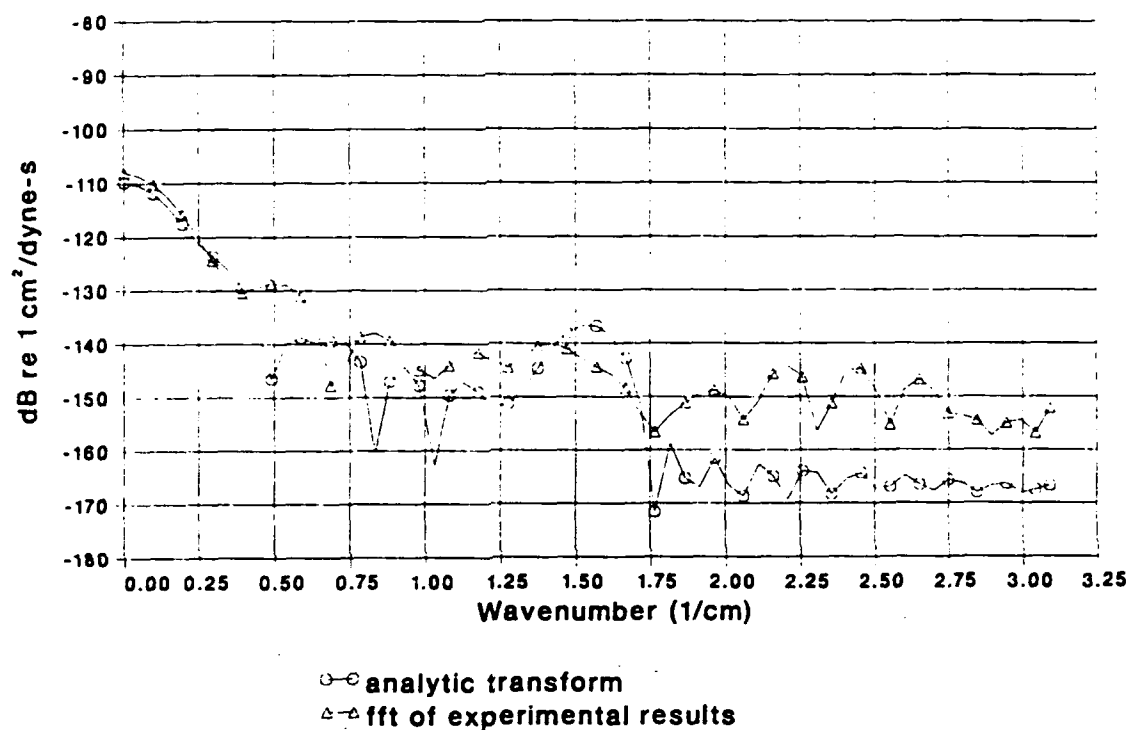


Figure 5.27 Comparison of the magnitude of the predicted versus the measured spectrum for Experiment 1 at a frequency of 11.5 kHz.

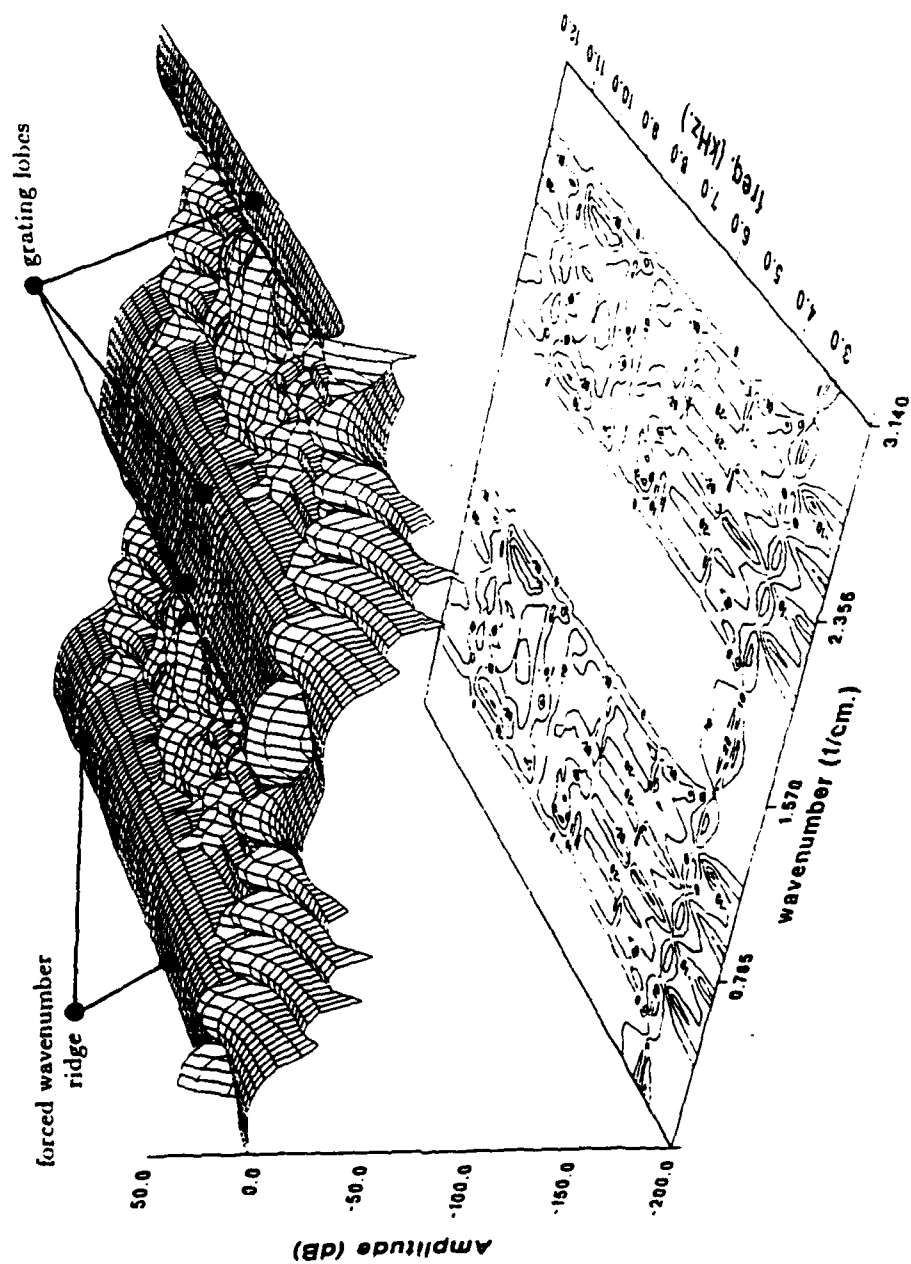


Figure 5.28 Wavenumber-frequency surface-contour plot of the measured force spectrum for Experiment 2. Force relative to  $F_c(\omega)$ .

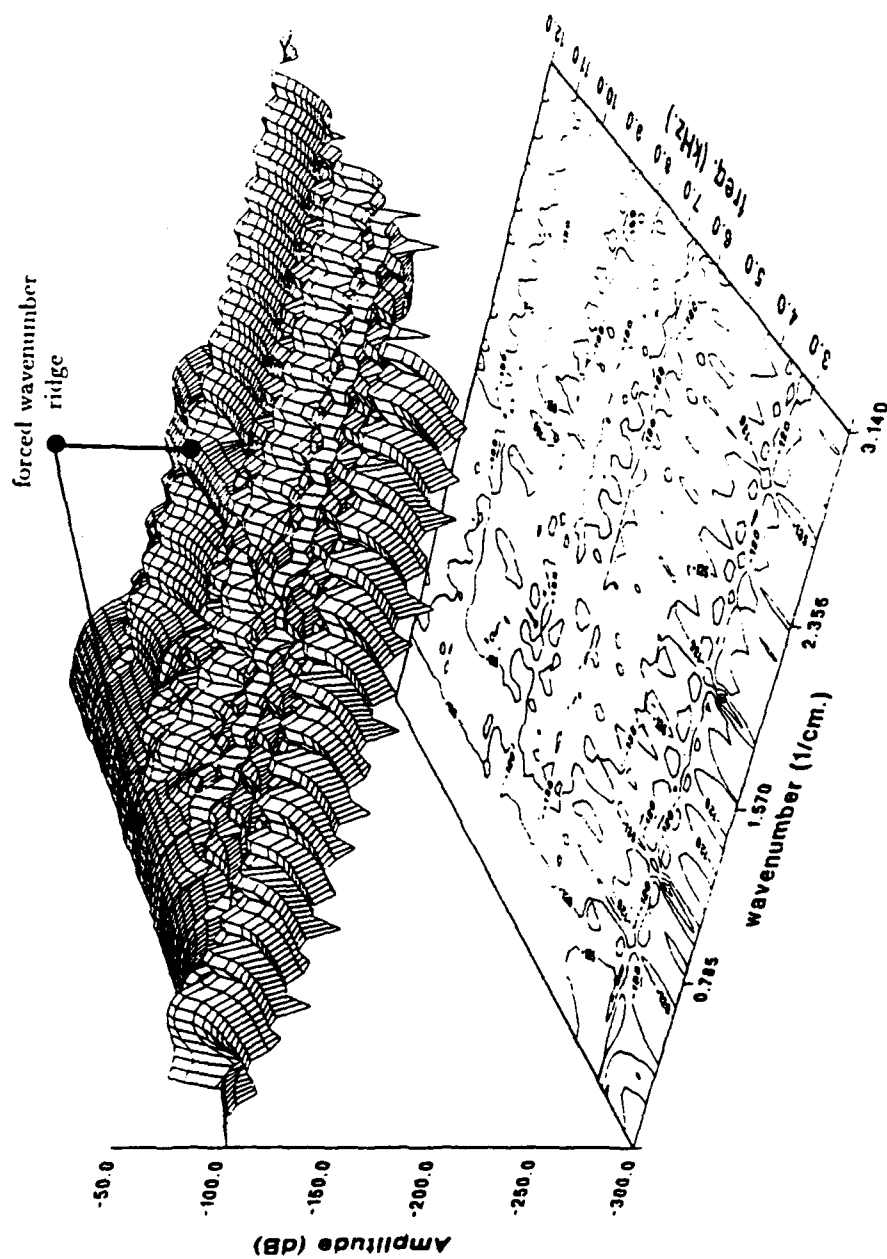


Figure 5.29 Wavenumber-frequency surface-contour plot of the predicted velocity spectrum (spectrum via the continuous transform) for Experiment 2. Velocity relative to  $F_c(\omega)$ .

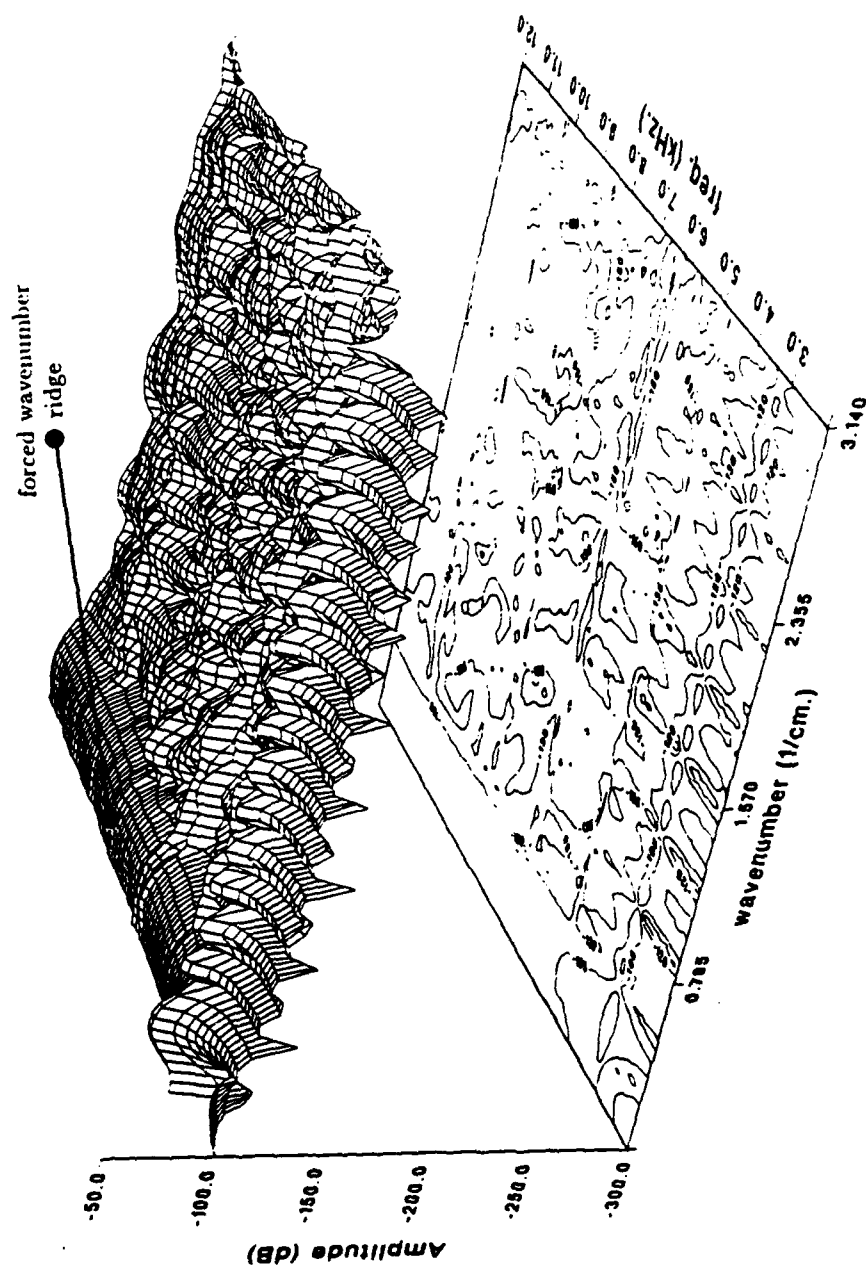


Figure 5.30 Wavenumber-frequency surface-contour plot of the measured velocity spectrum for Experiment 2. Velocity relative to  $F_c(\omega)$ .

The force wavenumber spectrum for Experiment 3 is displayed in Figure 5.31. The drive wavenumber for this experiment is  $k_d = 0.332 \text{ cm}^{-1}$ . The forced wavenumber ridge for this experiment is the least defined for any of the nine shaker experiments. From 2-6.5 kHz, the forced wavenumber ridge is fairly well defined and properly located. From 6.5-9 kHz, the forced wavenumber ridge (and the grating lobes as well) have shifted and become less defined. A forced wavenumber ridge once again appears from 9-12 kHz. For this experiment and for Experiment 7,  $k_d$  corresponds to a freebending wavenumber whose frequency is within the measurement range of 2-12 kHz. The frequency of a freebending wavenumber equal to  $0.332 \text{ cm}^{-1}$  is 5.0 kHz. It is not necessarily expected that there would be a peak in either the force wavenumber content or the velocity wavenumber content at this frequency. This is not expected for two reasons. One, this is not a resonance wavenumber of the beam. Two, even if it were a resonance wavenumber, the force distribution must match that particular mode in order to produce a highly resonance response.

Figures 5.32 and 5.33 are the surface contour plots showing the dependence of the velocity on wavenumber and frequency for Experiment 3. The velocity in general tracks with the force wavenumber main-lobe. As the main-lobe of the force shifts up or down in wavenumber so does the velocity response. Since the forced wavenumber ridge wanders, the velocity ridge does not stay at a constant wavenumber. The freebending wavenumber effect is not seen. Perhaps, it is the proximity of the drive wavenumber to the freebending wavenumbers in this frequency range that is the explanation for the lack of a nicely formed forced wavenumber ridge. The system resonance for the measured values is higher than the predicted value. However, if the mass loading would be removed, the two curves should compare more closely.

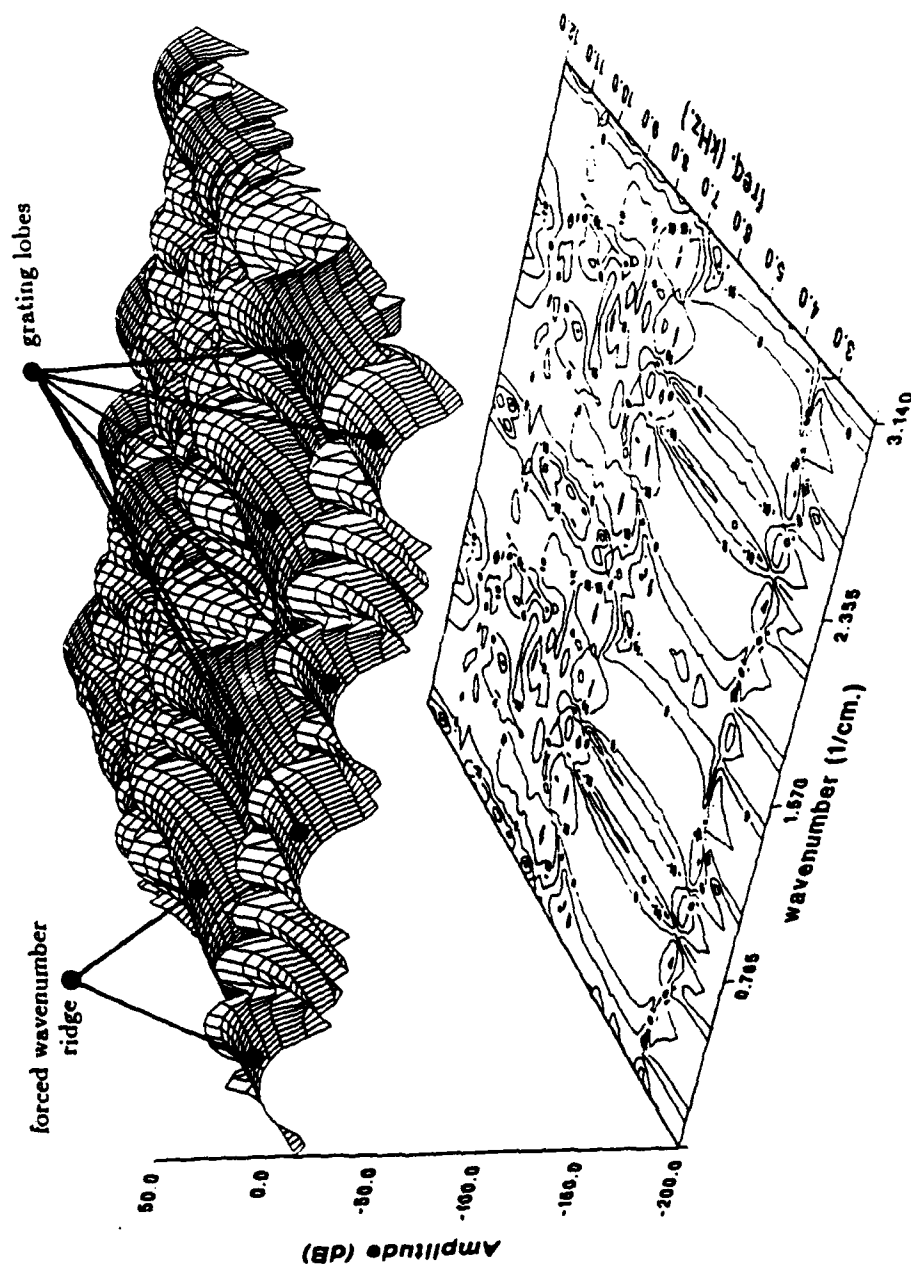


Figure 5.31 Wavenumber-frequency surface-contour plot of the measured force spectrum for Experiment 3. Force relative to  $F_c(\omega)$ .

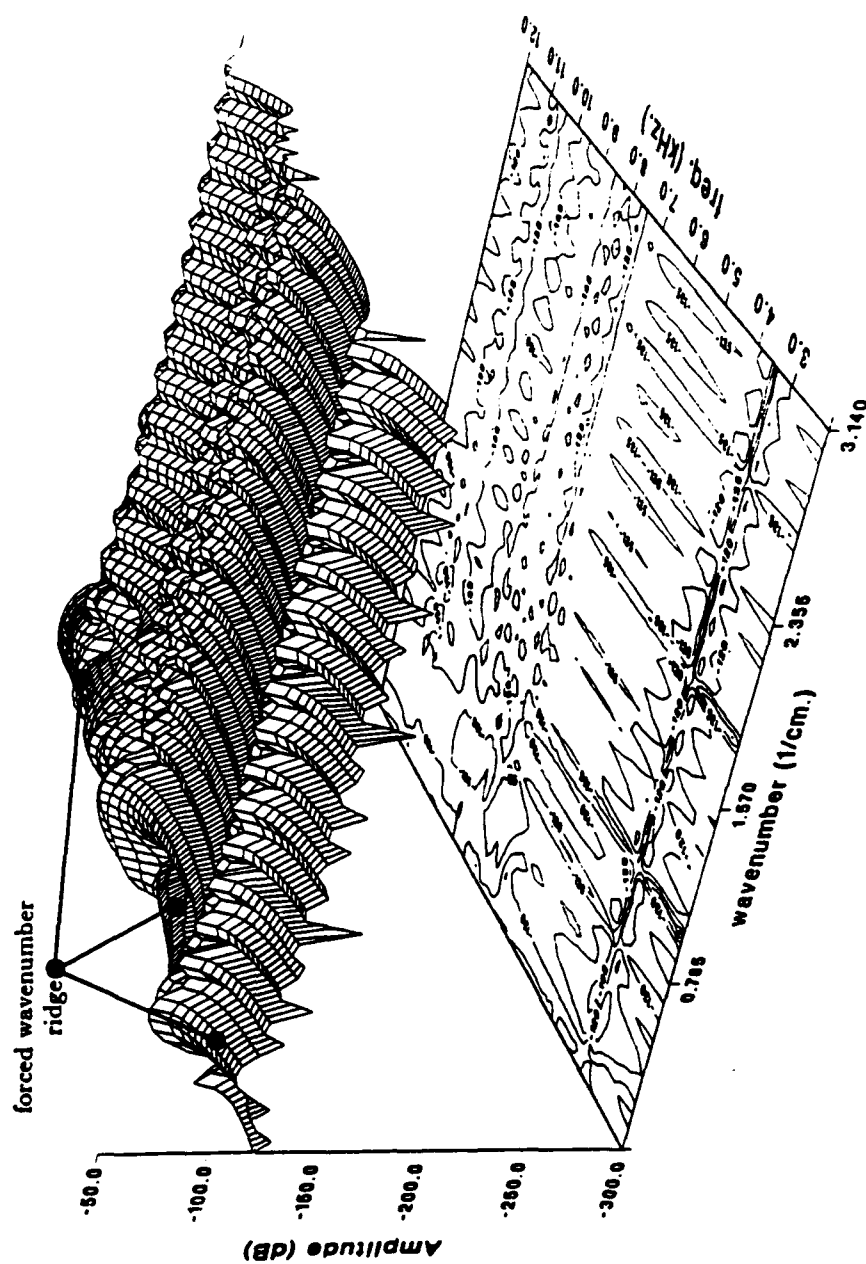


Figure 5.32 Wavenumber-frequency surface-contour plot of the predicted velocity spectrum (spec-trum via the continuous transform) for Experiment 3. Velocity relative to  $F_c(\omega)$ .

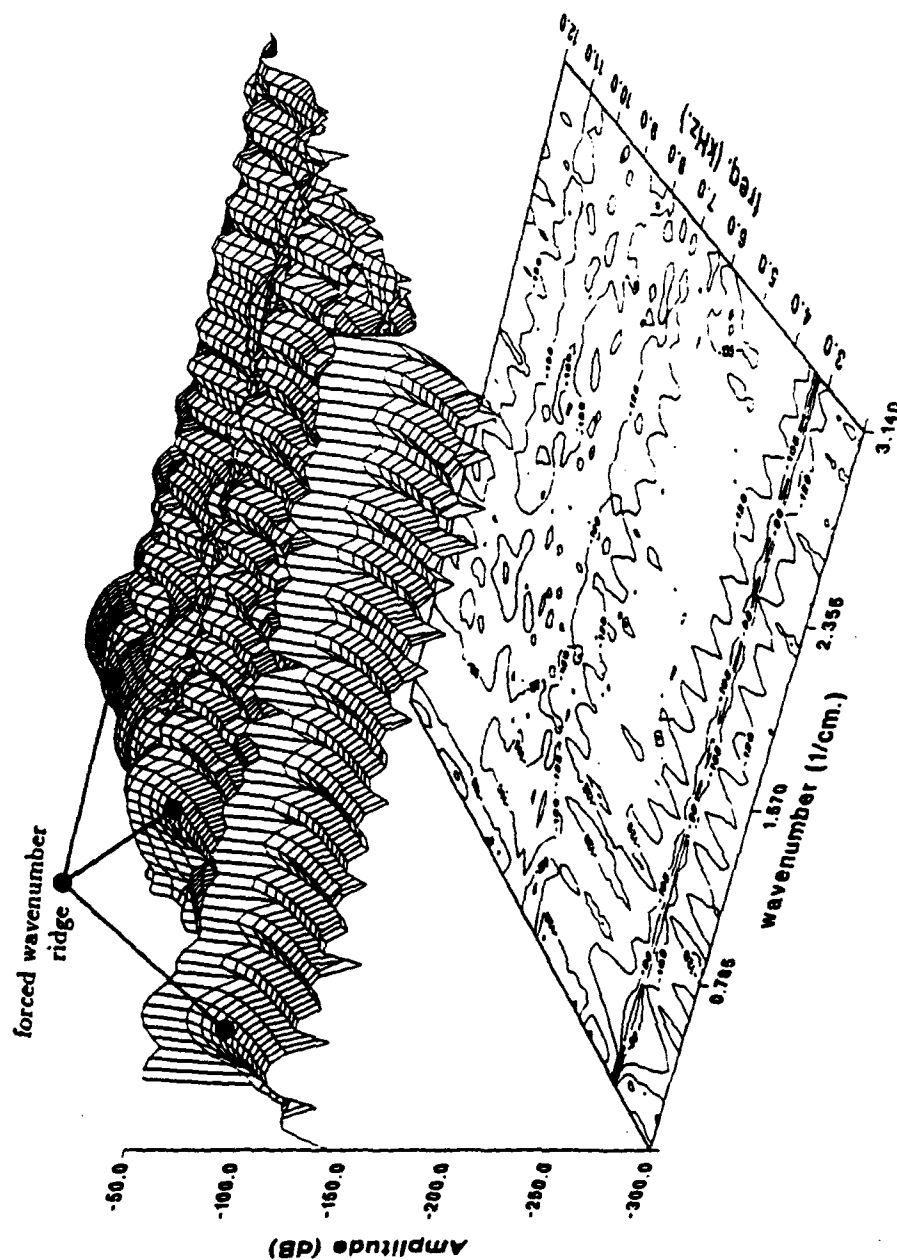


Figure 5.33 Wavenumber-frequency surface-contour plot of the measured velocity spectrum for Experiment 3. Velocity relative to  $F_c(\omega)$ .

The final nine shaker experiment is Experiment 4. Here, the shakers are driven in a pattern such that every other shaker is out of phase with the center shaker (i.e. the first shaker is in phase, the second out of phase). The force wavenumber content in Figure 5.34 displays the strong main and grating lobe pattern near the desired wavenumber until about 10 kHz. The peak of the forced wavenumber spectrum is found at  $k_x = \pi/4 \text{ cm}^{-1}$  instead of the value used to generate the weights in FORCE\_FILTER,  $0.746 \text{ cm}^{-1}$ . It is difficult to control the wavenumber spectra to this fine a degree. The influence of the freebending wavenumber can once again be seen and is labeled on the plot.

Figures 5.35 and 5.36 are the surface contour plots for the predicted and the measured velocity spectra for Experiment 4. The forced wavenumber ridge is seen to become more and more defined as frequency increases. At frequencies below 3 kHz, the admittance of the beam at  $k_d$  is so low, that even with the well defined forced wavenumber ridge, the velocity spectrum does not exhibit a ridge at the drive wavenumber. At these low frequencies, the freebending wavenumber dominates the response of the structure. The overall spectrum of the velocity response is much lower than the other experiments because most of the energy of the force spectrum falls into a low admittance region. The system resonance is very much subdued as compared to some of the other experiments, and cannot be seen in the force wavenumber content. The grating lobe appears at such a high wavenumber that the velocity content is not disturbed at that wavenumber.

#### 5.4.2. Seventeen Shaker Experiments

The results for the five seventeen shaker experiments are now presented. The force wavenumber-frequency spectra for the nine and seventeen shaker experiments are very similar. The major difference between the two is due to the shaker spacing; the periodicity of the seventeen shaker force spectra is

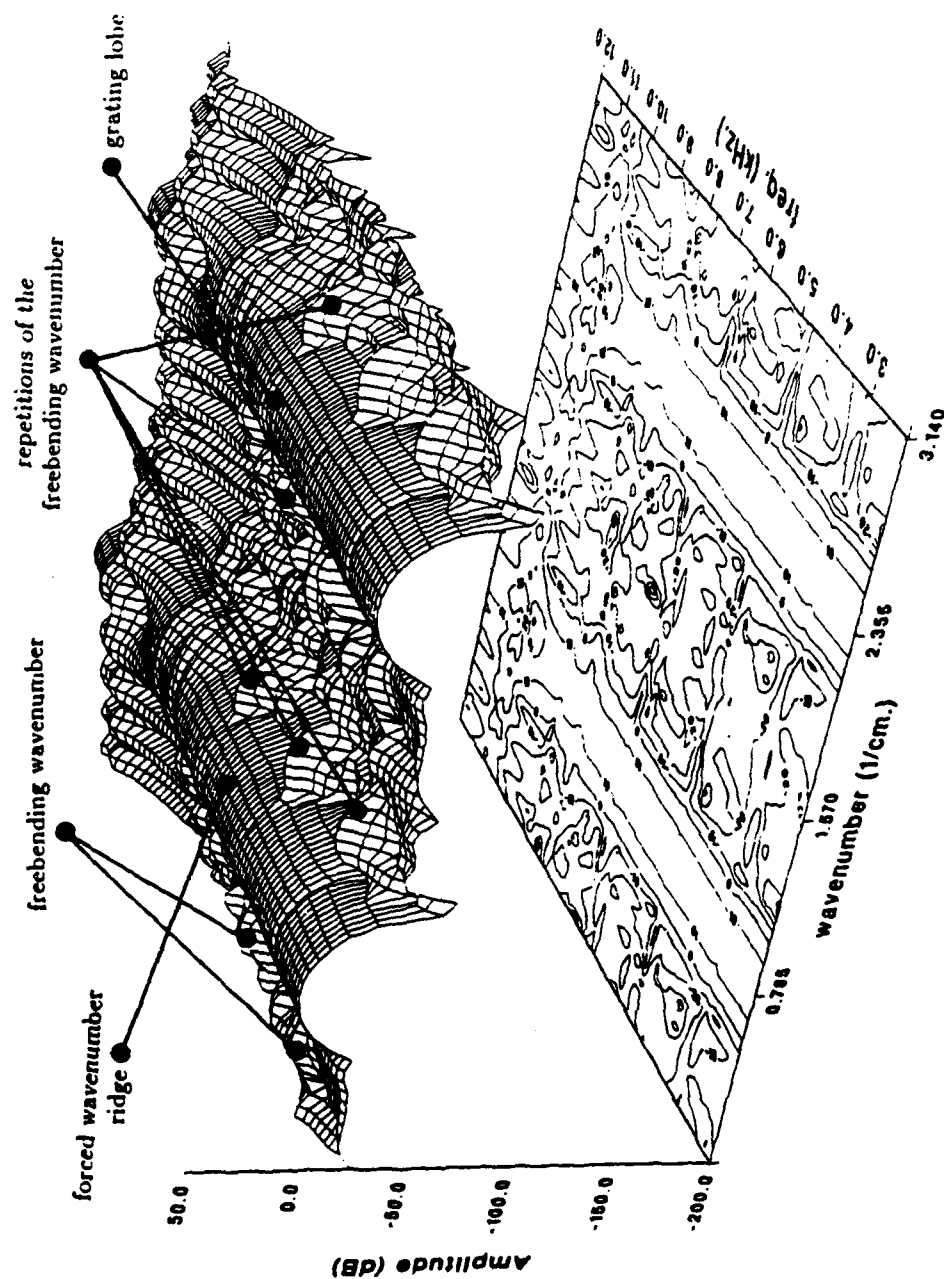


Figure 5.34 Wavenumber-frequency surface-contour plot of the measured force spectrum for Experiment 4. Force relative to  $F_c(\omega)$ .

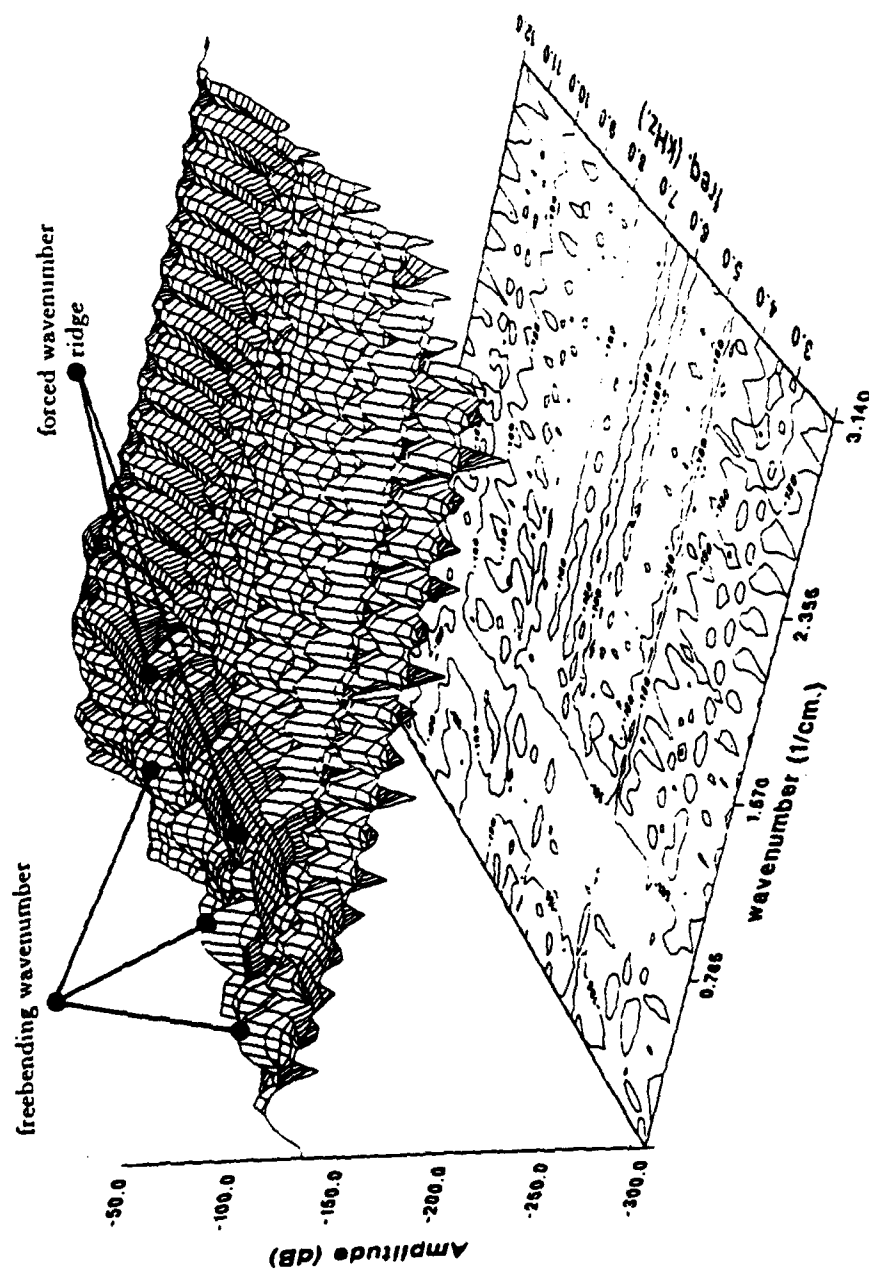


Figure 5.35 Wavenumber-frequency surface-contour plot of the predicted velocity spectrum (spectrum via the continuous transform) for Experiment 4. Velocity relative to  $F_c(\omega)$ .

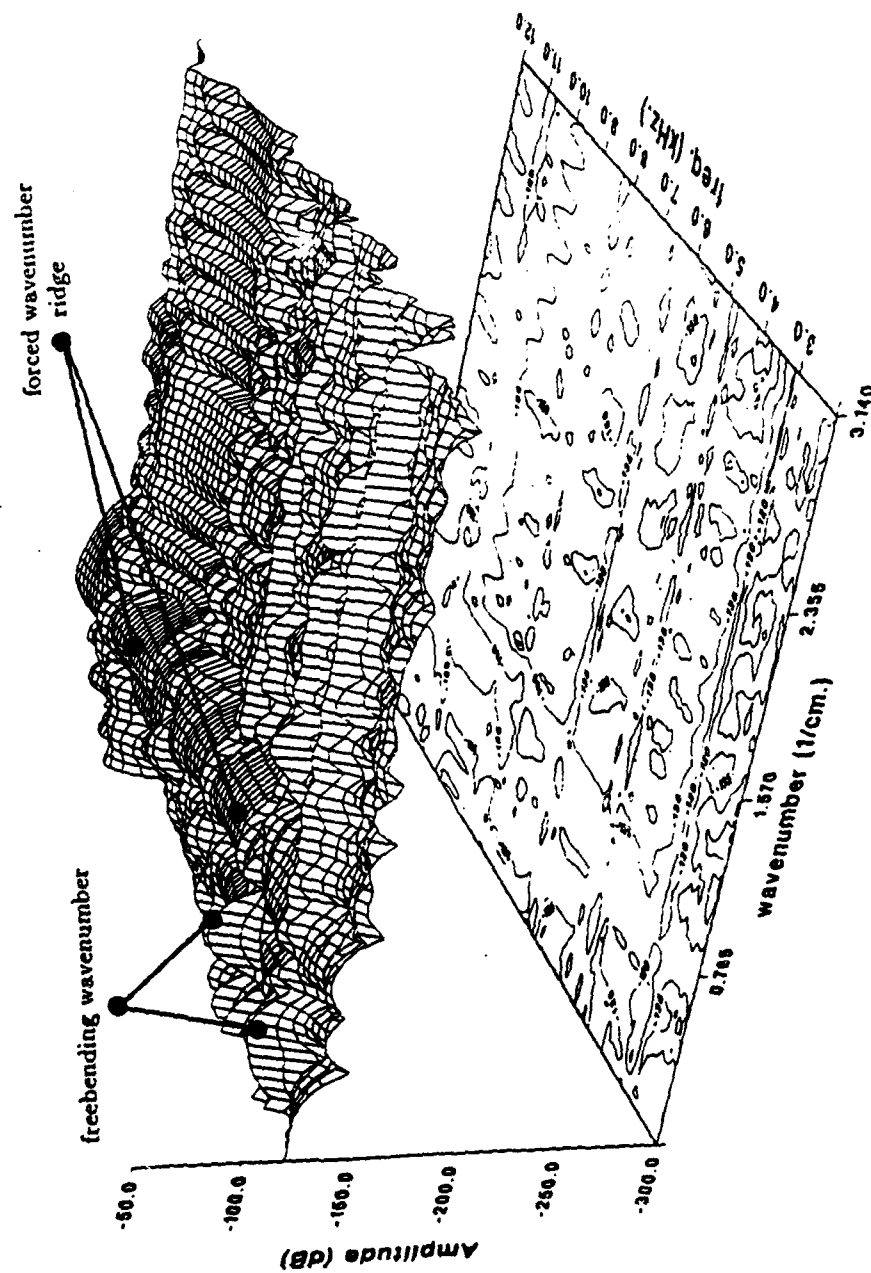


Figure 5.36 Wavenumber-frequency surface-contour plot of the measured velocity spectrum for Experiment 4. Velocity relative to  $F_c(\omega)$ .

$\pi \text{ cm}^{-1}$ . Hence, the grating lobes are separated farther from the main-lobe and the periodic repetition of the freebending wavenumber parabola is centered further away from the origin. The means by which the results from the first four seventeen shaker experiments are to be presented is to point out any differences from the corresponding nine shaker experiment and any other noticeable features.

The first four seventeen shaker experiments are driven at the same wavenumber as the nine shaker experiments (see Table 2.2). The force and velocity spectra for the matching experiments are very similar. The force, predicted velocity and measured velocity wavenumber-frequency distributions for Experiment 5 are shown in Figures 5.37-5.39 respectively, for Experiment 6 (one wavelength over the structure) in Figures 5.40-5.42, for Experiment 7 (two wavelengths over the structure) in Figures 5.43-5.45 and for Experiment 8 (4.5 wavelengths over the structure) in Figures 5.46-5.48.

The major differences seen between the nine shaker experiment of a particular force distribution and the seventeen shaker experiment with the same force distribution are summarized in this paragraph. In Experiments 5 and 6, there are no grating lobes present at  $k_x = \pi/2 \text{ cm}^{-1}$  (Figures 5.37 and 5.40). Thus, the velocity spectra for these two experiments (see Figures 5.38 and 5.41) do not exhibit a ridge at this wavenumber as do the predicted spectra for the nine shaker experiments. In all of the seventeen shaker experiments, the grating lobes of the force wavenumber distribution occur at a wavenumber that is too large to noticeably excite the velocity. In Experiment 6, the system resonance is very strongly excited, more so in the measurement than the theory. For Experiment 7, the forced wavenumber ridge is even more poorly defined than for Experiment 3 as can be seen in Figures 5.31 and 5.43. The velocity spectrum for this experiment looks, however, very similar to the corresponding nine shaker experiment. For

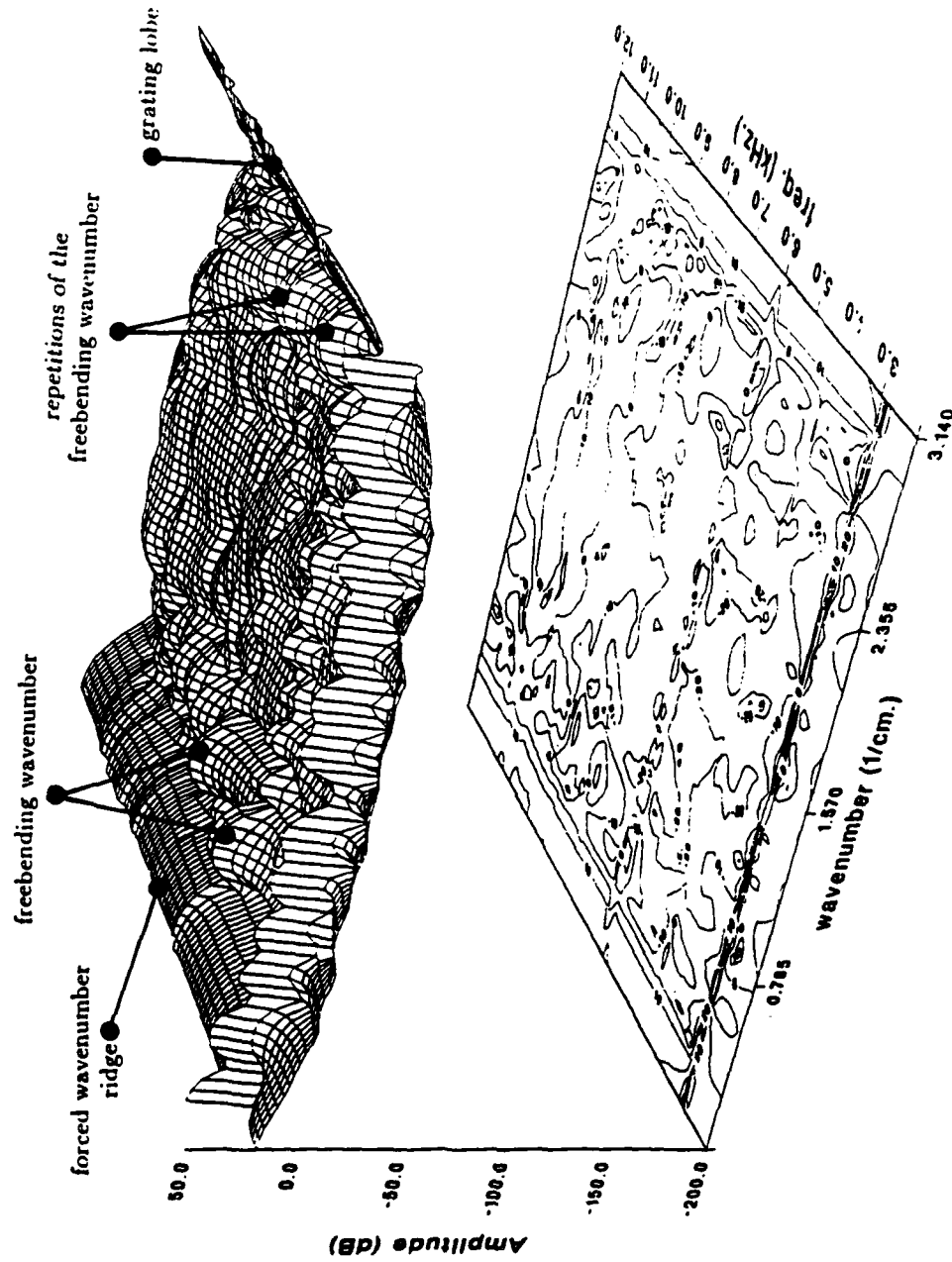


Figure 5.37 Wavenumber-frequency surface-contour plot of the measured force spectrum for Experiment 5. Force relative to  $F_c(\omega)$ .

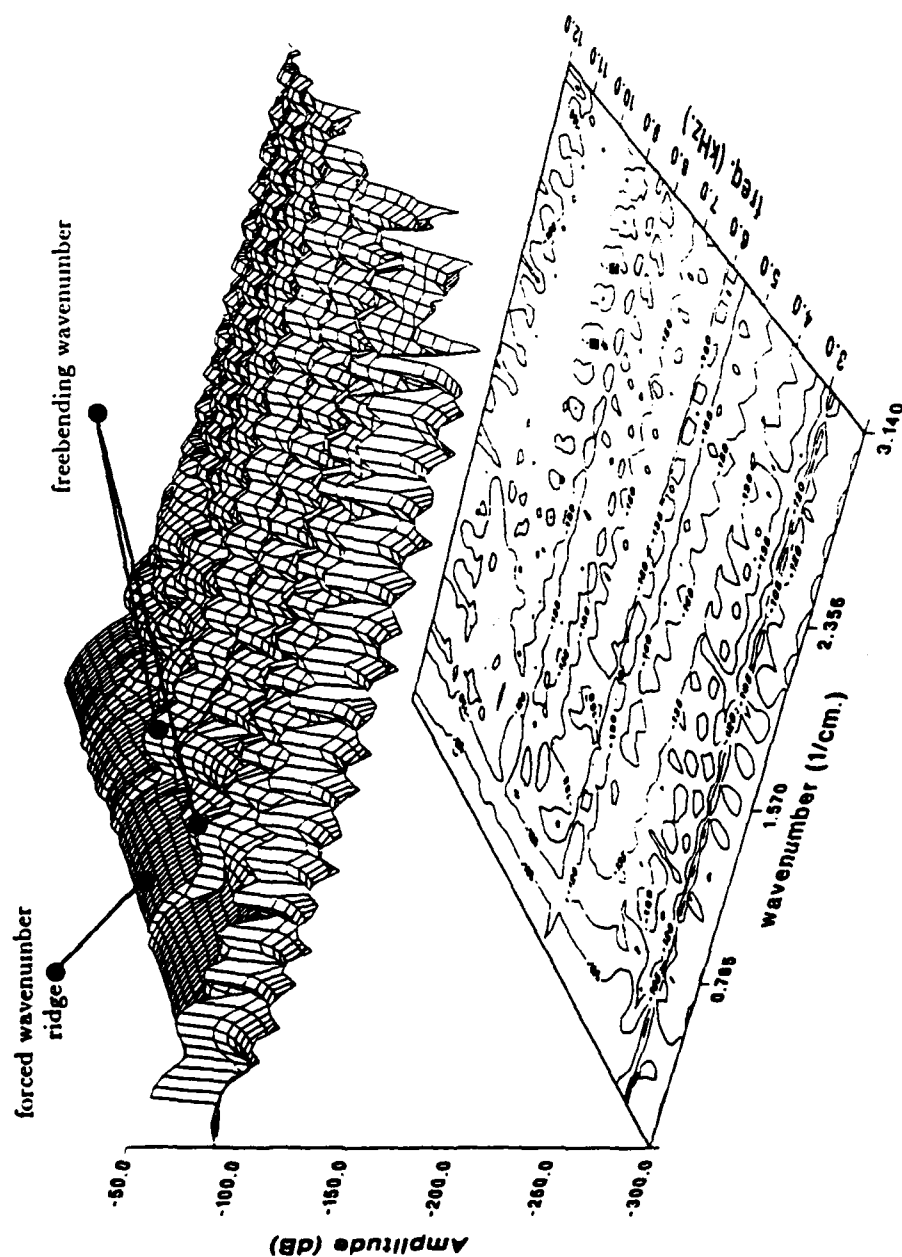


Figure 5.38 Wavenumber-frequency surface-contour plot of the predicted velocity spectrum (spectrum via the continuous transform) for Experiment 5. Velocity relative to  $F_c(\omega)$ .

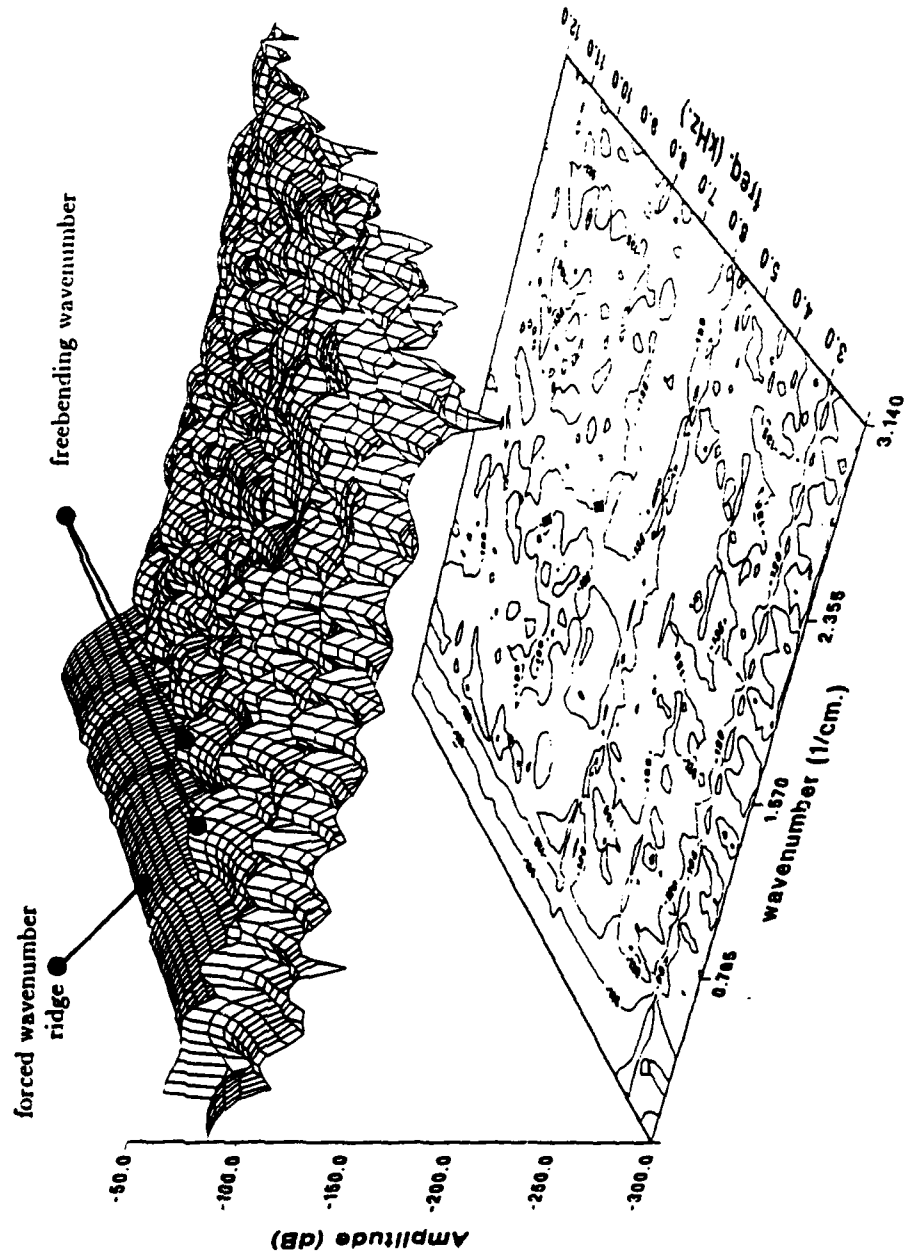


Figure 5.39 Wavenumber-frequency surface-contour plot of the measured velocity spectrum for Experiment 5. Velocity relative to  $F_c(\omega)$ .

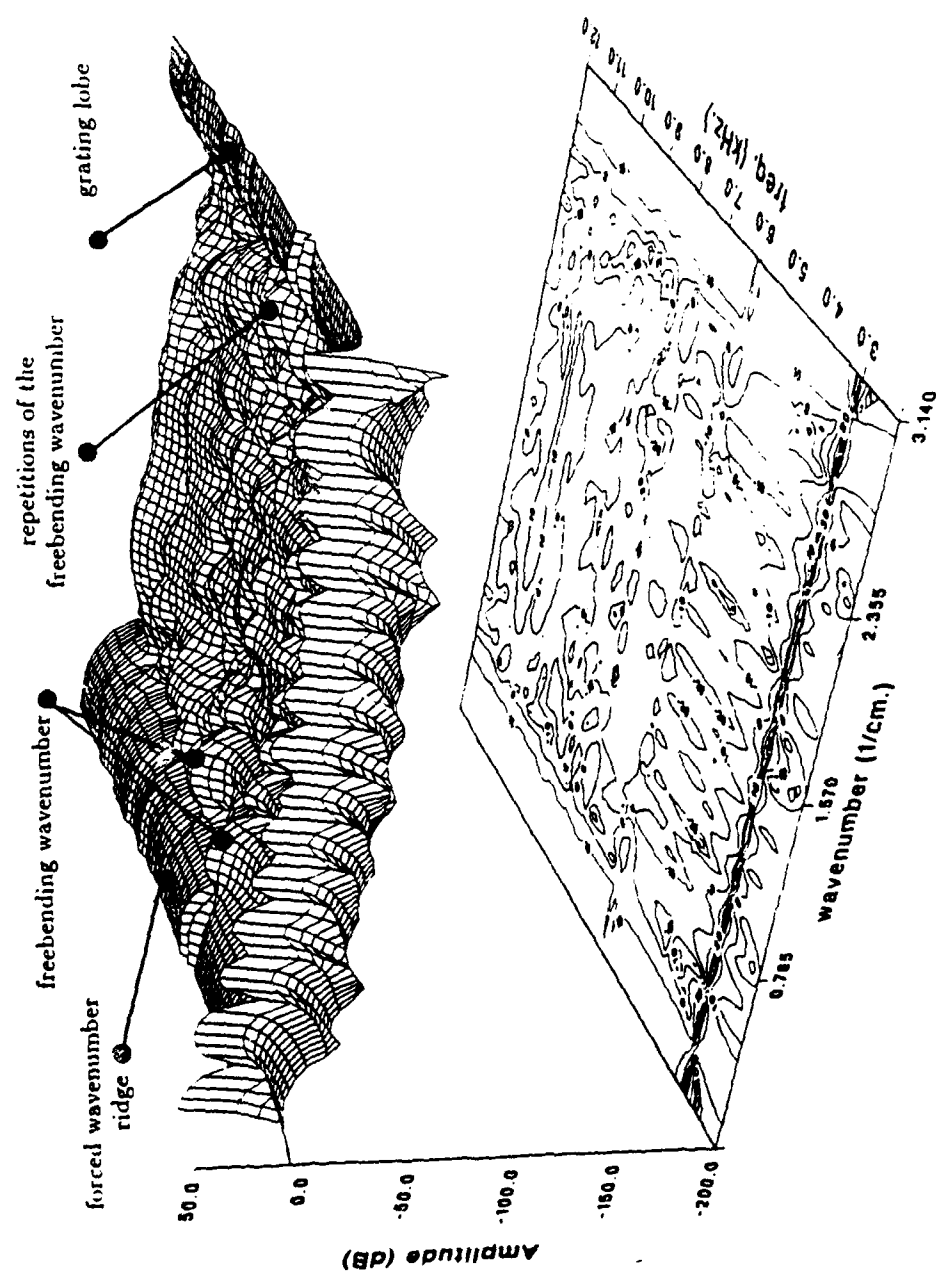


Figure 5.40 Wavenumber-frequency surface-contour plot of the measured force spectrum for Experiment 6. Force relative to  $F_c(\omega)$ .

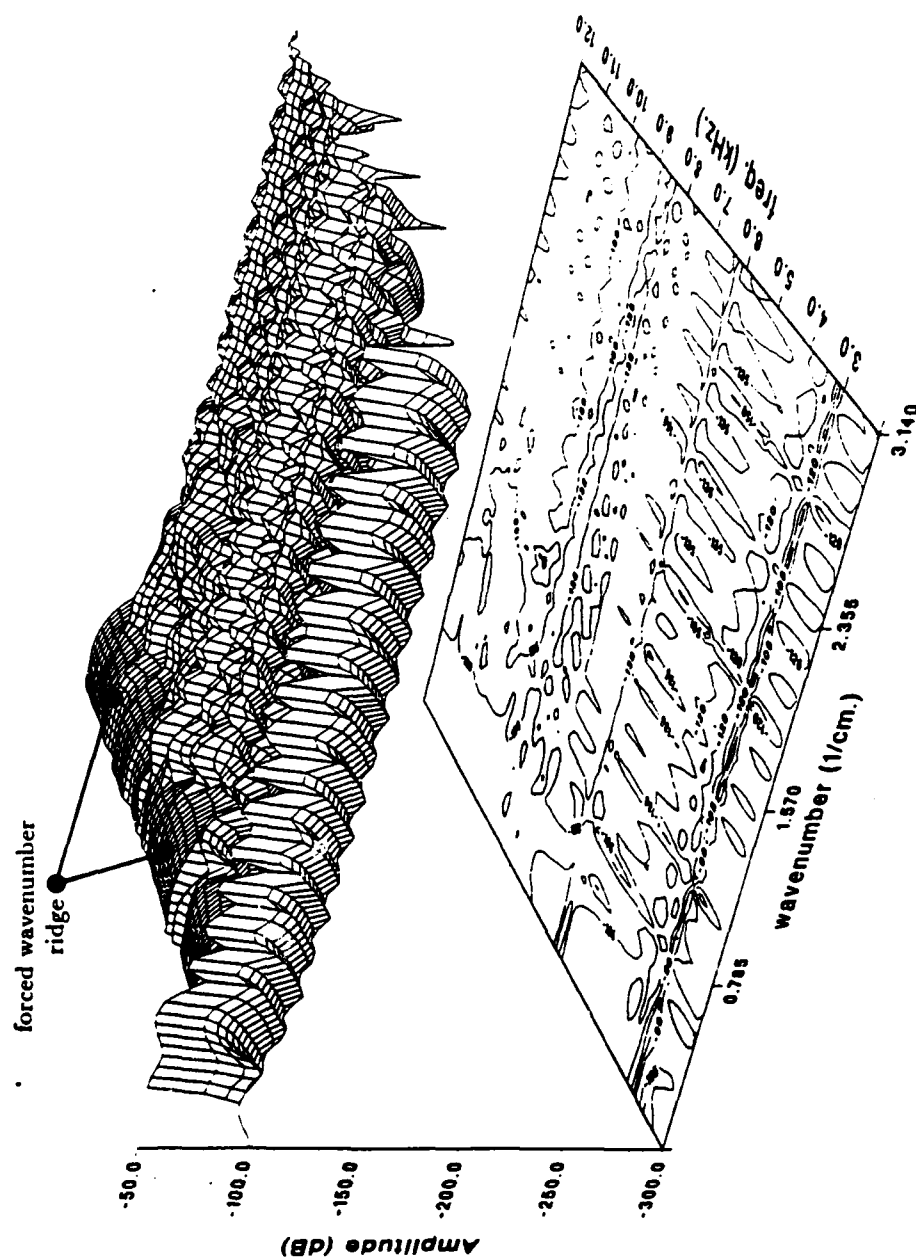


Figure 5.41 Wavenumber-frequency surface-contour plot of the predicted velocity spectrum (spectrum via the continuous transform) for Experiment 6. Velocity relative to  $F_c(\omega)$ .

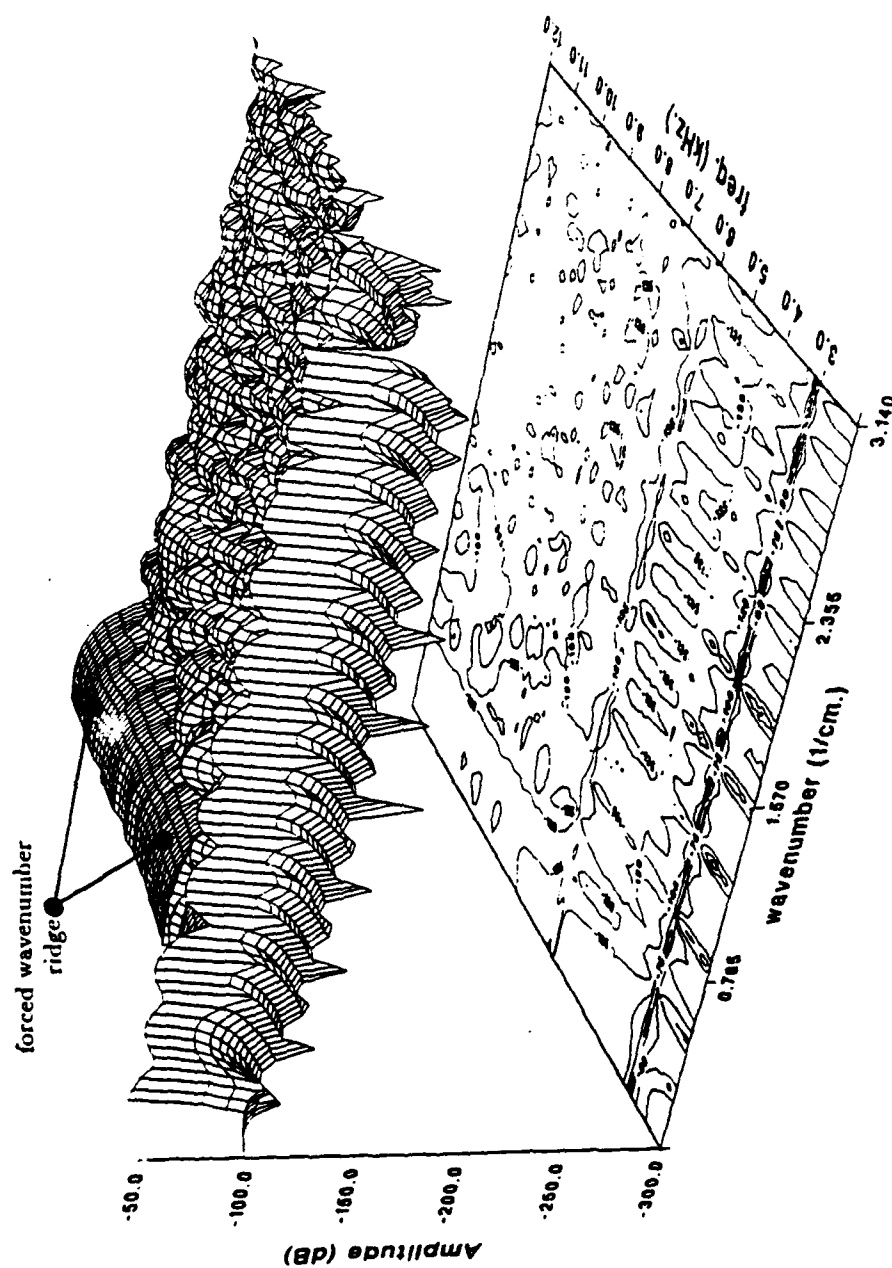


Figure 5.42 Wavenumber-frequency surface-contour plot of the measured velocity spectrum for Experiment 6. Velocity relative to  $F_c(\omega)$ .

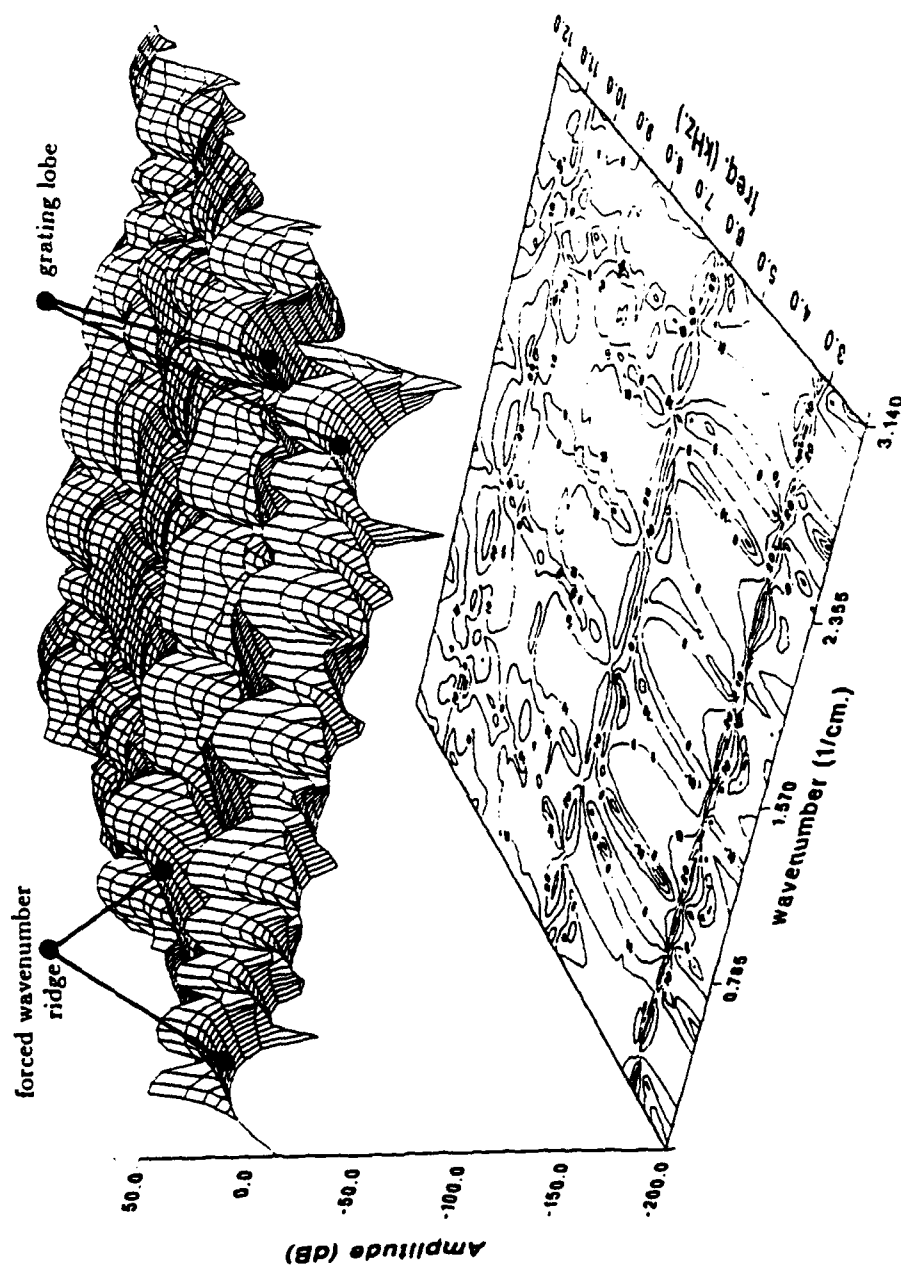


Figure 5.43 Wavenumber-frequency surface-contour plot of the measured force spectrum for Experiment 7. Force relative to  $F_c(\omega)$ .

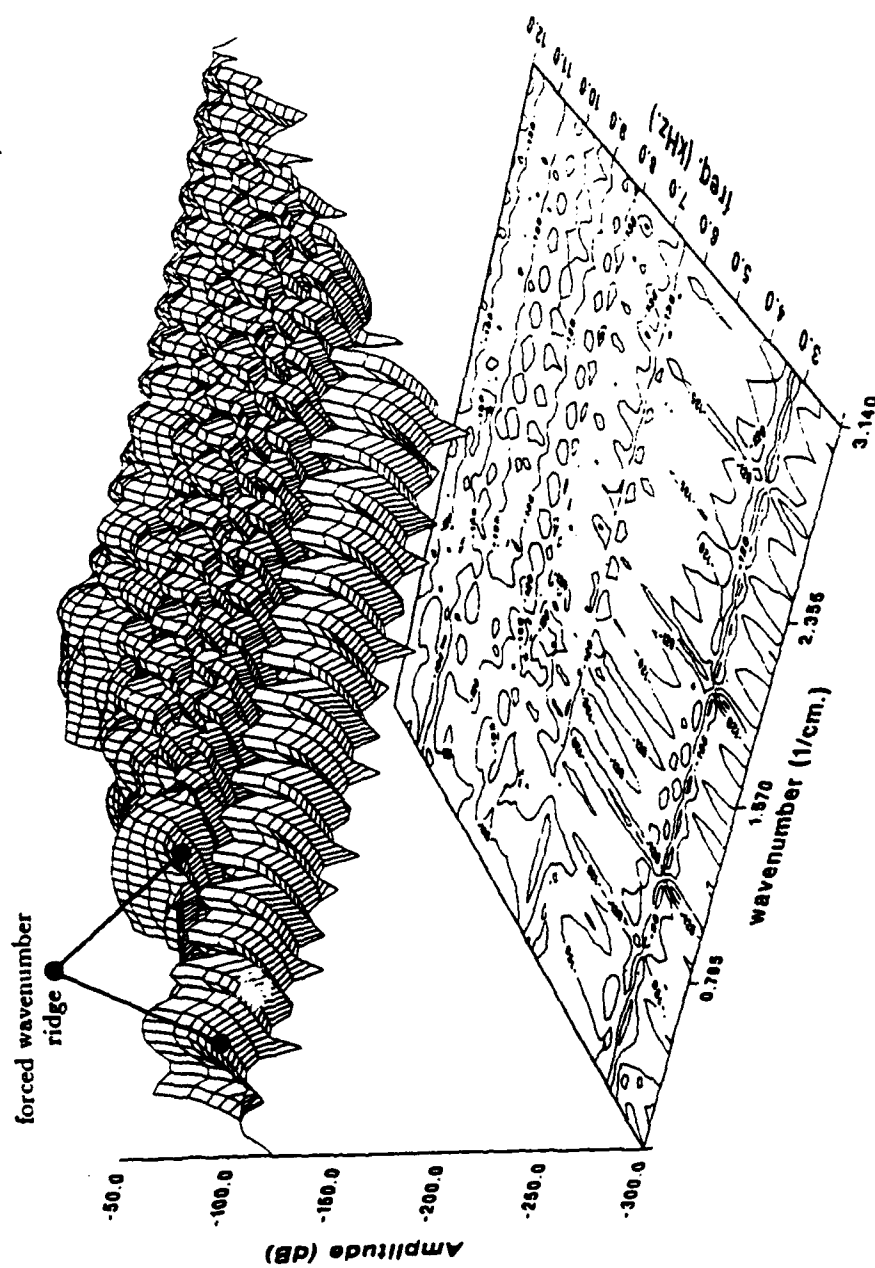


Figure 5.44 Wavenumber-frequency surface-contour plot of the predicted velocity spectrum (spectrum via the continuous transform) for Experiment 7. Velocity relative to  $F_c(\omega)$ .

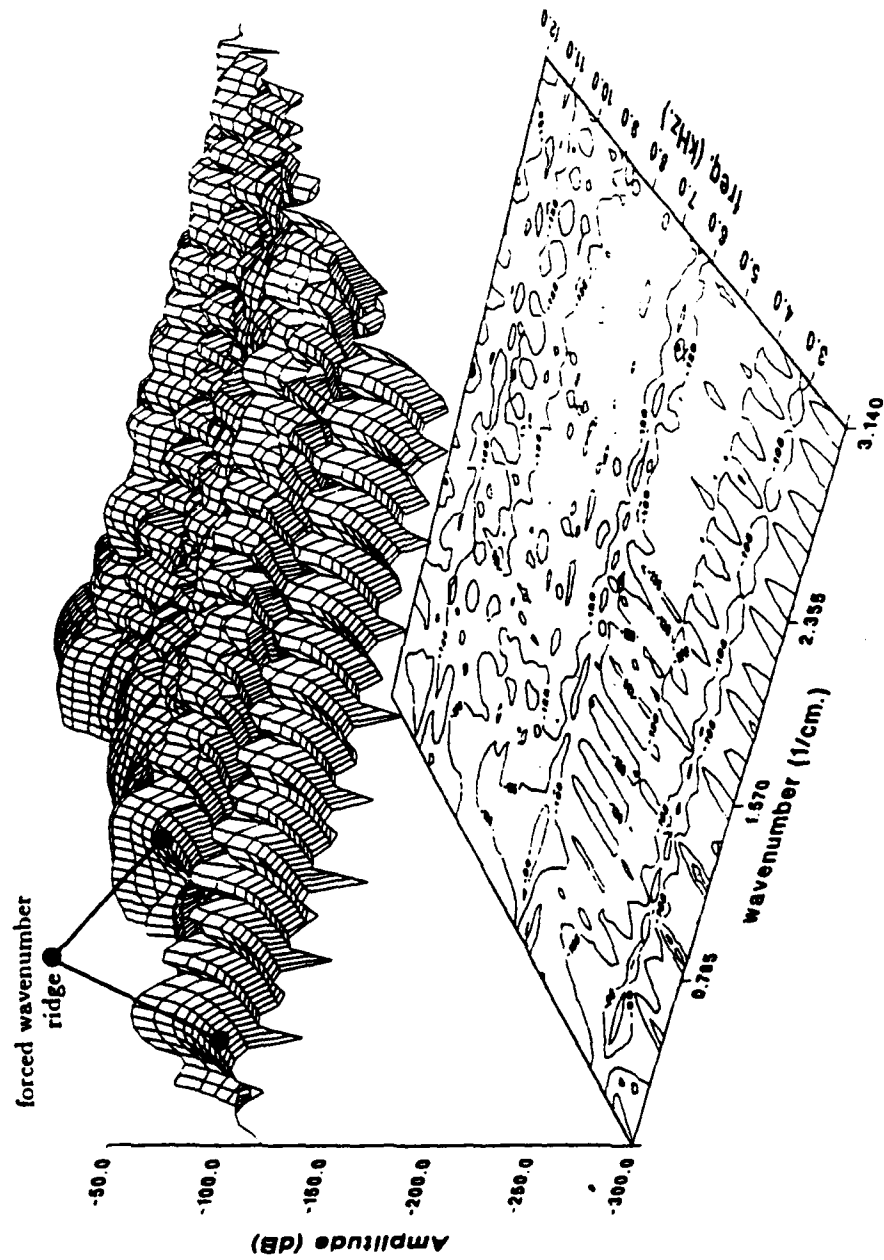


Figure 5.45 Wavenumber-frequency surface-contour plot of the measured velocity spectrum for Experiment 7. Velocity relative to  $F_c(\omega)$ .

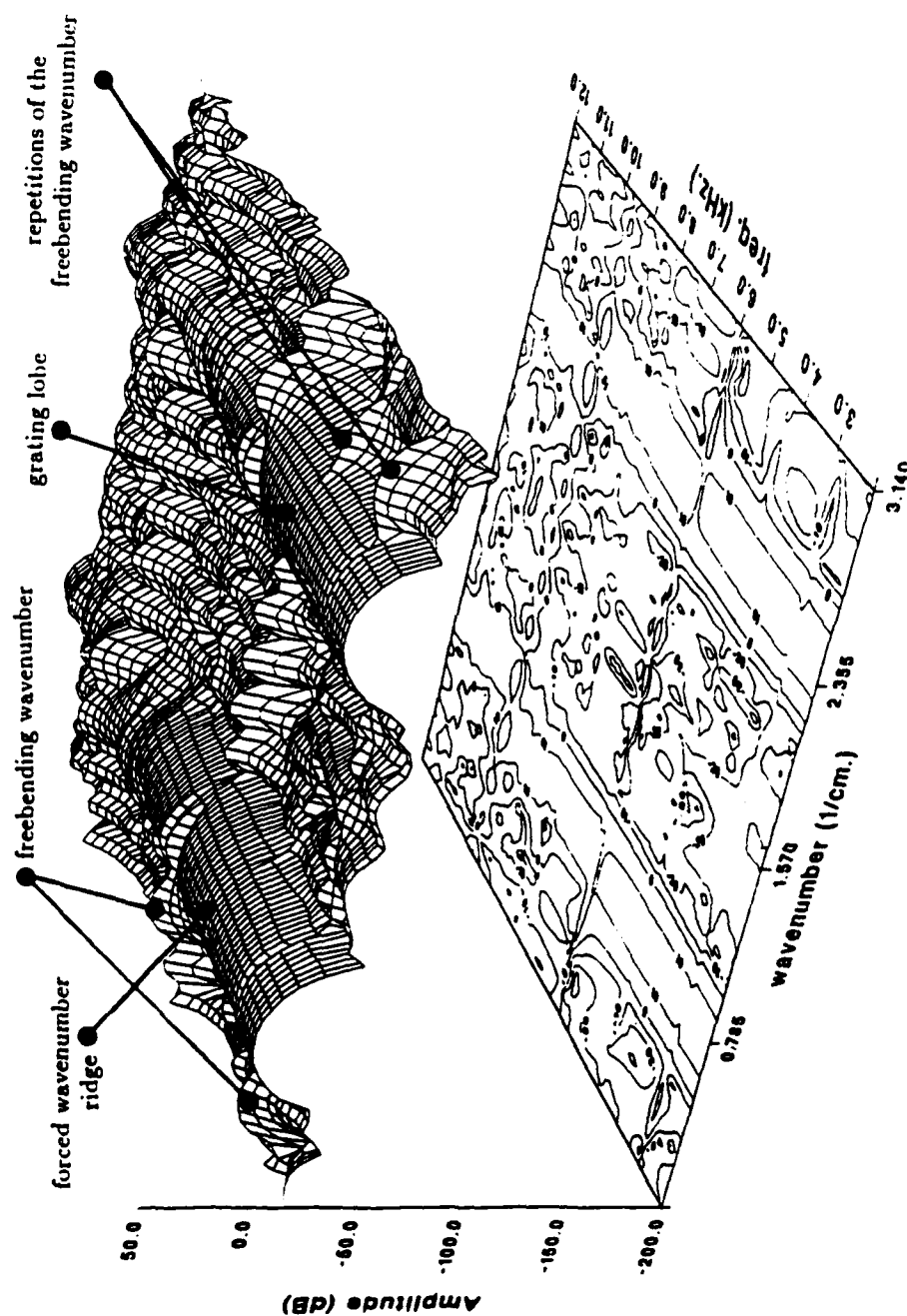


Figure 5.46 Wavenumber-frequency surface-contour plot of the measured force spectrum for Experiment 8. Force relative to  $F_c(\omega)$ .

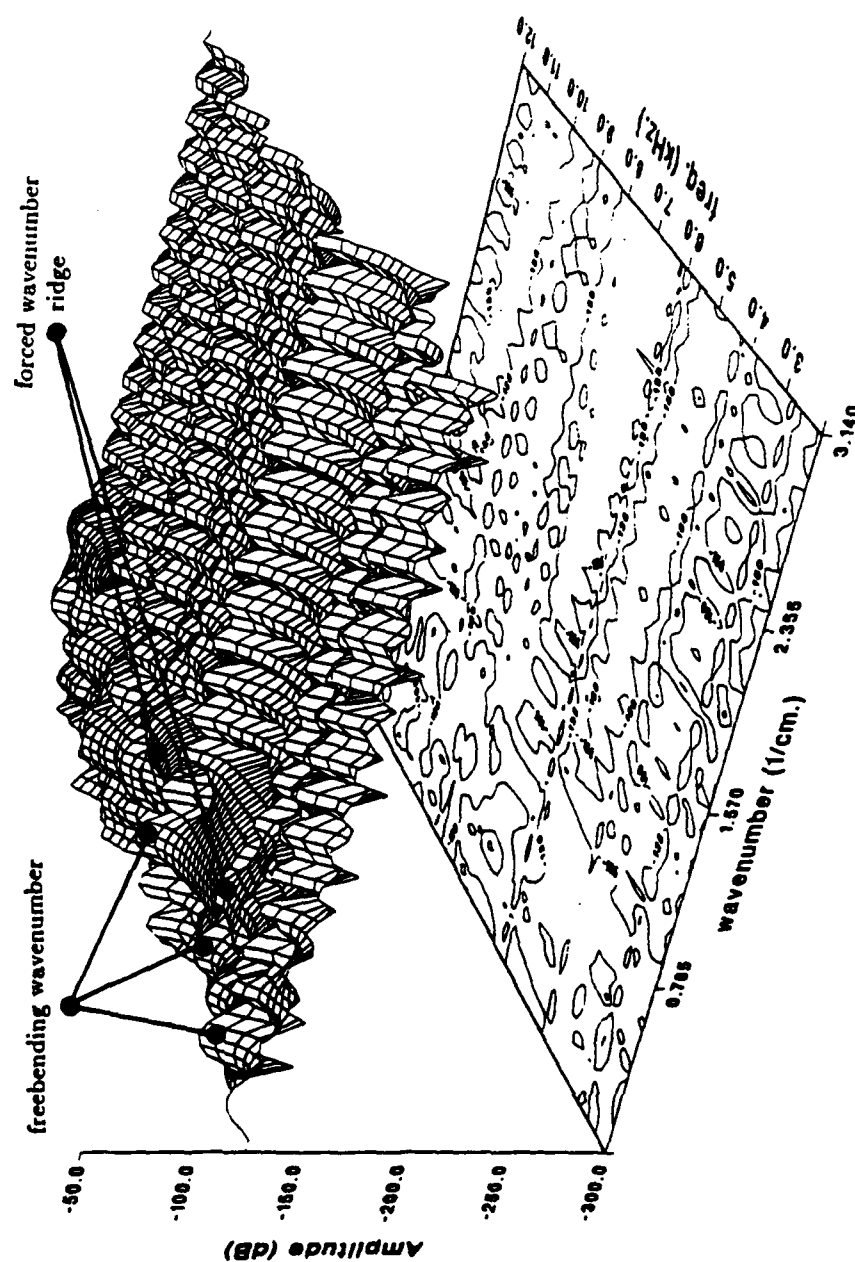


Figure 5.47 Wavenumber-frequency surface-contour plot of the predicted velocity spectrum (spectrum via the continuous transform) for Experiment 8. Velocity relative to  $F_c(\omega)$ .

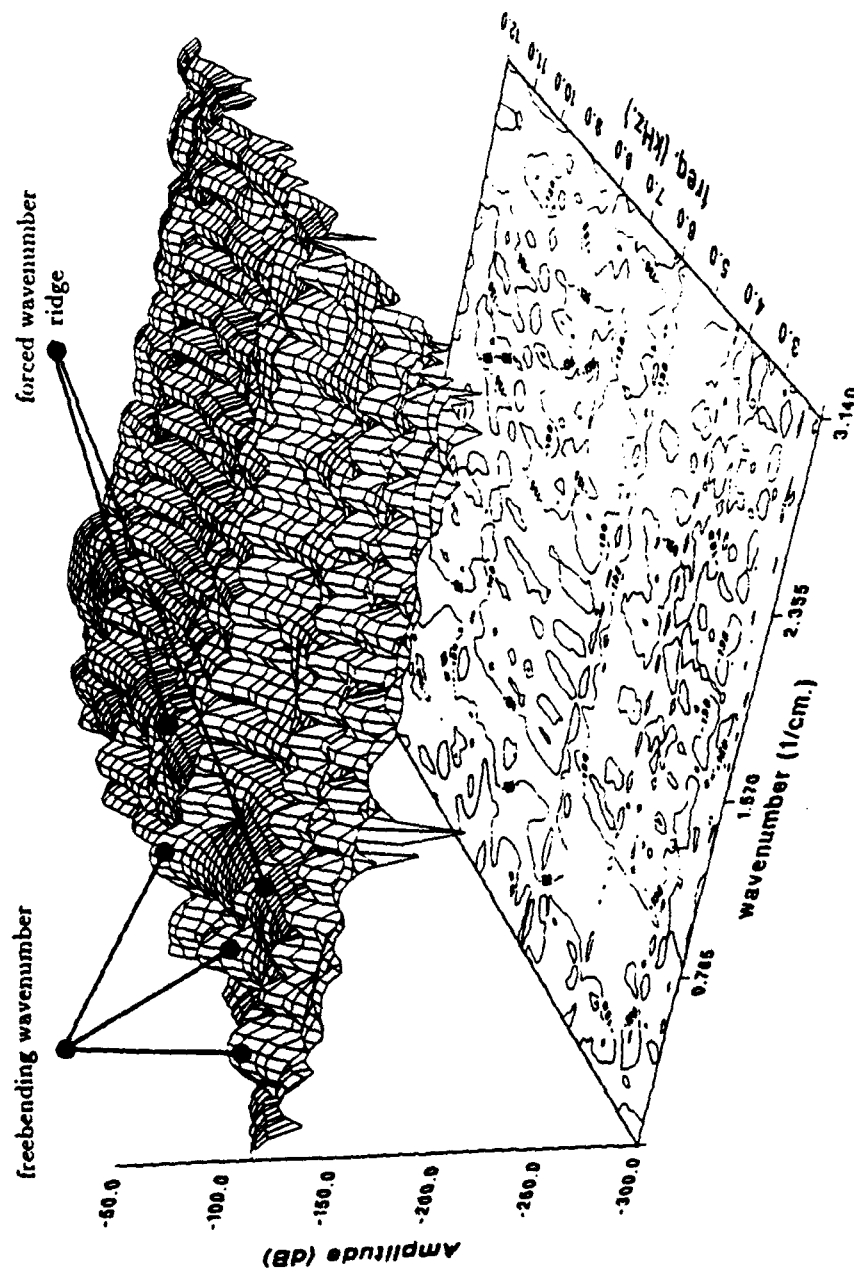


Figure 5.48 Wavenumber-frequency surface-contour plot of the measured velocity spectrum for Experiment 8. Velocity relative to  $F_c(\omega)$ .

the Experiment 8, again the nine shaker experiment seems to have had more success in prescribing a coherent forced wavenumber ridge at  $k_d$  as shown in Figures 5.34 and 5.46. Especially at the higher frequencies (above 9 kHz), the ridge for the seventeen shaker experiment breaks up. The resulting velocity response is characterized by a forced wavenumber ridge that is less coherent than for the nine shaker experiment.

Experiment 9 is unique to the seventeen shaker experiment as the shakers are excited at the Nyquist rate. The peak of the force wavenumber spectrum occurs at  $k_x = \pi/2 \text{ cm}^{-1}$ ; in Figure 5.49 the success in prescribing the drive wavenumber can be seen. Because the drive wavenumber corresponds to a freebending wavenumber at 60 kHz, the main-lobe of the force wavenumber content does not interfere with the freebending wavenumber region. So the influence of the freebending wavenumber along with the periodic repetition of the negative wavenumber branch emanating from  $k_x = \pi \text{ cm}^{-1}$  can be seen on the force wavenumber spectrum. The predicted velocity spectrum display the forced wavenumber ridge beginning at 7 kHz (see Figure 5.50). The measured velocity, presented in Figure 5.51, also shows a ridge at the forced wavenumber, but at higher frequencies. A slice of the predicted and measured velocity surfaces is presented in Figure 5.52 at a frequency of 11.9 kHz. The drive wavenumber for this experiment is the same as the grating lobe for Experiment 1. In the Experiment 1, the measured wavenumber velocity spectrum did not result in any ridge at the high wavenumber, while in Experiment 9, in the absence of the strong low wavenumber velocity field, the high wavenumber variations were detected experimentally.

In summary, several important results were discovered. The ability to steer the wavenumber content of the array of point sources merely by steering the drive

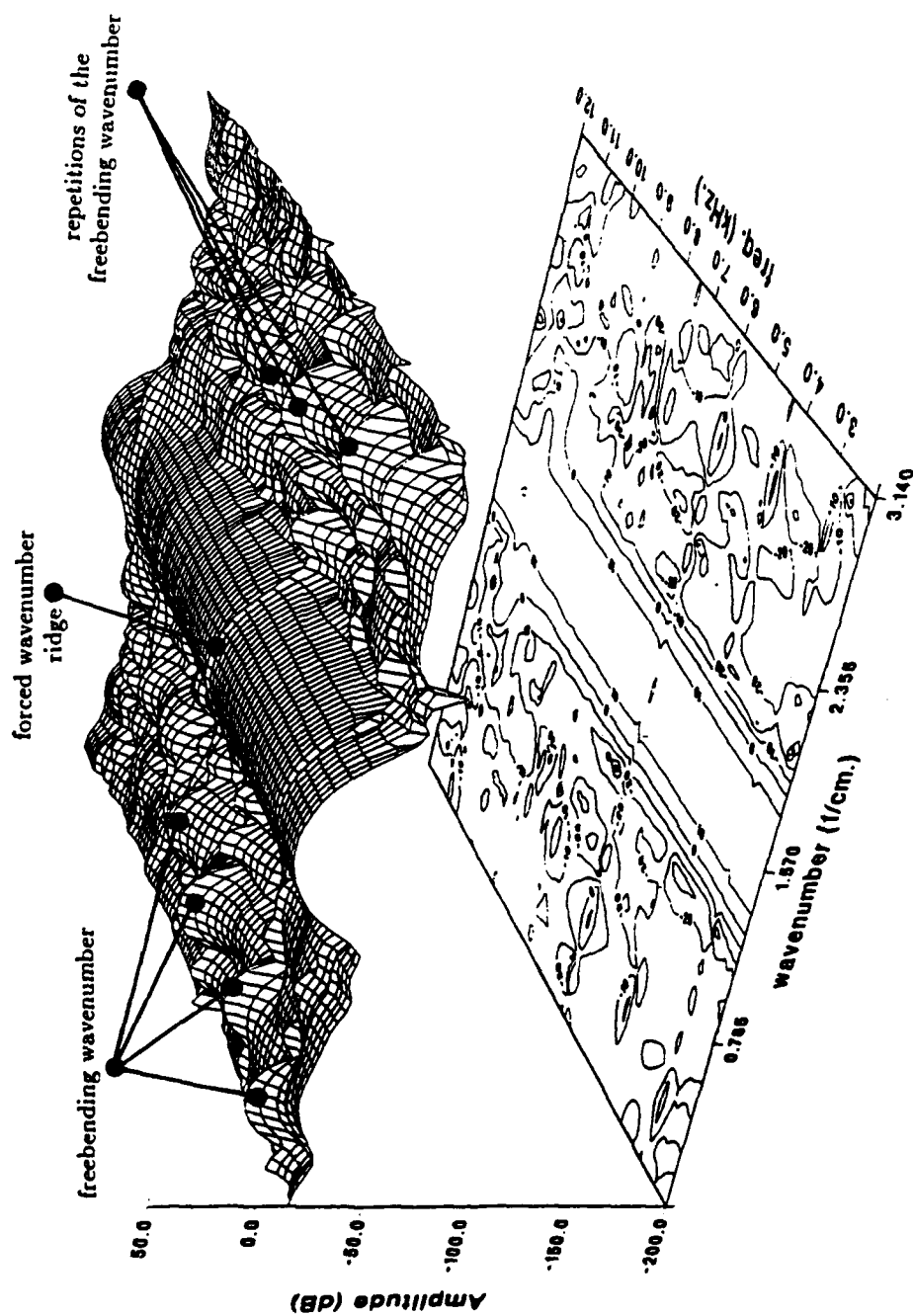


Figure 5.49 Wavenumber-frequency surface-contour plot of the measured force spectrum for Experiment 9. Force relative to  $F_c(\omega)$ .

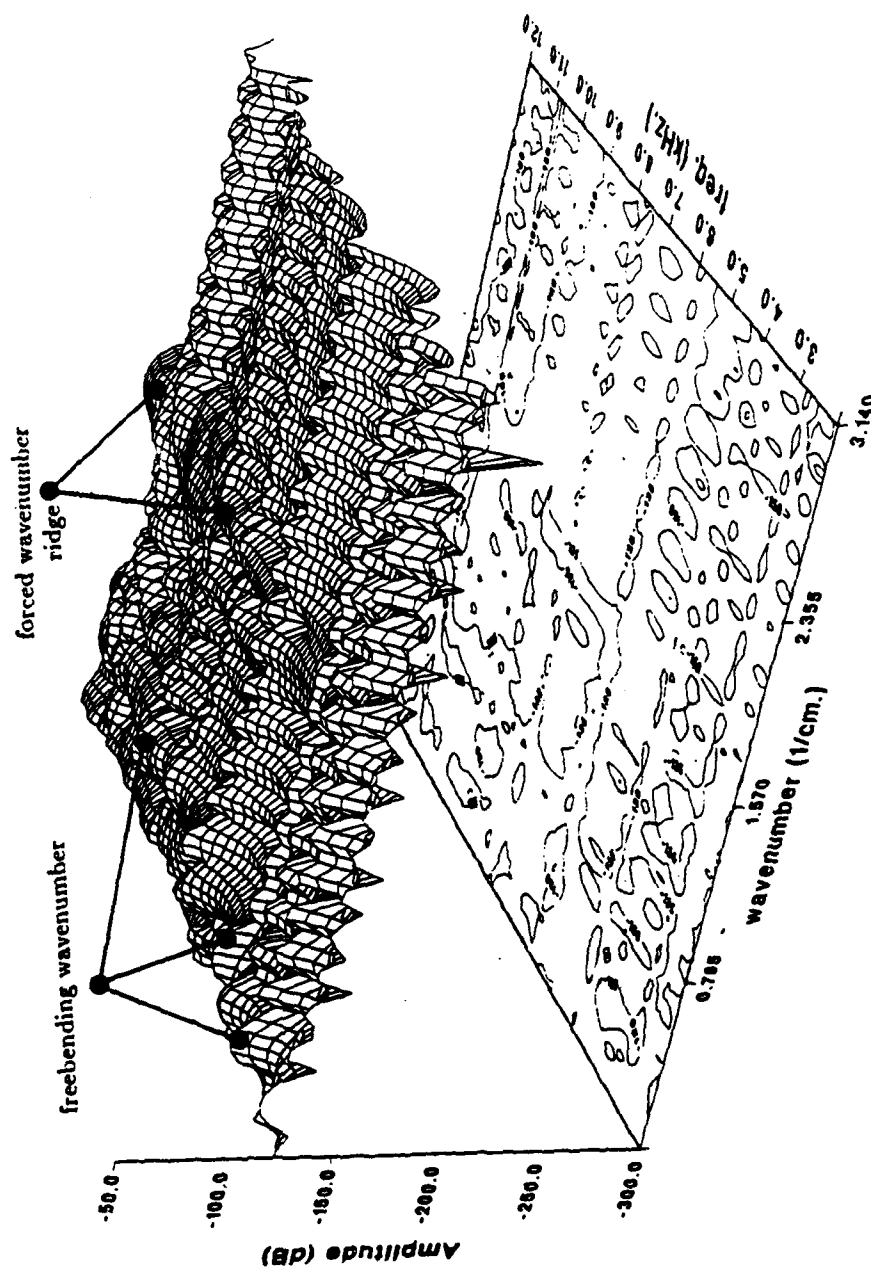


Figure 5.50 Wavenumber-frequency surface-contour plot of the predicted velocity spectrum (spectrum via the continuous transform) for Experiment 9. Velocity relative to  $F_c(\omega)$ .

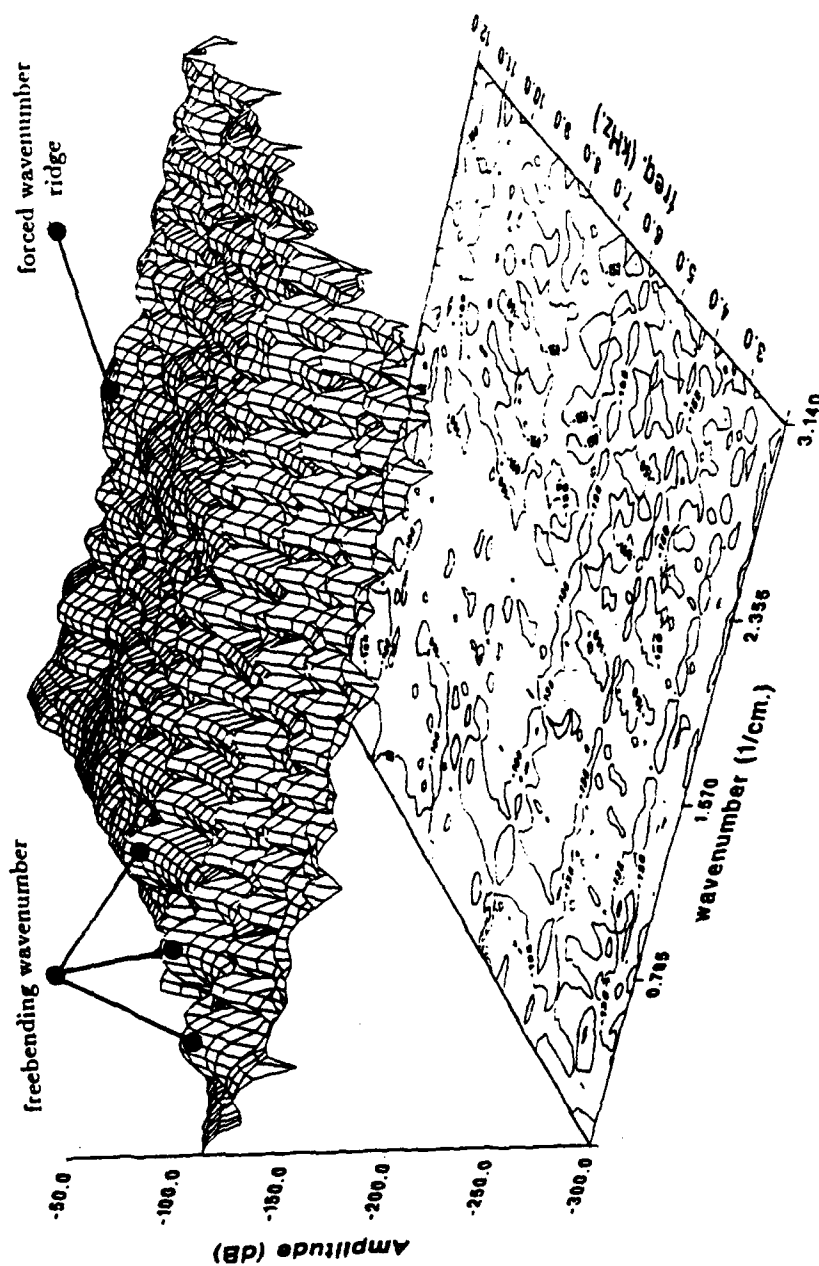


Figure 5.51 Wavenumber-frequency surface-contour plot of the measured velocity spectrum for Experiment 9. Velocity relative to  $F_c(\omega)$ .

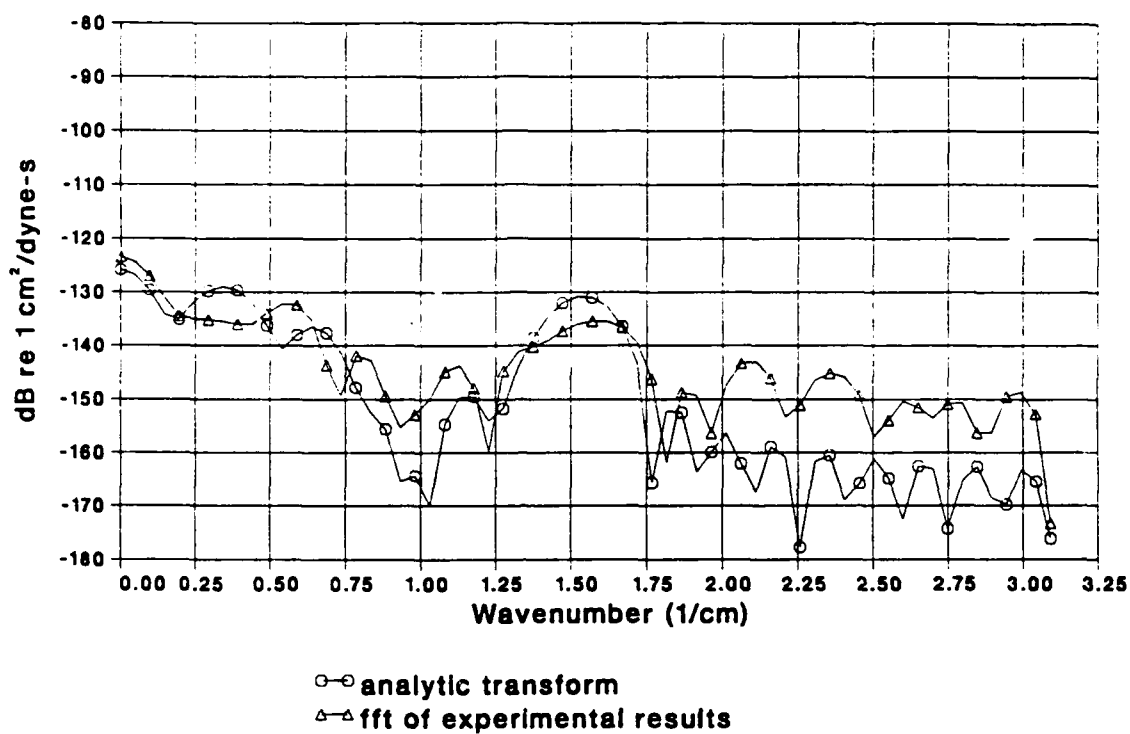


Figure 5.52 Comparison of the magnitude of the predicted spectrum versus the measured spectrum for Experiment 9 at a frequency of 11.9 kHz.

voltages was shown. In general, the velocity spectra in the low wavenumber region was accurately measured. The accuracy of the measurement system (using the theoretical values for comparison) in the high wavenumber region for this system (above  $1.5 \text{ cm}^{-1}$ ) was improved by using an array of shakers to provide excitation concentrated in the high wavenumber region. The ability in Experiment 9 to measure the forced wavenumber ridge while in Experiment 1 the system was not able to measure velocity components at the same wavenumber demonstrates the improved capability.

### 5.5. Relationship between Force and Velocity in Wavenumber Space

In this section, the relationship between the wavenumber-frequency spectrum of the force and that of the velocity field is investigated. The finite beam admittance as defined in Chapter 3 is

$$H_f(k_x, \omega) = \frac{\hat{V}(k_x, \omega)}{\hat{Q}(k_x, \omega)} \quad (5.5)$$

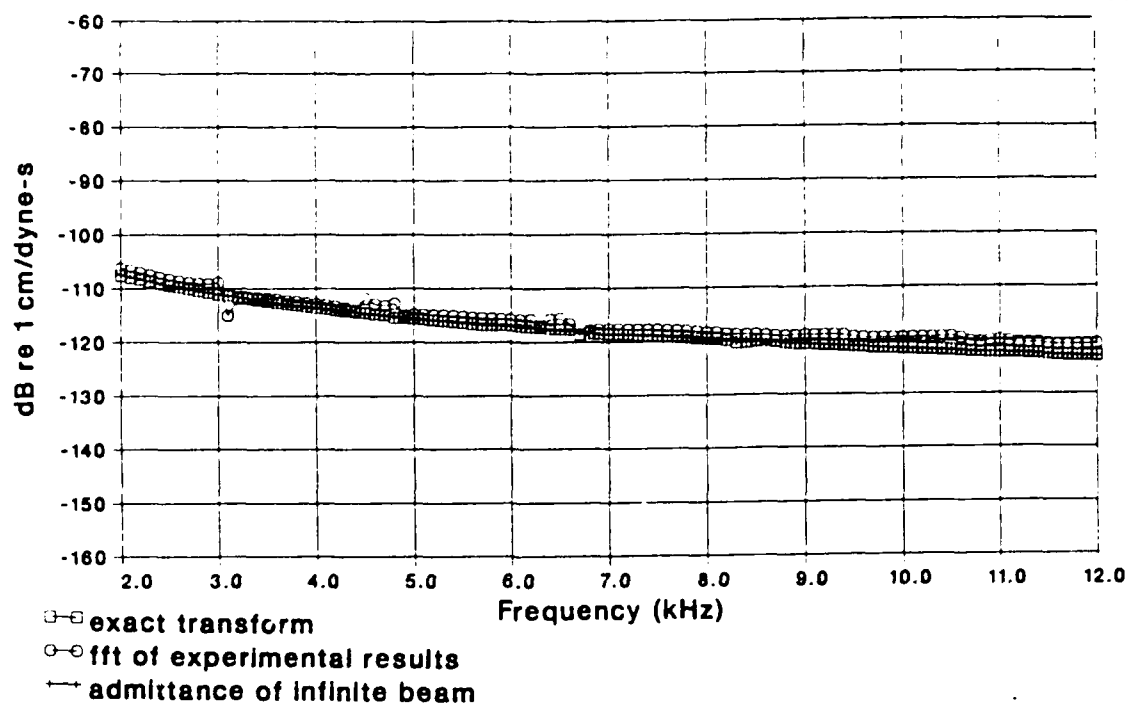
Both the normalized force and the normalized velocity spectra are normalized to the force measured at the center of the beam. The units of this function are those of admittance (centimeters per dyne seconds). The examination of this function centers around the postulation in Chapter 3 that the finite beam admittance should approach the infinite beam admittance when the amplitude of the force wavenumber spectrum is high. To this end, the frequency variation of the predicted and measured finite beam admittances are compared to the infinite beam admittance as a function of frequency at the drive wavenumber. The FORTRAN program COMPARE (see Appendix C), computes the admittance of the various functions at a wavenumber as a function of frequency and plots the results. The wavenumber at which the results are presented corresponds to the bin of the FFT that is closest to the drive wavenumber. The notation on the

plots. "exact transform", indicates that the finite beam admittance is calculated using the analytic Fourier transform solution to the wavenumber velocity.

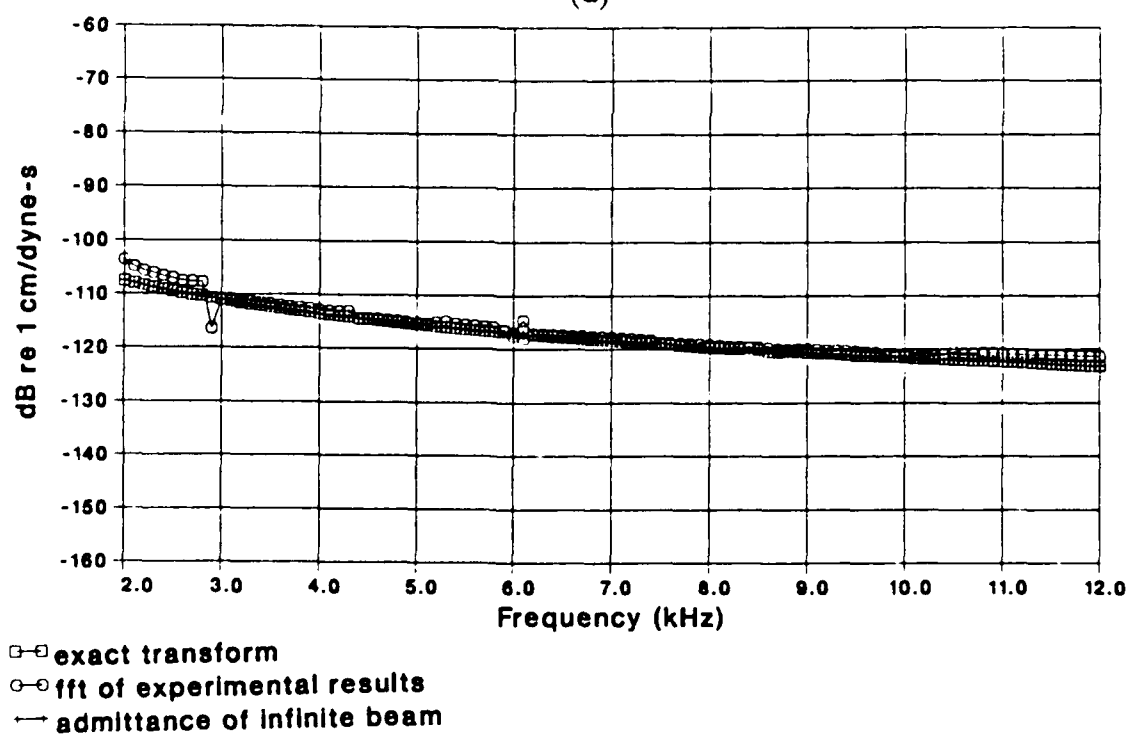
In Figures 5.53a and 5.53b, the three admittances for each of Experiment 1 and 5 are displayed. The drive wavenumber is  $0 \text{ cm}^{-1}$ . All six of the plots are virtually identical. The success in prescribing a high force output at the drive wavenumber resulted in the finite beam admittance being the same as the infinite beam admittance. At the zero wavenumber, the beam acts as a lumped mass and the admittance looks masslike.

The admittance for Experiment 2 and 6 are shown in Figure 5.54a and 5.54b (respectively). For the finite beam admittance a peak is seen around 3 kHz for both the nine and seventeen shaker experiments. This peak occurs at a lower frequency for the seventeen shaker experiment; otherwise the finite beam admittance for nine and seventeen shakers are the same. Note also the excellent agreement between the predicated and measured values for the finite beam admittance. Also, the infinite beam admittance is very close to the finite beam admittance except around 3 kHz. The drive wavenumber for this experiment is  $0.16 \text{ cm}^{-1}$  and the center of the nearest bin of the FFT (for which the data are presented) is  $0.147 \text{ cm}^{-1}$ .

The drive wavenumber for the third and seventh experiments is  $0.332 \text{ cm}^{-1}$ . A freebending wavenumber of the same value occurs around 5 kHz. The admittances are shown at  $k_x = 0.344 \text{ cm}^{-1}$  on Figure 5.55a and 5.55b. The maximum of the infinite beam admittance occurs at the freebending frequency for that wavenumber. The theory and experiment generally agree in the estimation of the admittance for the finite beam. For the finite beam admittance, the first peak in the admittance of the nine and seventeen shaker experiments takes place at nearly the same frequency. The second peak of the finite beam admittance



(a)



(b)

Figure 5.53 Plots of the analytic and experimental finite beam admittance along with the admittance of the infinite beam at  $k_z = 0$  for (a) Experiment 1 and (b) Experiment 5.

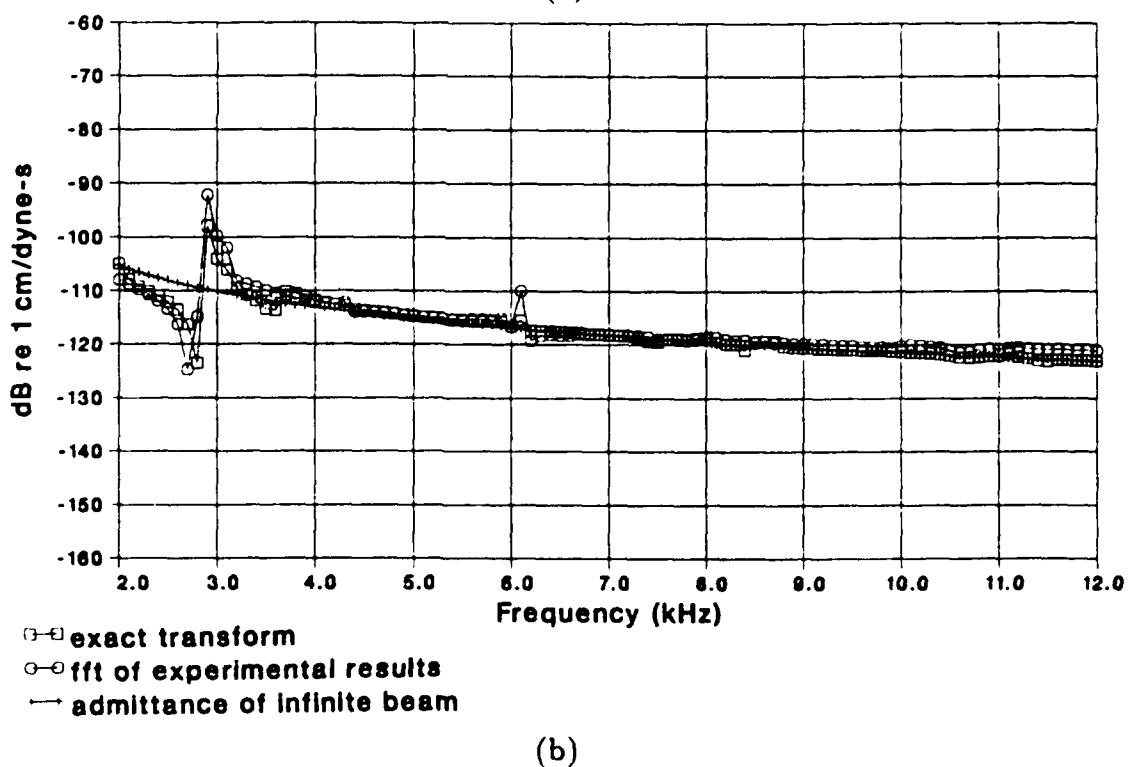
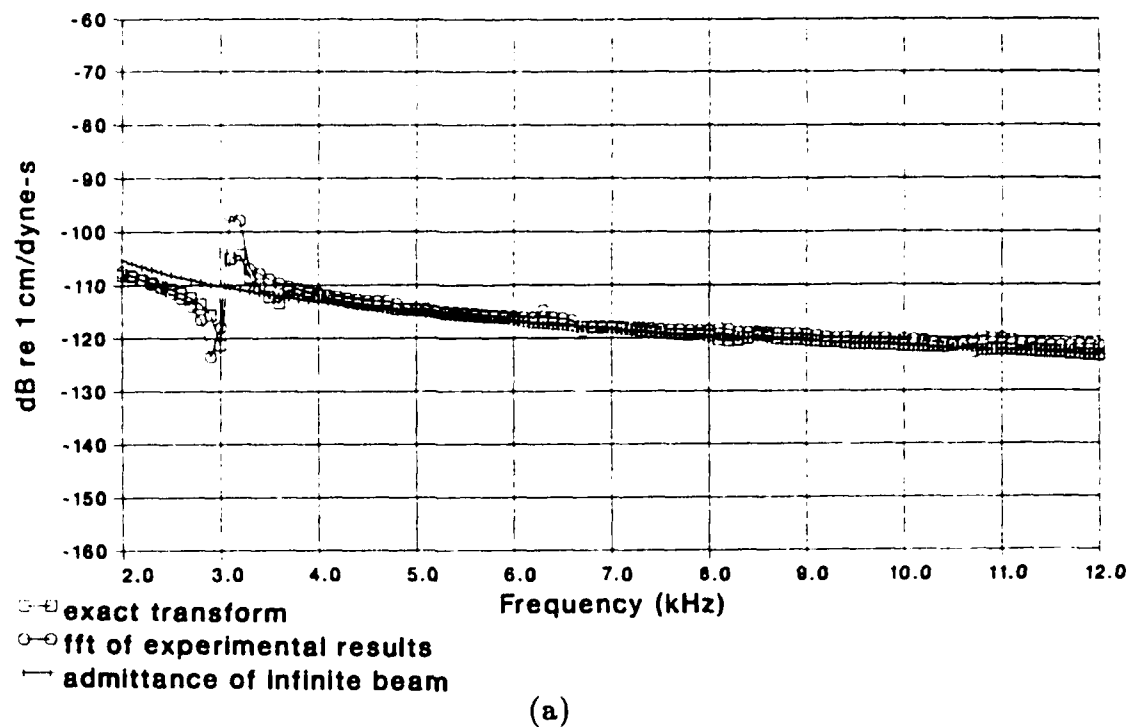


Figure 5.54 Plots of the analytic and experimental finite beam admittance along with the admittance of the infinite beam at  $k_z = 0.147 \text{ cm}^{-1}$  for (a) Experiment 2 and (b) Experiment 6.

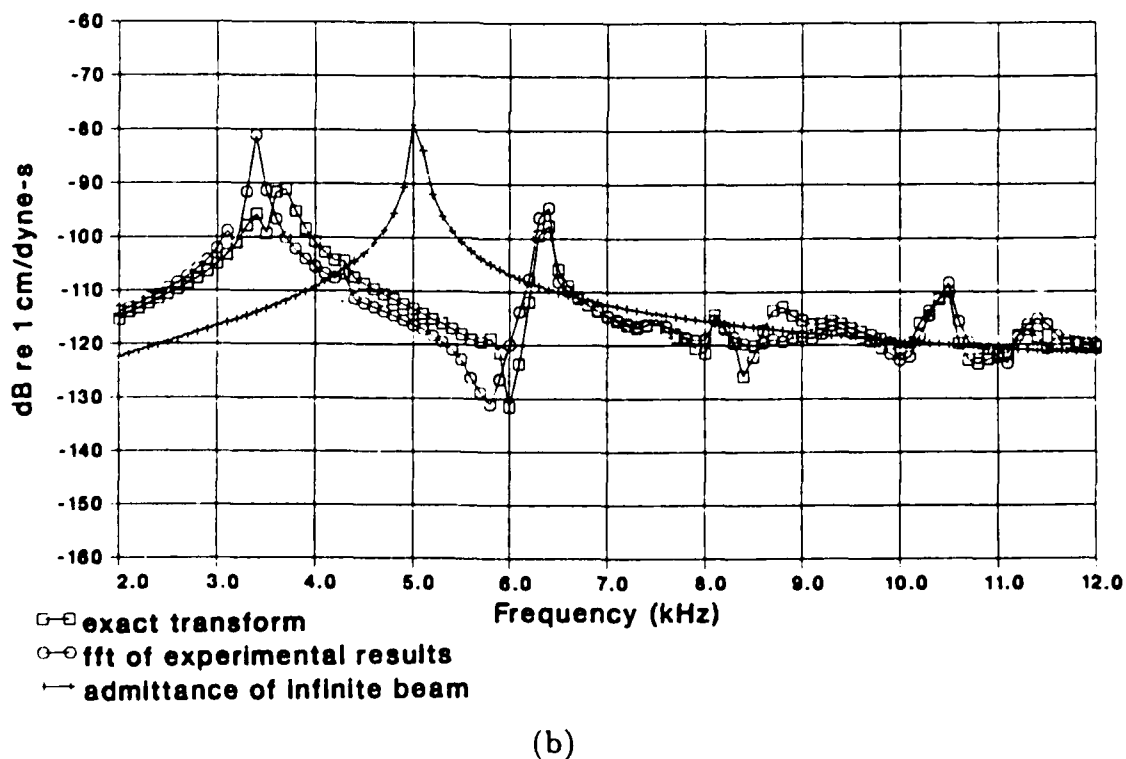
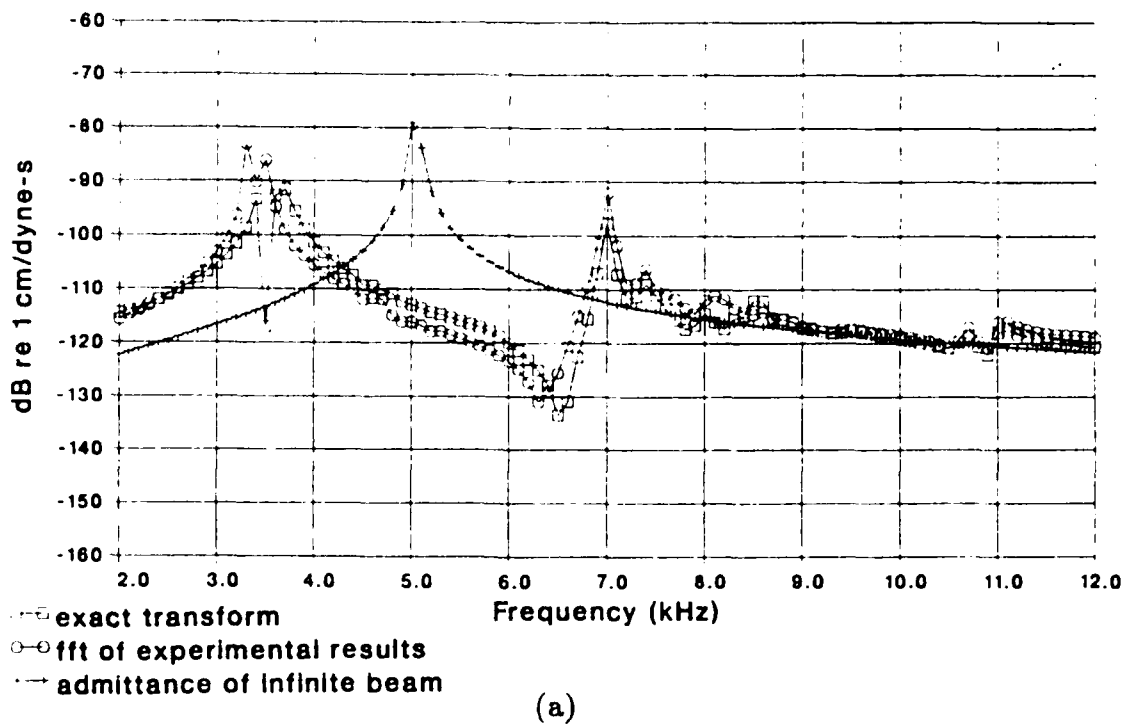


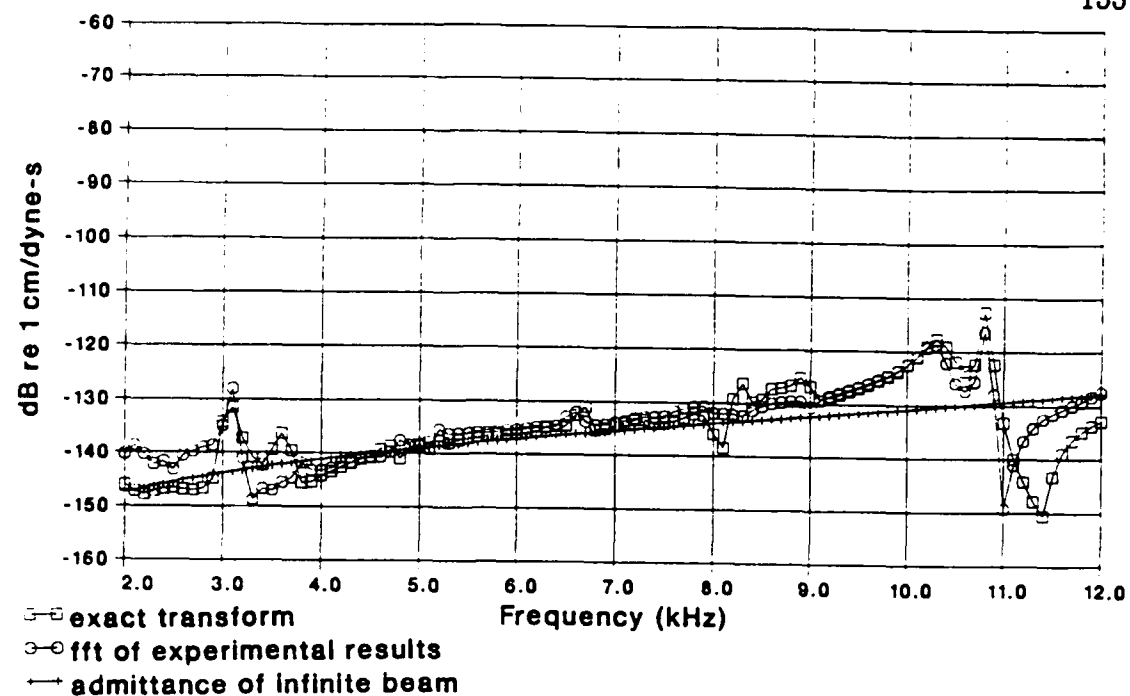
Figure 5.55 Plots of the analytic and experimental finite beam admittance along with the admittance of the infinite beam at  $k_x = 0.344 \text{ cm}^{-1}$  for (a) Experiment 3 and (b) Experiment 7.

for Experiment 7 occurs at a lower frequency than does the second peak for Experiment 3. Above the second peak, the admittances of the finite beam for both experiments collapses to the infinite beam admittance. Recall that the force wavenumber spectrum for these experiments was the least defined and this results in part of the discrepancy. However, further investigation is required to determine what effect the proximity of the freebending wavenumber has on the finite beam admittance.

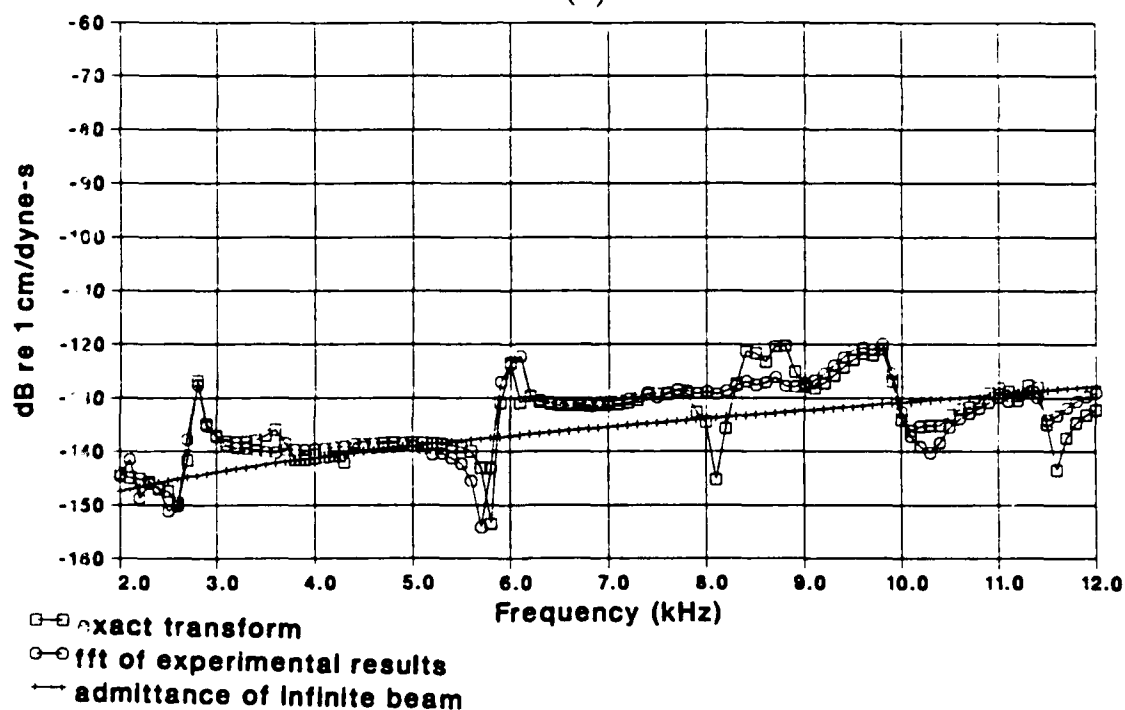
For the nine and seventeen shaker experiments whose drive wavenumber corresponds to 4.5 wavelengths across the length of the beam, the finite beam admittance generally stays close to that of the infinite beam; as pictured in Figure 5.56a and 5.56b. Upon examination of the force wavenumber spectra for both experiments (Figures 5.34 and 5.46), the main-lobe for the nine shaker spectra is better defined and this is probably why the finite beam admittance for this experiment stays closer to the infinite beam admittance.

The finite beam admittance for Experiment 9 is shown in Figure 5.57. There are some fairly large deviations between the predicted and measured values of the finite beam admittance. This is expected as the wavenumber here is  $1.57 \text{ cm}^{-1}$  and at these wavenumbers the measurements are more difficult. Note that the experimental results generally lie below those for the predicted admittance; this may be attributed to the decrease in the sensitivity of the accelerometer at the higher wavenumbers. The finite beam admittances still follow the trend of the infinite beam admittance.

For completeness, similar plots for Experiment 2 at the wavenumber of  $0.69 \text{ cm}^{-1}$  where the magnitude of the force wavenumber spectrum is low are shown in Figure 5.58. The finite beam admittances show no similarity to the infinite beam admittance except perhaps at the higher frequencies.



(a)



(b)

Figure 5.56 Plots of the analytic and experimental finite beam admittance along with the admittance of the infinite beam at  $k_z = 0.74 \text{ cm}^{-1}$  for (a) Experiment 4 and (b) Experiment 8.

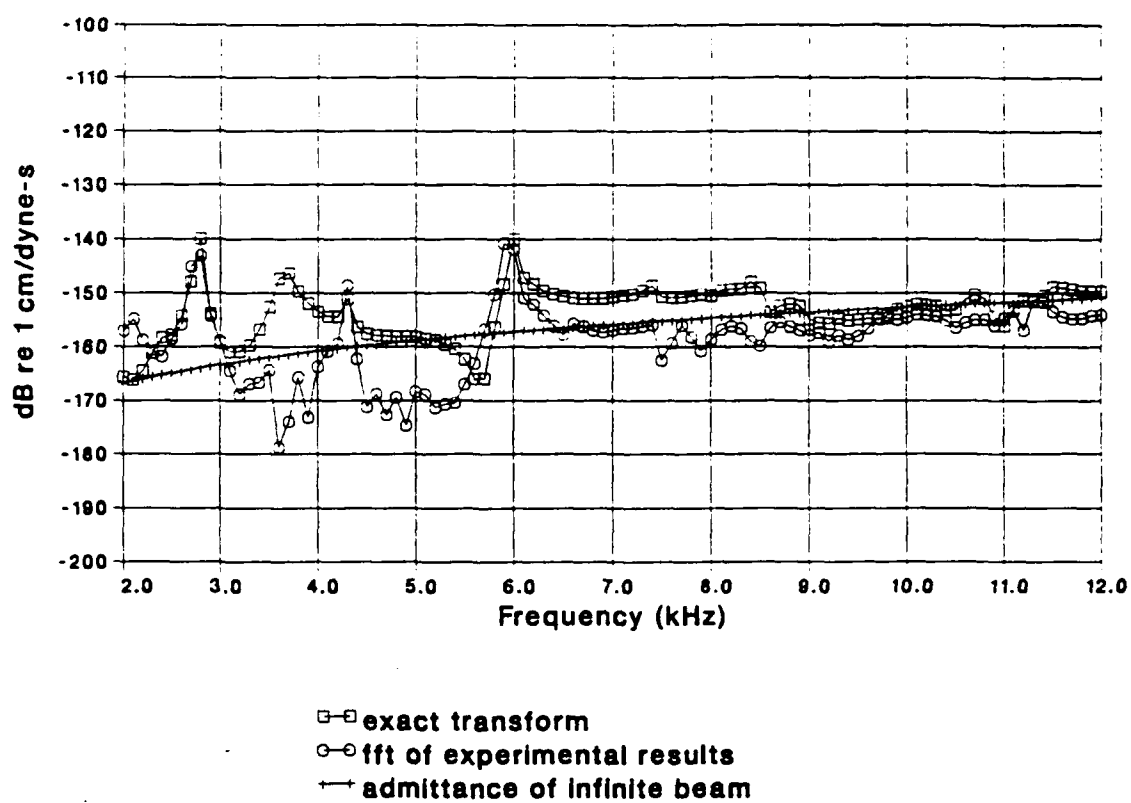


Figure 5.57 Plot of the analytic and experimental finite beam admittance along with the admittance of the infinite beam at  $k_x = 1.57 \text{ cm}^{-1}$  for Experiment 9.

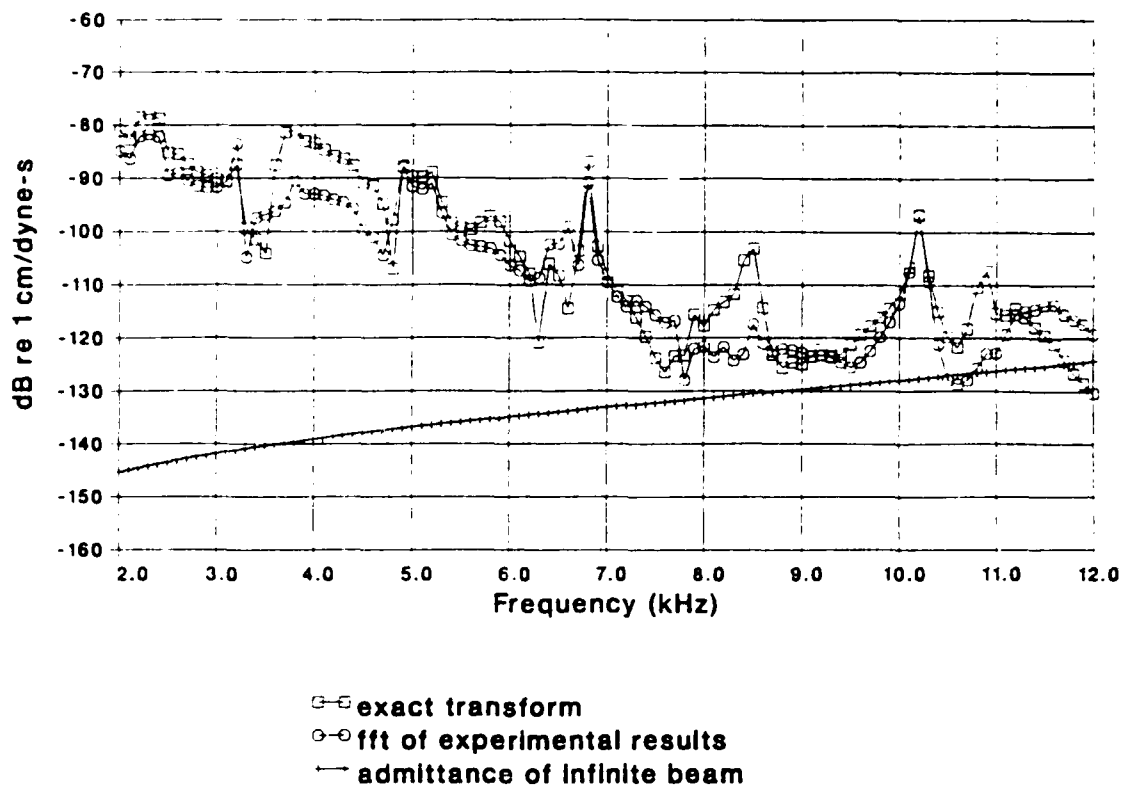


Figure 5.58 Plot of the analytic and experimental finite beam admittance along with the admittance of the infinite beam at  $k_x = 0.69 \text{ cm}^{-1}$  for Experiment 2.

The postulation has been made that the finite beam admittance should approach the infinite beam admittance at a wavenumber where the force amplitude is high. The analysis and results presented in this section certainly point in this direction.

## CHAPTER 6

### CONCLUSIONS AND RECOMMENDATIONS

#### 6.1. Conclusions

In this thesis, the experimental and theoretical aspects of exciting and measuring the wavenumber-frequency spectrum of a finite structure have been examined. A system that steers the force amplitude of an array of shakers to a particular wavenumber have been developed. The response of a free-free beam to this excitation have been measured experimentally and predicted theoretically. Experiment and theory have been shown to match very well, both in point transfer admittances and in the comparison of wavenumber spectra. The relationship between the wavenumber dependence of the force and the velocity have been examined and cast in terms of the finite beam admittance. The finite beam admittance have been shown experimentally to approximate the infinite beam admittance in regions of wavenumber-frequency space where the force amplitude is high. Also, in these regions the finite beam admittance for experiments using nine shakers and seventeen are nearly the same.

In order to measure the relation between the force and the velocity, one must be reasonably sure that it is the actual force and velocity spectra that are being measured. Hence, it have been a major emphasis of this study to understand the means by which the two quantities has been measured. To this end, the wavenumber sensitivity of an array of sensors has been developed. The effects of using different types of measurement arrays has been examined. Equivalent circuit modeling has been used both to predict the overall response and the output of the shaker/force gage. The predicted force output and force gage sensitivity have been shown to be commensurate with the measured values. These predictions have been a used as a check on the validity of the measurements and

the calibration procedure.

## 6.2. Recommendations

Further theoretical and experimental study into the relationship between the wavenumber-frequency content of the force and the velocity spectrum is indicated. A more complete analysis of the results of Section 3.6 would yield a theoretical model for analysis of any possible exceptions to the empirical observations made relating the force to the velocity. Also, further examination of the data obtained in this thesis would aid in this analysis.

This method of force excitation and velocity measurement could be applied to structures coated with compliant layers. By using the measurement system, the filtering action of these coatings might be parameterized. Hence, this system could be a useful tool in the better design of compliant layers.

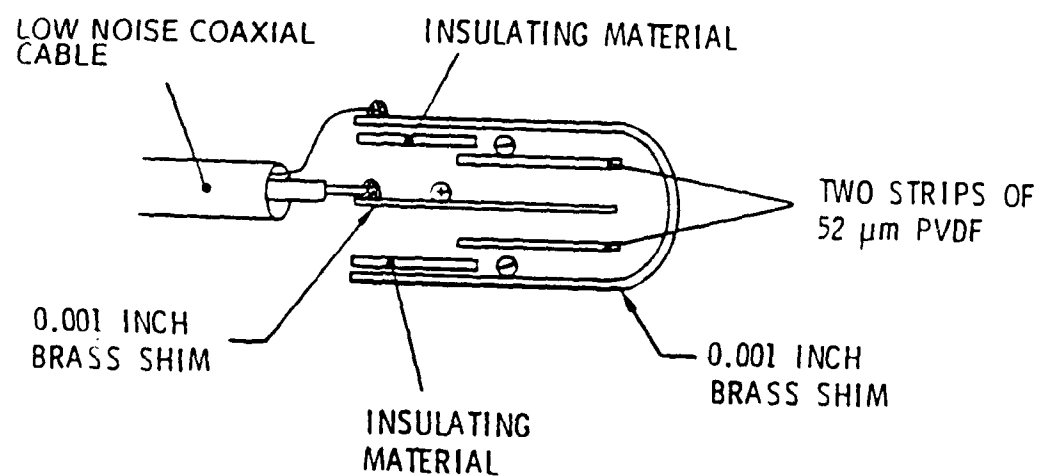
Finally, the use of other spectral estimation methods in examining the response of the structure would be useful [26]. By using so-called high resolution methods (e.g., maximum likelihood, maximum entropy and the extended Prony methods), the individual mode shapes might be resolved. With this information, the relation between the force and velocity would become more straightforward.

## APPENDIX A

### PVF-2 FORCE GAGE DESIGN

A schematic of the force gage design using PVF-2 as the piezo-active component is shown in Figure A.1. This design proved to be mechanically unsuitable. Upon repeated attachment and removal from the structure, the force gage would delaminate. This problem motivated the use of the PZT-4 force gage which is more sturdy.

The components and their dimensions are shown in Table A.1. The force gage is constructed in the following manner. First, two pieces of PVF-2 are sandwiched around the inner brass shimstock (which is the positive lead). The surface of positive polarity of each of the pieces of piezo-film are glued facing each other toward the inner brass using Devcon five-minute epoxy. Next, the longer and wider strip of brass shimstock is folded in half. The sandwiched combination is inserted into the the now folded outer brass shield. At this point, the area over the PVF-2 is glued to the outer brass shield and held in a vise while a bend is made at the point 1.27 cm from the fold point of the outer brass. This bend allows for the force gage to fit nicely over the headmass of the shaker. After this gluing is complete, the center conductor of a low noise coaxial cable is soldered to the inner brass shimstock. This is the positive electric terminal. The exposed positive connection (the combination inner brass shimstock and coaxial cable) is covered by flexible insulating material. The outer brass is then glued to the insulating material. Finally, the shield wire of the coaxial cable, which has been dressed back, is soldered or glued using conductive epoxy to the outer brass shimstock.



- TRANSDUCER THICKNESS OVER ACTIVE AREA  $\cong 0.010$  INCH

Figure A.1 Schematic of the PVF-2 force gage design.

Table A.1 Materials used in PVF-2 transducer.

Description of Section	Material	Dimensions (cm) length x width x thickness
Outer shield	Brass shim	3.49 x .4 x .00254
Force cell	PVF-2	1.43 x .35 x .0052
Positive lead	Brass shim	1.75 x .3 x .00254
Flexible insulation	Kapton	cut to size

The PVF-2 may be cleaned using a Freon based solvent. The other components of the force gage are cleaned before gluing using the procedures mentioned in Chapter 2.

The force gage is glued to the top of the headmass. The force gage/shaker is then glued to the test structure. Initially, the force gage sensitivity (measured using the same procedure as in Section 2.3.4) amplitude and phase was very flat as a function of frequency. However, as the force gage was removed and re-attached to the structure, the sensitivity was altered. It was obvious upon inspection, the the force gage layers were becoming unglued and the force gage was rendered useless.

## APPENDIX B

### MASS LOADING OF THE FORCE GAGE

In this appendix, the manner by which the effect of the mass below the force gage may be removed from the measured data is presented. There are three quantities which require the mass loading effect to be removed, the drive point admittance, transfer admittance and the normalized force measurements. The mass loading effect causes an error in the force measured by the force gage, as described in Chapter 4. Essentially, the force applied to the structure differs from that measured by the force gage by the impedance of the mass loading times the velocity at that point. The results are presented in the same order as the algorithm used to correct the errors must be written. This is because the first result is used to correct the second mass loaded quantity and the second to correct the third.

The first quantity examined is the measured drive point admittance at the center of the beam, denoted as  $\hat{A}_c$ . Note that all quantities are understood to be functions of frequency,  $\omega$ . The measured drive point admittance in the center is,

$$\hat{A}_c = \frac{v_c}{F_c + Z_L v_c} \quad , \quad (B.1)$$

where  $Z_L = j\omega M_L$ ,  $F_c$  is the force applied to the structure at the center of the beam, and  $v_c$  is the velocity measured at the center of the beam. The quantity  $M_L$  is known from the analysis of Section 4.4. The denominator of Equation (B.1) is the measured force. The desired quantity is  $A_c$  the velocity divided by the force applied to the structure.  $A_c$  is related to the measured quantity by,

$$A_c = \frac{v_c}{F_c} = \frac{\hat{A}_c}{1 - Z_L \hat{A}_c} \quad . \quad (B.2)$$

From this equation it can be seen that if the product of the measured admittance of the beam and the impedance of the mass loading is much less than one, the

measured and the actual admittance are the same. This product will generally be much lower than one for the beam and the shaker used in this thesis.

The second quantity of interest is the measured transfer admittance,  $\hat{A}_i$  or,

$$\hat{A}_i = \frac{v_i}{F_c + Z_L v_c} \quad , \quad (B.3)$$

where  $v_i$  is the velocity at the  $i$ th location. The actual transfer admittance,  $A_i$  is

$$A_i = \frac{v_i}{F_c} = \frac{\hat{A}_i}{\hat{A}_c} A_c \quad , \quad (B.4)$$

where both the measured and corrected drive point admittances have been used in the correction of the transfer admittance.

The final quantity to be corrected is the normalized force measured at each of the shakers,  $\hat{F}_i^N$ ,

$$\hat{F}_i^N = \frac{F_i + Z_L v_i}{F_c + Z_L v_c} \quad . \quad (B.5)$$

The desired quantity is  $F_i/F_c$  or  $F_i^N$  which is obtained using the previous correction for  $\hat{A}_i$ . The corrected normalized force is

$$F_i^N = [\hat{F}_i^N / \hat{A}_c - Z_L] A_i \quad , \quad (B.6)$$

which may be verified by substitution.

In Figure B.1, the difference between the corrected and uncorrected drive point admittance is shown for Experiment 3. This experiment was chosen because the admittance of the beam rises above the admittance of the mass loading. This means that the product of the beam admittance and the mass impedance will be around one. The plot shows that only when beam admittance is above the mass loading line does the corrected admittance vary from the measured. However, the general trend of the data is not significantly altered for the purposes of this study. Hence, the mass correction algorithm has not been implemented to correct the entire data set.

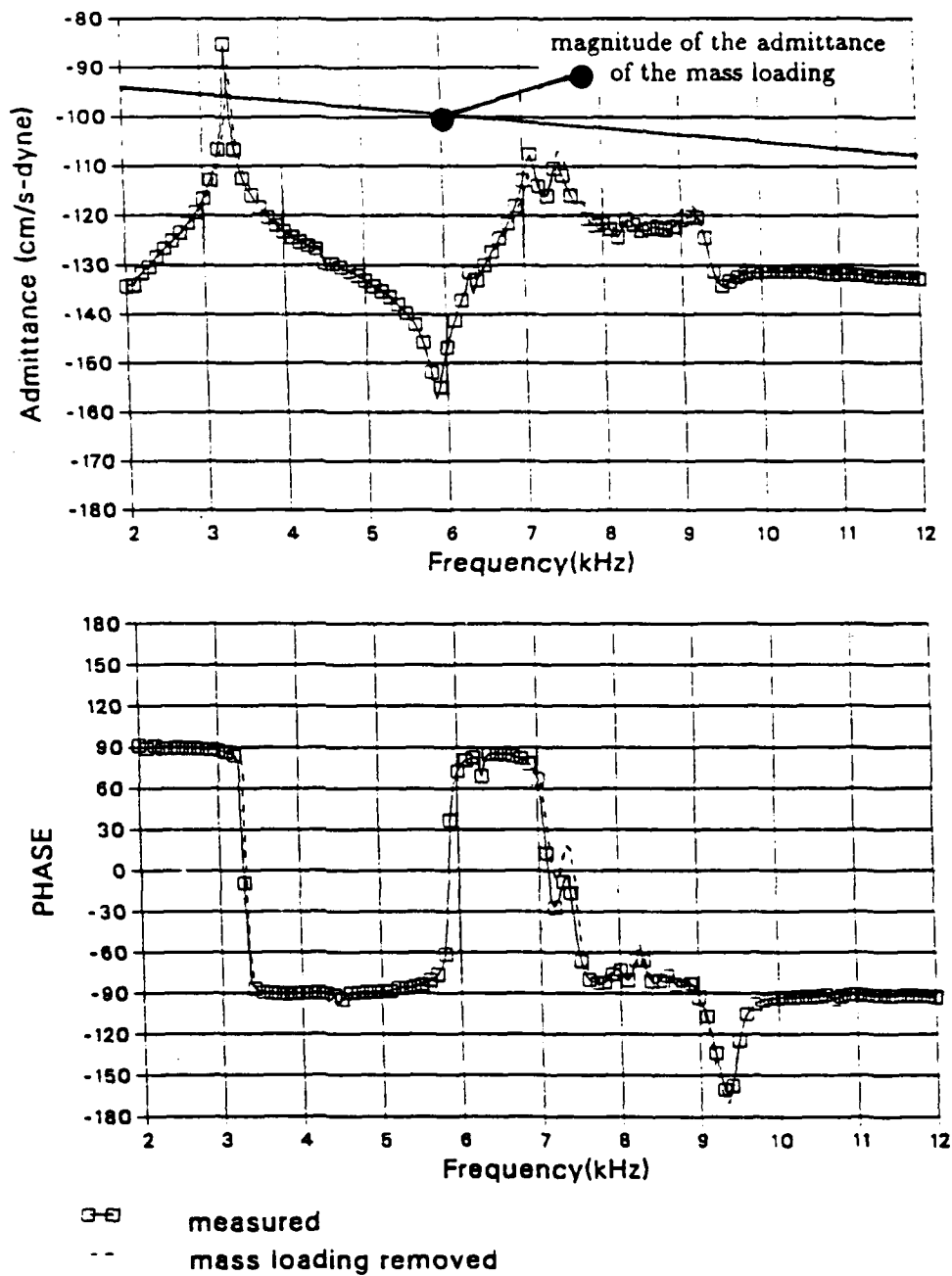


Figure B.1 Measured versus corrected driving point admittance for Experiment 3 at the center of the beam.

## APPENDIX C

### CITED COMPUTER CODE

In this appendix, the computer code cited in the text of the thesis is listed in order of citation. The first program listed is FORCE\_FILTER.

```

1      PROGRAM Force_Filter
2 c... This program caculates the weighting coefficients for the
3 c... drive voltages.
4      CHARACTER *20 name
5      REAL PLT(512),PHS(512)
6      COMPLEX W(512),etap(100)
7      COMPLEX WW(256),SUM,c_i
8      c_i = (0.0,1.0)
9      pi = 3.141592654
10     beam_length = 37.9
11     NUM_WAV = 128
12 c... input location for the number of shakers.
13 12121 write(6,*) ' input number of points in filter'
14     READ(5,*)num
15 c... finding spatial locations for the shakers in real non-dimensional
16 c.. space (length of the bar is one.)
17 c.. this method places one shaker in the middle and symmetrically out
18 c.. from this shaker locates the rest of the shakers
19     if(num.eq.9)then
20     do i = 1,num
21         etap(i) = (2.95 + float(i-1)*4.)/beam_length
22     enddo
23     elseif (num.eq.17) then
24     do i = 1,num
25         etap(i) = (2.95 + float(i-1)*2.)/beam_length
26     enddo
27     else
28     write(6,*) ' input either 9 or 17 shakers'
29     goto 12121
30     ENDIF
31 c...
32 c... forcing window options are:
33 c...          1) rectangular window
34 c...          2) Kaiser-Bessel window
35 c...          3) Hannning window
36 c...          4) Self input of window coefficients
37 c... option held in variable i_flag

```

```

38 c...
39      write(6,*) ' input rect (1), kaiser (2) or hanning(3) self(4)'
40      read (5,*) i_flag
41 c...
42 c...      rectangular window
43      if (i_flag . eq . 1) then
44      DO I = 1,NUM
45          W(I) = cmplx(1.0,0.)
46      ENDDO
47 c...      Kaiser-Bessel window
48      elseif(i_flag . eq . 2) then
49          write(6,*) ' input alpha'
50          read(5,*) alpha
51          CALL KAISER(W,NUM,ALPHA)
52 c...      Hannning window
53      elseif(i_flag . eq . 3) then
54      DO I = 1,NUM
55          arg = etap(i)*2.*pi
56          W(i) =.5*(1- cos(arg))
57      ENDDO
58 c...      self input option
59      elseif(i_flag.eq.4) then
60      do i = 1,num
61          write(6,1111)i
62          read(5,*)w(i)
63 dd          write(6,1112)i
64 dd          read(5,*)etap(i)
65      enddo
66      endif
67 1111      format(' input force number ',i2)
68 1112      format(' input location number ',i2)
69 c...
70 c...      In this section, the wavenumber content is shifted using a
71 c...      symmetrical cosine weighting. The number of waves across
72 c...      the length of the beam is used as the means for determining
73 c...      the drive wavenumber.
74      write(6,*) ' input cos weight(1) or not'
75      read (5,*) i_cos
76      if (i_cos.eq.1) then
77          write(6,*) ' input desired waves over the bar(k/2pi)'
78      read (5,*) x_k
79      do i = 1,num
80          arg = (etap(i)-.5)*2.*x_k*pi
81          W(i)= W(i)*cos(arg)
82      write (6,*)w(I)

```

```

83         enddo
84     endif
85 c....
86 c.... output files
87 c....
88         type 1512
89 1512 format(' input file for force mag wave-freq plot file-->', $)
90         read(5,10)name
91         open(unit=11,file = name , status = 'new')
92         type 1513
93 1513 format(' input file for force phase wave-freq plot file-->', $)
94         read(5,10)name
95         open(unit=12,file = name , status = 'new')
96         wavmm = -1000.
97 c...
98 c... This section performs the Fourier transform as per Equation 2.27.
99 c...
100         do k = -num_wav, num_wav
101             sum = cmplx(0.,0.)
102             x_wav_num = float((k))/2.
103             do j = 1,num
104                 sum = sum + w(j)*cexp(-x_wav_num*
105 >                 c_i*etap(j))
106             enddo ! enddo for j
107 c... set up for plotting routines. Normalize data to maximum point
108 c...
109                 temp = cabs(sum)
110                 if (temp.eq.0.0) then
111                     temp = .0000001
112                     sum = cmplx(0.000001,0.000001)
113                 write(6,*) ' zero'
114                 endif
115                 plt(k) = 20*log10(temp)
116                 phs(k) = atan2d(aimag(sum),real(sum))
117                 if (plt(k).gt.wavmm) then
118                     wavmm=plt(k)
119                     i_rem = k
120                 endif
121         enddo ! enddo for k
122 c...
123 1222 format(20a4)
124 10 format(a20)
125 c...
126 c... write transformed data to data files.
127 c...

```

```

128      DO I = -num_wav,num_wav
129          plt(i) = plt(i) - wavmm
130          phs(i) = phs(i) - phs(i_rem)
131          if (phs(i) .lt. -180.) phs(i) = phs(i) +360.
132          xx = float(i)/(2.*beam_length)
133          write(11,*)xx,plt(i)
134          write(12,*)xx,phs(i)
135      ENDDO
136 C...
137 C...
138      close(unit=11)
139      close(unit=10)
140      OPEN (UNIT=10,FILE='weight.DAT',STATUS='NEW')
141      OPEN (UNIT=11,FILE='wphase.DAT',STATUS='NEW')
142 C... write spatial weighting coefficients
143      DO I = 1,NUM
144          WRITE(10,*)float(I)-1.,cabs(W(I))
145          WRITE(11,*)float(I)-1.,atan2d(aimag(W(I)),real(W(I)))
146      ENDDO
147      CLOSE(UNIT=11)
148      CLOSE(UNIT=10)
149      STOP
150      END
151 C
152 C
153 C
154      SUBROUTINE KAISER (W,N,ALPHA)
155 C... Kaiser-Bessel weights. Algorithm from Carter Ackerman
156      COMPLEX W(512)
157      F = (FLOAT(N)+1.)/2.
158      PIA = 3.1415927*ALPHA
159      BD = AINO(PIA)
160      DO 1 I = 1,N
161          BW = AINO(PIA*SQRT(1.-(FLOAT(I)/F-1.）**2))
162      1 W(I)=CMPLX(BW/BD,0.0)
163      RETURN
164      END
165 C..
166      FUNCTION AINO(X)
167 C X BETWEEN 0. AND 20.
168      Y = X/2.
169      T = 1.E-8
170      E = 1.
171      DE = 1.
172      DO 1 I = 1,25

```

```

173             DE = DE*Y/FLOAT(I)
174             SDE = DE**2
175             E = E+SDE
176             IF(E*T-SDE)1,1,2
177 1          CONTINUE
178 2          AINO = E
179          RETURN
180          END

```

The next program listed is VALTIM, the program that compares the measured to the predicted admittance.

```

1          program valtim
2  c-----
3  c This program calculates the admittance and phase of a
4  c Timoshenko bar in cm-dyne-sec units and compares it to
5  c measured values. The measured data is in g's and pounds-force
6  c and must be converted to cm-dyne-sec.
7  c This program is a combination of the work of F.M. Hutto
8  c and K. Grosh.
9  c This specific program is for the first three nine shaker
10 c experiments.
11 c-----
12      REAL E,G,RHO,IM,AREA,AK,ONE,TWO,TWEN,LM,A1,FSH
13      REAL PI,ZERO,BBT,BAL,FREQ
14      REAL OMG(0:40),PHI(0:40),B(0:40),AL(0:40),CETA
15      REAL BT(0:40),DEL(0:40),CHE(0:40),LAMDA(0:40)
16      REAL DF,MB,q(2),qy(2)
17      REAL ETAP(10),BBTE,BALE,FRQ(450)
18      REAL YR(0:40,20)
19      REAL Y(201,2),XR,YI,PHS(201,2),fa
20      REAL ORT(0:40),PENS(2),PNTS(2)
21      INTEGER I,J,M,N,Z,ind
22      COMPLEX*8 DISP(250),CY,SUM,DNOI(250,0:40),K0(10),SSUM
23      COMPLEX*8 FC(250,20),SUMS
24      CHARACTER*20 NAME,N1,N2
25      CHARACTER*1 P,ff,esc
26  c...
27  c-----
28  c The values used are:
29  c   E (elastic modulus)           = 210E10 dynes/cm^2
30  c   G (shear modulus)            = 77E10 dynes/cm^2
31  c   IM (area moment of inertia) = bh^3/12
32  c   wd (width of beam)           = 1.27 cm.

```

```

33 c  ht (height of beam)           = 1.92 cm.
34 c  RHO (density of material)     = 7.8 grams/cm^3
35 c  LM (length of beam)          = 37.9. cm.
36 c  AK (cross sec. constant)      = .833
37 c  DF (damping factor)           = .05
38 c -----
39
40      DATA E,G,ONE,RHO,LM,wd,ht / 210E10 , 77E10 ,
41      1 1. , 7.8 , 37.9 , 1.27,1.91/
42      DATA ZERO,AK,TWEN,TWO / 0.0 , .833 , 19. , 2. /
43      PI=4*ATAN(ONE)
44      df = .05
45      PENS(1)=1.0
46      PENS(2)=2.0
47
48      PNTS(1)=201.
49      PNTS(2)=201.
50      area = wd*ht
51      im = wd*ht**3/12.
52      MB=(RHO*AREA*LM)
53      P='\'
54 C -----
55 C      There are nine point forces:
56 C
57      M=9
58 C
59 c -----
60 c
61 c      reading in the eigen-frequencies
62 c
63 c
64 c -----
65      OPEN ( UNIT=10 , FILE='[grosh.kg1.bar]bsfreq.DAT' ,TYPE='OLD' )
66      DO I=2,21
67      READ (10,*) OMG(I)
68      OMG(I)=OMG(I)*2*PI
69      END DO
70      CLOSE ( UNIT=10 )
71      OMG(0)=0.0
72      OMG(1)=0.0
73 c...
74 c...      Reading in the orthogonality constants
75 c...
76      OPEN(UNIT=10,FILE='[grosh.kg1.bar]bsort.dat',STATUS='OLD')
77      DO I=2,21

```

```

78      READ(10,*) ORT(I)
79      END DO
80      CLOSE(UNIT=10)
81      ORT(0)=1.0
82      ORT(1)=(LM**2)/12
83      c... reading in forcing function data -- this is assumed to be a constant
84      c... no matter where the accelerometer is
85      c----- opening file of force data -----
86          type 1511
87      1511 format('  input force file-->','$)
88          read(5,10)name
89          OPEN(UNIT=10,FILE=name,TYPE='OLD')
90          DO J = 1,M
91              IF(J.NE.(M+1)/2) THEN
92                  DO I=1,PNTS(1)
93                      READ(10,1300) FRQ(I),FA,PHASE
94                      FA      = 10** (FA/20.)
95                      FC(I,J) = FA*CMPLX(COSD(PHASE),SIND(PHASE))
96                  END DO
97              ELSEIF(J.EQ.(M+1)/2) THEN
98                  DO I=1,PNTS(1)
99                      FC(I,J) = CMPLX(1.0,0.0)
100              ENDDO
101          endif
102      END DO
103      CLOSE(UNIT=10)
104      1300  FORMAT(1X,F5.2,F12.6,F7.2)
105      c----- closing file of force data -----
106      C..
107          R=SQRT(IM/(AREA*LM**2))
108          S=SQRT(E*IM/(AK*AREA*G*LM**2))
109      C-----
110          DO I=2,21
111              B(I)=SQRT(RHO*AREA*OMG(I)**2*LM**4/(E*IM))
112              AL(I)=(((R**2-S**2)**2+4/B(I)**2)**.5-R**2-S**2)**.5
113              1 /SQRT(TWO)
114              BT(I)=(((R**2-S**2)**2+4/B(I)**2)**.5+R**2+S**2)**.5
115              1 /SQRT(TWO)
116              LAMDA(I)=AL(I)/BT(I)
117              CHE(I)=(BT(I)**2-S**2)/(AL(I)**2+S**2)
118              BAL=B(I)*AL(I)
119              BBT=B(I)*BT(I)
120              IF (BAL.GT.TWEN) GOTO 170
121              DEL(I)=(COSH(BAL)-COS(BBT))/(LAMDA(I)*SINH(BAL)-
122              1      CHE(I)*SIN(BBT))

```

```

123      GOTO 171
124      170 DEL(I)=1/LAMDA(I)
125      171 CONTINUE
126      END DO

127 C-----
128 C CALCULATIONS DUE TO THE FORCING FUNCTION.
129 C
130      do i = 1,m
131          etap(i) =(2.95 + (i-1)*4. )/lm
132      enddo
133 C=====
134      DO J=1,M
135          YR(0,J)=1.0
136          YR(1,J)=ETAP(j)-.5
137          DO I=2,21
138              BBT=B(I)*BT(I)
139              BAL=B(I)*AL(I)
140              BBTE=BBT*ETAP(J)
141              BALE=BAL*ETAP(J)
142              IF (BALE.GT.TWEN) GOTO 200
143              YR(I,J)=(COSH(BALE)+COS(BBTE)/CHE(I)-LAMDA(I)*DEL(I)
144              1 *SINH(BALE)-DEL(I)*SIN(BBTE))
145              GOTO 201
146          200 YR(I,J)=(COS(BBTE)/CHE(I)-DEL(I)*SIN(BBTE))
147          201 CONTINUE
148      END DO
149      END DO
150 c... loop point
151 c...
152 C-----
153 C SET FOR READING IN DATA
154
155      WRITE(5,*) 'WHAT IS THE NAME OF THE DATA FILE?'
156      READ(5,10) NAME
157      10  FORMAT (A20)
158      OPEN(UNIT=21,FILE=name,STATUS='OLD')
159      DO I=1,PNTS(2)
160          READ (21,*)ii, frq(i),Y(i,2),PHS(I,2)
161          phs(i,2)=phs(i,2)-180.
162          if (phs(i,2).gt.180.) phs(I,2)=phs(i,2)-360
163          if (phs(I,2).lt.-180.) phs(I,2)=phs(i,2)+360
164      END DO
165      CLOSE(UNIT=21)
166      name(20:20)='$'
167      TYPE 1313

```

```

168 1313  format (' input ceta-->', $)
169      READ(5,*) ceta
170 C-----
171 C   CALCULATING EIGENFUNCTION FOR A PARTICULAR POINT ON THE BEAM
172 C   FOR THE FIRST 21 MODES
173 C
174 C
175 C
176 C-----
177 C-----
178 C
179 C   CALCULATION OF THE EIGENFUNCTIONS FOR DIFFERENT FREQUENCIES
180 C   AT A SINGLE POINT "CETA". THE EIGENFREQUENCIES ARE FOR A FREE-FREE
181 C   BEAM OF THE TIMOSHENKO TYPE TAKING INTO ACCOUNT SHEAR AND ROTARY
182 C   INERTIA EFFECTS
183 C
184 C-----
185      DO I=2,21
186      BBT=B(I)*BT(I)
187      BAL=B(I)*AL(I)
188      BALE=BALE+CETA
189      BBTE=BBT*CETA
190      IF (BALE.GT.TWEN) GOTO 150
191      PHI(I)=COSH(BALE)-LAMDA(I)*DEL(I)*SINH(BALE)+
192      1      COS(BBTE)/CHE(I)-DEL(I)*SIN(BBTE)
193      GOTO 151
194 150 PHI(I)=COS(BBTE)/CHE(I)-DEL(I)*SIN(BBTE)
195 151 CONTINUE
196      END DO
197 C-----
198 C   THE RIGID BODY MODES. BOTH ROTARY AND TRANSLATIONAL
199 C
200      PHI(0)=1.0
201      PHI(1)=.5*(CETA-.5)
202 C-----
203      DO Z=1,PNTS(1)
204      FREQ=FRQ(Z)*1000.*2*PI
205      SSUM=CMPLX(ZERO,ZERO)
206      DO I=0,21
207      DNOI(Z,I)=1/(MB*ORT(I)*(OMG(I)**2*CMPLX(ONE,DF)-FREQ**2))
208      SUMS=CMPLX(0.0,0.0)
209      DO J=1,M
210      SUMS=SUMS+FC(Z,J)*YR(I,J)
211      END DO
212      SSUM=SSUM+DNOI(Z,I)*SUMS*PHI(I)

```

```

213      END DO
214      cy = SSUM*cmplx(0.0,freq)
215      y(z,1) = 20*log10(cabs(cy))
216      phs(z,1) = atan2d(aimag(cy),real(cy))
217      END DO
218 C=====
219 C
220 C
221 C PLOTTING ROUTINE GOES HERE
222 C
223 C
224 C
225 C=====
226 C
227      STOP
228      END
229
230

```

The source code for the FORTRAN program ARRAY\_EFFECT is given next.

```

1      program array_effect
2 c...
3 c... This program allows for the comparison of the analytic and
4 c... discrete Fourier transform of the velocity response of a
5 c... Timoshenko beam to the experimentally measured forcing function.
6 c... Also, the experimentally obtained velocity response may be
7 c... plotted as well. The number of sensors used to measure the
8 c... theoretical response may be varied as
9 c... well as the measurement frequency. These results are plotted as
10 c... a function of wavenumber at a particular frequency.
11      real x(64,4),y(64,4),fftfor(64,101)
12      complex fc(20,201)
13      character name*40
14      common frequency,irun,num_accel,ihan,m
15      type *,' input forcing file'
16      accept 100,name
17 100  format(a40)
18      type *,'number of shakers'
19      accept *,m
20      type *, 'run number'
21      accept *,irun
22      if (irun.le.3) num_rd_freq = 201
23      if (irun.gt.3) num_rd_freq = 101
24 c... Reading in the forcing function.
25      OPEN(UNIT=10,FILE=name,TYPE='OLD')
26      DO J = 1,M

```

```

27         IF(J.NE.(M+1)/2) THEN
28             DO I=1,num_rd_freq
29                 READ(10,133) xxx,FA,PHASE
30                 FA          = 10**(FA/20.)
31                 FC(J,i) = FA*CMPLX(COSD(PHASE),SIND(PHASE))
32             END DO
33         ELSEIF(J.EQ.(M+1)/2)THEN
34             DO I=1,num_rd_freq
35                 FC(J,i) = CMPLX(1.0,0.0)
36             ENDDO
37         endif
38     END DO
39 c...
40 133     format(1x,f5.2,f12.6,f7.2)
41     CLOSE(UNIT=10)
42 c...   Construction the name of the experimentally measured
43 c...   velocity response in case this option is desired
44         if (m.eq.9)name = 'fft_'//name(3:5)//'a'//name(8:8)//'m'
45         if (m.eq.17)name = 'fft_'//name(3:6)//'a'//name(9:9)//'m'
46         type *,name
47         open (unit=19,form='unformatted',status='old',file=name)
48         read(19)fftfor
49         close(unit=19)
50         call prompt(idev) ! plotting initialization subroutine.
51 c...
52 c...   Which frequency and then decide in which frequency bin does
53 c...   the chosen frequency falls.
54 11000   type *,' which frequency '
55         accept *,frequency
56         fmin = 2000.
57         fmax = 12000.
58         ibin = int(float(num_rd_freq-1)*(frequency-fmin)/10000.)+1
59         iibin=int(100.*(frequency-fmin)/10000.)+1
60 c...
61 c...   Call the analytic Fourier transform of the velocity response.
62         call exftfb(frequency,fc(1,ibin),m,x(1,1),y(1,1))
63         do i = 1,64
64             x(i,3)=x(i,1)
65             y(i,3)=fftfor(i,iibin)
66         enddo
67 c...
68 c...   Input the number of sensors for the theoretical FFT of the
69 c...   velocity.
70         type *,' input number of accel'
71         accept *,num_accel

```

```

72 c...    Call the theoretical FFT of the velocity.
73          call theo_fft(frequency,ihan,fc(1,ibin),num_accel,m,x(1,2)
74          >          ,y(1,2))
75          type *, ' enter numcurves'
76          accept *,num_curves
77          call xyplot(x,y,num_curves,idev) ! plotting routine.
78 c...    begin again?
79          type *, ' another frequency(1)'
80          accept *, iopt
81          if (iopt.eq.1)then
82          do i = 1,64
83              y(i,1)=0.0
84              y(i,2)=0.0
85              y(i,3) = 0.0
86          enddo
87          goto 11000
88          endif
89
90          call donepl(0)
91          stop
92          end
93 c...
94 c...
95          subroutine exftfb(frequency,fc,m,hold,vout)
96 c...    this program reads in the forcing function experimentally measured
97 c...    and uses it in a model for the exact spatial fourier transform
98 c...    of the timoshenko beam.
99 c...
100         REAL E,G,RHO,IN,AREA,AK,ONE,TWO,TWEN,LM,A1,FSN
101         REAL PI,ZERO,BBT,BAL,FREQ
102         REAL OMG(0:40),B(0:40),AL(0:40),CETA
103         REAL BT(0:40),DEL(0:40),CHE(0:40),LAMDA(0:40)
104         REAL DF,MB,resp(64,101)
105         REAL ETAP(20),BBTE,BALE,FRQ(450)
106         REAL YR(0:40,20)
107         REAL XR,YI,fa,hold(64)
108         REAL ORT(0:40),PENS(2),PNTS(2)
109         INTEGER I,J,M,N,Z,ind,kik
110         COMPLEX*8 CY,SUM,DNOI(0:40),SSUM,f_temp(20)
111         COMPLEX*8 FC(20),SUMS,temp1,temp2,PHI(0:40),c_i
112         real vout(64)
113         CHARACTER*20 NAME,N1,N2
114         CHARACTER*1 P
115         CHARACTER*21 NAMEP
116 c-----

```

```

117      DATA ONE / 1. /
118      DATA ZERO,TWEN,TWO / 0.0 , 12. , 2. /
119      PI=4*ATAN(ONE)
120 c... constants the units are cgs system.
121      e = 210e10 ! young's modulus
122      g = 77 e10 ! shear modulus
123      rho = 7.8 ! density
124      ak = .833 ! kappa the shape factor
125      df = .05 ! damping factor
126      num_eig=21 ! number of modes used
127      lm = 37.9 ! length of the beam
128      wd = 1.27 ! width of the beam
129      ht = 1.91 ! height of the beam
130      n1 = 'bsfreq' ! eigenfrequency file
131      n2 = 'bsort' ! orthogonality constant file
132      c_i = cmplx(0.0,1.0)
133      wav_min = 0.0
134 c... scaling of the variables back to inverse centimeters.
135      wav_max = pi*lm
136      area = wd*ht
137      im = wd*ht**3/12.
138      MB=(RHO*AREA)
139 c...
140 c... reading in the eigen-frequencies
141 c...
142      OPEN ( UNIT=10 , FILE='[grosh.kg1.bar] '//n1 ,TYPE='OLD' )
143      DO I=2,num_eig
144      READ (10,*) OMG(I)
145      OMG(I)=OMG(I)*2*PI
146      END DO
147      CLOSE ( UNIT=10 )
148      OMG(0)=0.0
149      OMG(1)=0.0
150 c...
151 c... reading in the orthogonality constants.
152 c...
153      OPEN(UNIT=10,FILE='[grosh.kg1.bar] '//n2,STATUS='OLD')
154      DO I=2,num_eig
155      READ(10,*) ORT(I)
156      END DO
157      CLOSE(UNIT=10)
158      ORT(0)=1.0
159      ORT(1)=(LM**2)/12
160 133      format(1x,f5.2,f12.6,f7.2)
161      CLOSE(UNIT=10)

```

```

162 c...
163 c... location of the point sources (shakers) depends on the number of
164 c... shakers
165         if (m.eq.9)delta=4.
166
167         if (m.eq.17)delta=2.
168
169         do i = 1,m
170             etap(i) =(2.95 + (i-1)*delta )/lm
171         enddo
172 c...
173 c...
174 c...   Begin the calculation of the necessary eigen constants
175 c...
176         R=SQRT(IM/(AREA*LM**2))
177         S=SQRT(E*IM/(AK*AREA*G*LM**2))
178         DO I=2,num_eig
179             B(I)=SQRT(RHO*AREA*OMG(I)**2*LM**4/(E*IM))
180             AL(I)=(((R**2-S**2)**2+4/B(I)**2)**.5-R**2-S**2)**.5
181             1 /SQRT(TWO)
182             BT(I)=(((R**2-S**2)**2+4/B(I)**2)**.5+R**2+S**2)**.5
183             1 /SQRT(TWO)
184             LAMDA(I)=AL(I)/BT(I)
185             CHE(I)=(BT(I)**2-S**2)/(AL(I)**2+S**2)
186             BAL=B(I)*AL(I)
187             BBT=B(I)*BT(I)
188             IF (BAL.GT.TWEN) GOTO 170
189             DEL(I)=(COSH(BAL)-COS(BBT))/(LAMDA(I)*SINH(BAL)-
190             1 CHE(I)*SIN(BBT))
191             GOTO 171
192         170 DEL(I)=1/LAMDA(I)
193         171 CONTINUE
194         END DO
195 c...
196 c...
197 c...   Calcualtion of the modal expansion coefficients, a function
198 c...   of mode shapes and the forcing function.
199 c...
200         DO J=1,M
201             YR(0,J)=1.0
202             YR(1,J)= .5*(ETAP(j)-.5)
203             DO I=2,num_eig
204                 BBT=B(I)*BT(I)
205                 BAL=B(I)*AL(I)
206                 BBTE=BBT*ETAP(J)

```

```

207      BALE=BAL*ETAP(J)
208      IF (BALE.GT.TWEN) GOTO 200
209      YR(I,J)=(COSH(BALE)+COS(BBTE)/CHE(I)-LAMDA(I)*DEL(I)
210      1 *SINH(BALE)-DEL(I)*SIN(BBTE))
211      GOTO 201
212  200 YR(I,J)=(COS(BBTE)/CHE(I)-DEL(I)*SIN(BBTE))
213  201 CONTINUE
214      END DO
215      END DO
216 c... at each frequency dnoi holds the information about the
217 c... orthogonality of the forcing function with any of the modes
218 c... at each frequency.
219      FREQ = 2.*PI*frequency
220      DO I = 0,num_eig
221          SUM=CMPLX(0.0,0.0)
222          DO J=1,M
223              SUM= SUM + FC(J)*YR(I,J)
224          END DO
225          TEMP1=1/(MB*ORT(I)*(OMG(I)**2*CMPLX(ONE,DF)-FREQ**2))
226          DNOI(I) = TEMP1*SUM*CMPLX(0.0,FREQ)!last part changes to velocity
227          enddo
228 c..
229 C-----
230 C CALCULATE THE WAVENUMBER RESPONSE OF EACH MODE SHAPE
231 C PHI IS THE COMPLEX ARRAY OF THE WAVENUMBER RESPONSE.
232 C-----
233 c      do loop over gammas-----
234 c... wavenumber response of the two rigid body modes
235      do 1010 kik = 1,64
236          hold(kik) = (wav_min + (wav_max-wav_min)*(kik-1)/64.)/ln
237          gamma = wav_min + (wav_max-wav_min)*(kik-1)/64.
238 c...
239      if ( gamma.ne.0.0) then
240          phi(0) = c_i/gamma*(cexp(-c_i*gamma)-1.)
241          phi(1) = (1./gamma**2)*(cexp(-c_i*gamma) - 1.)
242      >          +c_i/(2.*gamma)*(cexp(-c_i*gamma)+1 )
243      elseif(gamma.eq.0.0) then
244          phi(0) = CMPLX(1.0,0.)
245          phi(1) = CMPLX(.5,0.)
246      endif
247 C.. THE TRANSFORM OF THE NON-RIGID BODY MODES.
248      DO I=2,num_eig
249          BBT=B(I)*BT(I)
250          BAL=B(I)*AL(I)
251          call transform(bal,bbt,lambda(i),del(i),che(i),1.0,gamma

```

```

252      >                                ,temp2)
253      call transform(bal,bbt,lamda(i),del(i),che(i),0.0,gamma
254      >                                ,temp1)
255      phi(i) = temp2-temp1
256      enddo
257 C-----
258      SSUM=CMPLX(0.0,0.0)
259      DO I=0,num_eig
260      SSUM=SSUM+DNOI(I)*PHI(I)
261      END DO
262      vout(kik) = 20*log10(cabs(SSUM))
263 1010 continue ! enddo for wavenumber loop
264 10000 format(20a4)
265      return
266      end
267 C...
268      subroutine transform(bal,bbt,lambda,delta,zeta,xsi,gamma,val)
269 C... Evaluation of the analytic transform of the mode shapes.
270      real lambda
271      complex*8 val,temp1,temp2,c_i
272      c_i=cmplx(0.0,1.0)
273      bale = bal*xsi
274      bbte = bbt*xsi
275      game = gamma*xsi
276 C...
277      temp1 = cexp(-c_i*game)/(gamma**2 + bal**2)
278      temp1 = temp1*((c_i*gamma*cosh(bale) + bal*sinh(bale))
279      >      -lambda*delta*(c_i*gamma*sinh(bale) + bal*cosh(bale)))
280 C... if argument of the hyberbolic functions is too high
281      if(bale.gt.12) temp1 = 0.0
282      if (gamma . ne . bbt) then
283 C...
284      temp2 = cexp(-c_i*game)/(gamma**2 - bbt**2)
285      temp2 = temp2*(1./zeta*(c_i*gamma*cos(bbte) - bbt*sin(bbte))
286      >      -delta*(c_i*gamma*sin(bbte) + bbt*cos(bbte)))
287 C..
288      elseif(gamma . eq . bbt) then
289      temp2 = 1./zeta*(xsi - 1./(2.*c_i*gamma)*cexp(-2.*c_i*game))
290      >      -delta*(xsi + 1/(2.*c_i*gamma)*cexp(-2.*c_i*game))
291      endif
292      val = temp1+temp2
293      return
294      end
295 C...
296      subroutine theo_fft(frequency,ihan,fc,num_accel,m,hold,vout)

```

```

297 c... calc fft of response theoretically
298 c... First the spatial response of the beam is obtained at num_accel
299 c... points. Then the FFT is taken of the response
300 c-----
301 c-----
302     REAL E,G,RHO,IM,AREA,AK,ONE,TWO,TWEN,LM,A1,FSM
303     REAL PI,ZERO,BBT,BAL,FREQ
304     REAL OMG(0:40),PHI(0:40),B(0:40),AL(0:40),CETA
305     REAL BT(0:40),DEL(0:40),CHE(0:40),LAMDA(0:40)
306     REAL DF,MB
307     REAL ETAP(20),BBTE,BALE,FRQ(450)
308     REAL YR(0:40,20),x(64)
309     REAL XR,YI,PHS(500),fa,vout(64),hold(64)
310     REAL ORT(0:40),PENS(2),PNTS(2)
311
312     INTEGER I,J,M,N,Z,ind
313
314     COMPLEX*8 CY,SUM,DNOI(0:40),SSUM,temp1
315     COMPLEX*8 FC(20),SUMS,a(1024),ww(512),resp(303)
316     CHARACTER*20 NAME,N1,N2
317     CHARACTER*1 P,cone
318     CHARACTER*2 ctwo
319     CHARACTER*21 NAMEP
320     character*5 base
321 c...
322 c...
323 c...
324 c... The same physical constants are used in this routine as in EXFTFB
325 c...
326 c...
327     DATA E,G,ONE,RHO,LM,wd,ht / 210E10 , 77E10 ,
328     1 1. , 7.8 , 37.9 ,1.27,1.91/
329     DATA ZERO,AK,DF,TWEN,TWO / 0.0 , .833 , .05 , 12. , 2. /
330     PI=4*ATAN(ONE)
331     PENS(1)=1.0
332     PENS(2)=2.0
333     area = wd*ht
334     im = wd*ht**3/12.
335     num_fft=128
336     MB=(RHO*AREA*LM)
337     P='\ '
338     num_eig=21
339 c.. before things get started calculate fft weights
340     call cafft(a,ww,num_fft,0) ! FFT algorithm
341 c... hanning window option.

```

```

342         type *, ' hanning option(1)'
343         accept *, ihan
344 c...
345 c... option to use spacing exactly the same as per the experiments
346 c... or a spacing that evenly spreads the accelerometers over the
347 c... beam for any spacing.
348 c...
349 141         type *, ' same as exp.(1) or even dist.(2)'
350         accept *, imatch
351         if(imatch.ne.1.and.imatch.ne.2)goto 141
352 c
353 c reading in the eigen-frequencies from the file
354 c BSFREQ.DAT
355 c
356         OPEN ( UNIT=10 , FILE='[grosh.kg1.bar]bsfreq.DAT' ,TYPE='OLD' )
357         DO I=2,num_eig
358         READ (10,*) OMG(I)
359         OMG(I)=OMG(I)*2*PI
360         END DO
361         CLOSE ( UNIT=10 )
362         OMG(0)=0.0
363         OMG(1)=0.0
364 c...
365 c... reading in the orthogonality conatants.
366 c...
367         OPEN(UNIT=10,FILE='[grosh.kg1.bar]bsort.dat',STATUS='OLD')
368         DO I=2,num_eig
369         READ(10,*) ORT(I)
370         END DO
371         CLOSE(UNIT=10)
372         ORT(0)=1.0
373         ORT(1)=(LM**2)/12
374 1222 format(1x,f5.2,f12.6,f7.2)
375         CLOSE(UNIT=10)
376 c... Eigenfunciton constants
377 c...
378         R=SQRT(IM/(AREA*LM**2))
379         S=SQRT(E*IM/(AK*AREA*G*LM**2))
380         DO I=2,num_eig
381         B(I)=SQRT(RHO*AREA*OMG(I)**2*LM**4/(E*IM))
382         AL(I)=(((R**2-S**2)**2+4/B(I)**2)**.5-R**2-S**2)**.5
383         1 /SQRT(TWO)
384         BT(I)=(((R**2-S**2)**2+4/B(I)**2)**.5+R**2+S**2)**.5
385         1 /SQRT(TWO)
386         LAMDA(I)=AL(I)/BT(I)

```

```

387      CHE(I)=(BT(I)**2-S**2)/(AL(I)**2+S**2)
388      BAL=B(I)*AL(I)
389      BBT=B(I)*BT(I)
390      IF (BAL.GT.TWEN) GOTO 170
391      DEL(I)=(COSH(BAL)-COS(BBT))/(LAMDA(I)*SINH(BAL)-
392      1      CHE(I)*SIN(BBT))
393      GOTO 171
394      170 DEL(I)=1/LAMDA(I)
395      171 CONTINUE
396      END DO

397 C-----
398 C CALCULATIONS DUE TO THE FORCING FUNCTION. EVALUATING THE POINT FORCES
399 C AT THE DIFFERENT POINTS
400 C
401      if (m.eq.9) delta = 4.
402      if (m.eq.17) delta = 2.
403      do i = 1,m
404          etap(i) =(2.95 + (i-1)*delta)/lm
405      enddo
406 C=====
407      DO J=1,M
408          YR(0,J)=1.0
409          YR(1,J)=.5*(ETAP(j)-.5)
410          DO I=2,num_eig
411              BBT=B(I)*BT(I)
412              BAL=B(I)*AL(I)
413              BBTE=BBT*ETAP(J)
414              BALE=BAL*ETAP(J)
415              IF (BALE.GT.TWEN) GOTO 200
416              YR(I,J)=(COSH(BALE)+COS(BBTE)/CHE(I)-LAMDA(I)*DEL(I)
417      1      *SINH(BALE)-DEL(I)*SIN(BBTE))
418              GOTO 201
419      200 YR(I,J)=(COS(BBTE)/CHE(I)-DEL(I)*SIN(BBTE))
420      201 CONTINUE
421          END DO
422      END DO
423 c... at each frequency dnoi holds the information about the
424 c... orthogonality of the forcing function with any of the modes
425 c... at each frequency.
426          FREQ = 2.*PI*frequency
427          DO I = 0,num_eig
428              SUM=CMPLX(0.0,0.0)
429              DO J=1,M
430                  SUM= SUM + FC(J)*YR(I,J)
431              END DO

```

```

432      TEMP1=1/(MB*ORT(I)*(OMG(I)**2*CMPLX(ONE,DF)-FREQ**2))
433      DNOI(I) = TEMP1*SUM*CMPLX(0.0,FREQ)!last part changes to velocity
434      enddo
435 c... At this point all of the information concerning the
436 c... forcing function has been obtained. Now, the sensor
437 c... location is varied.
438 c...
439 C -----
440 10      FORMAT (A20)
441 C...
442 C...
443 c... begin acclerometer loop
444 c...
445      do kkj = 1,num_accel
446 1000      format(i1)
447 2000      format(i2)
448 c...
449 c... what is the location of the accel. for this kkj.
450      if(num_accel.eq.17) then
451          x_off=2.95/lm
452          ceta = (2.95+float(kkj-1)*2.)/lm
453          delta_fft = 2.
454      elseif(num_accel.eq.9) then
455          x_off=2.95/lm
456          ceta = (2.95+float(kkj-1)*4.)/lm
457          delta_x = 4.
458          delta_fft = 4.
459      else
460          if(imatch.eq.1)then
461              x_off=0.95/lm
462              delta_x= (lm-1.9)/float(num_accel-1)
463              ceta =x_off+(float(kkj-1))*delta_x/lm
464              delta_fft=delta_x
465          elseif (imatch.eq.2 )then
466              ceta = (float(kkj)-.5)/float(num_accel)
467              delta_fft=lm/float(num_accel)
468          endif
469      endif
470 c...
471 C -----
472 C
473 c... evaluate the mode shapes at ceta.
474 c...
475      DO I=2,num_eig
476      BBT=B(I)*BT(I)

```

```

477      BAL=B(I)*AL(I)
478      BALE=BALE*CETA
479      BBTE=BBT*CETA
480      IF (BALE.GT.TWEN) GOTO 150
481      PHI(I)=COSH(BALE)-LAMDA(I)*DEL(I)*SINH(BALE)+
482      1      COS(BBTE)/CHE(I)-DEL(I)*SIN(BBTE)
483      GOTO 151
484      150 PHI(I)=COS(BBTE)/CHE(I)-DEL(I)*SIN(BBTE)
485      151 CONTINUE
486      END DO
487 C -----
488 C   THE RIGID BODY MODES. BOTH ROTARY AND TRANSLATIONAL
489 C
490      PHI(0)=1.0
491      PHI(1)=.5*(CETA-.5)
492 C -----
493      SSUM=CMPLX(0.0,0.0)
494      DO I=0,num_eig
495      SSUM=SSUM+DNOI(I)*PHI(I)
496      END DO      ! enddo for kkj
497 C...
498 C...
499      type *,jjj,ceta,ceta*lm,cabs(ssum)
500      write(10, *)jjj,ceta,cabs(ssum)
501      cy=ssum
502      resp(kkj) = cy
503      enddo      ! enddo kkj
504 C...
505 C... Next, perform FFT on the velocity data and return to main
506 C... routine.
507      const = 2.*pi*delta_fft
508      x_norm = lm/float(num_accel) ! proper normalization
509      do j = 1,num_accel
510          if (ihan.eq.1) then
511              weight=.5*(1.-cos((x_off+float(j-1))*const))
512          else
513              weight=1.
514          endif
515          a(j) = weight*resp(j)
516      enddo
517      do j = num_accel+1,num_fft
518          a(j)=cmplx(0.0,0.0)
519      enddo
520      call cafft(a,ww,num_fft,1)
521      do ik = 1,64

```

```

522             vout(ik) = 20.*alog10(cabs(a(ik)*x_norm))
523             hold(ik) =float(ik-1)*pi/(float(num_fft/2)
524             >                                     *delta_fft)
525             enddo
526             return
527         end
528

```

Finally, the FORTRAN program that compares the finite and infinite beam admittances at a particular wavenumber, titled COMPARE, is listed.

```

1      program compare
2 c...  This program compares the predicted, experimentally measured
3 c...  finite beam admittance to the theoretically derived infinite beam
4 c...  admittance.
5 c...
6      CHARACTER FNAME*30
7      LOGICAL*1 TEXT(80)
8 C
9      real *8 gamma
10     DIMENSION X(101),q(2),qy(2)
11     real mag(101,4)
12     CHARACTER FILEIN*40,txpl*40,header*40
13     CHARACTER*30 LINE_TYPE(4),cone*1,ctwo*2
14 C
15     pi = 3.141592654
16     type *, ' input number of shakers '
17     accept 211,ctwo
18     type *, ' input exper no in the series (ie,<=5) '
19     accept 112,cone
20 211   format (a2)
21 112   format(a1)
22 190   format(a40)
23     ncurves = 3
24     npts = 101
25 c...  variables for the plotting routine
26 c...  theses are the line descriptions
27     line_type(1) = 'exact transform$'
28     line_type(4) = 'fft of theoretical results$'
29     line_type(2)='fft of experimental results$'
30     line_type(3)='admittance of infinite beam$'
31 1804   format(' input filename ',i1,' -->',$)
32 1806   format(' input LINETITLE',i1,' -->',$)
33 10     format(a30)

```

```

34 c...
35 c...   begin frequency loop
36 c...
37       do i = 1,101
38         x(i) = 2. +float(i-1)*.1
39       enddo
40       CALL PROMPT(IDEV) ! plotting initialization subroutine
41       type *, ' fill letters (1)'
42       accept 999,ifil
43 999     format(i1)
44 10000   type *, ' automatic option or self input (1,2)'
45       accept 999,iopt
46       if (iopt.eq.1) then
47       if (ctwo.eq.'9') then
48       if (cone.eq.'1'.or.cone.eq.'5')then
49         ibin = 1
50         gamma=.0
51       elseif (cone.eq.'2')then
52         ibin = 16
53         gamma = .73631
54       elseif (cone.eq.'4')then
55         ibin = 4
56         gamma=.14726
57       elseif (cone.eq.'3')then
58         ibin = 8
59         gamma = .34361
60       endif
61       endif
62 c...
63       if (ctwo.eq.'17') then
64         if (cone.eq.'1')then
65           ibin = 1
66           gamma=.0
67       elseif (cone.eq.'4')then
68         ibin = 16
69         gamma = .73631
70       elseif (cone.eq.'2')then
71         ibin = 4
72         gamma=.14726
73       elseif (cone.eq.'3')then
74         ibin = 8
75         gamma = .34361
76       elseif(cone.eq.'5') then
77         ibin = 31
78         gamma = 1.4726

```

```

79         endif
80     endif
81     elseif (iopt.eq.2)then
82         type *, ' input bin number (calculates gamma)'
83         accept *,ibin
84         gamma = pi*(ibin-1)/64.*1.d0
85     endif
86
87 c...    read in calculated and measured velocity responses.
88 c...    these values are stored in a data file
89 c...
90         call indat(mag,cone,ctwo,ibin)
91 c...
92 c...    program that calculates infinite beam admittance
93         call inf_admit(mag(1,3),x,gamma)
94         xmin = x(1)
95         xmax= x(101)
96 c
97 c...    scaling for plot
98         header=cone//' '//ctwo//'$'
99         if (ibin.le.20) then
100             ymin=-160
101             ymax=-60
102         elseif (ibin.gt.20) then
103             ymin=-200
104             ymax=-100
105         endif
106 c
107 60      continue
108 c...
109 c...
110 c...
111 c...    plotting routine resides in this space
112 c...
113 c...
114 c...
115 c...
116 c...
117 c...    do you wish to continue questions,
118 c...
119         type *, ' TYPE 1 for another plot, 0 to ask for another run'
120         accept 999, iplag
121         if(iplag.eq.1) go to 60
122         type *, ' TYPE 1 for another run, 0 to exit'
123         accept 999, irflag

```

```

124      if (irflag.eq.1) goto 10000
125  44  CALL DONEPL(0)
126      stop
127      end
128  C...
129  C...
130  C...
131      subroutine inf_admit(xmag,frq,gamma)
132  C...
133  C...      this subroutine calculates the wavenumber-frequency
134  C...      admittance of an infinite beam.
135  C...
136      implicit real*8 (a-h,o-z)
137      real*8 rho,im,area,ak,one,two,twen,lm
138      real*8 pi,zero,bbt,bal,freq
139      real*8 df
140      real*4 xmag(101),frq(101)
141      real*8 first
142      real*8 kappa
143      complex*16 resp,arg1,arg2,g,e,bomega,zeta,theta
144      complex *16 wav_free_4
145      integer i,j,m,n,z,ier,IWEIGH
146  ccccccccccccc input material and dimension parameters ccccccccccccc
147      data real_e,real_g,one,rho / 210e10 , 77e10 ,
148      1 1. , 7.8 /
149      data zero,ak,df,twen,two / 0.0 , .833 , .05 , 12. , 2. /
150      pi=4.*datan(one)
151 212      format (a15)
152      ht=1.92d0
153      wd= 1.27d0
154      area = ht * wd
155      kappa = ak
156      im = wd*ht**3/12.
157      g = real_g*dcmplx(1.0d0,df)
158      e = real_e*dcmplx(1.0d0,df)
159      write(6,*)g,e,ak,df
160  C... THIS PART OF THE PROGRAM CALCULATES THE wavenumber
161  C... admittance AT VARIOUS frequencies
162      zeta = kappa * g * area
163      DO jj = 1,101
164      freq = frq(jj)*1000.
165      hold_max=-1000.
166      bomega = rho * area * (2.*pi *freq)**2
167      theta = rho * im * (2.*pi *freq)**2
168      wav_free_4 = bomega /e/im

```

```
169         arg1 = gamma**2/zeta+1/e/im*(1-theta/zeta)
170         arg2 = gamma**4 + gamma**2 * (-theta/e/im -
171     >         bomega/zeta) + wav_free_4*(theta/zeta - 1)
172         resp = -arg1/arg2
173         rmag = 20*dlog10( cdabs(resp)*freq*2.*pi)
174         phase=datan2d(dimag(resp) , dreal(resp))
175     xmag(jj) = sngl(rmag)
176     enddo
177     return
178     END
```

## APPENDIX D

### EXPERIMENTAL EXCEPTIONS

In this appendix, any problems associated with collecting the data and the remedies are delineated. In some of the experiments, accelerometer data were lost. When FFT's of the experiments were performed, these data locations were taken to be zero. Obviously, this induces error into the measured wavenumber velocity response. The accelerometer data at location one were missed in Experiments 1 and 4. Additionally, locations 34 and 37 were lost in Experiment 4. There was one problem associated with the force gage records. In Experiment 6, the last force record was lost. After examining the force records at the other locations, a strong symmetry was noticed (fortunately). Using this symmetry, an approximation was made which was to use the first shaker force record for the seventeenth shaker. As can be seen by the excellent agreement between theory and experiment for the Experiment 6, this was a good approximation.

Also, a note should be made concerning the storage of the data on the computer. For the second and fourth experiments, the data are stored in different subdirectories on the computer than the experiment number listed in this thesis. Experiment 4 is stored in the second subdirectory and Experiment 2 is stored in the fourth subdirectory. Also, experimentally there is a difference in the number of frequencies measured from the first three experiments and the last six experiments. In the first three experiments the data was taken using 50 Hz increments while the final six were taken using 100 Hz increment. The range of frequencies measured was same for all experiments (2 kHz to 12 kHz).

Finally, it should be noted that the 180 degree phase factor present in the force gage calibrations was not subtracted out in the data acquisition programs. This phase factor is removed by any FORTRAN program that made use of the measured admittance data.

## BIBLIOGRAPHY

1. Powell, A., "On the Failure of Structures Due to Vibrations Excited by Random Pressure Fields," *Journal of the Acoustical Society of America*, 30, pp. 1130-1135 (1958).
2. Bozich, D. J., "Spatial Correlation in Acoustic-Structural Coupling," *Journal of the Acoustical Society of America*, 36(1), pp. 52-58 (1967).
3. Aupperle, F. A. and R. F. Lambert, "Acoustic Radiation from Plates Excited by Flow Noise," *Journal of Sound and Vibration*, 26(2), pp. 223-245 (1973).
4. Aupperle, F. A. and R. F. Lambert, "On the Utilization of a Flexible Beam as a Spatial Filter," *Journal of Sound and Vibration*, 24(2), pp. 259-267 (1972).
5. Uberoi, M.S. and S.G. Kovasznay, "On the Mapping and Measurement of Random Fields," *Quarterly of Applied Math*, 10, pp. 375-393 (1953).
6. Maidanik, G. and D. W. Jorgensen, "Boundary Wave-Vector Filters for the Study of the Pressure Field in a Turbulent Boundary Layer," *Journal of the Acoustical Society of America*, 42(2), pp. 494-501 (1967).
7. Blake, W. K. and D. M. Chase, "Wavenumber-Frequency Spectra of Turbulent Boundary Layer Pressure Measured by Microphone Arrays," *Journal of the Acoustical Society of America*, 49(3-II), pp. 862-877 (1971).
8. Gaskill, J. D., *Linear Systems, Fourier Transforms, and Optics*, John Wiley and Sons, New York, 1978.
9. Hutto, F. M., "Wavenumber-Frequency Response of Free-Free Timoshenko Beams with Multiple Sources," Master's Thesis, The Pennsylvania State University (1986).
10. Robert, G. and J. Sabot, "Use of Random Forces to Simulate the Vibroacoustic Response of a Plate Exited by a Hydrodynamic Turbulent Boundary Layer," *Symposium on Flow-Induced Noise and Vibrations*, pp. 53-61 ASME Winter Annual Meeting, Dec. 9-14 (1984).
11. Strawderman, W., "Development of a Prototype Wavector-Frequency Spectral Analysis System," *NUSC TD 7295*, 1978.
12. Thompson, W. Jr., personal communication (1987).
13. Sackrider, D. J., W. J. Hughes and R. L. Kerlin, personal communications, (1986-1987).

14. Brigham, O. E., *The Fast Fourier Transform*, Prentice-Hall Book Inc., Englewood Cliffs, NJ, 1974.
15. Bracewell, R. N., *The Fourier Transform and Its Applications*, McGraw-Hill Book Company, New York, 1978.
16. Oppenheim, A. V. and R. W. Schaffer, *Digital Signal Processing*, Prentice-Hall, Inc., Englewood Cliffs, NJ, 1975.
17. Huang, T. C., "The Effect of Rotary Inertia and Shear Deformation on the Frequency and Normal Mode Equations of Uniform Beams with Simple End Conditions," *Journal of Applied Mechanics*, 28(4), pp. 579-584 (1961).
18. Cowper, G. R., "The Shear Coefficient in Timoshenko's Beam Theory" *Journal of Applied Mechanics*, 33, pp. 335-340 (1966).
19. Huang, T. C., "Orthogonality and Normalizing Conditions of Normal Modes and Forced Vibrations of Timoshenko Beams," *Developments in Mechanics, Proceedings of the Ninth Midwestern Mechanics Conference*, 3(2) pp. 63-70 (1965).
20. Dallas, A. G., personal communication (August, 1988).
21. Magrab, E. B., *Vibrations of Elastic Structural Members*, Sijthoff and Noordhoff, Germantown, MD, 1979.
22. Junger, M. C. and D. Feit, *Sound, Structures, and Their Interaction*, MIT Press Cambridge, MA, 1986.
23. Berlincourt, D. A., D. R. Curran and J. Jaffe, "Piezoelectric and Piezomagnetic Materials and Their Functions in Transducers," *Physical Acoustics Vol I part A*, W.P. Mason, editor, Academic Press (1964).
24. Beranek, L., *Acoustics*, American Institute for Physics (for the Acoustical Society of America), Cambridge, MA, 1986.
25. "Piezoelectric Technology Data for Designers," Vernitron Piezoelectric Division, Bedford, OH.
26. Chapman, J. R., "Model-Scale Measurements of the Transmission and Radiation of Hull-Borne Vibrational Energy Using Frequency/Wavenumber Analysis," *Shipboard Acoustics, Proceedings ISSA*, J. Buiten editor, Martinus Nijhoff Publishers (1986).